Approach to consider welding residual stresses in fatigue analysis using numerical simulations

Vom Promotionsausschuss der
Technischen Universität Hamburg

zur Erlangung des akademischen Grades

Doktor-Ingenieur (Dr.-Ing.)

genehmigte Dissertation

von
Nils Johan Friedrich

aus
Göttingen

2020

Gutachter:

Prof. DSc. (Tech.) Sören Ehlers

Prof. Dr.-Ing. Shahram Sheikhi

Prof. Mohammad Al-Emrani

Tag der mündlichen Prüfung: 14.09.2020

Abstract

Although it is known that residual stresses may influence the fatigue strength of welded structures, they are usually not included explicitly in fatigue assessments. In this thesis the influence of welding residual stresses on fatigue is investigated using numerical simulations and experimental tests to develop an approach to consider welding residual stresses in fatigue analysis. A numerical welding simulation approach using a prescribed temperature heat source is described and the influence of various simulation parameters on the resulting residual stresses is assessed. The simulations are used to design small-scale specimens containing a multilayer K-butt weld and a longitudinal stiffener with tensile transversal residual stresses at the weld toe. Residual stresses are measured by X-ray diffraction and hole drilling on both specimen geometries and the simulation results are verified. Fatigue tests at different load ratios are conducted on both specimen geometries. The initiation of macroscopic cracks is detected using digital image correlation. The influence on crack initiation and propagation show differences for both investigated weld geometries. A correlation between the fatigue test results and the calculated stresses is found. Based on these findings an approach to predict S-N curves depending on the residual stress condition and stress ratio is developed. The approach is based on the presented numerical welding simulations and allows to consider the influence of welding residual stresses in fatigue analysis.

Contents

List of symbols

a	throat thickness
b	width
e	linear misalignment
F	force
$f(R_{toe})$	correction factor for stress ratio at the weld toe
h_s	height of the stiffener
k	slope exponent
l	length
l_s	length of the stiffener
N	endurable number of load cycles
N_{total}, $N_{initiation}$, $N_{propagation}$	endurable number of load cycles for total fatigue life, crack initiation and propagation
N_R	reference number of load cycles $= 2 \cdot 10^6$
R	load ratio $\sigma_{nominal,min}$ / $\sigma_{nominal,max}$
R_{toe}	stress ratio at the weld toe
R_{eH}	yield strength
t	thickness
t_s	thickness of the stiffener
u_x, u_y, u_z	displacement in x, y and z-direction
Δf	deviation from loading frequency at the start of the test
$\Delta\sigma$	stress range
$\Delta\sigma_R$	reference stress range at $N_R = 2 \cdot 10^6$
$\Delta\sigma_{effective}$	effective stress range at the weld toe considering the correction factor $f(R_{toe})$
$\Delta\sigma_{toe}$	stress range at the weld toe
φ	angular distortion
σ_{max}, σ_{min}	upper and lower stress of a load cycle
$\sigma_{nominal}$	nominal stress

Abbreviations

APDL	ANSYS Parametric Design Language
ASTM	American Society for Testing and Materials
CL	Centre Line
DIC	Digital Image Correlation
FE	Finite Elements
FEM	Finite Element Method
FKM	Forschungskuratorium Maschinenbau
HFMI	High Frequency Mechanical Impact treatment
IIW	International Institute of Welding
LTT	Low Transformation Temperature filler materials
MAG	Metal Active Gas welding
TIG	Tungsten Inert Gas
TRIP	Transformation Induced Plasticity

1 Introduction

1.1 Motivation

Over a century after the introduction of arc welding for industrial applications, the involved distortions and residual stresses still represent a challenge for engineering applications. Especially in fatigue analysis of welded structures they are sources of uncertainties.

Distortions due to temperature and phase dependent strains, caused by welding, may become clearly visible and may affect manufacturing accuracy, particularly on large structures (Malisius 1977). Experience and calculation approaches of different complexity allow the prediction of these distortions and to take action to reduce them. Less obvious are the residual stresses induced by welding. Although they can reach the magnitude of yield strength, their measurement requires some effort and is not always possible without destroying or damaging the welded component. Therefore it is often difficult to quantify their influence on strength properties. In addition, welding residual stresses depend on many parameters such as material, welding technique, conditions and sequence or the size of the component, making it difficult to predict them or establish universal rules to cope with them. Adding to the complexity, they are superimposed to load stresses which may lead to yielding and redistribution of the original residual stresses. Because of these difficulties and the resulting uncertainties in many engineering applications residual stresses are not directly considered.

Although it is long known that residual stresses influence the fatigue strength of welded components, the quantification of this influence is still problematic. The common assumption of residual stresses in the amount of yield strength is probably excessively conservative for many applications (Krebs et al. 2012; Hensel et al. 2017).

Under fatigue loading residual stresses are superimposed to load stresses. This changes the acting mean stress, respectively the stress ratio R, thus influencing fatigue. Tensile residual stresses will augment the mean stress deteriorating fatigue strength. Compressive residual stresses, on the contrary, will act beneficially. Although these effects are in principle known, many uncertainties still remain, making a practical consideration of welding residual stresses in fatigue assessments difficult.

It is often assumed that the influence of residual stresses is comparable to that of mean stresses, not taking into account that they are not equally distributed over the plate thickness. Furthermore, tensile residual stresses at the weld toe may be reduced due to plastification. It is therefore questionable if a residual stress value retrieved from the surface is adequate to assess the influence on fatigue. These uncertainties still demand for further investigations in order to fully understand the relationship between welding residual stresses and fatigue strength and to take practical benefit from it.

One challenge in the investigation and assessment of residual stresses is that their measurement is relatively complex and costly, the calculation by simulation still time consuming and often with limited accuracy. Adding to the difficulty, they are variable under loading since they may in part be relieved by plastic deformation. The influence of residual stresses will therefore depend not only on their initial value but also on the applied load.

Another difficulty when investigating the influence of residual stresses is that in small-scale specimens often no relevant residual stresses are present due to the lack of structural

constraints. Therefore most of the recent studies on the residual stress influence on fatigue have been conducted on weld geometries where residual stresses are present also in small specimens due to local restraints, e.g. stiffeners spaced longitudinally to the loading direction (longitudinal stiffeners). These specimens however, may not be considered representative for all weld geometries because of their particularly high stress concentration and often relative sharp notch radius. Fewer investigations exist on weld geometries for which residual stresses depend strongly on structural constraints (e.g. cruciform joints or butt welds) or on large-scale components.

Aim of this work is to develop an approach to improve fatigue analysis by including welding residual stresses with the aid of welding simulations. The state of the art of these three fields will be presented in the following.

1.2 State of the art

1.2.1 Welding residual stresses

Residual stresses are present inside a structure or component without external forces acting, thus they have to be in equilibrium (Radaj 1992). They are generally distinguished into first order residual stresses, extending over macroscopic areas and averaged over multiple crystallites. Second order residual stresses acting between crystallites and third order between atomic areas. In the following only macroscopic, first order residual stresses are considered.

Residual stresses are caused by fabrication processes or loads involving plastic or thermal strains. These cause a change in shape or dimension of the component, or part of it, which then result in residual stresses within the component. In particular, welding may induce high residual stresses. Welding residual stresses are mainly caused by the shrinkage of the weld zone during cooling and the restraint by the surrounding material. As the weld cools from melting to room temperature it contracts and exercises a force on the surrounding material. The shrinkage and the resulting residual stresses are sketched for the example of a butt weld in Figure 1-1. The weld contracts in all directions: longitudinal, transversal and thickness direction. The longitudinal shrinkage causes a curvature of the plate's edge along the weld. In the centre of the weld, this curvature is opposed to the transversal shrinkage of the weld. This causes the distribution of transversal residual stresses with tension in the centre and compression on the edges of the plate. Transversal and longitudinal residual stresses thus condition each other (Hänsch 1984).

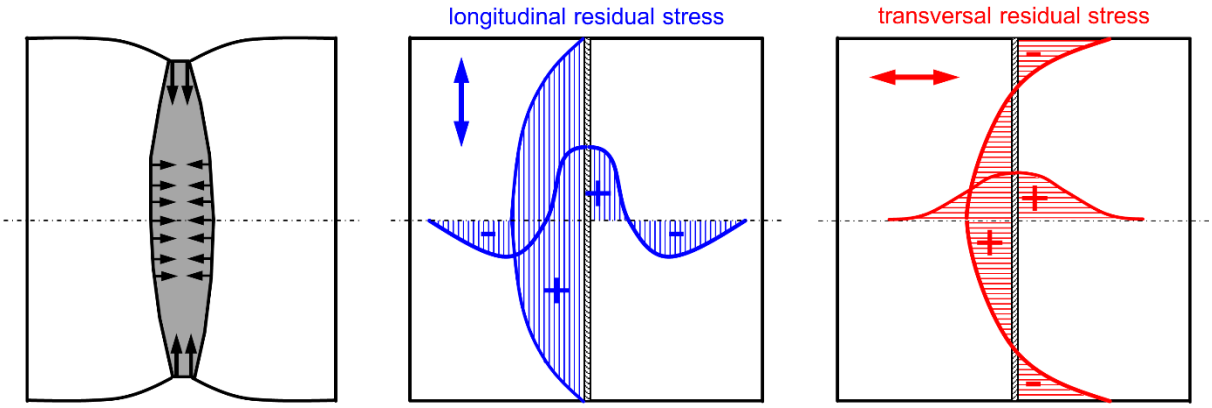

Figure 1-1: Shrinkage and residual stresses on a butt-weld; based on (Hänsch 1984).

This basic principle considers only the temperature dependent volume change in the residual stress formation. The actual height and distribution of welding residual stresses is influenced by a multitude of factors including phase transformation that will occur depending on the alloy. If the temperature exceeds the austenitising temperature, austenite forms in mild steels (Radaj 1992). During cooling, the austenite transforms back to a combination of martensite, ferrite, pearlite or bainite (Francis et al. 2007). The crystal system changes from face-centred cubic to body-centred cubic which results in a dilatation. The temperature interval in which this back transformation occurs depends on the carbon content of the material, the peak temperature, austenitisation time and cooling rate. The dilatation during the phase transformation causes the formation of compressive residual stresses. When the transformation is completed, the material contracts again as it cools to lower temperatures, leading to tensile residual stresses. The temperature interval of the back transformation has thus an influence on the final residual stress level. The effect of phase transformation depends also on the transformation induced plasticity (TRIP), which limits the forces exercised on the surrounding material and therefore reduces the residual stress reduction due to the dilatation (Radaj 2003).

Also geometric factors influence the formation of welding residual stresses. Plate thickness and the number of weld passes affect residual stresses as they determine local restraint (Nitschke-Pagel and Dilger 2006). They also influence cooling rates which affect phase transformation. Furthermore, the ratio between weld pass and surrounding material volume determines how the core and the borders of the weld cool off (Christian and Elfinger 1978). Both effects can influence the residual stress level at the weld toe relevant for fatigue. The weld sequence may as well affect residual stresses as it influences the restraint by the surrounding material. Tensile residual stresses adding to those resulting from previous welds may cause local yielding and thus relaxation of present residual stresses (Hänsch 1984).

Besides the local restraint by the surrounding material, also the global degree of constraint affects residual stresses. In which way residual stresses depend on the heated cross-section and structural constraints is discussed e.g. in (Malisius 1977). The length of the plate available to compensate the shrinkage of the weld zone by elastic strains determines the residual stress level in the plate adjacent to the weld. In this way also the size of a component influences residual stress levels. Residual stresses in small specimens will therefore differ from those in larger structures. Even the same geometry in different scales may not contain the same residual stresses.

An overview of welding distortions and residual stresses for different kinds of joints is given in (Neumann and Röbenack 1978). A catalogue of residual stress profiles for different weld geometries can be found in (Bate et al. 1997). Residual stresses are typically not constant over the plate thickness and often range from tensile to compressive.

To assess residual stresses several measuring techniques exist (Kandil 2001; Schajer, ed. 2013). These are generally divided in destructive and non-destructive techniques. In destructive methods, also called relaxation methods, the structural restraints are released by cutting, drilling or removing material. Residual stresses will consequently cause strains and distortions which can be measured and allow to calculate the original residual stresses. Destructive measurement methods include splitting, sectioning, layer removal, ring-coring and the contour method (Schajer, ed. 2013). Most popular is the hole drilling technique. The strains measured on the surface around the hole, by strain gauges or optically, allow the calculation of the residual stress profile from the surface to a depth of approximately half the

diameter of the hole. Although this method is practical because of its technical simplicity, it is limited to even surfaces and it is therefore difficult to apply on or very close to the weld. Furthermore, if residual stresses are high compared to yield strength, local yielding may affect the measured strains and compromise the accuracy of the calculated residual stresses (Pohle 1990).

Non-destructive methods are usually based on measuring the diffraction of radiation which depends on the elastic strain in the measured object. The radiation is reflected under a certain angle, which depends on the distance between atomic planes (Eigenmann and Macherauch 1995; Spieß et al. 2009; Schajer, ed. 2013). When the material is strained, the atomic plane distance and thus the diffraction angle changes. By determining the diffraction angle, stresses in the material are deduced. Most common is the use of X-ray diffraction which allows residual stress measurements up to a depth of a few microns (Kandil 2001). The use of synchrotron X-ray or neutrons as radiation, allows measurements up to a greater depth depending on the kind of radiation and the material of the specimen (Hutchings 2005). Due to the limited availability and costs involved in these methods, their use is very restricted, especially for large-scale structures.

Other non-destructive or semi-destructive methods are magnetic, ultrasonic, thermoelastic, photoelastic and indentation measurements (Schajer, ed. 2013).

All in all, residual stress measuring techniques are not generally available and often involve high expenses. On the other hand, results can easily be affected by inaccuracies or errors especially when measurements involve mechanical work on the specimen. A round robin showed large scatter between residual stresses measured at different laboratories and emphasized the need “for great care and for diversity in making such measurements” (Smith et al. 2019). Therefore, in most investigations, where residual stresses are not the main objective, they are usually not considered explicitly.

1.2.2 Welding simulations

Since the possibilities to measure residual stresses are often limited, assessing residual stresses by calculation might be advantageous. With respect to fatigue assessments, simulations offer the additional benefit that they provide the complete stress distribution including residual stresses at the weld toe, where fatigue cracks will typically initiate, and over the plate thickness, where they may affect crack propagation.

Simplified calculation approaches, in which shrinkage forces longitudinal to the weld or shrinkage in transversal direction are calculated analytically or empirically, exist and may provide relatively good results for welding distortions (Hänsch 1984; Radaj 1988; Neumann 1996). Such approaches in combination with the finite element method (FEM) have been applied for the calculation of distortions in (Jang et al. 2003; Xu et al. 2008; Deng 2010) and residual stresses in (Hill and Nelson 1995; Murakawa et al. 2010). However, when aiming for the residual stresses close to the weld, these methods will not provide satisfying results. For instance, the application of a longitudinal shrinkage force will cause compression in the weld, where instead it should be tension due to the shrinkage of the weld material and the restraints by the surrounding material. Furthermore, phase transformation effects will not be considered.

Welding simulations employing FEM have been developed and have become more and more applicable (Lindgren 2007; Radaj 2003). These simulations usually involve two steps. First, in a thermal analysis the temperature field due to a moving heat source is calculated.

Different types of heat sources exist, from simple point or line sources over volumetric distributed heat sources, prescribed temperature source, to more complex models including fluid dynamics or modelling of the arc. According to Goldak and Akhlaghi (2005) the best heat source model to choose depends on how accurately the heat source should be modelled, on the objective of the modelling and on what information is available. To predict distortions and residual stresses in low alloy steel structures, accurate temperatures below approximately 600 to 800°C are described to be most important. Commonly for arc welding a double ellipsoid heat source according to Goldak et al. (1984) is used (Figure 1-2). The asymmetrical shape approximates the heat distribution at the real molten pool. In order to set the dimensions of the heat source and the heat input correctly, it is necessary to calibrate the temperature calculation by means of experimental data. This is done by comparing measured and calculated temperatures close to the weld. Furthermore, the temperature distribution at the weld is compared to the weld pool and the heat affected zone in a macrograph of the weld. Simulation parameters are then iteratively adapted in order to match the calculated temperature distributions with the acquired experimental data. The calibration of the heat input in the thermal part of the analysis is often considered a pre-requisite for reliable residual stress and distortion results (Caprace et al. 2017).

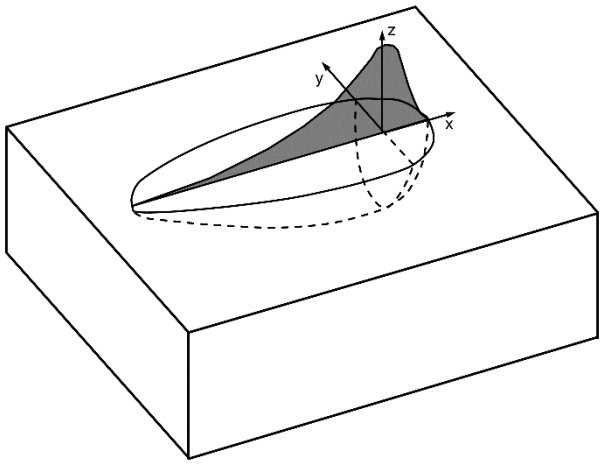

Figure 1-2: Double ellipsoid heat source and power distribution function along the x axis; after (Goldak et al. 1984).

More complex models have been developed including e.g. the simulation of the weld pool geometry (Sudnik et al. 2000; Kong et al. 2012), weld pool dynamics to predict the final weld shape (Cho et al. 2013) or heat and fluid flow in laser welding (Curtois et al. 2019).

After calculating the temperature distribution, it is used as load input in an elastic-plastic structural analysis to calculate the structural response in terms of residual stresses and distortions. Both simulation parts require temperature dependent material properties. In (Wichers 2006) these have been determined for S355J2G3 steel.

Phase transformation might also be included in the simulations (Lindgren 2007). Depending on the material and the welded geometry this may have significant influence on the calculated residual stresses close to the weld. In (Dilger, ed. 2006) dilatometer curves for different steels were determined and parameters influencing phase transformation have been investigated. Numerical investigations on different influencing factors for residual stresses including phase transformation have been conducted by Hildebrand (2008).

For the calculation of global welding distortions and residual stresses, shell-element models can be used (Olsen et al. 2001; Dong et al. 2002; Kim et al. 2014). For geometries with constant cross-section and relative long welds it might be suitable to use 2D-models as in (Grünitz and Fricke 2004; Barsoum and Barsoum 2009). However, if the local residual stress at the weld in a complex geometry has to be assessed, the use of 3D-solid elements is necessary. In combination with a relatively fine mesh at the weld to account for high temperature and stress gradients, this results in large numbers of elements even for relatively small components. The model size further increases when multilayer welds are included.

With the number of weld layers also the number of load steps to be solved increases. The combination of a complex simulation, large numbers of elements and of load steps can quickly lead to simulation times of several days or weeks (Fricke and Zacke 2014). This still limits the practical application of welding simulations to relatively small models. To reduce the number of load steps and thus the calculation time, multiple weld layers have been combined in (Josefson and Karlsson 1988; Shim et al. 1992; Hong et al. 1998). Another possibility to reduce the calculation time is to summarize sections of the weld and perform a blockwise simulation. This method, called block dumping (Pahkamaa et al. 2010), has been applied in (Elcoate et al. 2005; Karlsson et al. 2011) and further developed in (Bhatti and Barsoum 2012). In (Zacke 2012) the joining of two ship sections has been simulated by combining multiple weld layers and using a relatively large time step size to reduce the number of load steps. Although these methods yield good results for surface residual stresses, if the correct parameters are chosen, the residual stress distribution over the plate thickness may differ significantly from a transient simulation (Klassen et al. 2016). Simplified simulation approaches for multilayer welds were studied in (Klassen 2018). It was found that geometrical simplifications of the modelled weld shape can produce good results in terms of residual stresses while reducing simulation times. Whereas, approaches aiming to reduce the number of calculated load steps (e.g. application of thermal cycles or lumping of weld passes) may produce poor results compared to transient simulations.

Since fatigue strength depends on the stabilised residual stress state under cyclic loading, also the residual stress redistribution due to loading has been included in simulations e.g. in (Varfolomeev et al. 2011). Different hardening laws for the simulation of residual stress relaxation under loading have been compared in (Stoschka et al. 2014). Recently, post-weld mechanical impact treatments have also been included in FEM simulations to investigate the stability under loading of beneficial compressive residual stresses (Yuan and Sumi 2015; Tsutsumi et al. 2016; Foehrenbach et al. 2016; Leitner et al. 2016).

Despite the high numerical effort necessary to carry out welding simulations, the resulting residual stresses have to be evaluated with caution. Often results obtained with different modelling techniques or different simulation parameters differ significantly (Wohlfahrt et al. 2012). The comparison with measurements often shows quite large divergences as well. On the other hand, it has to be considered that also measurement results may scatter significantly. A study on joining process simulations (Stadtaus and Dilger 2004), including welding simulations, concluded that a verification through measurements is still necessary and that their application is still restricted to research and development by large concerns and research institutions.

1.2.3 Residual stress influence on fatigue

Although many studies have been conducted on how residual stresses affect the fatigue strength of welds, the results are often not consistent (Krebs et al. 2012). In many cases in which as-welded and stress-relieved specimens have been compared, other influencing factors have not been precisely determined. In addition, the residual stress level at the weld is influenced by so many parameters and often shows large scatter even for the same geometry, that it becomes difficult to draw generalized conclusions.

As residual stresses are superimposed to load stresses they shift the actual stress ratio as shown in Figure 1-3. Without residual stresses the actual stress ratio corresponds to the nominal stress ratio. Since compressive stresses contribute less (or not at all) to the fatigue damage, high stress ratios are more damaging than lower stress ratios. Thus, for the same stress range, the number of endurable load cycles will increase with decreasing stress ratios. In the presence of residual stresses the actual stress ratio does not correspond to the applied nominal stress ratio. In case of tensile residual stresses the actual stress ratio is shifted towards tension. The upper stresses are limited by the yield limit. Depending on the height of the residual stresses and the applied stress range, the actual stress ratio will be the same independently of the applied load ratio (Gurney 1979). Thus, the influence of the applied stress ratio on the fatigue strength is diminished in presence of residual stresses.

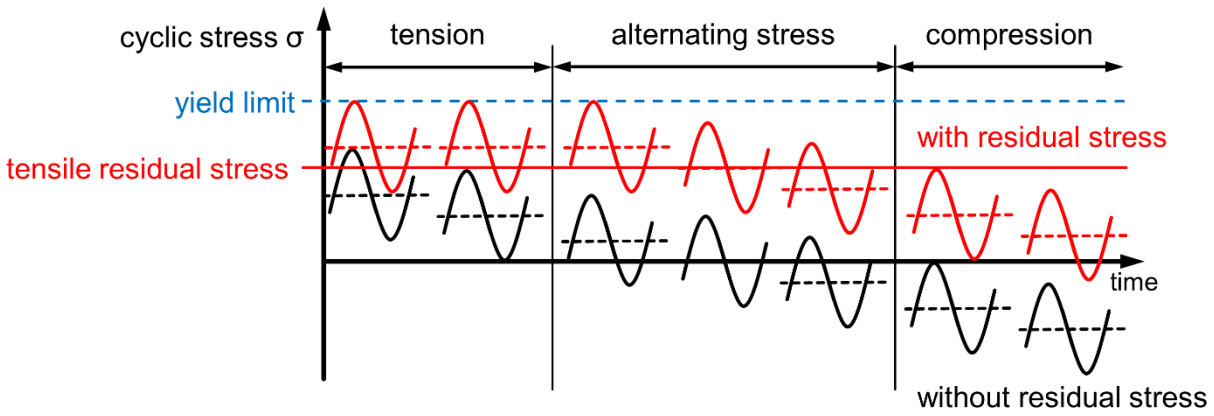

Figure 1-3: Load cycles without residual stresses (nominal stress ratio) and with residual stresses (actual stress ratio); based on (Gurney 1979).

In fatigue assessments it is often assumed that tensile residual stresses to the amount of yield strength are present (Maddox 1991). In current standards such as the IIW recommendations (Hobbacher 2016) or the guidelines by FKM (2012) residual stresses may be considered through the mean stress sensitivity. Depending on the geometry and size of the component three levels are distinguished: low, medium and high residual stresses. For welds high (tensile) residual stress is assumed to be the standard case if no information on the actual residual stress level is given, thus no benefit from low stress ratios ($R < 0.5$) is allowed. In Eurocode 3 (2010) for non-welded or stress-relieved welded details a reduction of the compressive portion of the stress range to 60% is possible. A consideration of the actual residual stress levels is not allowed. An extensive review of investigations on the residual stress influence on fatigue has been performed by Krebs and Kassner (2007). Based on the results they have proposed to consider the mean stress sensitivity based on four cases of weld geometries with different residual stress levels.

On the other hand, it has been shown that high tensile residual stresses at the weld may be relaxed in the first load cycles when subjected to tensile loading (Farajian et al. 2010; Varfolomeev et al. 2011; Farajian 2013) and so the influence on fatigue is reduced. Since

this relaxation is caused by local yielding according to the von Mises criterion, it depends on the superposition of residual stresses and load stresses. The latter are determined by the stress concentration depending on the weld geometry.

On longitudinal stiffeners residual stresses are often found to have only little influence on fatigue strength under pulsating tensile stress (Baumgartner and Bruder 2013; Yuan and Sumi 2013). In (Varfolomeev et al. 2011; Siegele et al. 2013) numerical and experimental investigations showed a reduced residual stress influence on longitudinal stiffeners. This was explained by the decrease of transversal residual stresses in proximity of the weld and residual stress relaxation after the first load cycles. In (Hensel et al. 2016) tests on straightened specimens showed an influence also for longitudinal stiffeners, leading to the conclusion that welding distortion may have covered residual stress effects in some previous studies.

According to Nitschke-Pagel (1995), on transversal welds the highest (transversal) residual stresses occur in the middle of the weld, not at the weld toe critical for fatigue cracks. And only in certain cases including high strength steels, residual stresses will have a noticeable influence on fatigue strength. These results are based on small-scale specimens. Buxbaum (1986) has found different mean stress sensitivities for small-scale and structure-like specimens on butt welds and transversal stiffeners due to lower residual stresses in small specimens. Farajian et al. (2010; Farajian 2013) tested large-scale specimens with butt joints and found that the residual stresses were partly relaxed during the first load cycles and that in high strength steel this relaxation resulted lower if the same load level was applied. On the other hand, in the study by Krebs and Kassner (2007) it is assumed that on thick-walled cruciform joints residual stresses will affect fatigue strength because their relaxation is reduced due to multiaxial residual and load stresses. However, this assumption has not been proved yet. Although it is commonly assumed e.g. in (Buxbaum 1986; Hobbacher 2016) that welding residual stresses in large structures are higher than in small specimens, a systematic investigation to quantify how residual stress levels and distributions differ due to structural constraints needs still to be done.

It can be seen that the effective residual stress level relevant for fatigue depends on the residual stress relaxation under loading. This relaxation on the other hand is determined by the initial residual stress level but also by the applied load level, the weld geometry and the yield strength of the material. In other cases the initial residual stresses may even be compressive at the weld toe having a beneficial influence on fatigue strength (Fricke 2005; Yuan and Sumi 2013; Baumgartner 2013). This calls for a fatigue approach that includes the actual residual stresses acting at the weld. Based on his findings, Baumgartner (2013) has developed an approach to calculate crack initiation and propagation considering the local notch geometry and residual stresses. Yet the determination of the residual stress at the weld toe has resulted problematic.

These considerations often take into account only the residual stresses at the surface. But the residual stress distribution at the weld is usually not uniform over the plate thickness as it may vary between tensile and compressive values. Apart from the residual stress level at the surface, which will affect crack initiation, crack propagation will be influenced by the residual stress state at the tip of the crack. Therefore also the residual stress distribution over the thickness will affect their influence on fatigue strength. Relationships between size respectively plate thickness effect and residual stresses are described in (Gurney 1979; Ohta et al. 1984; Niemi et al. 2006). In (Rörup 2003) the influence under compressive pulsating

stresses has been investigated for longitudinal stiffeners. Crack initiation under compressive loading has been explained by tensile residual stresses at the weld. Compressive residual stresses have been shown to slow down crack propagation in (Tateishi et al. 2013).

The residual stress distribution over plate thickness will therefore influence both crack initiation and propagation. Assuming e.g. that the highest tensile residual stresses act on the surface in equilibrium with compressive residual stresses present deeper in the plate, crack initiation and propagation will be affected differently by residual stresses. In (Chattopadhyay et al. 2011) numerical investigations on the crack initiation and crack propagation considering residual stresses at a tubular joint with the weld geometry similar to a longitudinal stiffener have been performed. In presence of residual stresses the part of crack initiation in total fatigue life was approximately doubled. Since different weld geometries show different ratios between crack initiation and crack propagation, also the influence by residual stresses is expected to differ.

Different approaches to reduce welding residual stresses and obtain better fatigue properties exist. Inducing compressive residual stresses by mechanical impact treatments such as peening or high frequency mechanical impact treatment (HFMI) has been shown to effectively improve fatigue strength especially for high strength steel (Leitner et al. 2014). The influence of mechanical post-weld treatments and their consideration in fatigue assessments has been investigated in (Weich 2008). Another possibility is to reduce residual stress using low transformation temperature (LTT) filler materials (Bhatti et al. 2013; Shiga et al. 2015). These methods become more relevant with the increasing use of high strength steel, for which residual stresses have been found to be higher and more stable under loading. In order to make effective use of such procedures and benefit from them, methods to identify critical cases and rules to account for the beneficial effects have to be developed. Procedures to include post-weld treatments in fatigue assessments have been investigated in (Günther and Kuhlmann 2009; Ummenhofer and Weidner 2014). The effect is in part attributed to compressive residual stresses induced on the component surface. These compressive residual stresses have been considered explicitly in (Weich 2008). Unlike residual stresses from mechanical post-weld treatments, welding residual stresses are not limited to the component surface and may vary from tensile to compressive over the plate thickness. Furthermore, they strongly depend on the weld geometry and structural constraints. The findings from mechanical post-weld treatments may therefore not be transferred to welding residual stresses without further verification. An approach considering the effective stabilised welding residual stress level under loading is proposed by Hensel et al. (2017) based on findings from longitudinal stiffeners. Other weld geometries were not included, which demands for further investigations. Residual stresses were determined at the weld toe. On the other hand, in (Hensel et al. 2016) prestressing or annealing resulted in a higher fatigue strength improvement than shot peening. This was explained by lowered residual stresses through the plate thickness, as compared to shot peening affecting only the specimen surface. The question if a single residual stress value on the surface is sufficient to determine the influence on fatigue strength demands for further research.

An obstacle in the research on welding residual stresses and in their explicit consideration in fatigue assessments still remains their determination. Because of the many influencing factors a case by case identification of the residual stresses and their variation under loading is generally necessary. More and more, numerical simulation methods are employed to investigate residual stresses (Do et al. 2015; Lee et al. 2016; Yuan and Sumi 2016). Simulation methods will also become important to practically include welding residual stress

values in fatigue design, since measurements are not commonly available and not applicable during design phase.

All in all, experimental data and knowledge on the influence of welding residual stresses on fatigue has already been established. Small specimens with longitudinal stiffeners, used in most studies, offer the advantage to be practicable and less expensive for experimental tests and contain relatively high tensile residual stresses at the weld. Small-scale specimens with transversal welds on the other hand, usually show only little transversal residual stresses at the weld toe. It has to be assessed in which way findings on the residual stress influence on a certain weld geometry are applicable to others, since residual stress distributions and relaxation but also crack initiation to propagation ratios may differ significantly.

1.3 Objectives and scope

The overall objective is to develop an approach to include the influence of welding residual stresses in fatigue analysis through numerical welding simulations. For this purpose it has to be determined, how welding residual stresses influence fatigue strength on different weld geometries, how the residual stresses may be determined using welding simulations and how they can be considered in fatigue analysis.

Experimental tests will give insights into the following questions:

- How do residual stresses influence crack initiation and propagation?
- How does this influence compare for a weld transversal to the loading direction and longitudinal stiffeners?
- Is the influence equal to that of mean stresses?

From the numerical investigations these objectives will be elaborated:

- Practical numerical simulation approach to determine welding residual stresses and stresses under loading
- Development of an approach to include residual stresses in fatigue analysis

Since welding residual stresses and fatigue properties depend on the weld geometry, two different geometries are included in the investigations. This allows to clarify how the residual stress influence compares for transversal welds and longitudinal stiffeners. Furthermore it allows to validate the final approach on both types of geometry.

Residual stresses are not uniform over the plate thickness. This leaves the question how residual stresses influence crack initiation and propagation. And if it has to be considered when including welding residual stresses in fatigue analysis.

Associated with this is the question how the influence of residual stresses compares to the mean stress influence. Is it suitable to predict the influence of residual stresses using a single value that shifts the actual mean stress?

The developed approach will be based on numerical simulations. To be applicable also during design phase, the selected welding simulation approach should work without experimental calibration. Furthermore, it must allow to include the simulation of external loads to calculate the stresses at the weld during loading.

Moreover, it has to be assessed how such residual stress values determined at the weld can be incorporated in a fatigue analysis based on nominal stress.

1.4 Limitations

The approach to include welding residual stresses in fatigue analysis will be based on numerical simulations and experimental tests. Residual stresses and fatigue properties are influenced by a vast number of factors, which cannot all be included in the investigations. Therefore, the following limitations apply to the results and the proposed approach.

- The investigations are limited to steel of grade S355 and metal active gas (MAG) welding. The results should not be transferred to other materials or weld processes without further verification.
- In the welding simulations the same material properties are used for base material, weld and heat affected zone. Phase transformation is included by a simplified model and restricted to the elements within the weld. The influence of different weld materials, e.g. LTT filler materials, cannot be considered with this model.
- Welding residual stresses may be changed by post-weld treatments, e.g. peening or tungsten inert gas (TIG) remelting. Such processes could theoretically be included in a numerical simulation but are not within the scope of this thesis.
- The specimens used for the verification of the calculated residual stresses have a plate thickness of 10 mm. On thin plates a more accurate consideration of heat convection and radiation on the surface might be necessary. The simulation approach should not be applied to thin plate thicknesses (smaller than approx. 5 mm) without further verification.
- In the simulations the loads are applied statically and cyclic material properties are not included in the models. Thus, only the residual stress relaxation after the first load cycle is included in the numerical results. A possible influence of cyclic material properties on residual stresses is not considered.
- The fatigue tests are conducted with constant amplitude loading. Due to residual stress relaxation under loading, variable amplitude loading or high static preloads will affect the influence of welding residual stresses on fatigue.
- The fatigue tests are conducted in the high-cycle domain ($N < 10^7$). The fatigue limit, where the S-N curve presents a knee point and enters infinite endurance, is not determined in the tests.
- Small-scale specimens without external constraints are used in the tests. The influence of structural constraints, e.g. within a larger structure, are not investigated.
- The studied FE models and test specimens contain only one weld. The influence of multiple welds within a component are not investigated.
- Only welding residual stresses and fatigue cracks at the weld toe are investigated. Residual stresses within the weld or cracks originating from the weld root are not considered.
- Welding distortions calculated in the numerical simulations are not validated in detail. It is just verified that they lie within the scatter of measurements. The investigations are focused on residual stresses.

1.5 Outline of the work

To meet the objectives outlined in section 1.3 both numerical and experimental investigation are performed (Figure 1-4).

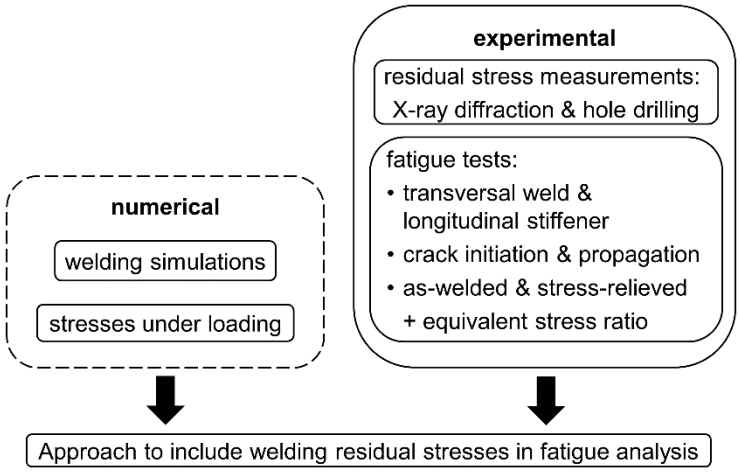

Figure 1-4: Numerical and experimental investigations.

First, the welding simulation approach is examined. The welding simulations will be used in combination with experimental tests to investigate welding residual stresses and their influence on fatigue. But they will also be the base of the approach to consider welding residual stresses in fatigue assessments. Therefore, a simulation approach without experimental calibration of the heat source is selected. In a parameter study the influence of different simulation parameters on the resulting residual stresses is determined.

Welding simulations are then used to design the small-scale specimens for the following experimental investigations. Two different weld geometries with a multilayer transversal weld and a longitudinal stiffener are included. Except for longitudinal stiffeners, welding residual stresses generally have little influence on the fatigue properties of small-scale specimens. Therefore, the simulations are used to identify geometrical and welding parameters that will produce considerable tensile residual stresses at the weld toe of a multilayer weld. The test specimens are produced according to the design established using the simulation results.

Residual stresses are measured on the prepared specimens. To overcome the uncertainties of a single measurement, two different measuring techniques are applied, X-ray diffraction and hole drilling. The measurements are used to assess the residual stresses present in the test specimens and to verify the results of the welding simulations.

Fatigue tests are performed with the two specimen geometries. To determine the residual stress influence the specimens are tested in the as-welded and stress-relieved condition. Since the residual stress influence depends on the stress ratio, the tests are performed at different load ratios from compressive to tensile. To differentiate the influence on crack initiation and propagation, the initiation of macroscopic cracks is detected during the fatigue tests using digital image correlation. In this way, besides the S-N curves for total fatigue life, S-N curves for crack initiation and propagation are established. To compare the residual stress influence to that of mean stresses, in a further test series, stress-relieved specimens are subjected to equivalent loads that produce the same stresses at the weld toe as the combination of residual stress and load stress.

Based on the findings from the fatigue tests and the correlation with the simulation results, an approach to consider welding residual stresses in fatigue analysis is developed.

2 Welding simulation approach

In this thesis welding simulations are used alongside measurements and experiments to study and understand the distribution of welding residual stresses and their influence on fatigue. The final objective is then to develop an approach using simulations to predict the influence of welding residual stresses on fatigue properties.

This poses certain requirements to the selected simulation approach. The investigated fatigue cracks are expected to initiate at the weld toe and then propagate orthogonal to the loading direction. Therefore, correct residual stresses have to be calculated at the weld and within the investigated structure. Since residual stresses will be superimposed to load stresses, the simulations need to include welding and loading too. The accuracy of the resulting residual stresses has to be good enough to assess their influence on fatigue. As the simulations will be used to predict residual stresses, the selected approach should work with minimal input data and without experimental calibration.

To fulfil the above requirements an approach is selected that includes the transient simulation of all weld passes, is implemented in a common structural mechanics FE software and uses a prescribed uniform temperature heat source.

The simulations are performed in the FE code ANSYS Mechanical 15.0 using user-subroutines written in APDL (ANSYS Parametric Design Language). The routines are based on (Wichers 2006) but were rewritten and expanded.

The welding simulations are intended for arc welding and consist of two parts. First, the welding energy is applied to the model and the temperature distribution over time is calculated in a transient thermal analysis. In the following elastic-plastic structural analysis the calculated temperatures are applied as load and the resulting residual stresses and distortions are calculated.

2.1 Thermal analysis

The first part of the welding simulation consists in a transient thermal analysis in which the welding energy is applied to the FE model as load. The only degree of freedom of the elements is temperature. The temperature distribution in the model is calculated by solving the heat conduction equation.

A prescribed uniform temperature heat source is used to apply the welding energy to the model. The heat source is compared to the widely used heat source according to (Goldak et al. 1984) in Figure 2-1. The Goldak heat source describes a volumetric double ellipsoid power density distribution (Figure 1-2). The plotted temperatures are the result of the heat input on the elements reached by the heat source. The dimension of the heat source and the efficiency coefficient for the heat input are usually calibrated using experimental data. In the prescribed temperature heat source a uniform temperature is applied directly to the nodes of the weld cross-section.

At the beginning of the simulation all weld elements are deactivated i.e. their heat conductivity is set close to zero. In each time step a short section of the weld (12 mm) is selected and activated. A temperature of 1300°C is applied to this section. This temperature and the length of the section are based on experience but are largely arbitrary. Each time step the selected section advances along the weld by the welding speed times the time step size. The time step size is set to 0.5 s respectively 0.25 s close to the region of interest or for

the last applied weld passes in case of multilayer welds. Welding speed is assumed to be 7.8 mm/s based on a mean value from previous experimental works. With this combination the heated element selection will overlap with that from the previous time step.

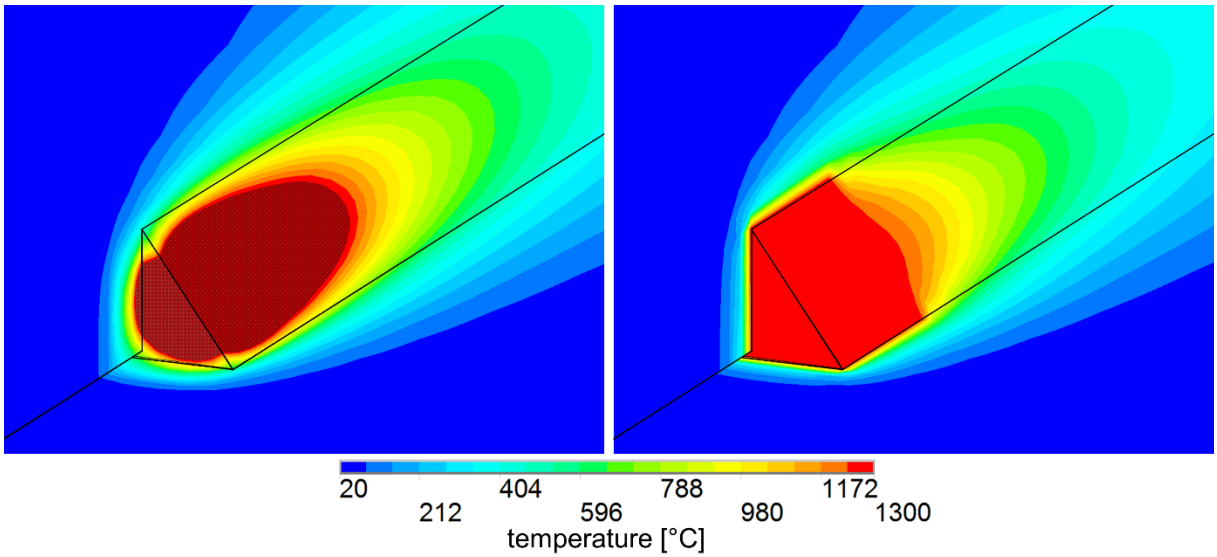

Figure 2-1: Temperatures at a double-ellipsoid Goldak heat source (left) and prescribed uniform temperature (right) applied on a fillet weld (dark red > 1300°C) (Friedrich and Ehlers 2019a).

Starting from the heat source at the weld, the energy will spread in the model. The resulting temperature distribution is determined by the heat conductivity and specific enthalpy of the simulated material. Temperature dependent material properties are taken from (Wichers 2006) and plotted in Figure 2-2.

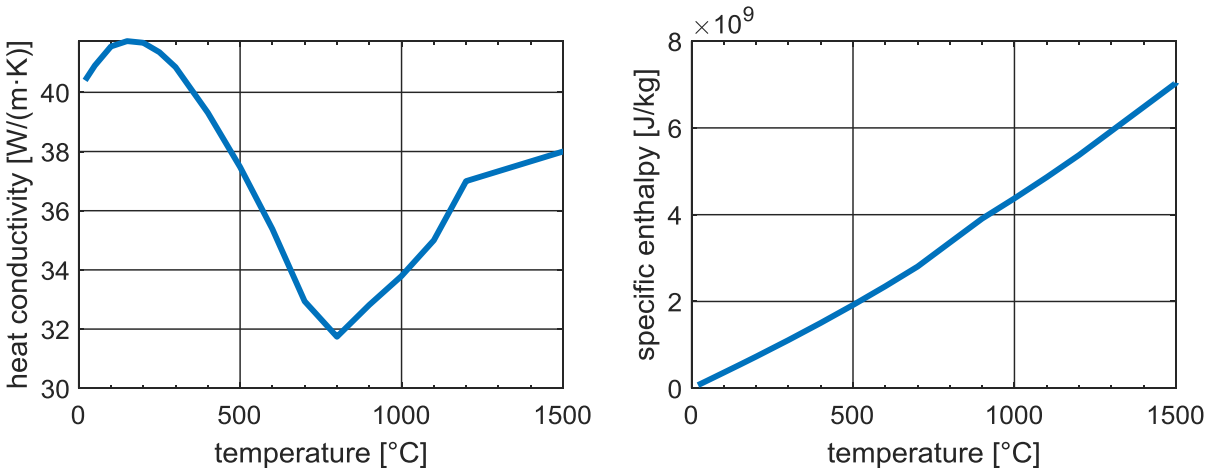

Figure 2-2: Temperature dependent material properties for the thermal analysis from (Wichers 2006).

To consider the heat exchange with the surrounding air for each time step the radiation and convection at the surface of the geometry is calculated according to the analytical formulas given in (VDI 2010). The surface of the model, including the surface of the top weld passes, is roughly divided into rectangles. The average temperature is then calculated for each rectangle and the coefficients for radiation and convection are applied to calculate the heat exchange. The emission rate is set to 0.8. For the considered plate thicknesses > 5 mm cooling close to the weld is mainly driven by heat conductivity in the plate. Thus, radiation and convection have little influence on the temperature at the weld and even less on the resulting residual stresses. During cooling, between the application of each weld pass and after the last weld pass, time step size is kept constant until the temperature decrease per

time step is smaller than 5 K. At this point, the time step size is doubled and kept constant until the decrease is again smaller than 5 K.

The result of the thermal analysis is the temperature distribution in the model for each time step.

2.2 Structural analysis

In the following structural analysis the calculated temperatures are applied as loads. The same time steps as before are now solved statically. The same FE model as for the thermal analysis is used but the element type is changed to structural solid elements with translation degrees of freedom in *x*, *y* and *z*-direction. All elements of the simulated welds are first deactivate. They are sequentially activated when reached by the temperature field of the heat source. Strains and stresses are calculated based on temperature dependent material data. The curves for stress-strain, Poisson ratio, thermal expansion are taken from (Wichers 2006) and have been slightly smoothened (Figure 2-3 and Figure 2-4). The Young's modulus is increased to 215 GPa between 20°C and 300°C in order to improve the stability of the simulations. Kinematic hardening is used to determine the elastic–plastic material behaviour.

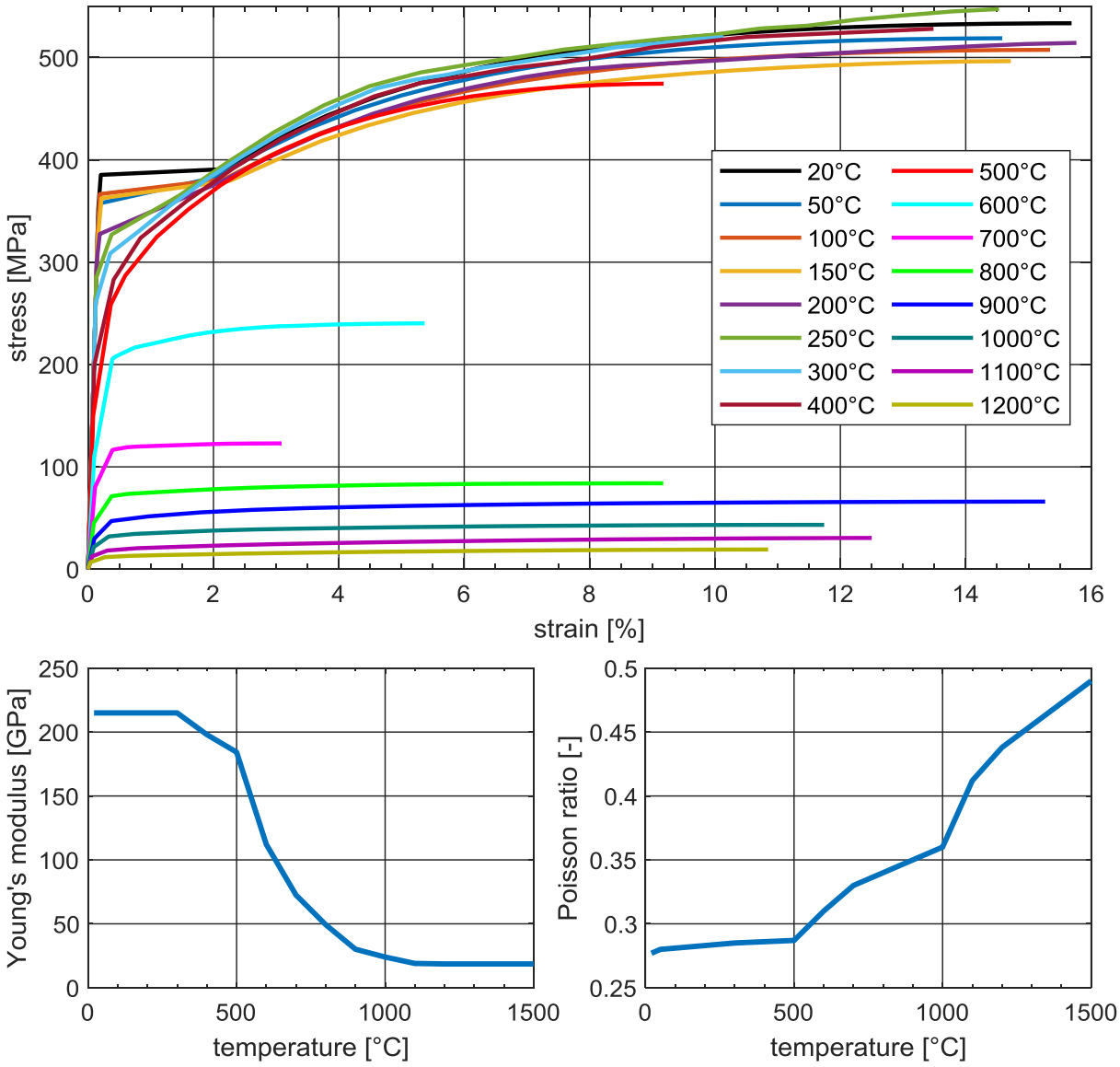

Figure 2-3: Temperature dependent material properties for the structural analysis from (Wichers 2006).

To consider dilatation during austenite back transformation a set of two thermal expansion curves is used as shown in Figure 2-4. When a node reaches 900°C the attached elements are switched to the second curve for cooling. The curve used for cooling is based on experimental data from (Dilger, ed. 2006). Austenite phase transformation is assumed between 400°C and 500°C. As a simplification this curve is used independently of the maximum reached temperature and the cooling rate. As the temperature is applied uniformly in the weld cross-section the temperature distribution close to the weld will not accurately reflect reality. Therefore, only elements of the weld are switched to the second curve for cooling simulating austenite phase transformation at a lower temperature. All other material properties are the same for weld, base material and heat affected zone. To consider transformation-induced plasticity, the yield strength is decreased during phase transformation (Figure 2-4).

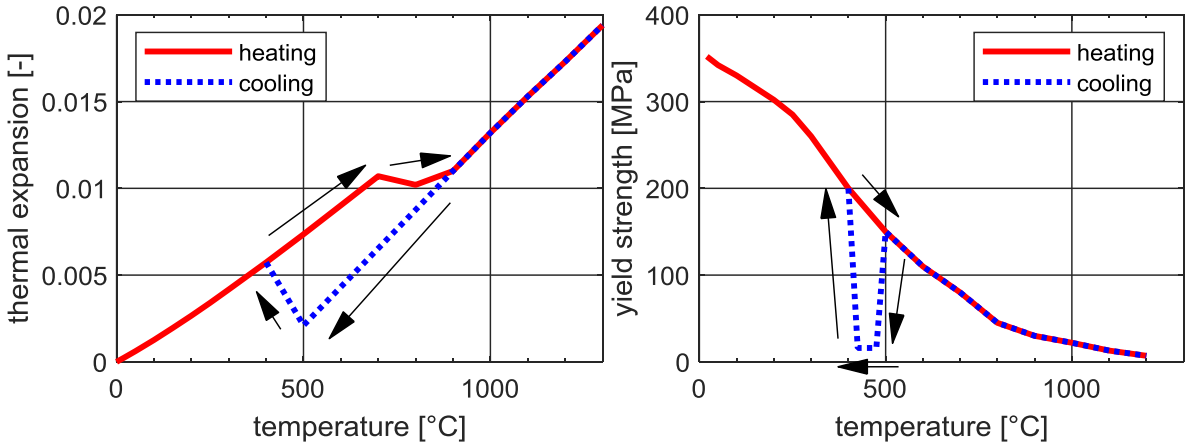

Figure 2-4: Thermal expansion coefficient with austenite phase transformation between 400°C and 500°C and yield strength considering transformation induced plasticity (TRIP), based on (Klassen et al. 2017).

2.3 Parameter variation

The simulation is not calibrated by experimental data. Input parameters, e.g. the welding speed, are chosen in the magnitude of realistic values. In the following, some of the input parameters for the simulation are varied to verify in which way they influence the resulting residual stresses.

The simulations are performed on FE models of two geometries including two different welded details: a cruciform joint with a multilayer weld and a longitudinal stiffener with a fillet weld. Although the models represent small-scale specimens as they might be used for experimental fatigue tests, the geometries are fictitious and not based on real, existing specimens. Both models have the same dimensions, a plate thickness of 10 mm and material properties of steel S355.

2.3.1 Cruciform joint

The described simulation procedure is applied to a multilayer cruciform joint with the dimensions and welding sequence as in Figure 2-5. Only the right side of the cruciform joint is simulated, the weld on the left side is assumed to be already present. A simulation including the welding of the left side of the joint resulted in larger distortions, but residual stresses on the right side of the model were the same with differences of less than 10 MPa. Welding alternately left and right side would probably lead to a different result. This case is not regarded here. The geometry is modelled by 8 node solid elements. Element size is 0.25 mm around the weld toe with a coarser mesh on the rest of the model (Figure 2-5). The

model is constrained at three nodes to only suppress rigid body motion without restraining the deformation of the model.

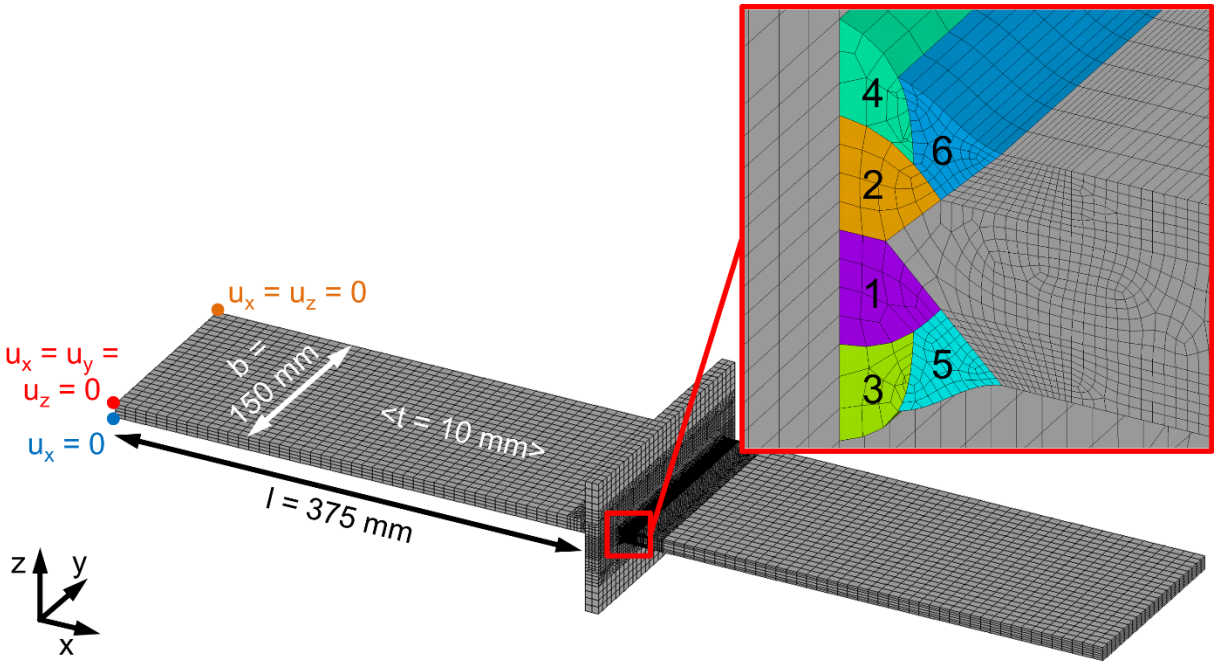

Figure 2-5: Dimensions, welding sequence and structural boundary conditions of the cruciform joint FE model (Friedrich and Ehlers 2019a).

The results presented in the following show the residual stresses transversal to the weld, both on the top and bottom side of the right plate (compare Figure 2-5). Since the highest residual stress values do not necessarily occur at the centre line of the specimen the results are evaluated at the position along the weld where the highest transversal residual stresses occur at the weld toe or in front of it (Figure 2-6).

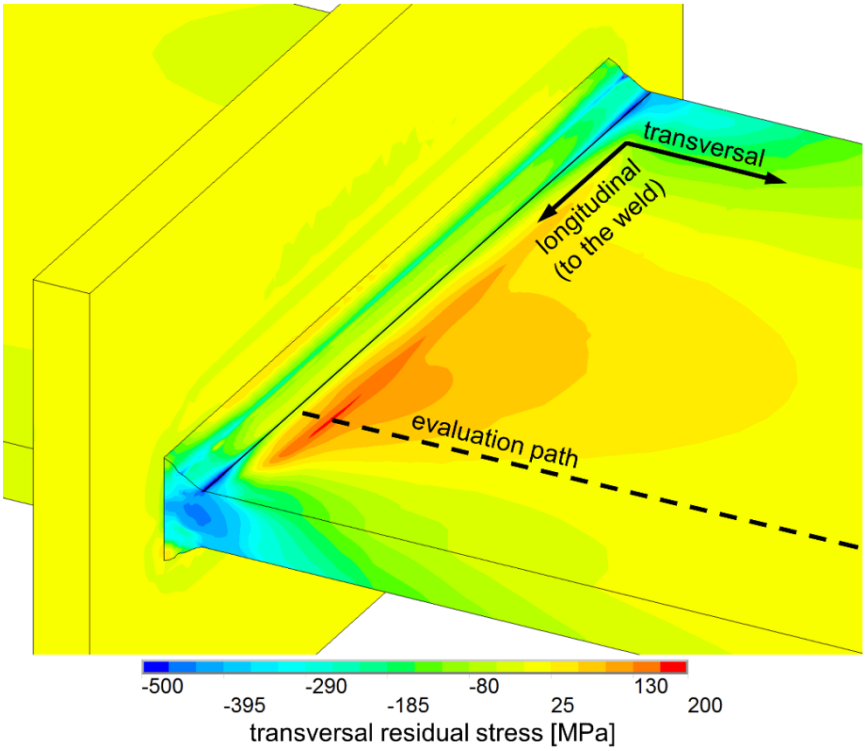

Figure 2-6: Evaluation path at the position of the highest transversal residual stresses and definition of residual stress directions (Friedrich and Ehlers 2019a).

Applied temperature

The temperature applied to the weld elements, i.e. the prescribed temperature of the heat source, is varied between 1100 and 1500°C. Welding speed is 7.8 mm/s for all simulations. Figure 2-7 shows the resulting transversal residual stresses. The markers serve only to distinguish the lines and do not represent the distribution of the FE nodes. This applies to all simulation results represented in the following. On the top side of the plate transversal residual stresses at the weld toe vary only slightly depending on the applied temperature. The maximum value reached in front of the weld increases and is shifted further from the weld with higher temperatures. This is expectable as a bigger volume is heated up and undergoes shrinkage as it cools. On the bottom side the maximum situated at the weld toe decreases slightly with higher temperatures. This is because when the last applied layer on the top side cools and shrinks the bottom side is heated to almost the same temperature. The temperature distribution and shrinkage is more homogenous over the plate thickness, so that the bending moment causing tension on the bottom side is reduced.

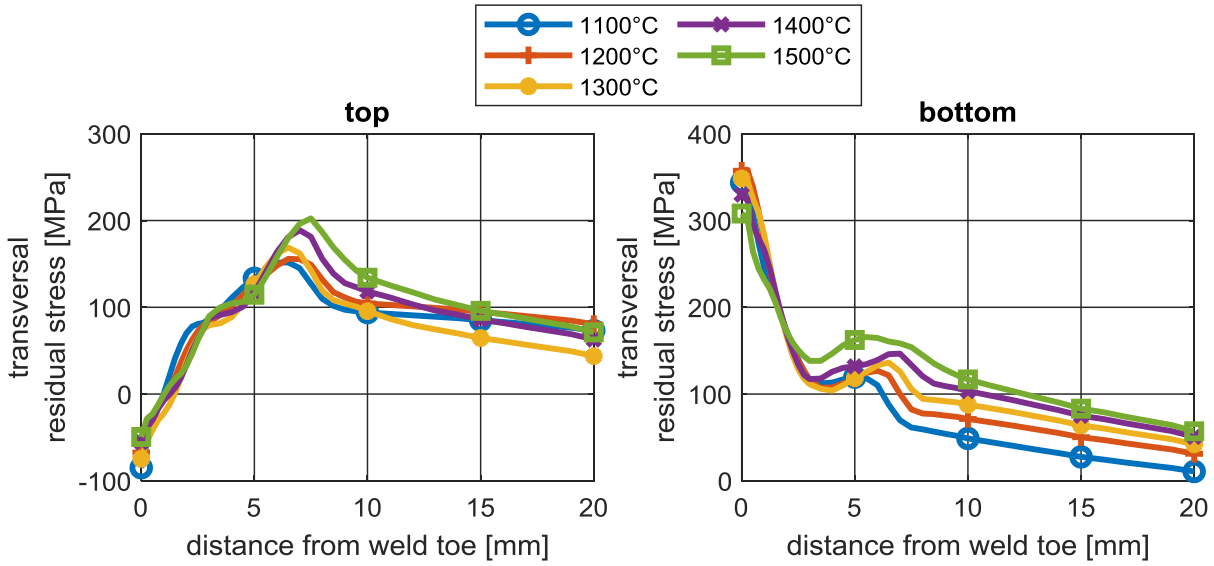

Figure 2-7: Calculated transversal residual stress depending on the temperature applied to the weld elements (Friedrich and Ehlers 2019a).

Since the actual values determined by measurements are not known, it cannot be said which temperature yields the best results. But it can be seen that the results are very similar, thus the selected temperature does not impact the resulting residual stresses substantially. For the following simulations a temperature of 1300°C is applied. In reality the reached peak temperature and the holding time at this temperature would influence phase transformation. In the simplified consideration of phase transformation (described in section 2.2) these factors will not have a direct influence.

Welding speed

Based on previous work by the author of this thesis on a similar weld geometry an average welding speed of 7.8 mm/s is determined. The speed is varied between 3.9 and 15.6 mm/s (Figure 2-8). The size of the assumed weld passes, which in reality would depend on the welding speed, is left unchanged for all simulated speeds. The weld is modelled with an idealized shape and the size of each weld pass is a rough estimate. The parameter variation is intended only to determine how the welding speed assumed in the simulation would affect the resulting residual stresses, not to find a realistic combination of welding speed and weld deposit. On the top side the results are similar for all four speeds. For lower speeds with a higher energy input the maximum is slightly higher and farther from the weld. At the weld toe all three curves drop to a similar value. On the bottom side of the plate the values at the notch are lower for the lowest speed as more energy is put into the plate and the temperature is distributed more equally over the plate thickness.

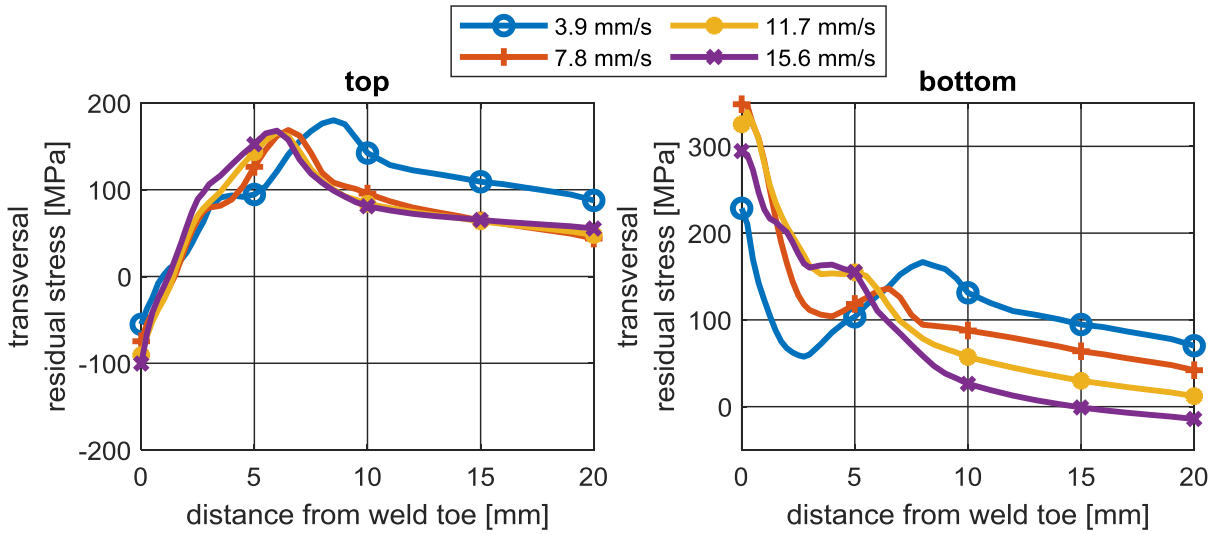

Figure 2-8: Calculated transversal residual stress depending on the welding speed (Friedrich and Ehlers 2019a).

It has to be kept in mind that, because of the simulation approach applying directly temperatures (1300°C) to the weld, the welding energy input is not completely proportional to the welding speed. Even for very low speeds the temperatures will not exceed 1300°C. Furthermore, phase transformation during cooling is not adapted to different cooling speeds which do also depend on the heat input. And as mentioned, in reality the welding speed would influence also the volume of the weld which will affect residual stresses.

The influence of the selected welding speed appears to be bigger than that of temperature, especially for relatively low speeds. For speeds in the magnitude of 10 mm/s, which may be assumed realistic for this type of weld, the resulting residual stresses are similar. The speed of 7.8 mm/s is maintained for the following simulations.

Phase transformation temperature interval

As described in section 2.2 phase transformation is considered through a second thermal expansion curve for cooling. The same thermal expansion curve with a fixed temperature interval for the austenite phase transformation is assumed for all weld elements, independently of the cooling rate and the maximum reached temperature. In a previous work (Klassen et al. 2017) it was shown that even this simplified consideration of the phase transformation yields more realistic results than not considering it at all. To determine the influence of the assumed temperature interval in which the transformation occurs, simulations with different heat expansion curves for cooling (compare Figure 2-4) are performed (Figure 2-9). As expected, values at the weld toe decrease for lower transformation temperature intervals, which in reality would correspond to higher cooling rates and higher peak temperatures (Dilger, ed. 2006). Results on the bottom side are influenced only little by the assumed temperature interval.

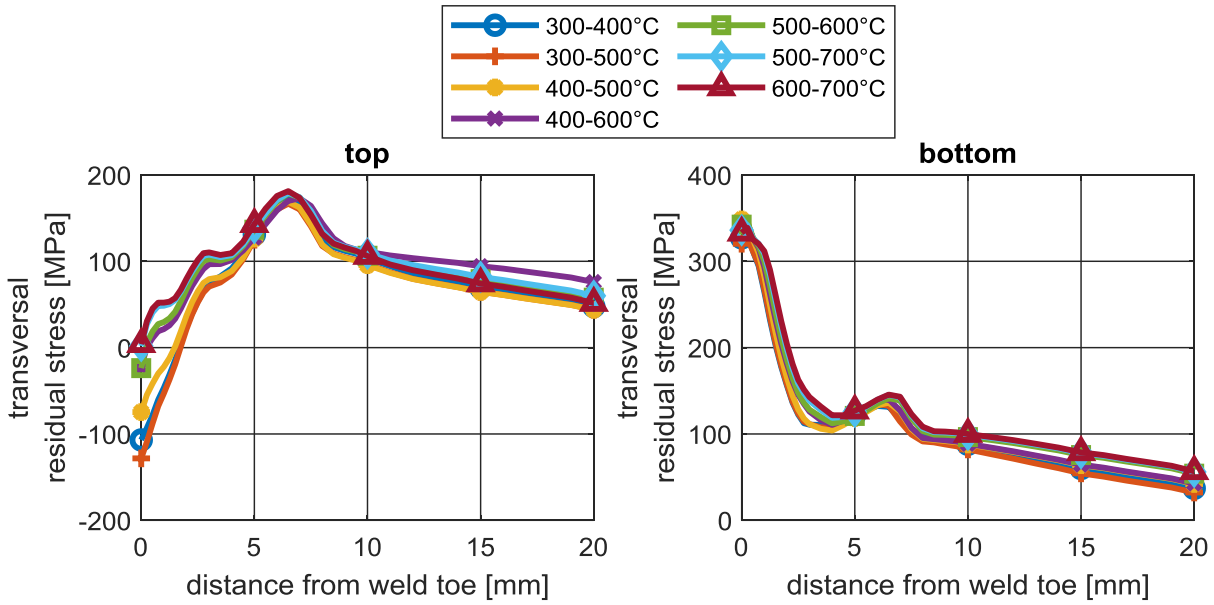

Figure 2-9: Calculated transversal residual stress depending on the temperature interval for phase transformation (cooling curve in Figure 2-4) (Friedrich and Ehlers 2019a).

Further simulations with two respectively three different phase transformation intervals depending on the maximum reached temperature are run (Figure 2-10). In these simulations the heat expansion curve is switched also for elements close to the weld if they reach at least 900°C, as opposed to the previous where this was applied only to weld elements. The results differ only little from the simulation with only one temperature interval between 400 and 500°C. Figure 2-10 shows two more curves from simulations with only one thermal expansion curve for heating and cooling. In one case austenite phase transformation is assumed at the same temperature interval as for heating (700-900°C), in the other the thermal expansion is straightened as for an austenitic steel. The results show, that even without phase transformation the maximum transversal residual stress is reached some millimetres in front of the weld and values decrease towards the weld toe. In this case, the decrease of the transversal residual stresses can therefore not be attributed exclusively to the volume expansion during phase transformation.

For the following simulations a temperature interval between 400 and 500°C is assumed. Based on the experimental results in (Dilger, ed. 2006) this seems to be a realistic and probable range for many combinations of cooling rates and peak temperatures.

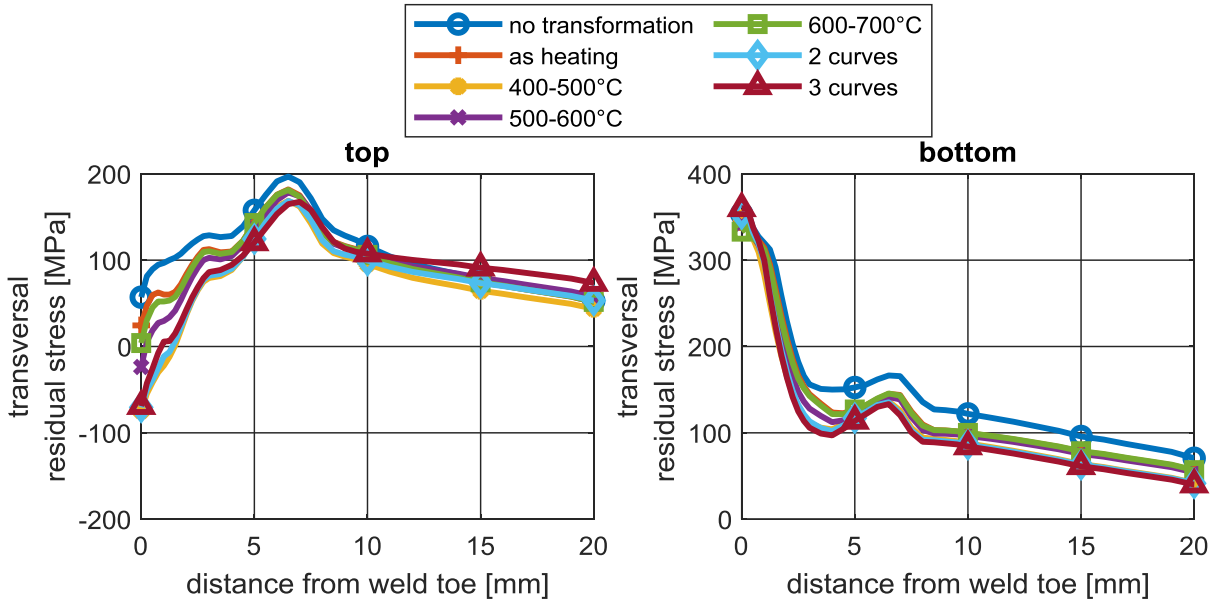

Figure 2-10: Calculated transversal residual stress without phase transformation, depending on the temperature interval for phase transformation and with two respectively three thermal expansion curves for cooling depending on the maximum reached temperature (Friedrich and Ehlers 2019a).

2.3.2 Longitudinal stiffener

Since certain parameters may have a different influence on the resulting residual stresses depending on the weld geometry, a second model with a different weld typology is investigated. The model of a small-scale specimen with a longitudinal stiffener used for the parameter variation is shown in Figure 2-11. As in the cruciform joint model, element size is 0.25 mm in front of the weld toe at the end of the stiffener and coarser on the rest of the model. Constraints are applied to three nodes only to avoid rigid body motion.

It is assumed that the welding starts and ends at half length of the stiffener.

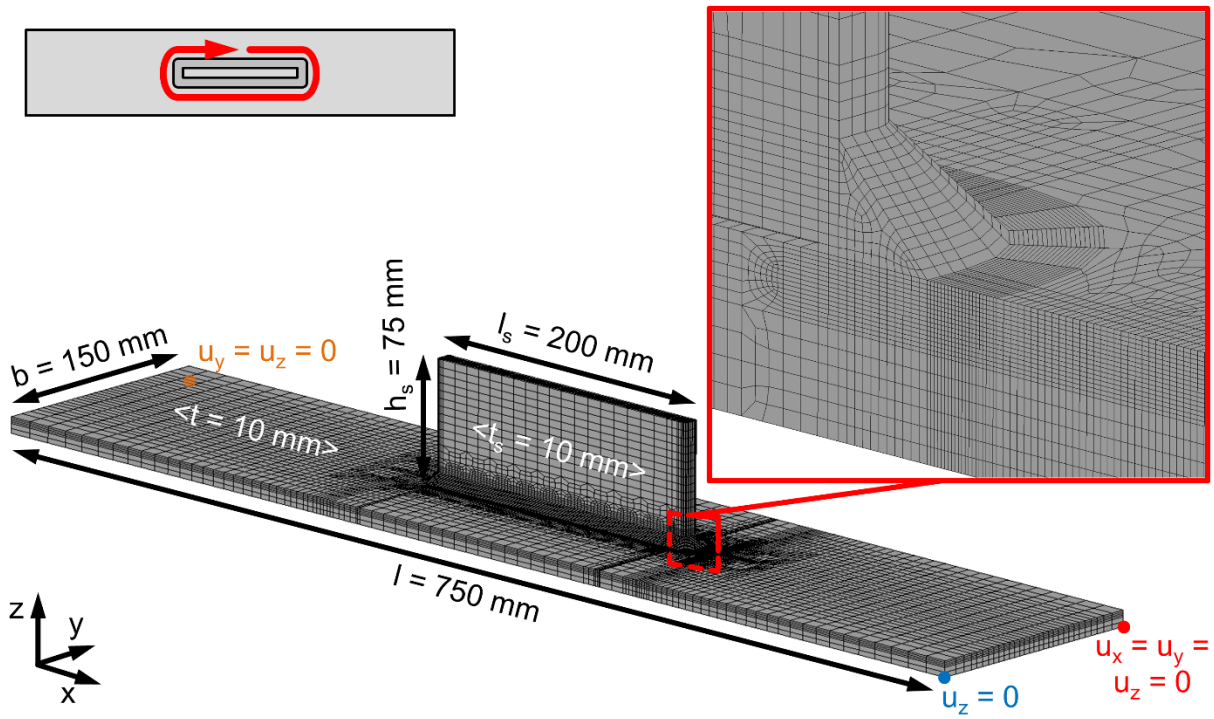

Figure 2-11: Dimensions, welding sequence and structural boundary conditions of the longitudinal stiffener FE model (Friedrich and Ehlers 2019c).

The following results are evaluated on the symmetry line of the model starting at the weld toe at the end of the stiffener (Figure 2-12). The directions of the residual stresses are defined with respect to the weld at the end of the stiffener. The transversal direction is parallel to the long side of the model.

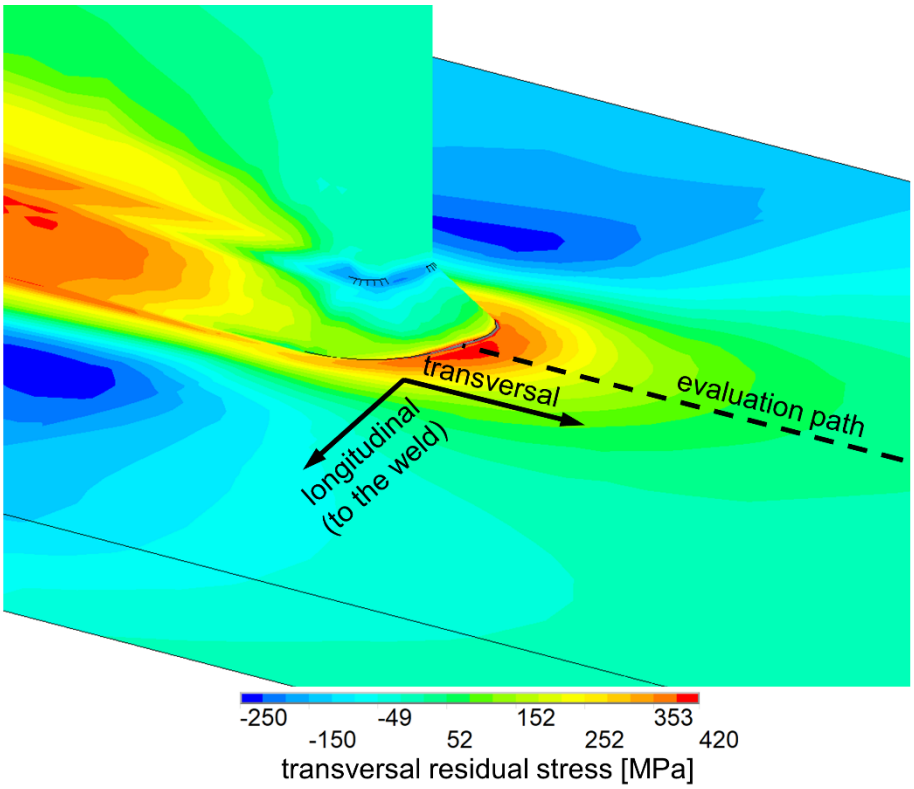

Figure 2-12: Evaluation path on the symmetry line, at the end of the stiffener and definition of residual stress directions.

Applied temperature

The temperature applied to the weld cross-section is varied between 1000 and 1500°C. The resulting residual stresses in front of the weld toe at the end of the stiffener are shown in Figure 2-13. For temperatures of 1400°C and more the cut-off temperature above which the elements are deactivated had to be below 1200°C in order to run the simulations. In the diagram this is indicated by a dashed line.

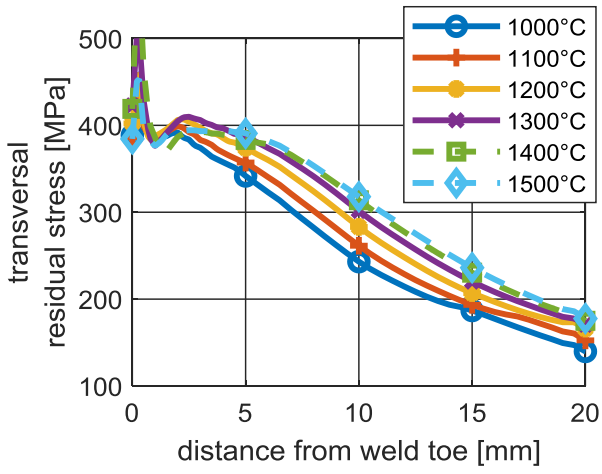

Figure 2-13: Calculated residual stress depending on the temperature applied to the weld elements (dashed line: cut-off temperature lower than applied temperature) (Friedrich and Ehlers 2019c).

The curves show a steep increment on the first element from the weld toe. At the weld toe, the elements of the weld are activated as they cool below the applied temperature while the adjacent elements are always active. At the moment of the activation, large deflections can occur in the neighbouring elements, which at that point present elevated temperatures themselves and thus low stiffness. This may cause a peak in the resulting residual stresses at the first node in front of the weld toe. Moreover, the weld toe is not modelled with a radius and thus shows a sharp notch. This represents a singularity in the FE model, which will cause an unrealistic stress concentration at the weld toe. The residual stress values on the first elements, up to approximately 1 mm from the weld toe, should therefore not be evaluated and will not be considered in the following.

Neglecting the peak at the first node from the weld toe, transversal residual stresses reach a value of about 400 MPa some millimetres from the weld with decreasing tendency towards the weld toe. With increasing temperatures, the curves become wider and the residual stresses decrease farther from the weld.

All in all, the residual stress curves and the highest values in front of the weld differ only little depending on the applied temperature. This is in agreement with the findings for the cruciform joint in section 2.3.1. For the following simulations a temperature of 1300°C is applied.

Throat thickness

The throat thickness of the weld is varied between 3.0 and 6.5 mm. With an increasing weld cross-section more thermal energy is applied to the model and thus the heated volume undergoing shrinkage during cooling is larger. The resulting residual stresses in front of the weld toe at the end of the stiffener are shown in Figure 2-14.

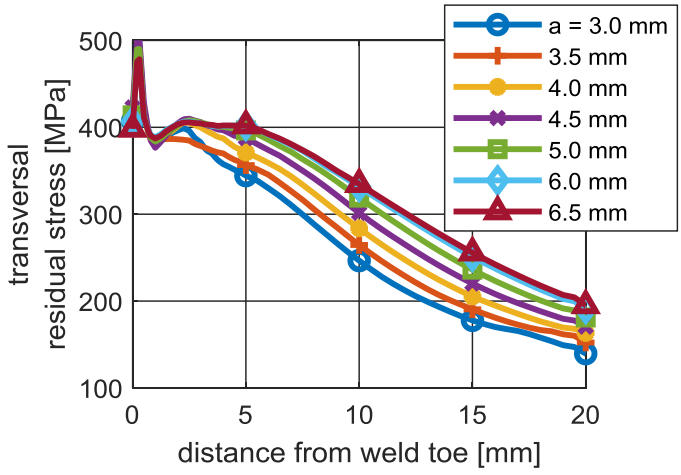

Figure 2-14: Calculated residual stress depending on the throat thickness *a* (Friedrich and Ehlers 2019c).

Analogue to the results with varied temperatures, the curves become wider and the residual stresses decrease farther from the weld as the throat thickness increases. The highest values reached in front of the weld differ only little depending on the throat thickness. For the following simulations a throat thickness of 4.5 mm is applied.

Phase transformation temperature interval

As described in section 2.2 phase transformation is considered by using two different curves for the thermal expansion coefficient for heating and cooling. On all weld elements the same curve is used for cooling, independently of the reached peak temperature and cooling time. The temperature interval in which the phase transformation and thus a volume expansion is assumed during cooling is varied between 300 and 700°C. The resulting residual stresses are shown in Figure 2-15. The results include those from simulations without phase transformation (with straightened thermal expansion curve as for an austenitic steel) and with the same thermal expansion curve as for heating (austenite phase transformation between 700 and 900°C). The assumed temperature interval for phase transformation shows no influence on the calculated residual stresses in front of the weld. As described above, it is not possible to evaluate the simulation results at the weld toe.

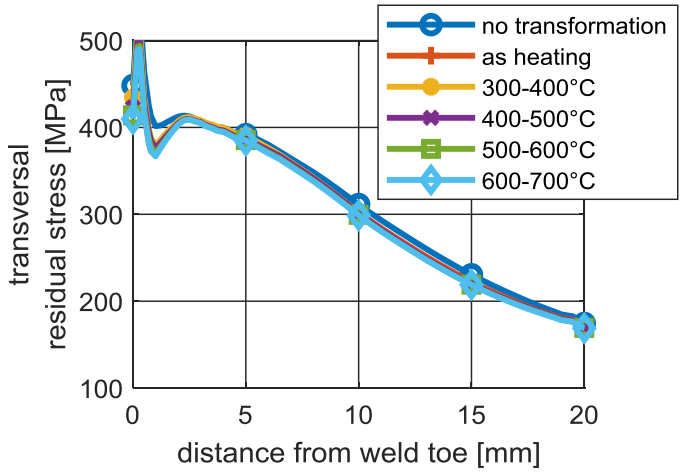

Figure 2-15: Calculated residual stress without phase transformation and depending on the temperature interval for phase transformation (Friedrich and Ehlers 2019c).

For the following simulations phase transformation during cooling is assumed between 400 and 500°C. According to experimental results in (Dilger, ed. 2006) this should be a realistic range.

Yield strength

The yield strength is varied between 385 and 470 MPa. Temperature dependent material data, including stress-strain curves, for S355 is taken from (Wichers 2006). At room temperature these show a yield strength of approximately 385 MPa. Tensile test data (at room temperature) for steel of grade A36 and S460 showing yield strengths of 430 and 470 MPa, respectively, are used for the stress-strain curves. Curves for elevated temperatures of the S355 are adapted by scaling the yield strength with the ratio of yield strengths at room temperature. The elastic-plastic zone is scaled by the ratio of the difference between yield limit and tensile strength. All other material properties, including young's modulus, are kept the same for all simulations. The resulting residual stresses are shown in Figure 2-16. In transversal direction the maximum reached residual stress increases with the yield strength of the material.

For the following simulations material properties of the S355 are assumed.

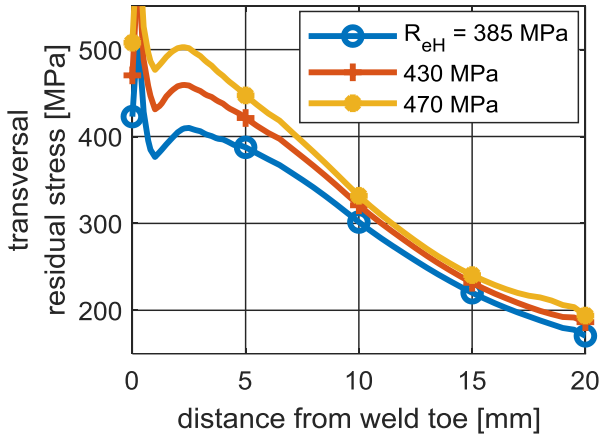

Figure 2-16: Calculated residual stress depending on the yield strength R_{eH} (Friedrich and Ehlers 2019c).

2.3.3 Findings

The performed simulations show the influence of different simulation parameters on the resulting transversal residual stresses for a multilayer cruciform joint and a longitudinal stiffener. For both weld geometries parameters determining the heat input, i.e. prescribed temperature, welding speed, throat thickness, have only little influence on the resulting residual stresses. The assumed temperature interval for phase transformation affects residual stress values at the weld toe of the cruciform joint. However, the characteristic distribution with the maximum residual stresses in front of the weld and a decrease towards the weld toe does occur also without transformation. The assumed yield strength has a direct influence on transversal residual stresses at the longitudinal stiffener.

In conclusion, the simulation parameters for the applied prescribed temperature heat source have only little influence on the resulting residual stresses. As long as they are in a realistic range, the magnitude and characteristic distribution of the results will be the same. Phase transformation should be considered but is not essential for the investigated cases. Yield strength is of more importance for the resulting residual stresses.

The simulation approach and results presented in chapter 2 have been published by the author of this thesis in (Friedrich and Ehlers 2019a) and (Friedrich and Ehlers 2019c).

3 Specimen design

The simulation results in section 2.3 show that the longitudinal stiffener presents significant tensile residual stresses at the weld also in a relatively small, unconstraint small-scale specimen. Therefore, this geometry is often used to study welding residual stresses in experimental investigations. However, the simulations of the cruciform joint show that also in this geometry, with a transversal weld, relatively high tensile residual stresses may be present. On the top side, where the last weld pass is applied, the maximum is located some millimetres in front of the weld. At the weld toe, values are close to zero or even compressive. Therefore, it is not expected that these residual stresses would significantly affect fatigue behaviour.

As mentioned before, it is often found that the residual stress influence in larger structures is higher than in small specimens. This is attributed to the constraint of the weld by the surrounding structure which may lead to higher residual stress levels. Using numerical simulations this can easily be demonstrated by including the same weld in a small-scale geometry and in a larger structure. The transversal residual stresses on the models used before, cruciform joint and longitudinal stiffener, are compared to those of a frame corner containing the same weld geometries in Figure 3-1. For the frame corner the simulations included the weld between the horizontal web and the lower girder, and the right part of the cruciform joint between the inner girders. This is welded last in order to maximize the possible constraint. It can be seen that on the longitudinal stiffener (b) the residual stress distribution is similar to that at the cut out in the frame corner (a.1). This is expectable as the girder is still free when the weld is applied. In the frame corner the values are even slightly reduced due to the influence of the following multilayer weld. For the multilayer weld it appears that residual stresses are higher in the frame corner (a.2) than in the small specimen (c).

The example shows how welding residual stresses in small-scale specimens used for experimental tests may differ from those in larger structures. Geometries like the frame corner are sometimes used as test specimens, usually loaded with a servo-hydraulic cylinder (Fricke et al. 2014). But they are unsuitable for larger test series because of the expensive specimen production, complicated test setup and long test durations. Another possibility to obtain test specimens with increased residual stresses is to constrain a smaller specimen within a rigid structure which is then tested (Farajian 2011). But also this possibility is laborious and difficult to apply in resonance testing machines. Therefore, in this thesis welding simulations are used to design a small-scale specimen containing a transversal multilayer weld with tensile residual stresses at the weld toe.

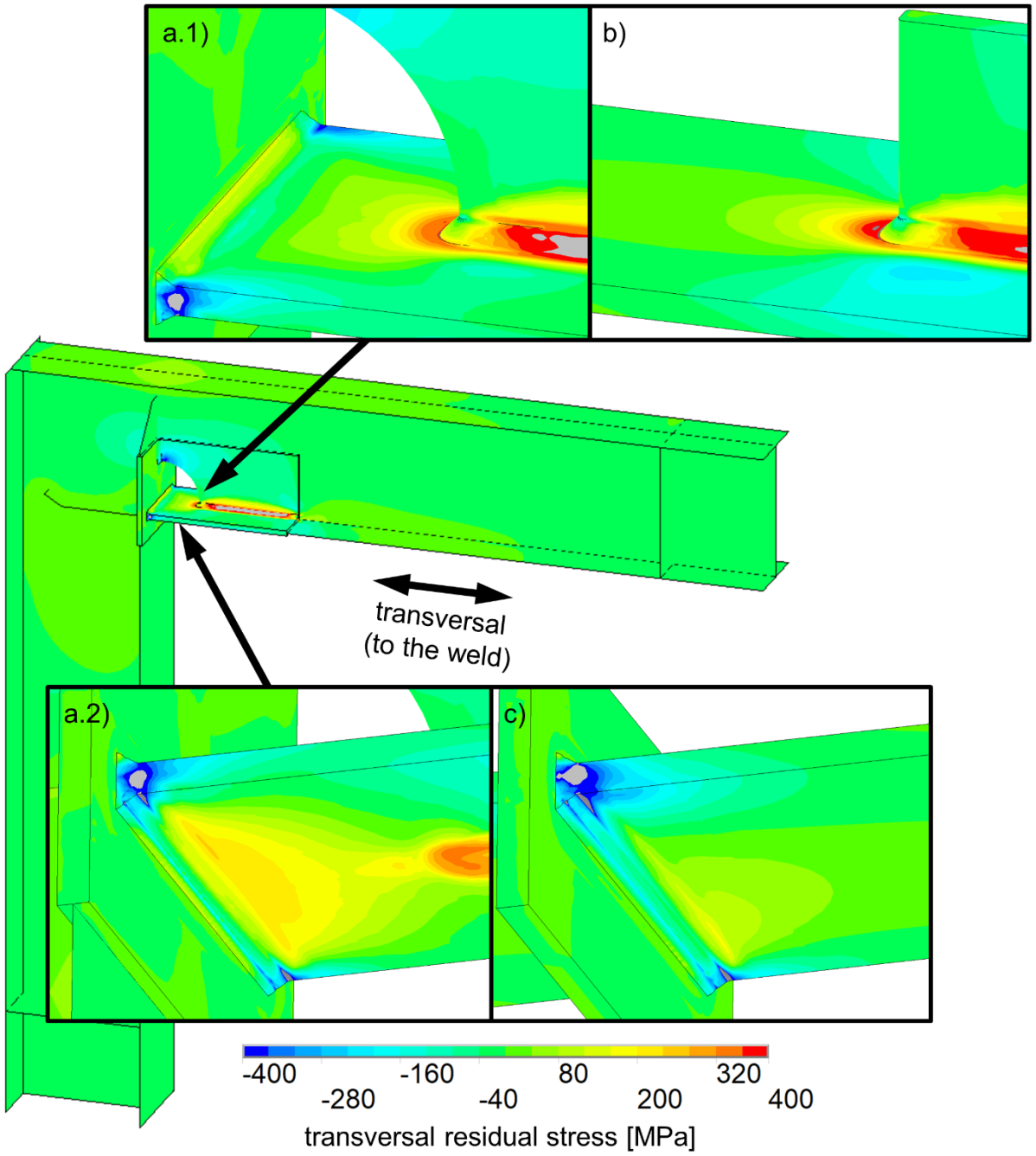

Figure 3-1: Calculated transversal residual stress on (a.1 and a.2) a frame corner compared to small-scale specimens with (b) a longitudinal stiffener and (c) a cruciform joint.

3.1 Variation of geometry parameters

Starting from the cruciform joint model described in section 2.3.1 a variation of weld and geometry parameters is performed to assess their influence on the resulting residual stresses. The objective is to identify those parameters that can be altered to create a small-scale specimen of a cruciform joint containing tensile residual stresses at the weld. As in section 2.3, the results are shown in terms of the transversal residual stresses at the position of the highest tensile values, on the top and bottom side of the plate.

3.1.1 Plate thickness

The thickness, of both the horizontal and the vertical plates (compare Figure 2-5), is varied between 5 and 30 mm (Figure 3-2). All other parameters are kept as before. With the plate thickness also the number of applied weld passes increases from a total of 2 passes for a

5 mm plate to 26 for a 30 mm plate. The last weld pass is applied on the top side, at the weld toe to the horizontal plate. The resulting transversal residual stresses are plotted in Figure 3-3. With exception of the 5 mm plate, residual stresses on the top side increase with increasing plate thickness. This might be explained by the larger cross-section opposing more resistance to the shrinkage of the heated volume. Furthermore, the heat conduction in a thicker plate is faster and the plate is not heated completely through. On the bottom side residual stresses decrease with increasing plate thickness. Due to the larger section modulus the tension on the bottom side caused by the shrinkage on the top side is decreased. Although the welds for the different plate thicknesses are modelled with a similar cross-section for the single weld passes, in some cases they are slightly larger, e.g. t = 15 mm in Figure 3-2. To verify the influence of the weld pass cross-section, the number of weld passes is varied for the thicknesses between 15 mm and 25 mm. The results are contained in the appendix 12.1. Although residual stress values at the weld toe change slightly, the overall distribution is not altered. Also in these models the last weld pass is applied at the weld toe to the horizontal plate. A variation of the weld pass sequence will be investigated in section 3.1.3.

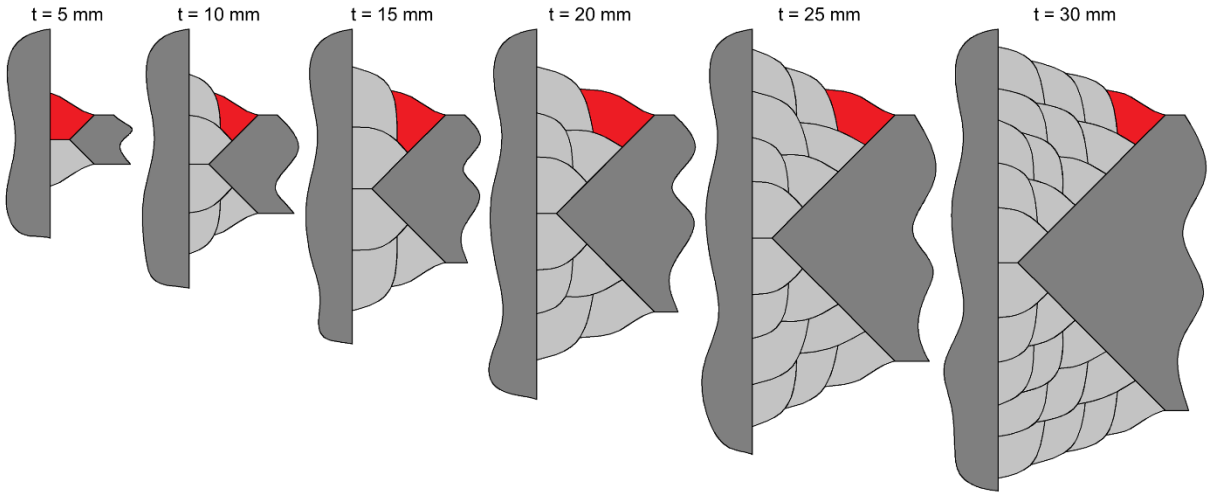

Figure 3-2: Variation of the plate thickness t (last weld pass marked red).

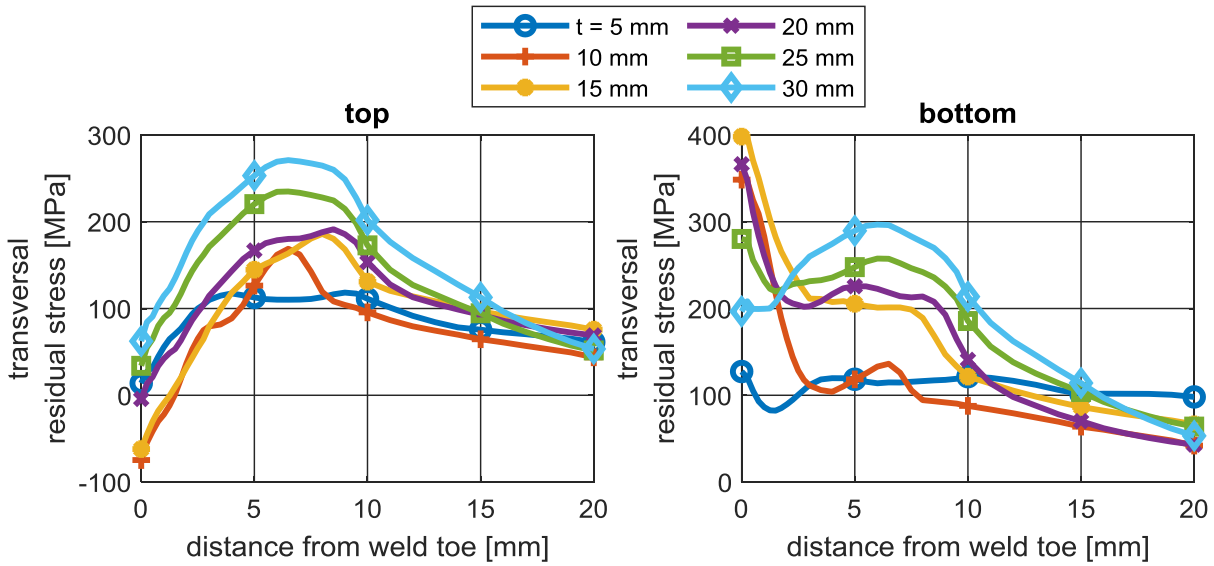

Figure 3-3: Calculated transversal residual stress depending on the plate thickness (t in Figure 3-2) (Friedrich and Ehlers 2019a).

Regarding the top side of the plate a greater plate thickness would be preferable to obtain specimens with tensile residual stresses. But the shift towards tension is not substantial. With a thickness of 20 mm values would still be close to zero at the weld toe. Due to the limited force of the testing machine the thickness of the test specimens is restricted to 10 mm.

3.1.2 Plate width

The plate width (*b* in Figure 2-5) is varied between 50 and 1000 mm. The resulting transversal residual stresses are plotted in Figure 3-4. On both sides of the plate transversal residual stresses decrease for larger plate widths. This can be explained by the equilibrium condition in the plate (Figure 3-5, a). For a quarter model the moments caused by longitudinal and transversal residual stresses must be in equilibrium (Hänsch 1984). Since for plates over a certain width the longitudinal residual stresses are independent of the plate width, transversal residual stresses will be smaller for wider plates (i.e. longer welds). Analogue to the scheme (Figure 3-5, a) residual stresses calculated by welding simulations for models with widths of 100 mm and 400 mm are plotted in (Figure 3-5, b, c). Longitudinal residual stresses show similar distributions independent of the width of the plate. Since the distance $a_{transv.}$ increases with the width, the height of the tensile transversal residual stress will decrease. For the present case of a multilayer joint this is valid only qualitatively since the residual stresses are not constant over the plate thickness.

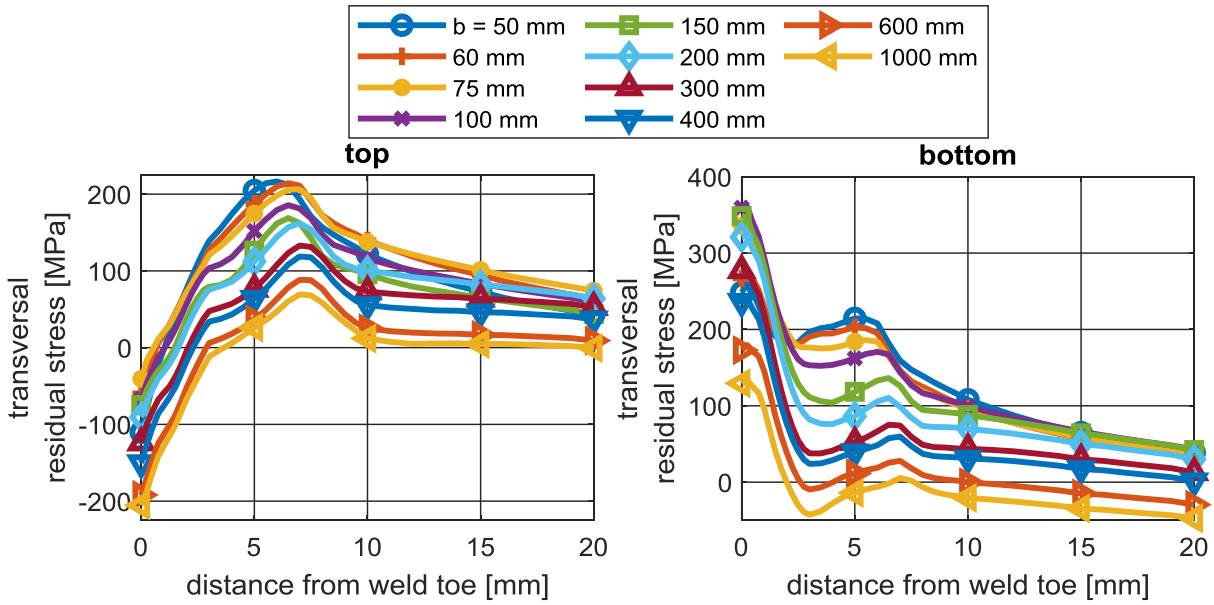

Figure 3-4: Calculated transversal residual stress depending on the plate width (*b* in Figure 2-5) (Friedrich and Ehlers 2019a).

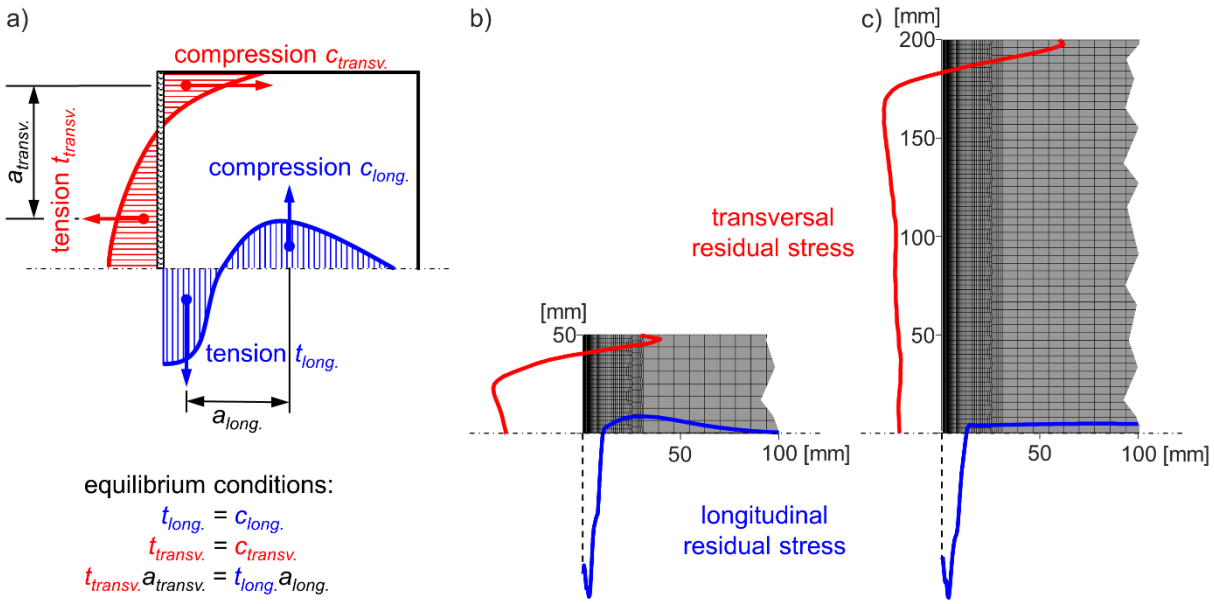

Figure 3-5: (a) Equilibrium conditions on a butt-weld (Hänsch 1984). (b) FE simulation results for a cruciform joint with b = 100 mm and (c) b = 400 mm (transversal residual stresses evaluated at the distance from the weld where the maximum occurs ≈ 5 mm).

In reality it is convenient to weld larger plates and cut them into strips to produce larger numbers of specimens. This cutting of the specimens is included in the simulation by deactivating the elements along the assumed cut after welding and cooling to room temperature. Figure 3-6 shows the resulting residual stresses for a 400 mm plate cut into four strips of 100 mm. Two different cutting sequences are shown: on the left the model is cut in the centre line and the resulting pieces are then cut again in the centre, on the right the plate is cut sequentially from one side. The resulting residual stress distributions show no significant differences for the two cutting sequences. This is reasonable as long as no plastification occurs. All four resulting specimens show similar residual stress values (peak and weld toe) as the original plate. The distribution is similar to a plate with a 100 mm weld but the values are somewhat lower. Simulating each cut in a single load step or piecewise produces no relevant differences in the final residual stress distributions.

From the simulations it is concluded that welding residual stresses tend to increase with a decreasing specimen width. Small specimens, with a width of approximately 50 mm should not present lower transversal residual stresses than wider plates. Furthermore it has been shown that residual stresses are preserved also after cutting orthogonal to the weld.

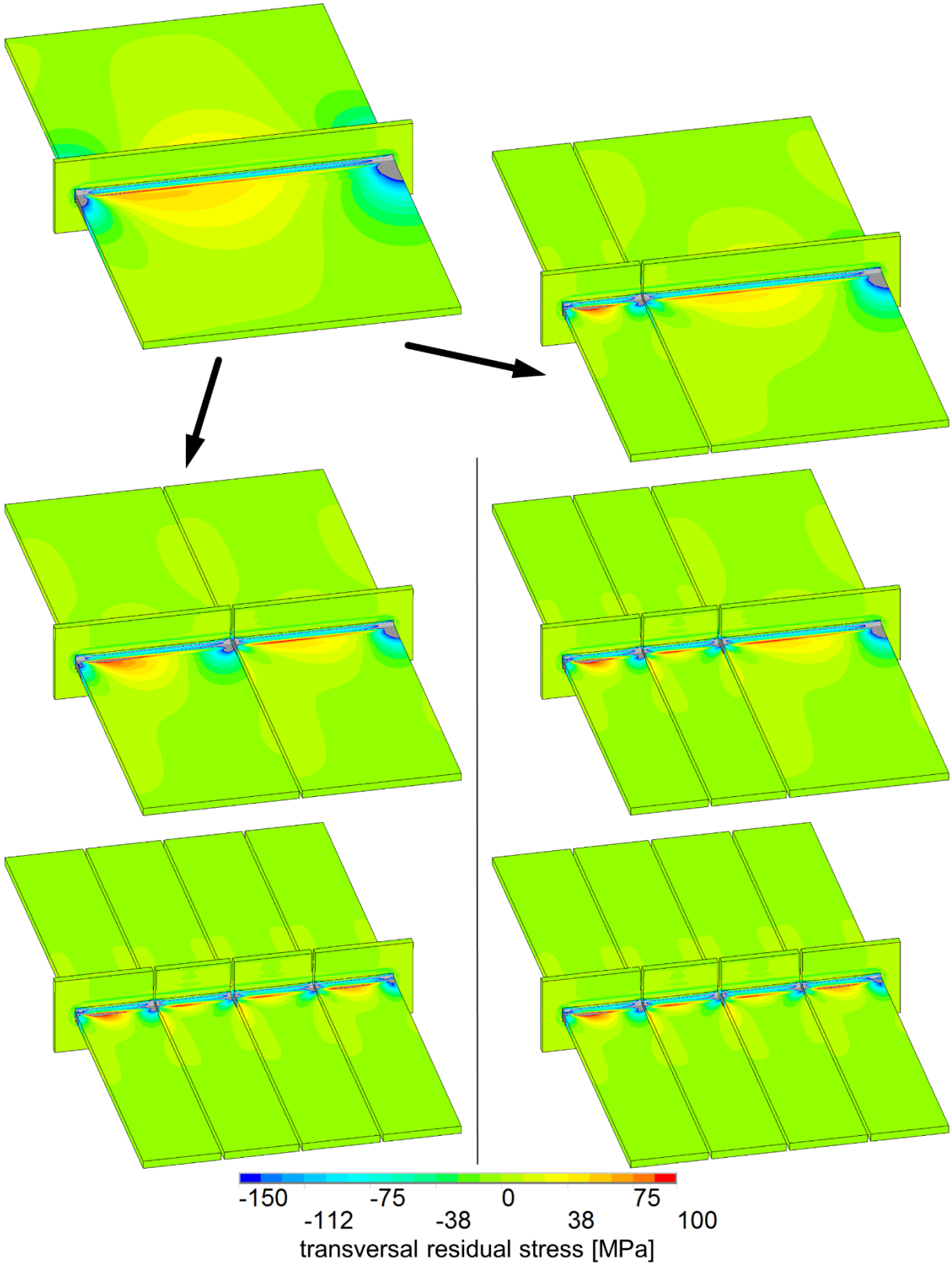

Figure 3-6: Calculated transversal residual stress on a 400 mm plate cut into four 100 mm strips using two different cutting sequences.

3.1.3 Welding sequence

So far, the bottom side of the plate resulted in tensile residual stresses at the weld toe. On the top side the maximum was reached in front of the weld and values at the weld toe were close to zero or in compression.

The distortion would be so that the plate is pulled towards the top side where the last weld pass is applied. Applying a tensile load would therefore cause a bending moment with tension on the top side and compression on the bottom. In fatigue tests cracks would therefore probably initiate on the top side, where no tensile residual stresses are present at the weld toe. To achieve tensile residual stresses also on the top side, the welding sequence is modified (Figure 3-7). The last weld passes (red) are applied close to the vertical plate, as opposed to the original sequence where they lay at the horizontal plate (compare Figure 3-2). As indicated in (Fricke and Tchuindjang 2016) and (Klassen et al. 2017) this should lead to tensile residual stresses at the weld toe with the horizontal plate. The resulting transversal residual stresses are shown in Figure 3-8. With the modified sequence transversal residual stresses on both sides of the plate show an increase towards the weld resulting in higher tensile residual stresses at the weld toe compared to the original sequence (Figure 3-3). On the 5 mm plate, only two weld passes are applied, thus the sequence is not changed.

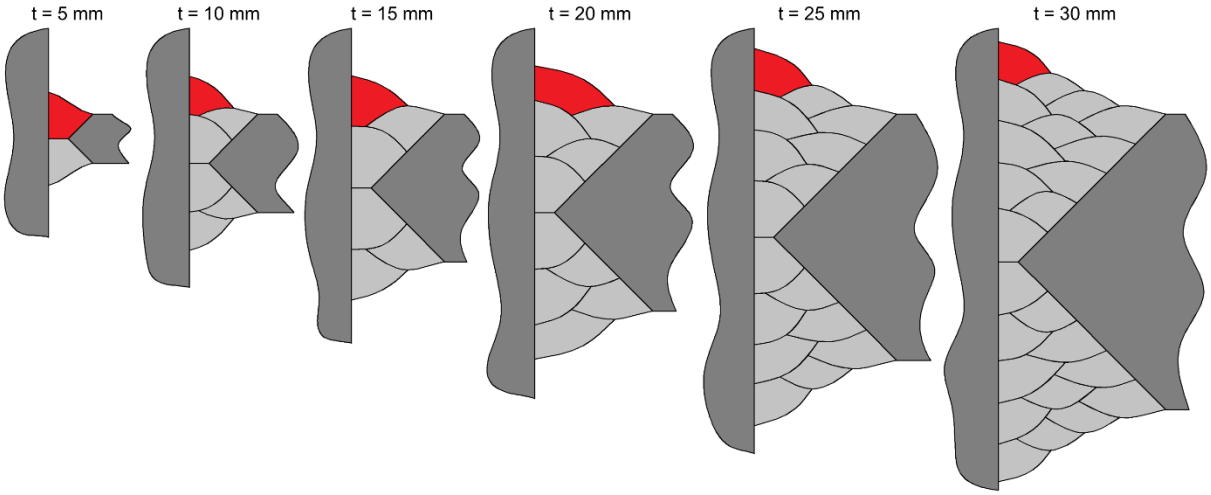

Figure 3-7: Variation of the plate thickness *t* with modified welding sequence (last weld pass marked red).

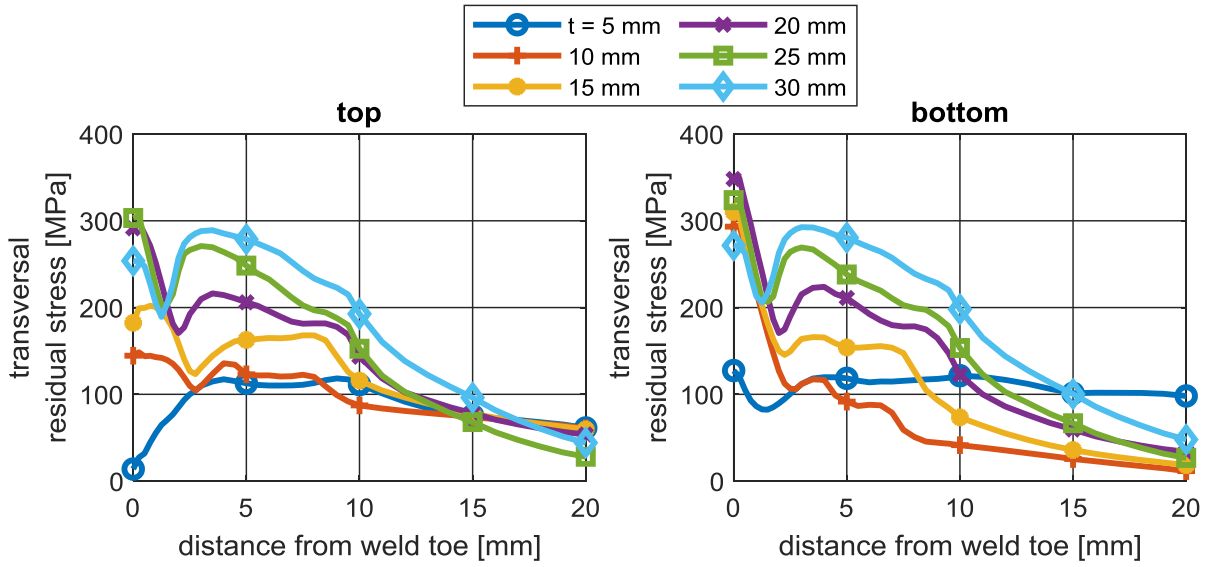

Figure 3-8: Calculated transversal residual stress with modified welding sequence depending on the plate thickness (*t* in Figure 3-7) (Friedrich and Ehlers 2019a).

3.2 Specimen preparation

The simulations in chapter 3.1 show the influence of geometry parameters on the transversal residual stresses at a cruciform joint. According to the simulations higher plate thicknesses lead to higher tensile residual stresses. Tensile residual stresses may be present also in relatively narrow, unconstrained specimens cut from a larger plate. By modifying the weld pass sequence the maximum of the tensile residual stresses on the top side can be shifted to the weld toe. Based on these results the specimens for the following fatigue tests are prepared.

To limit production efforts and at the same time reduce distortion the cruciform joint is reduced to a K-butt weld between two plates of different thicknesses (Figure 3-9). Numerical simulations indicate that the residual stress distribution on this geometry shows no significant differences to that on a cruciform joint. Regarding fatigue, both weld details fall into the same fatigue class FAT 71 for nominal stress (Hobbacher 2016).

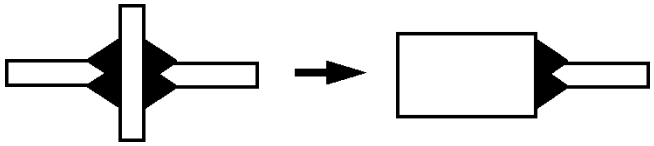

Figure 3-9: Reduction of the cruciform joint to a K-butt weld between plates of different thickness.

3.2.1 K-butt weld

As apparent in Figure 3-6, tensile residual stresses in the centre of the plate will be balanced by compressive residuals stresses towards the edge of the plate. According to the simulations the extension of this compressive zone along the weld is not dependent on the width of the specimen i.e. the length of the weld. In order to obtain specimens with tensile residual stresses on a great portion of the weld, the width of the specimens should be maximized. On the other hand, the maximum cross section and thereby its width is limited by the capacity of the testing machine for the fatigue tests.

The specimens are prepared as shown in Figure 3-10. Two plates of 10 mm and 25 mm thickness are welded by a K-butt weld with a total of six weld passes. The weld has a length of 330 mm. Five specimens of 55 mm width are cut out using a band-saw. A total of 26 plates respectively 130 specimens is produced. The steel used is of grade S355J2C+N normalised rolled. Mechanical properties of the 10 mm plate are determined by tensile tests: yield strength R_{eH} = 394 MPa; tensile strength R_m = 524 MPa; Young's modulus E = 204 GPa. The stress-strain curves are shown in Figure 3-11. The tests are carried out transversal to the rolling direction of the plate, this corresponds to the loading direction of the fatigue test specimens.

Welding is performed manually by metal active gas (MAG). Values for current (240 A) and voltage (30 V) are read out from the welding generator during welding and are not actually measured. The weld is executed in flat position in the sequence shown in Figure 3-10. The last weld pass is applied towards the thicker plate a few millimetres away from the weld toe at the thinner plate. Between the weld passes the plates cool off in air. Temperature is monitored by means of an infrared thermometer to achieve comparable interpass temperatures on all welded plates between all weld passes. The next weld pass is applied not before the recorded temperature has dropped below 80°C. The accuracy of these measurements is questionable. A comparison with two specimens where temperatures were

measured by thermocouples showed that the temperatures were actually at about 100°C. It is therefore assumed that the actual interpass temperature is < 100°C.

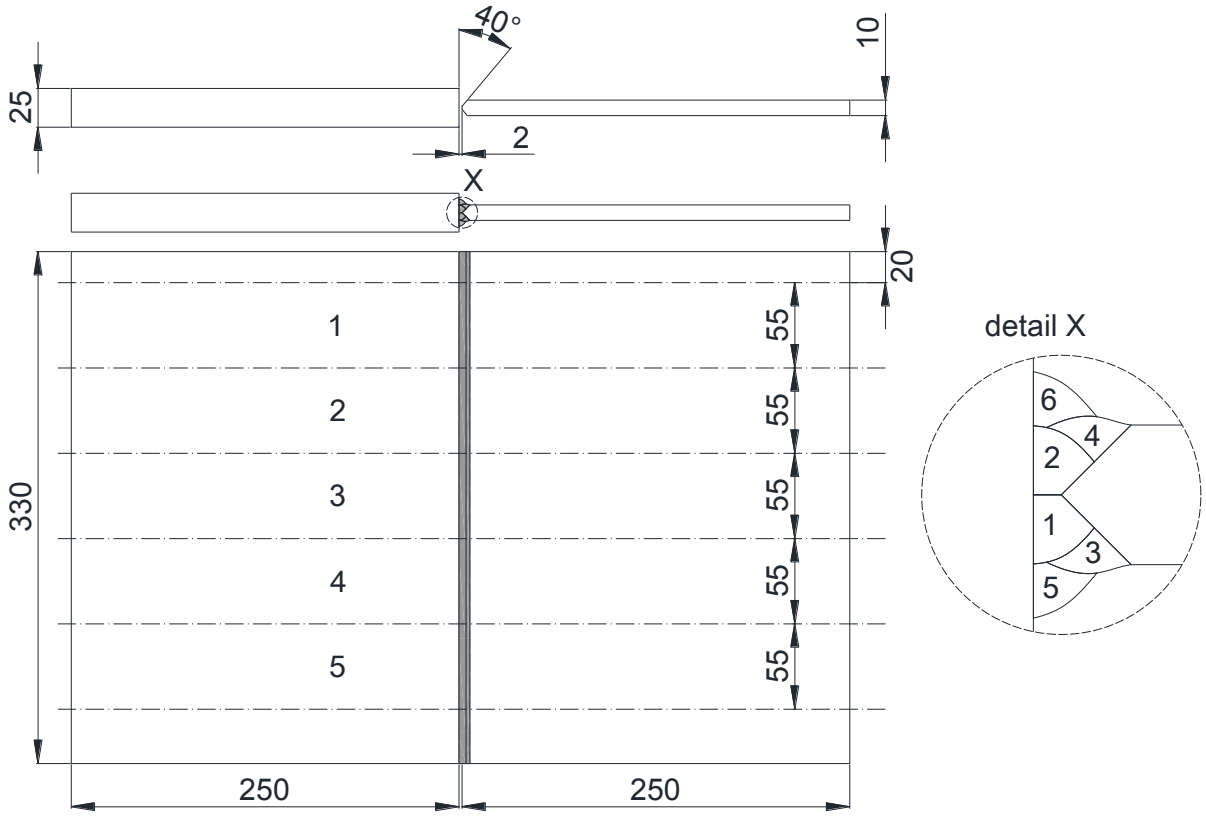

Figure 3-10: Specimen preparation (Friedrich and Ehlers 2019a).

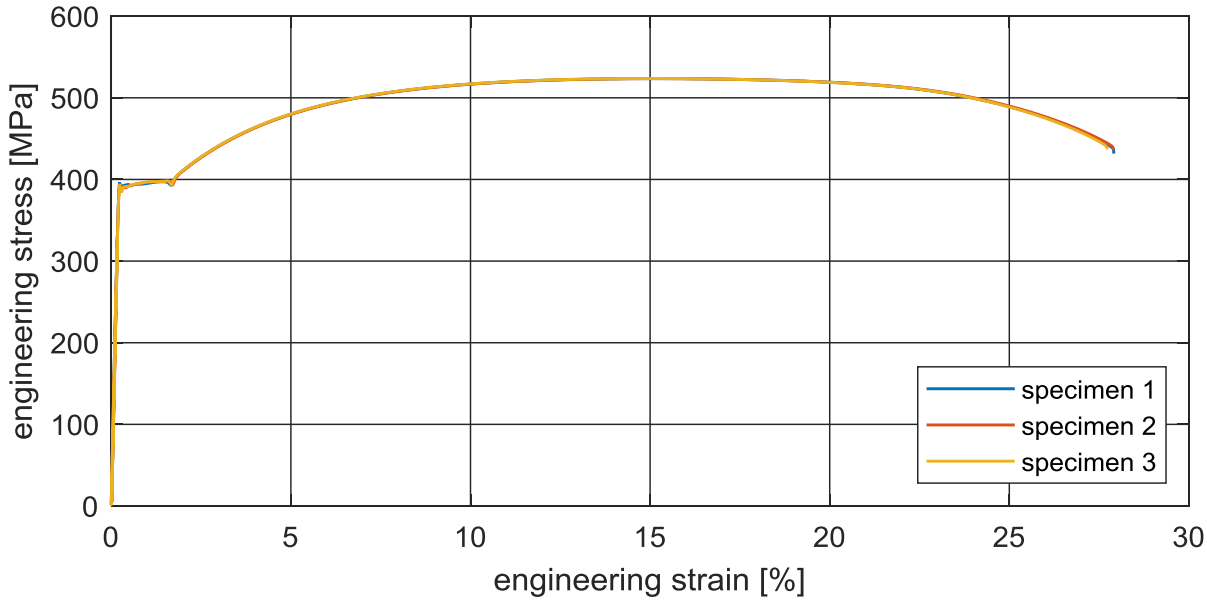

Figure 3-11: Stress-strain curves from tensile tests (S355J2C+N for K-butt weld specimens).

To reduce welding distortions the plates are temporarily tack welded to two profiles along the edge of the plates orthogonal to the weld, as shown in Figure 3-12. The profiles used have a u-section of 100 x 50 x 6 or a comparable cross-section. The profiles are removed after the plates have cooled to room temperature.

Figure 3-12: Plates temporarily restrained by u-profiles during welding (Friedrich and Ehlers 2019a).

About two-thirds of the specimens are thermally stress-relieved. The treatment is performed under nitrogen shielding gas at 580°C for a holding time of three hours.

3.2.2 Longitudinal stiffener

The geometry of the longitudinal stiffener specimens is shown in Figure 3-13. The cross-section of 10 x 55 mm^2 is the same as for the K-butt weld specimens. To allow hole drilling measurements close to the weld toe, on a number of specimens the right end of the stiffener is cut at a 45° angle before welding. According to simulations, residual stresses in the base plate should be the same as in specimens with straight stiffeners.

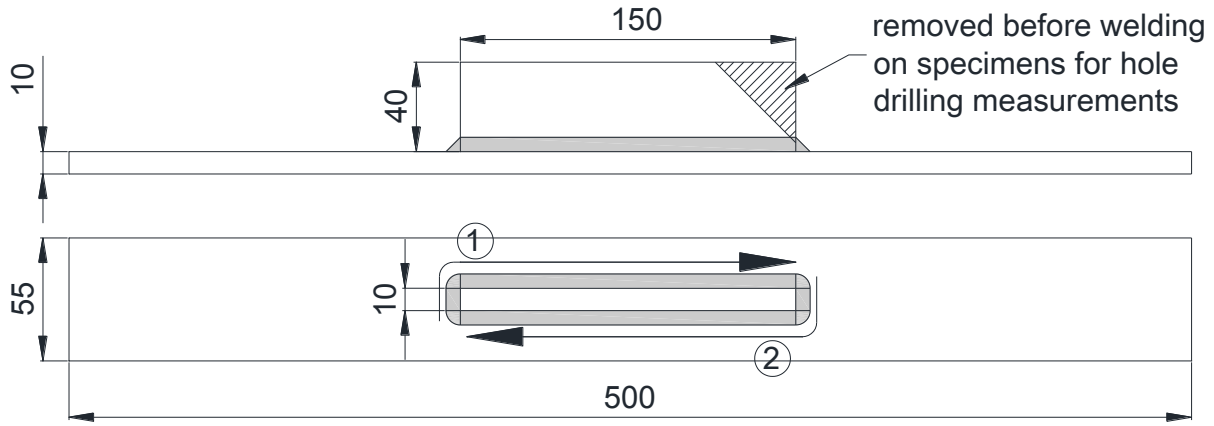

Figure 3-13: Longitudinal stiffener specimens, welding sequence indicated by ① and ② (Friedrich and Ehlers 2019c).

The specimens are made of steel S355J2+N, from a different charge than the K-butt weld specimens. The base plates are cut from a 10 mm plate using a band saw. Tensile tests give the following values: yield strength $R_{p0.2}$ = 370 MPa; tensile strength R_m = 543 MPa; Young's modulus E = 201 GPa. The stress-strain curves are shown in Figure 3-14. Flat bars 40 x 10 (S355) are used for the stiffeners.

MAG welding is applied. Welding starts at the left end of the stiffener (referred to Figure 3-13). Welding current is 250 A and voltage 29 V. During welding the ends of the specimens are fixed on a square tube 80 x 80 x 3.5 by screw clamps to reduce distortion (Figure 3-15, left). The clamps are removed after the specimens have cooled below 100°C (measured by infrared thermometer). To avoid cracks at the left end of the stiffener the weld toe is mitigated by grinding (Figure 3-15, right).

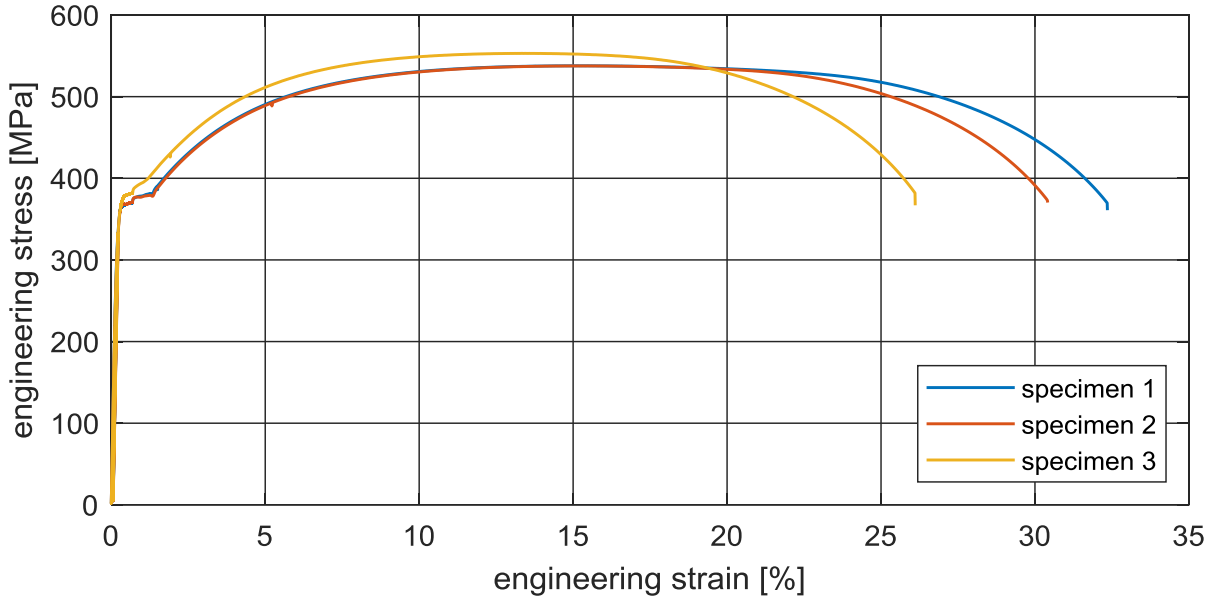

Figure 3-14: Stress strain curves from tensile tests (S355J2+N for longitudinal stiffener specimens).

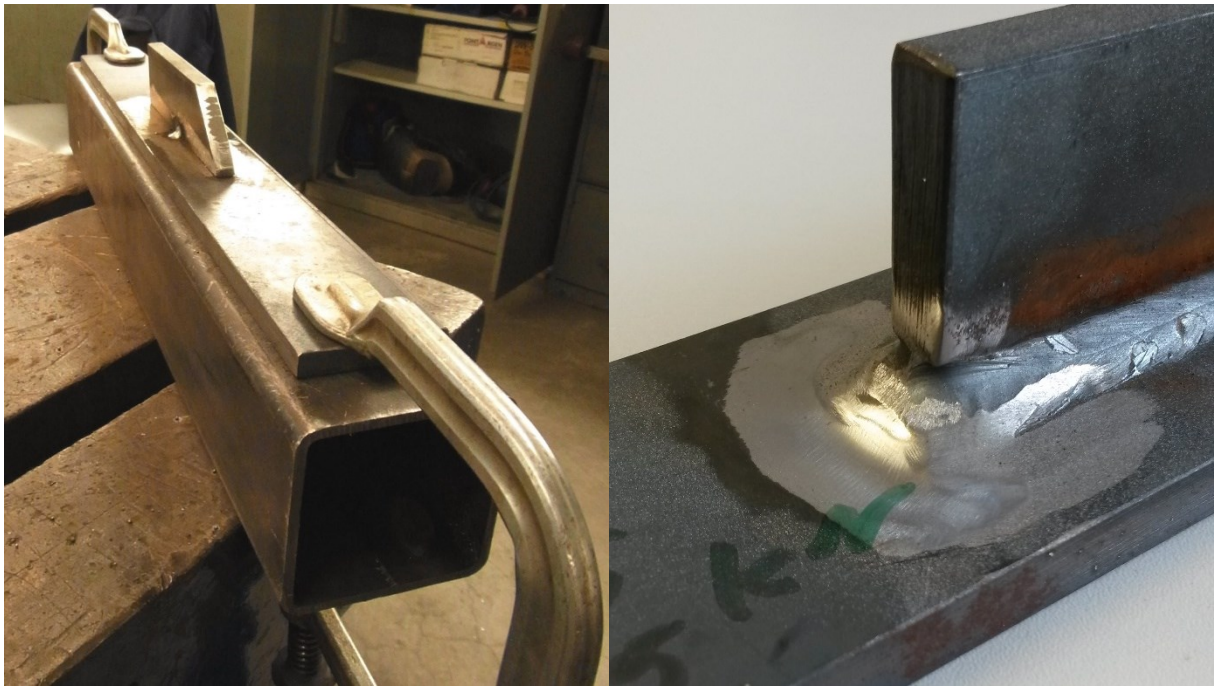

Figure 3-15: Specimen clamped on a square tube during welding (left) and weld toe at left end of the stiffener grinded to avoid cracks (right).

About two-thirds of the specimens are thermally stress-relieved. The treatment is performed under nitrogen shielding gas at 580°C for a holding time of three hours.

The simulation results and specimen preparation presented in chapter 3 have been published by the author of this thesis in (Friedrich and Ehlers 2019a) and (Friedrich and Ehlers 2019c).

3.2.3 Specimen distortion

When clamping a distorted specimen in the testing machine the distortion will result in a bending moment and thus bending stresses. These will be added to the applied load stress and therefore affect the effective stress ratio. As also the residual stresses affect the effective stress ratio with excessive clamping stresses the effect of residual stresses will not be recognisable. Furthermore, welding distortions and residual stresses are closely related. Processes that change residual stresses can also result in changes of distortions. A part of the specimens is thermally stress-relieved. To determine the residual stress influence it is important that distortions are similar for the as-welded and the stress-relieved specimens.

The distortion of the K-butt weld specimens is determined by measuring the height difference between two points on each side of the weld (Figure 3-16), compare (Fricke et al. 2009).

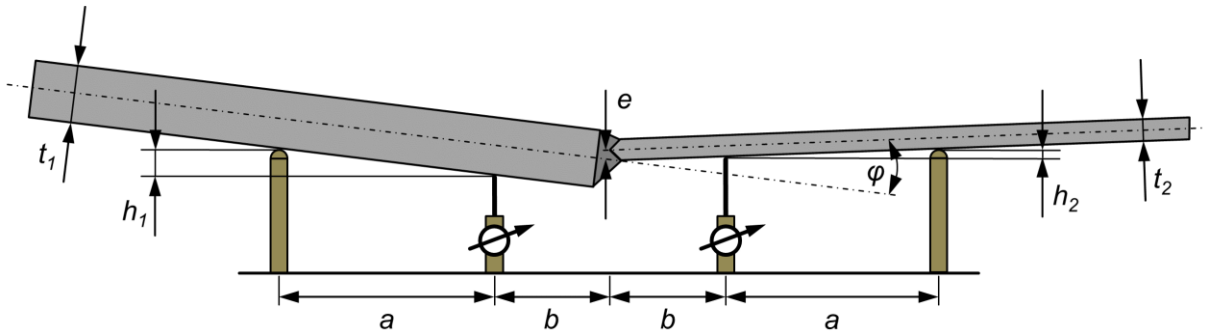

Figure 3-16: Distortion measurements on the K-butt weld specimens.

The resulting misalignments and distortions on the as-welded and the stress-relieved specimens are plotted in Figure 3-17. The plotted lines refer to half plate thickness (dash-dot lines in Figure 3-16). For better comparability the curves are rotated so that the left side is horizontal. The angular distortion appears to be similar for as-welded and stress-relieved specimens. Some specimens are measured before and after stress-relieve treatment. No change of the measured distortion is found.

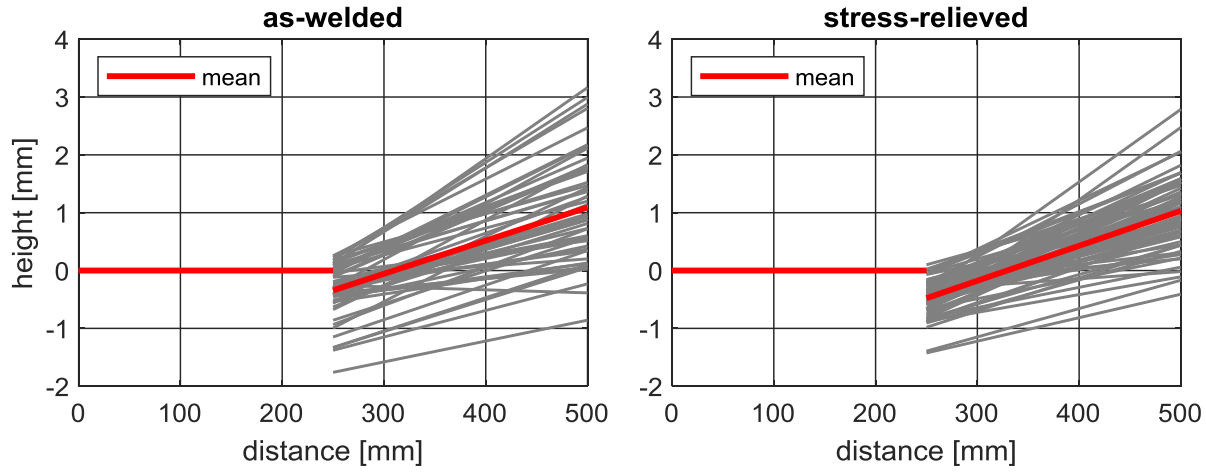

Figure 3-17: Distortion measured on the K-butt weld specimens.

For the K-butt weld the misalignment *e* and angular distortion *φ* are calculated according to the following equations:

$$e = (h_1 - h_2)\left(1 + {}^{b}/_{a}\right) - \frac{t_1 - t_2}{2} \tag{3.1}$$

$$\varphi = \tan^{-1}\left(\frac{h_1}{a}\right) + \tan^{-1}\left(\frac{h_2}{a}\right) \tag{3.2}$$

with the parameters shown in Figure 3-16. The calculated mean values are given in Table 3-1. The differences lie within the measurement accuracy.

Table 3-1: Mean values of distortion for the K-butt weld specimens.

	as-welded	**stress-relieved**
angular distortion φ	0.33°	0.35°
linear misalignment e	0.33 mm	0.47 mm

The same setup is used to measure the distortion on the longitudinal stiffeners (Figure 3-18). For the longitudinal stiffener the results are only qualitative. The specimens have an angular distortion at both ends of the stiffener. Because of minor differences in the specimens' lengths it is difficult to position the centre of the stiffener accurately between the measuring points. The resulting distortion curves are plotted in Figure 3-19. For the plots it is assumed that the specimens bend at the ends of the stiffener.

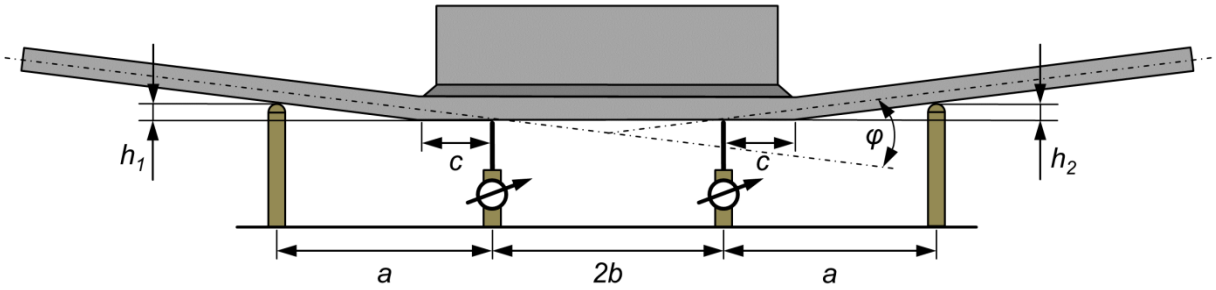

Figure 3-18: Distortion measurements on the longitudinal stiffener specimens.

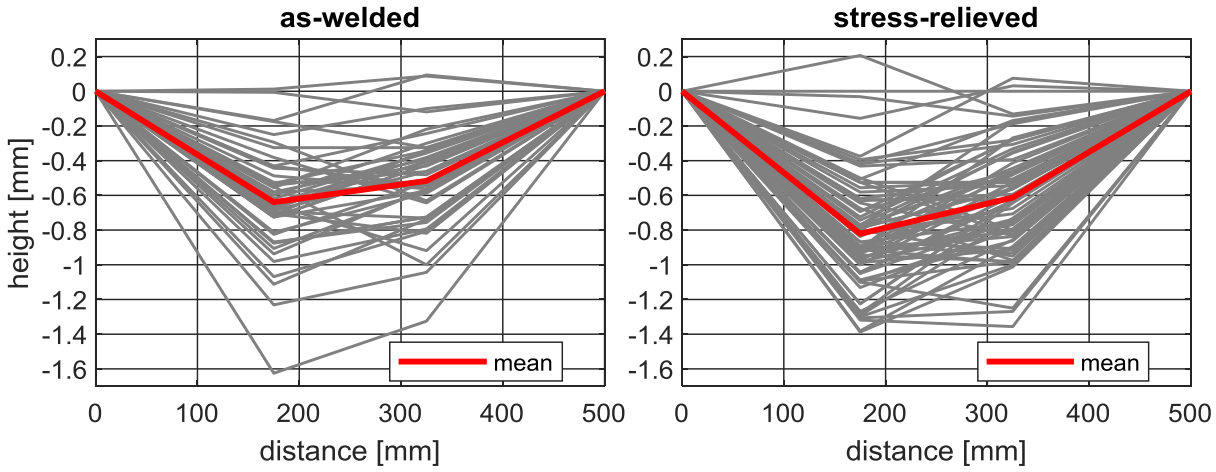

Figure 3-19: Measured height differences on the longitudinal stiffener specimens.

For the longitudinal stiffener specimens the angular distortion φ between the two stiffener ends is calculated according to the following equation:

$$\varphi = \tan^{-1}\left(\frac{h_1 - \frac{c(h_2 - h_1)}{2b}}{a - c}\right) + \tan^{-1}\left(\frac{h_1 + \frac{(2b + c)(h_2 - h_1)}{2b}}{a - c}\right) \tag{3.3}$$

with the parameters from Figure 3-18. The calculated mean values of the angular distortion and the deflection at the centre of the specimen with respect to its ends are given in Table 3-2. The distortion increases slightly after stress-relieving. This is in line with findings in (Fricke and Tchuindjang 2016), where the deflections were between 0 and 1 mm in the as-welded condition and up to 8 mm after stress-relieving on longitudinal stiffener specimens of

600 mm length. In (Hensel et al. 2016) angular distortions of more than 1.0° were corrected mechanically to between 0.09° and 0.15°.

Table 3-2: Mean values of distortion for the longitudinal stiffener specimens.

	as-welded	**stress-relieved**
angular distortion φ	0.38°	0.47°
deflection	0.58 mm	0.72 mm

Although the performed measurements are not accurate they allow a qualitative assessment of the welding distortions. Compared to distortion values found in literature the measured values appear to be on the lower side. For the K-butt weld no difference between as-welded and stress-relieved specimens was found. For the longitudinal stiffeners the distortion increased slightly after stress-relieve treatment. In the following fatigue test levelling plates will be used to compensate the distortions. Thus, it will not be possible to calculate the clamping stresses or secondary bending stresses analytically and the measurements are used only for verification purposes. The distortion measurements are therefore not repeated by more adequate means (e.g. laser scanner).

The distortion measurements presented in section 3.2.3 have been published by the author of this thesis in (Friedrich 2020).

4 Residual stress assessment

Two sets of test specimens with a K-butt weld and a longitudinal stiffener have been prepared. To understand their influence on the fatigue behaviour the welding residual stresses have to be known. The residual stresses at the weld are determined by measurements and numerical simulations.

4.1 Residual stress measurements

Residual stresses are measured by two different measurement methods. X-ray diffraction, in which the deflection of X-rays is used to determine the distances in the atomic lattice and deduce residual stresses out of it. It has the advantage that it is non-destructive and it is possible to measure close to the weld toe. The measurement is performed on the surface up to approximately 5 micrometres depth. The second measurement technique is the hole drilling method, where a hole is drilled and the relieved strains are measured by strain gauges to determine the residual stresses. The residual stress distribution is measured up to about 1 mm depth.

4.1.1 K-butt weld

X-ray diffraction

Residual stress measurements by X-ray diffraction are performed on three specimens. The measurements are done by the *Institute of Joining and Welding*, TU Braunschweig. The residual stresses are calculated according to the $\sin^2\psi$ technique. The interference peaks of the {211} plane in ferrite and martensite are determined using CrKα radiation. The measurement spot has a diameter of 1.5 – 2 mm.

Residual stresses are measured at the centre line on the top side of the specimen. On one specimen measurements are performed also on the bottom side. The measured residual stresses transversal to the weld are shown in Figure 4-1 including the error bar for each measuring point. The curves are referenced by the specimen they were measured on, indicated by the number of the plate (23, 24 and 34) and the number of the specimen (1, 2 and 5 according to Figure 3-10). Two of the three specimens show transversal residual stresses rising towards the weld to up to about 100 MPa. The third (23-5) shows a peak in front of the weld and a decrease to about 60 MPa. Measurements on this specimen have been repeated at about 2 mm from the centre line confirming the first measurement with about 80 MPa measured at the weld toe. On the bottom side of the plate transversal residual stresses rise to about 240 MPa at the weld toe. The compressive residual stresses far away from the weld, on both sides of the plate, could result from the production process of the plates. The plates have not been stress-relieved before welding.

Figure 4-2 shows the longitudinal residual stresses. In longitudinal direction values at the weld toe lie between -130 MPa and +50 MPa on the top side of the plate. As in transversal direction, the values measured on specimen 23-5 are higher than on the other two specimens.

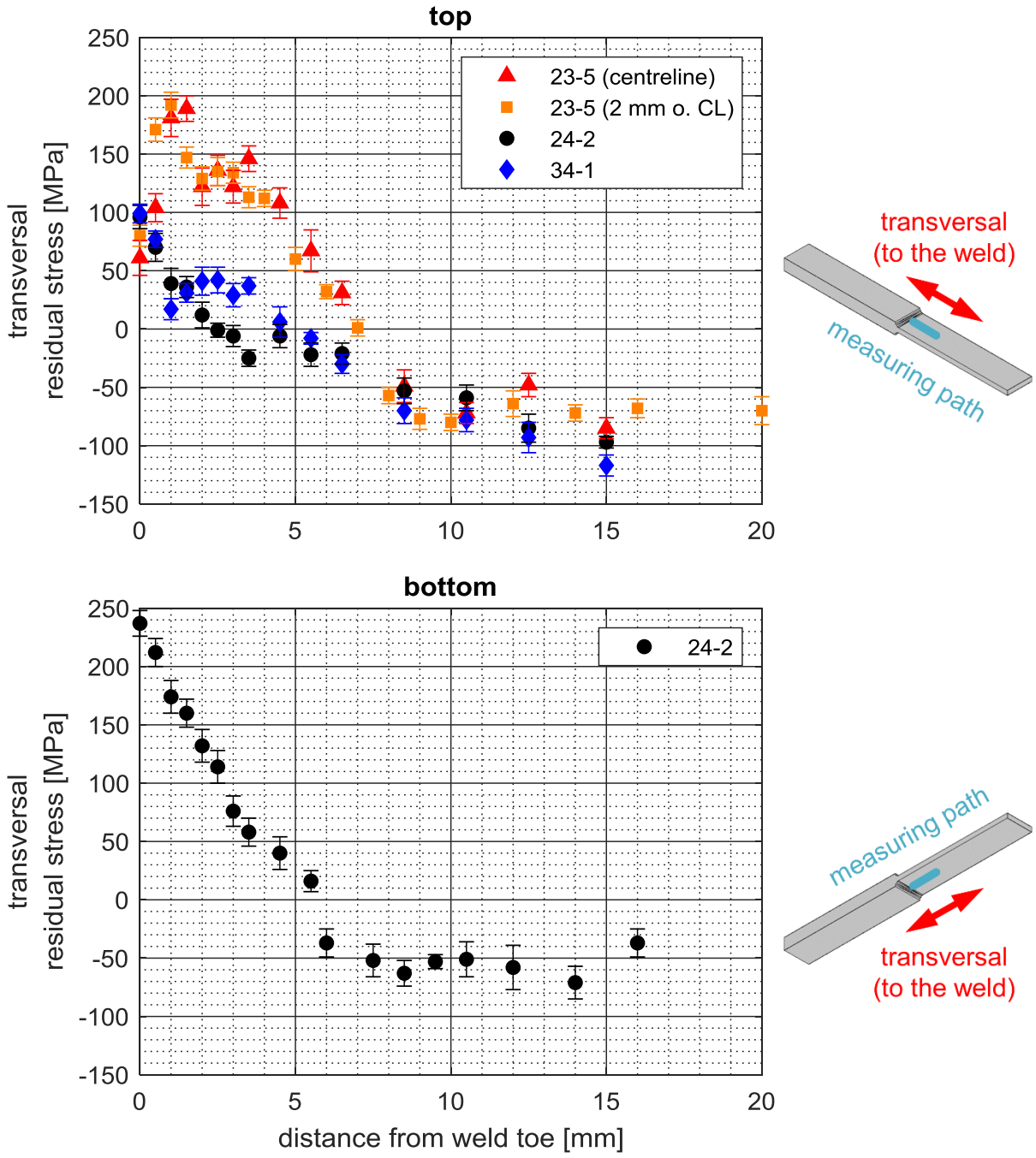

Figure 4-1: Transversal residual stress measured by X-ray diffraction on three specimens (specimens referenced by the plate number XX and the position of the specimen 1 – 5 according to Figure 3-10) (Friedrich and Ehlers 2019a).

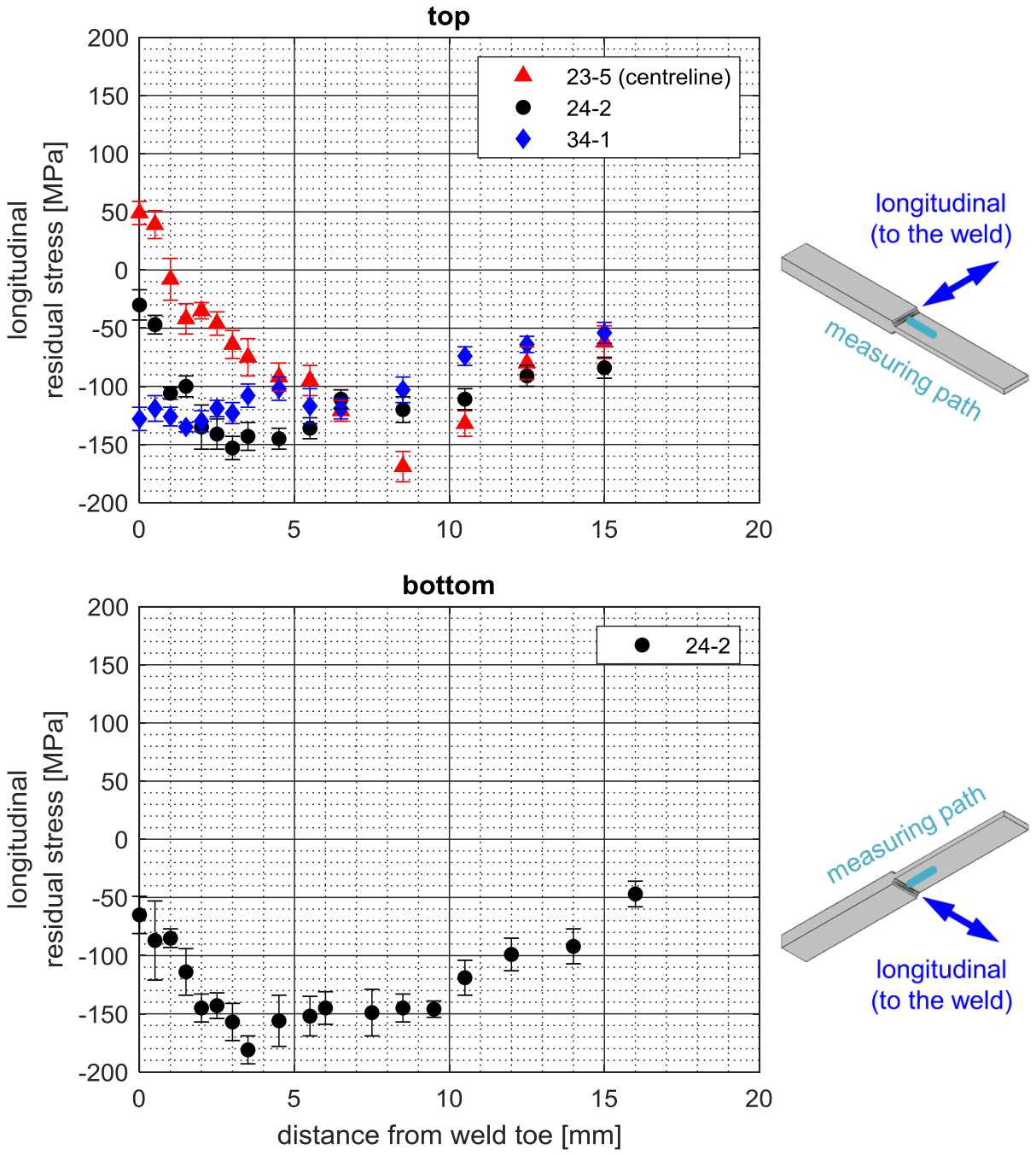

Figure 4-2: Longitudinal residual stress measured by X-ray diffraction on three specimens (specimens referenced by the plate number XX and the position of the specimen 1 – 5 according to Figure 3-10) (Friedrich and Ehlers 2019a).

Hole drilling

Further measurements are done by the hole drilling method. The method consists in drilling a hole and measuring the relieved strain around the hole by strain gauges. Residual stresses are then calculated from the measured relieved strain. Measurements are carried out with a SINT MTS3000 system and evaluated using Restan evaluation software v.7.14. The applied strain gauge rosettes are of Type A according to ASTM E837-13a, respectively Type B for measurements closer than 5 mm to the weld. Nominal drill diameter is 1.6 mm. By incrementally increasing the drilled depth a curve of the residual stresses over depth can be calculated. This is done by the integral method (Schajer 1988). In addition, the value according to ASTM E837-13 assuming a uniform stress distribution up to 1 mm depth is

calculated. The applicability of the hole drilling method is limited by the yield limit of the material. According to ASTM E837-13a residual stresses should not exceed 80 % of yield limit for “thick workpieces”, according to (Schajer, ed. 2013) 70 % for the applied hole depth and gauge circle diameter. The highest measured residual stresses are in the range of 60 % of yield strength and thus within these limits.

The residual stress distribution over the hole depth measured at a distance of 1.2 mm respectively 6 mm from the weld toe is exemplarily shown in Figure 4-3. Besides the residual stresses also the measured strains from the strain gauges are plotted. For these measurements the depth increment was 0.01 mm up to a depth of 0.1 mm and 0.05 mm between 0.1 mm and 1.0 mm. The plots show the following:

- Strains have been measured, thus residual stresses must have been relieved. The strains measured in orthogonal directions were of different signs, thus also the residual stresses should have been. Tensile residual stresses yield negative (compressive) measured strains and vice versa.
- The residual stress level between 0.1 and 1 mm depth is represented well by the value according to ASTM E837-13 assuming a uniform residual stress distribution. Since it is a mean value over the drilled depth it is less affected by inaccuracies than the evaluation for every single depth increment (ASTM E837-13a, Schajer, ed. 2013).
- The determined residual stress values tend to decrease close to the surface. However, because of measurement inaccuracies on the first drilling increment steps, the measurements should not be used to determine residual stress values at the surface (compare ASTM E837-13a).

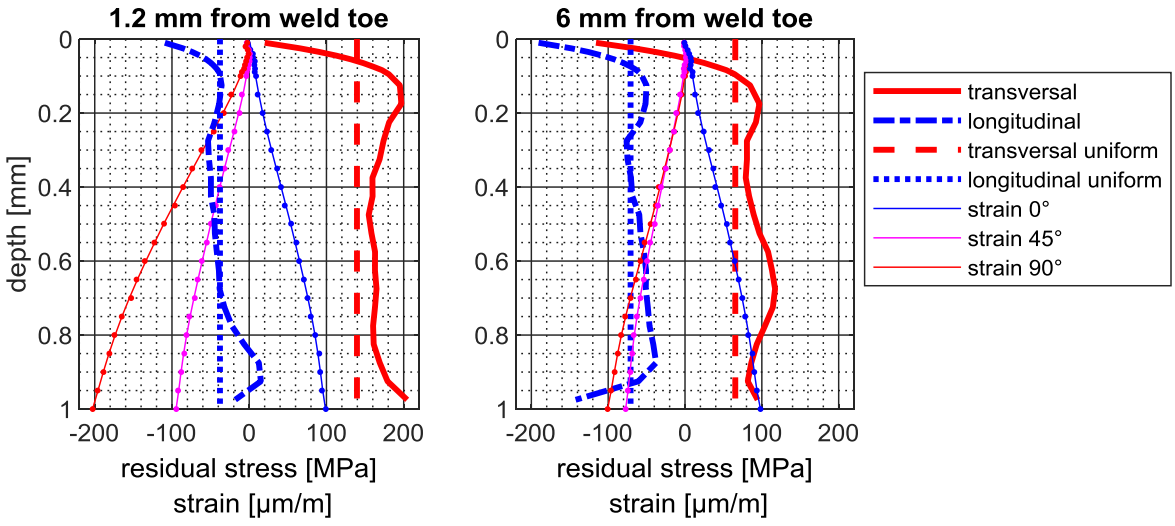

Figure 4-3: Residual stresses measured by hole drilling on the top side of the plate (specimen 24-2). Strains refer to their orientation relative to the weld (Friedrich and Ehlers 2019a).

The measurements on other specimens show similar curves with stable values between 0.1 and approximately 1 mm depth. To what extent the steep gradient at the surface is caused by actually lower residual stresses or by the measurement technique cannot be said without further verification. The evaluation over 1 mm depth is generally less affected by errors than the stepwise evaluation for each drilling increment. For better comparability, the uniform values will be used in the following. In the evaluation of the measurement data in the context of fatigue assessments it has to be considered that these values represent a mean value over a depth of 1 mm and might differ from the value on the surface. Whether the uniform

values are suitable for fatigue assessments has to be verified in the following experimental investigations.

Several measurements at a distance of approximately 2 mm from the weld are done distributed over the width of one specimen. Tensile transversal residual stresses of 175 MPa are measured up to 12 mm from the centre line. Further outside, 5 mm from the edges of the specimen, values are compressive close to zero.

Transversal residual stresses measured on several specimens are shown in Figure 4-4 along with the X-ray diffraction measurements. The results show similar values as the upper curve from the X-ray diffraction measurements (specimen 23-5). On specimen 24-4 the hole drilling measurement closest to the weld (distance 1 mm) shows a decreased transversal residual stress value. The principal stress however remains unvaried at about 170 MPa. The principal stress direction is turned 37° from the specimen's longitudinal axis. This was not noticed on other hole drilling measurements at this distance from the weld.

The longitudinal residual stresses are shown in Figure 4-5. Also in this direction, the hole drilling results lie close to the highest curve from the X-ray diffraction measurements (specimen 23-5).

It has to be noted, that the hole drilling values are evaluated over a depth of 1 mm, the X-ray diffraction values are measured at a depth of approximately 5 µm. Furthermore, the surface has to be slightly grinded with sandpaper in order to assure a proper installation of the strain gauge rosettes for the hole drilling measurements. Thus, the results obtained with the two measuring methods should be seen as complementary rather than comparable. This applies to both, transversal and longitudinal residual stresses.

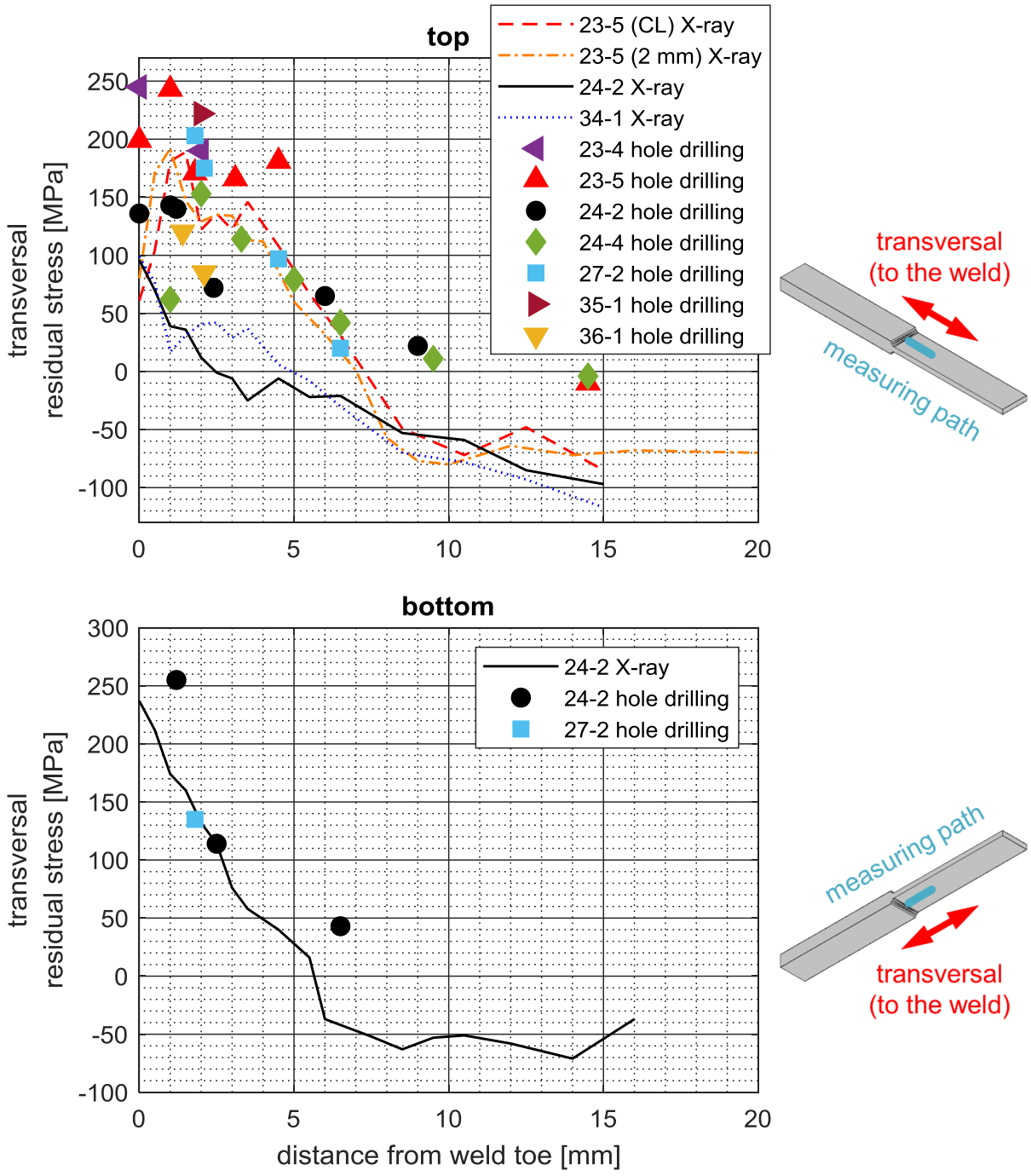

Figure 4-4: Transversal residual stress measured by hole drilling and X-ray diffraction (specimens referenced by the plate number XX and the position of the specimen 1 – 5 according to Figure 3-10) (Friedrich and Ehlers 2019a).

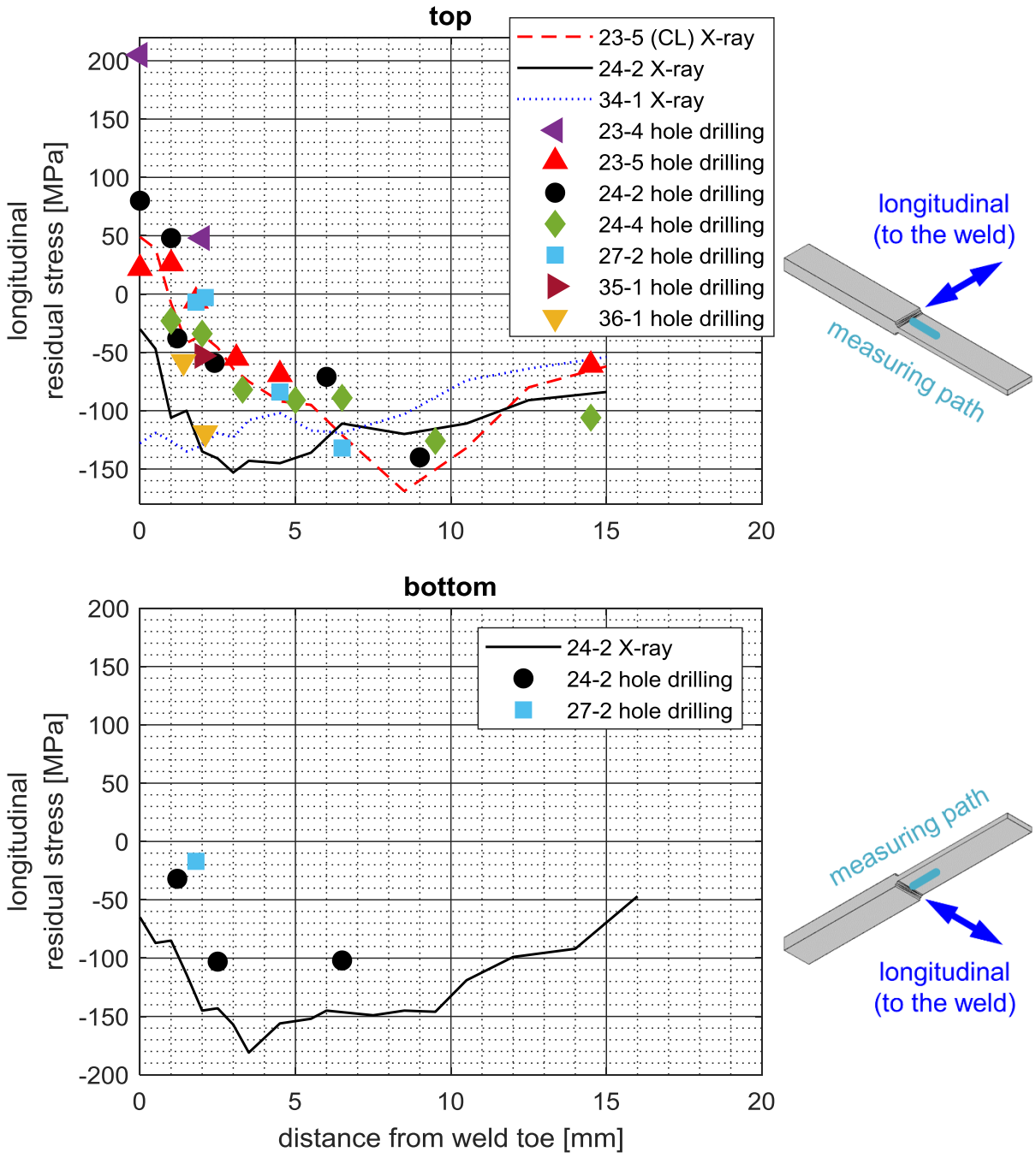

Figure 4-5: Longitudinal residual stress measured by hole drilling and X-ray diffraction (specimens referenced by the plate number XX and the position of the specimen 1 – 5 according to Figure 3-10) (Friedrich and Ehlers 2019a).

4.1.2 Longitudinal stiffener

X-ray diffraction

Residual stresses are measured by X-ray diffraction on three specimens. The measurements are performed at the centre line of the specimens at the right end of the stiffener (Figure 3-13). The measurements are executed by the *Institute of Joining and Welding*, TU Braunschweig.

The residual stresses measured in transversal and longitudinal direction are shown in Figure 4-6. Specimens 16 and 19 have a straight stiffener, specimen 5 has a bevelled stiffener as

the specimens for hole drilling (compare Figure 3-13). Transversal values on all three specimens show a maximum of about 200 MPa situated approximately 2 – 3 mm in front of the weld. The values decrease to about 90 to 190 MPa at the weld toe. In longitudinal direction residual stresses are compressive at about -200 MPa up to 5 mm in front of the weld and increase to values between 3 and 67 MPa at the weld toe.

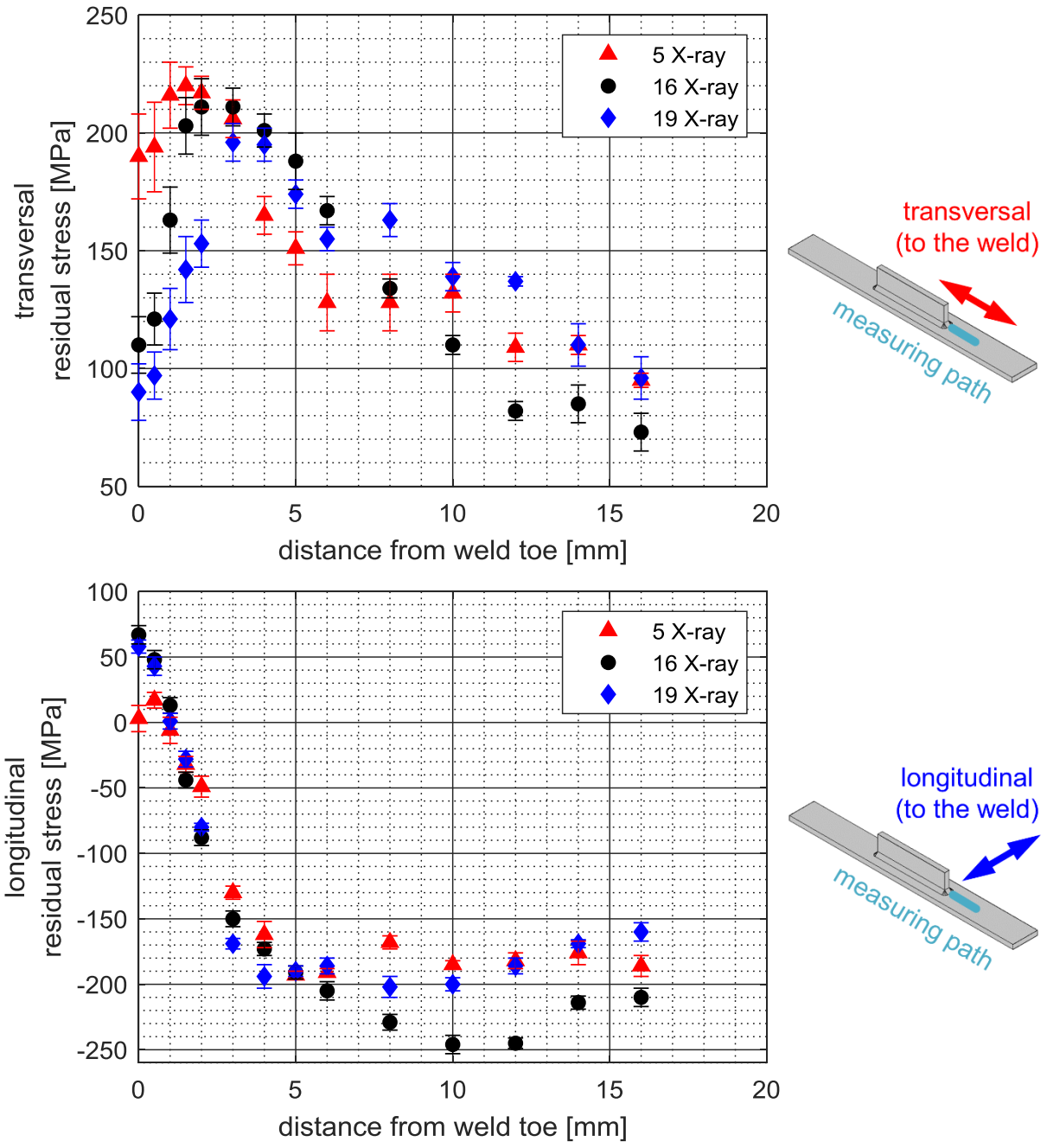

Figure 4-6: Residual stress measured by X-ray diffraction on three longitudinal stiffener specimens.

Hole drilling

Residual stress measurements by hole drilling are executed analogue to the measurements on the K-butt weld specimens in section 4.1.1. The measurements are done at the right end of the stiffener. The holes are distributed leaving at least 4 mm in between and so that they do not shadow each other with respect to the stiffener. The residual stresses over the hole depth measured on a specimen at two different distances from the weld toe are exemplarily shown in Figure 4-7. As before, residual stresses are calculated by the integral method and assuming a uniform residual stress distribution up to 1 mm depth according to ASTM E837-13. Transversal residual stresses show a steep increment on the first 0.1 mm and then stabilize on a value slightly higher than the result assuming a uniform distribution.

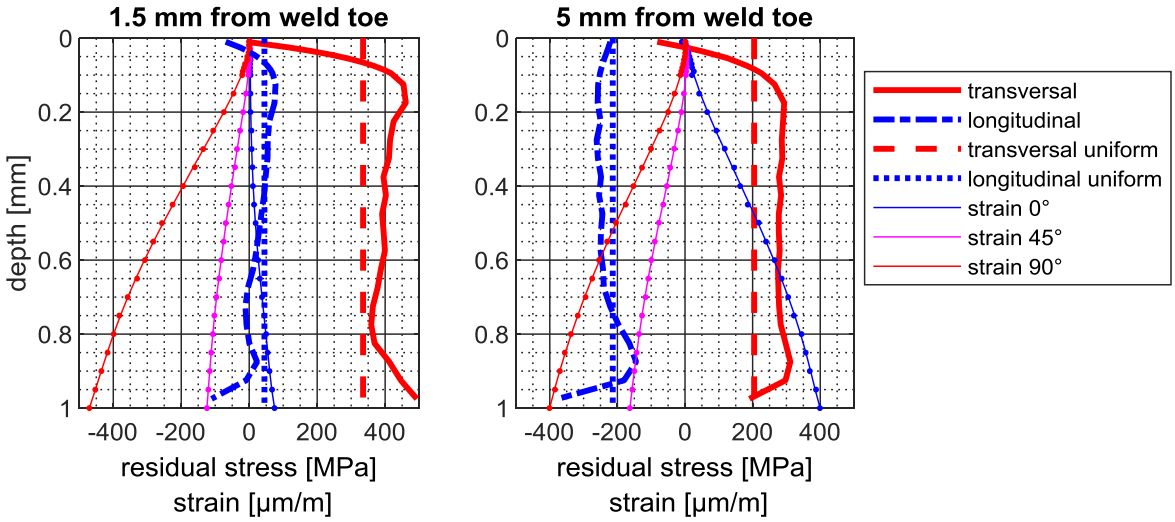

Figure 4-7: Residual stresses measured by hole drilling at the right end of the stiffener (specimen 1). Strains refer to their orientation relative to the weld.

The residual stresses measured by hole drilling are plotted together with the X-ray diffraction measurements in Figure 4-8. The results obtained with both methods show similar values beyond 5 mm from the weld. Closer to the weld, where welding residual stresses are expected to dominate over those resulting from the production or surface treatment of the plate, transversal residual stresses show different trends. While the hole drilling results increase to over 300 MPa, the X-ray diffraction values show a maximum of about 200 MPa and decrease towards the weld. Longitudinal residual stresses measured by hole drilling increase to about 180 MPa approximately 1 mm in front of the weld toe.

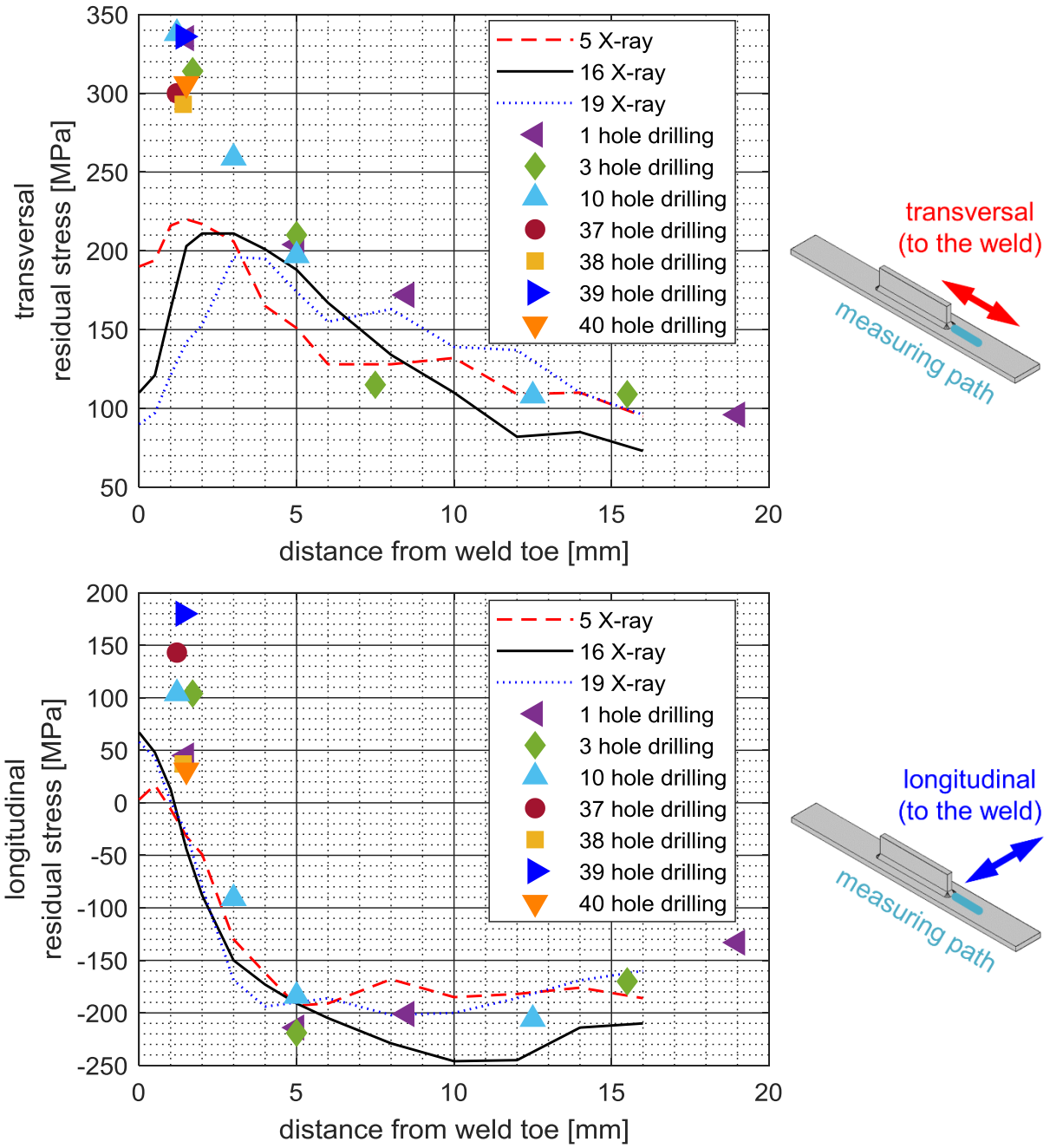

Figure 4-8: Residual stress measured by hole drilling and X-ray diffraction on different longitudinal stiffener specimens.

4.1.3 Stress-relieved specimens

About two-thirds of the specimens have been stress-relieved after welding. To verify that residual stresses were significantly reduced they are measured on some of the stress-relieved specimens.

K-butt weld

Measurements by hole drilling are performed on two specimens. On a third specimen residual stresses are measured by X-ray diffraction. The values from hole drilling assuming a uniform value over 1 mm depth are plotted together with the results from the X-ray diffraction measurements in Figure 4-9. Hole drilling measurements lie between +7 and +21 MPa. X-ray

diffraction shows values of +28 MPa in transversal direction and -17 MPa in longitudinal direction at the weld toe. Values farther from the weld lie in the range of -100 MPa.

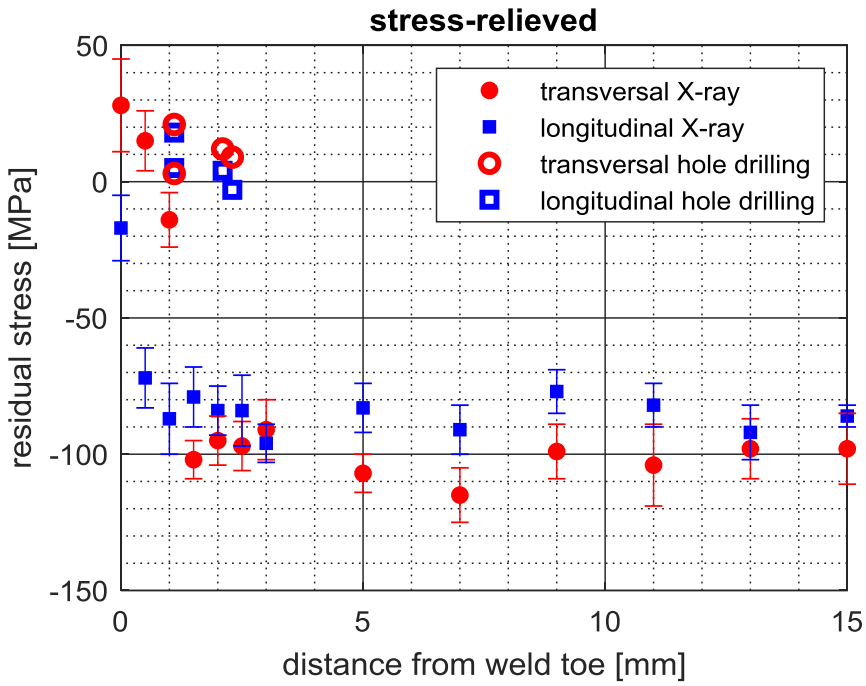

Figure 4-9: Residual stress measured by X-ray diffraction and hole drilling on stress-relieved K-butt weld specimens.

Longitudinal stiffener

Residual stresses measured on the stress-relieved longitudinal stiffener specimens by hole drilling and X-ray diffraction are plotted in Figure 4-10. Values measured by hole drilling are between -2 MPa and +12 MPa. The X-ray diffraction shows values of +30 MPa in transversal and -24 MPa in longitudinal direction at the weld toe and in the range of -10 MPa farther away.

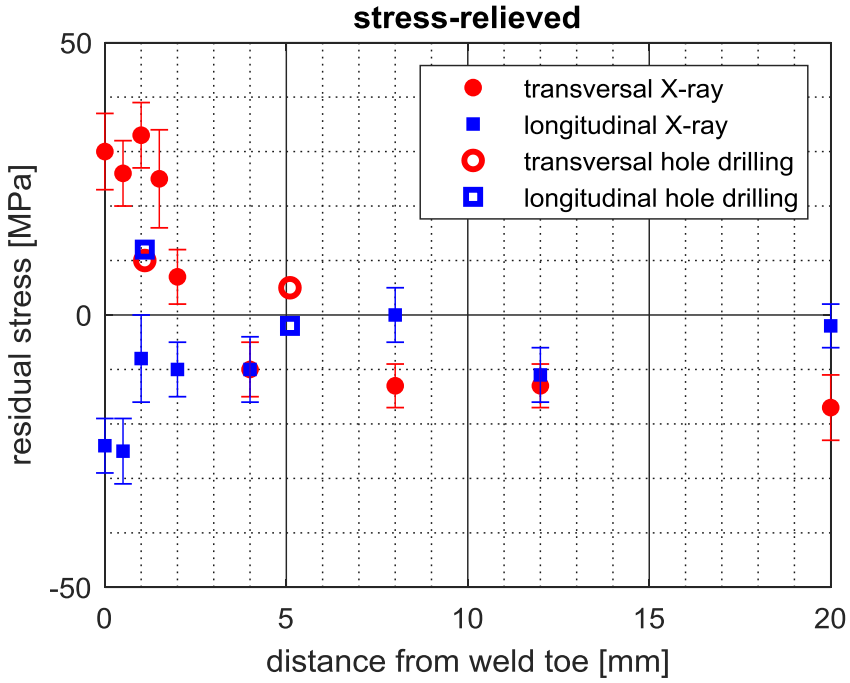

Figure 4-10: Residual stress measured by X-ray diffraction and hole drilling on stress-relieved longitudinal stiffener specimens.

4.2 Welding simulations

Welding residual stresses for both specimen geometries are calculated by the welding simulation approach presented in chapter 2.

4.2.1 K-butt weld

The FE model used for the K-butt weld simulation is shown in Figure 4-11. An idealized weld cross-section with 6 passes is assumed. The element size in front of the weld toe is 0.25 mm with a coarser mesh on the rest of the model. The temporary u-profiles to reduce distortion (compare Figure 3-12) are modelled by shell elements. Boundary conditions are applied on three nodes only to prevent rigid body motion.

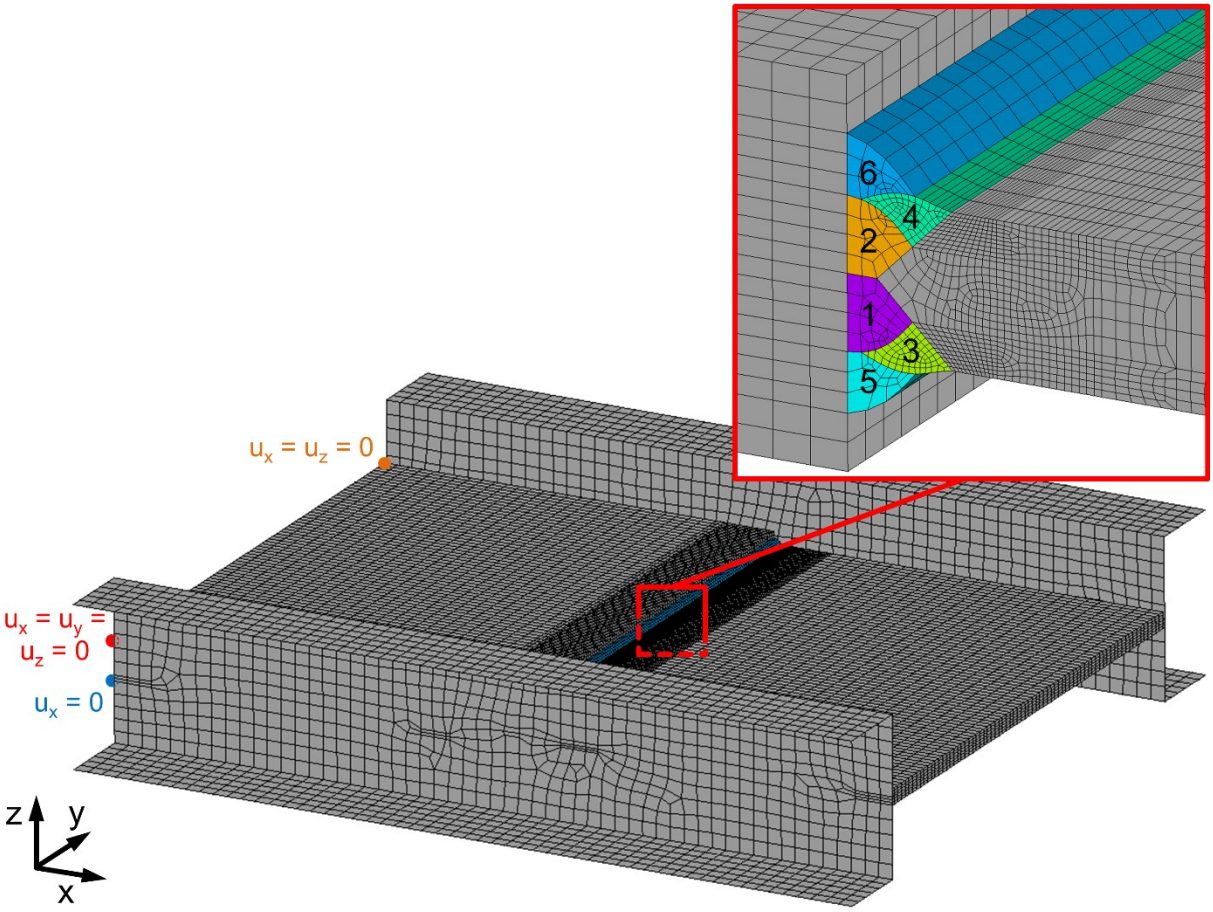

Figure 4-11: FE model of the K-butt weld specimen preparation and detail of the weld including the weld pass sequence.

After the welding simulation the cutting of the specimens is simulated by deactivating the elements on the cutting line as described in section 3.1.2. The resulting transversal residual stresses after welding and after cutting the specimens are plotted in Figure 4-12. The residual stresses are redistributed during cutting. In the end, residual stresses show a similar distribution on all five specimens. From the detail, cut on the centre line of the centre specimen, it can be seen that transversal residual stresses on the surface are tensile in the centre of the specimen and compressive close to the edge. Over the plate thickness, at the weld values go from tensile at the top surface to compressive in the middle and again tensile on the bottom. The highest tensile residual stresses occur at the bottom weld toe.

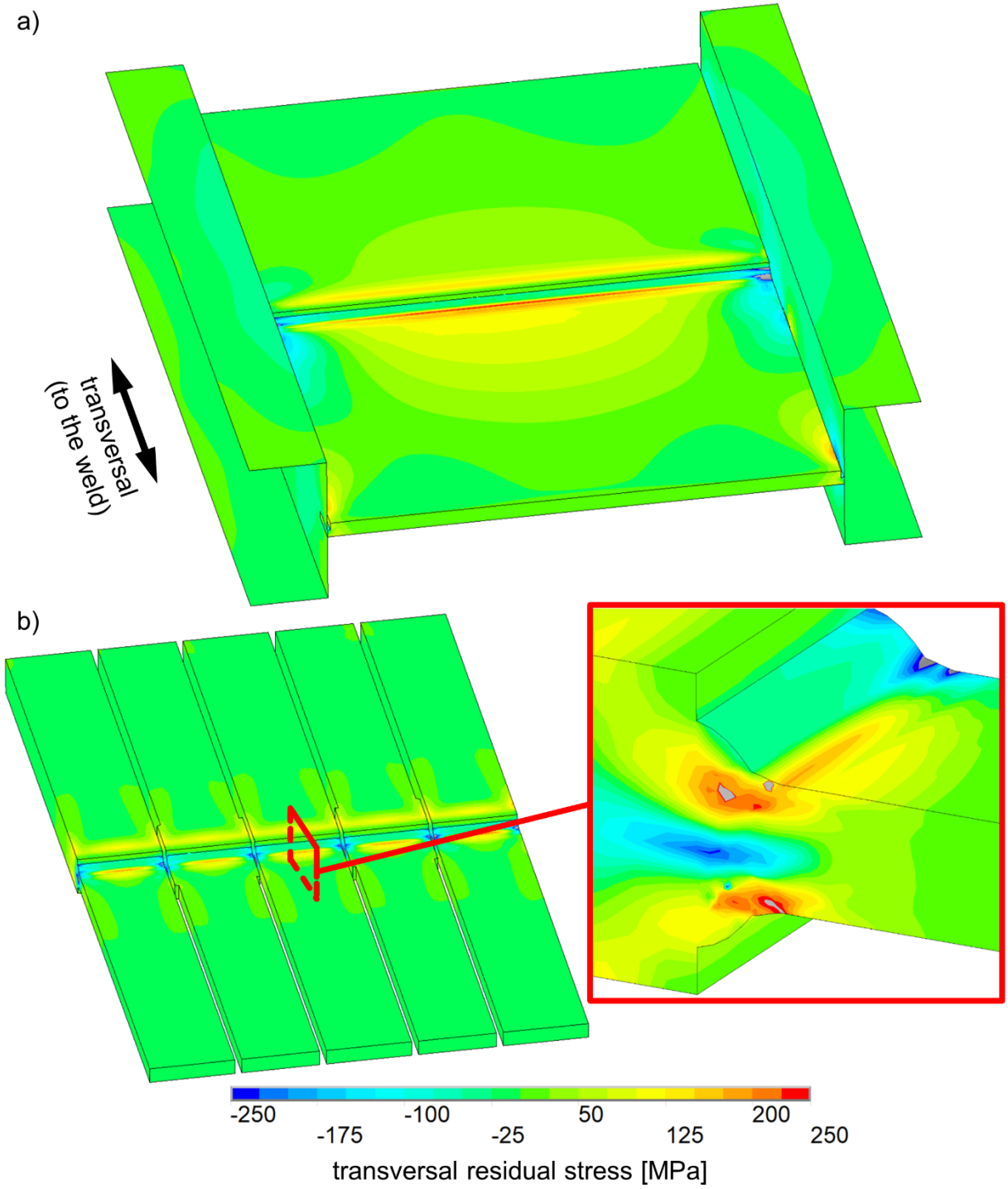

Figure 4-12: Transversal residual stresses (a) after welding and (b) after cutting out the specimens.

To validate the simulation results the calculated transversal residual stresses are compared to the measurements in Figure 4-13. The calculated values are in good agreement with the hole drilling results and the highest X-ray diffraction measurements. For distances of more than 7 mm from the weld X-ray diffraction measurements show compressive values and run lower than the simulation values and the hole drilling results. These compressive residual stresses probably result from the production process of the plates.

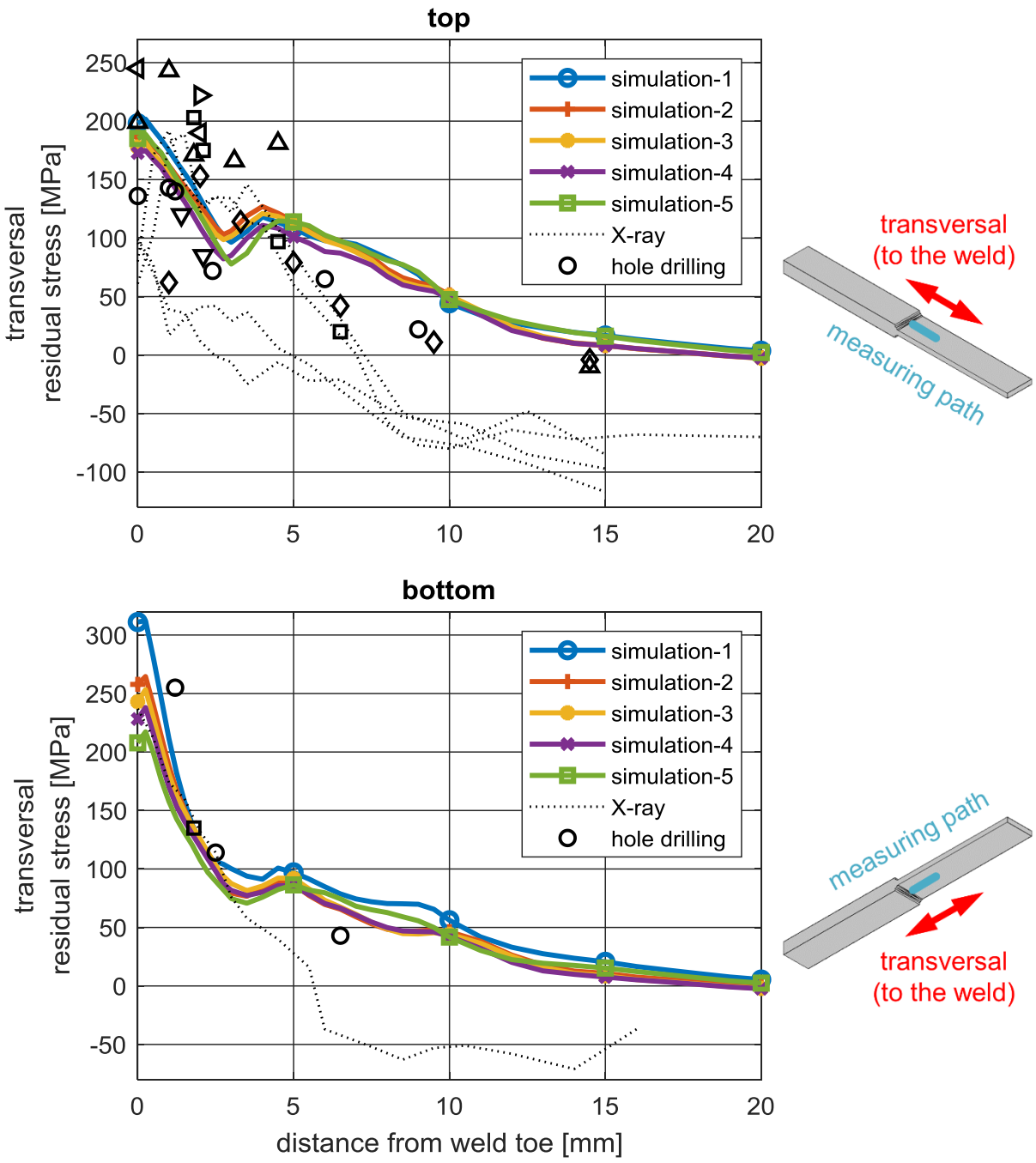

Figure 4-13: Calculated and measured transversal residual stresses. Same black symbols indicate measurement on the same specimen. Simulation 1 - 5 refer to specimen numbers according to Figure 3-10 (Friedrich and Ehlers 2019a).

The longitudinal residual stresses are shown in Figure 4-14. Calculation results show about 100 to 150 MPa more than the hole drilling measurements and the highest of the X-ray diffraction measurements up to about 5 mm from the weld. At a greater distance the differences are smaller. By comparing the simulation results only to the X-ray diffraction measurements no agreement is apparent. These measurements scatter between -128 MPa and +49 MPa at the weld toe while the simulation results reach values of 133 to 200 MPa. All in all, although the simulation results show the same trend as the hole drilling measurements, quantitative agreement between measurement and simulation results is not good in the longitudinal direction. However, this direction is of less importance if the residual stresses are to be considered in a fatigue assessment since it runs parallel to the expected crack.

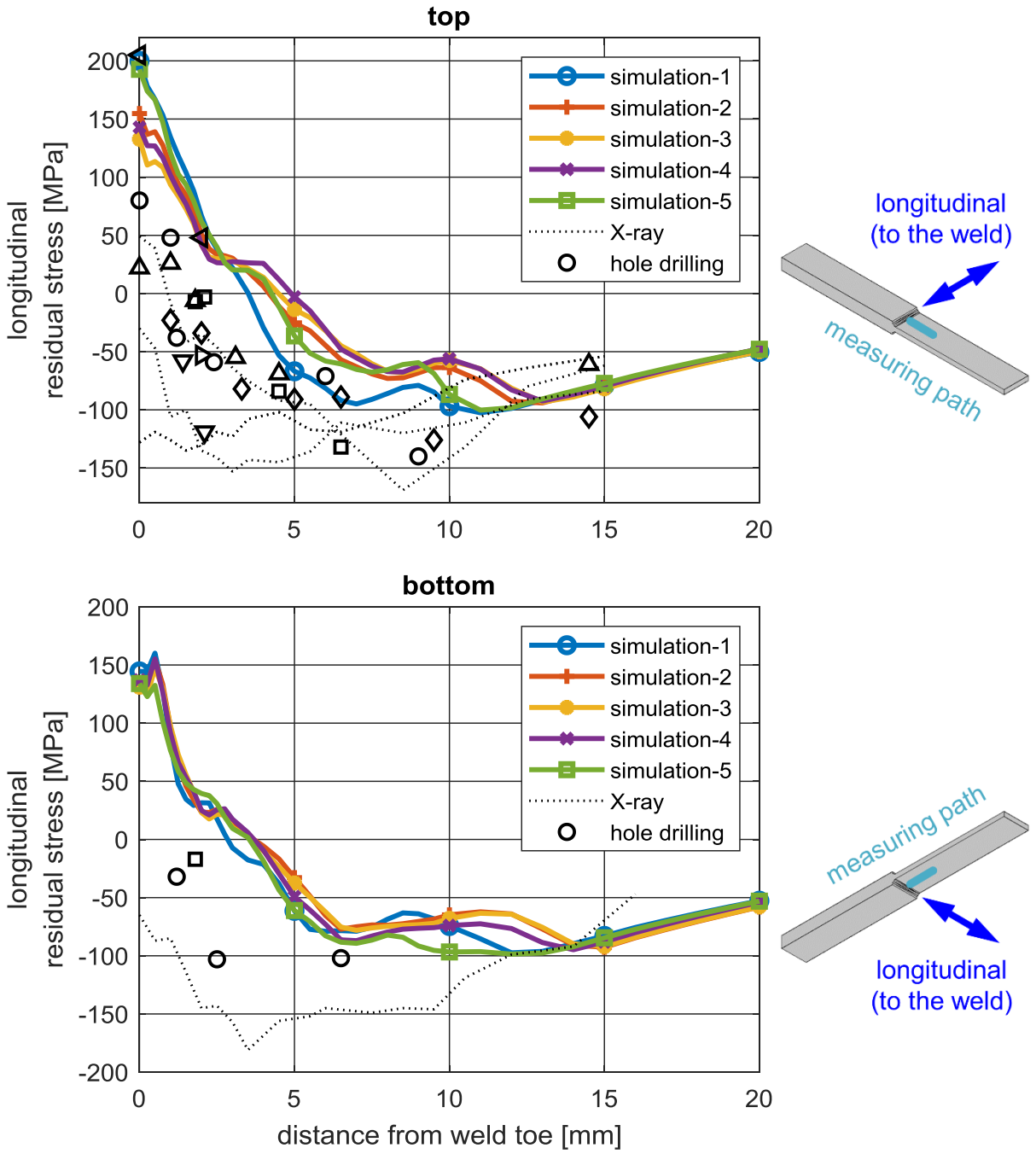

Figure 4-14: Calculated and measured longitudinal residual stresses. Same black symbols indicate measurement on the same specimen. Simulation 1 - 5 refer to specimen numbers according to Figure 3-10 (Friedrich and Ehlers 2019a).

4.2.2 Longitudinal stiffener

The FE model of the longitudinal stiffener specimens is shown in Figure 4-15. Element size in front of the weld is 0.25 mm. The structural boundary conditions are simplified by restraining the displacement in vertical direction at the ends of the model and relieving these restraints in the last load step, when the model has cooled to room temperature. Two additional nodes are constrained to avoid rigid body motion.

The resulting transversal residual stresses are plotted in Figure 4-16. Tensile residual stresses in front of the stiffener are balanced by compressive residual stresses at the edges of the specimen. From the cut on the centre line of the specimen it appears that the highest tensile values occur some millimetres below the weld.

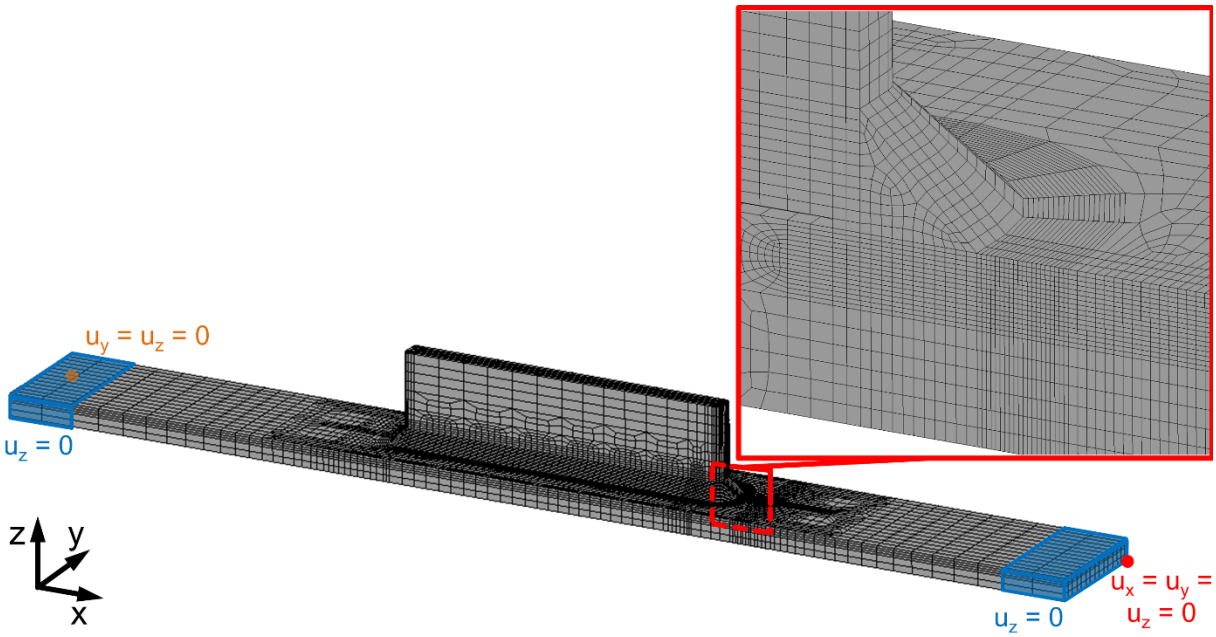

Figure 4-15: FE model of the longitudinal stiffener specimens and detail of the weld.

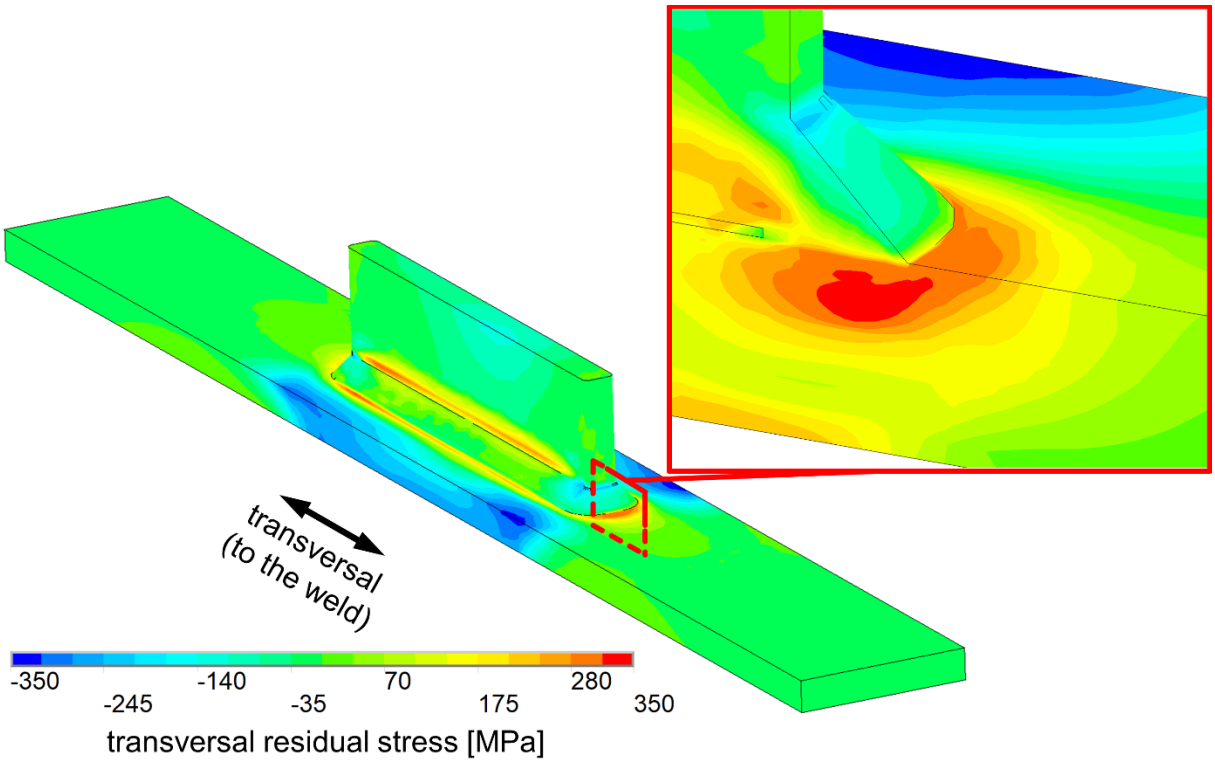

Figure 4-16: Transversal residual stresses calculated for the longitudinal stiffener specimens.

The calculated residual stresses are compared to the measurements in Figure 4-17. As mentioned in section 2.3.2, the calculated residual stresses should not be evaluated on the first 1 mm from the weld toe because of the singularity in the FE model and errors caused by element deformations upon activation of the weld elements. In both directions simulation results lie close to the hole drilling measurements. Both curves show an offset of about 2 mm compared to the measurements. This may indicate that too much energy is put into the model (compare Figure 2-13 and Figure 2-14).

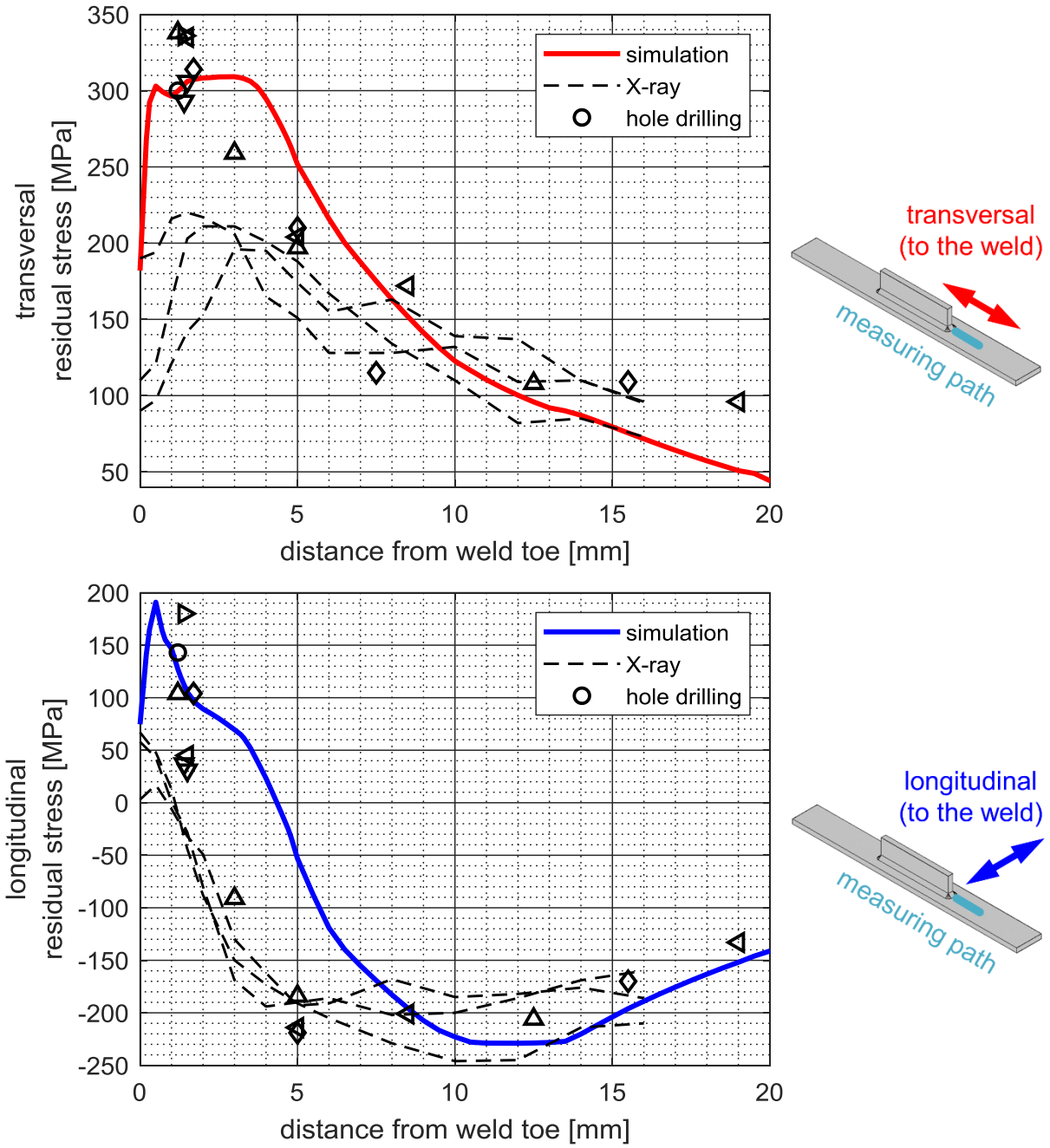

Figure 4-17: Calculated and measured residual stresses for the longitudinal stiffener specimens. Same symbols indicate measurement on the same specimen (Friedrich and Ehlers 2019c).

4.3 Findings

The residual stress measurements show tensile residual stresses transversal to the weld for both specimen geometries. In general the hole drilling measurements evaluated over a depth of 1 mm resulted in higher values than the X-ray diffraction measurements on the specimen surface. The measurements on the stress-relieved specimens show a clear reduction of the residual stresses and values close to zero at the weld toe. The simulation results fall within the scatter of the measurements with a tendency towards the hole drilling results. This is regarded as a good agreement, considering the simplification of the simulation approach, the scatter of the measurements and the accuracy of welding simulations in general.

The measurements and simulations presented in chapter 4 have in part been published by the author of this thesis in (Friedrich and Ehlers 2019a) and (Friedrich and Ehlers 2019c).

5 Fatigue tests

Fatigue tests are performed on both specimen geometries. The tests should reveal the residual stress influence on fatigue and show possible differences between the two weld geometries. Furthermore, in the tests the residual stress influence on crack initiation and propagation will be studied, as there may be differences due to the non-uniform residual stress distribution over the thickness and different crack initiation to propagation ratios. It will also be investigated if the influence of residual stresses determined at the specimen surface is the same as of a mean stress acting throughout the specimen.

An overview of the fatigue tests is given in Figure 5-1. K-butt weld and longitudinal stiffener specimens are tested in as-welded and stress-relieved conditions. The residual stress influence depends on the applied load ratio. Tensile residual stresses will be more effective at low load ratios than at higher load ratios where the mean stress is already tensile. Therefore, four different load ratios *R* are applied in the tests. In a further test series stress-relieved specimens are tested at the stress ratio resulting from the superposition of residual stresses and load stresses. The required loads are obtained from numerical simulations. In all tests the number of load cycles until initiation of a macroscopic crack is determined using digital image correlation (DIC). For each test series, approximately 10 specimens are tested at different load ranges to establish the S-N-curves.

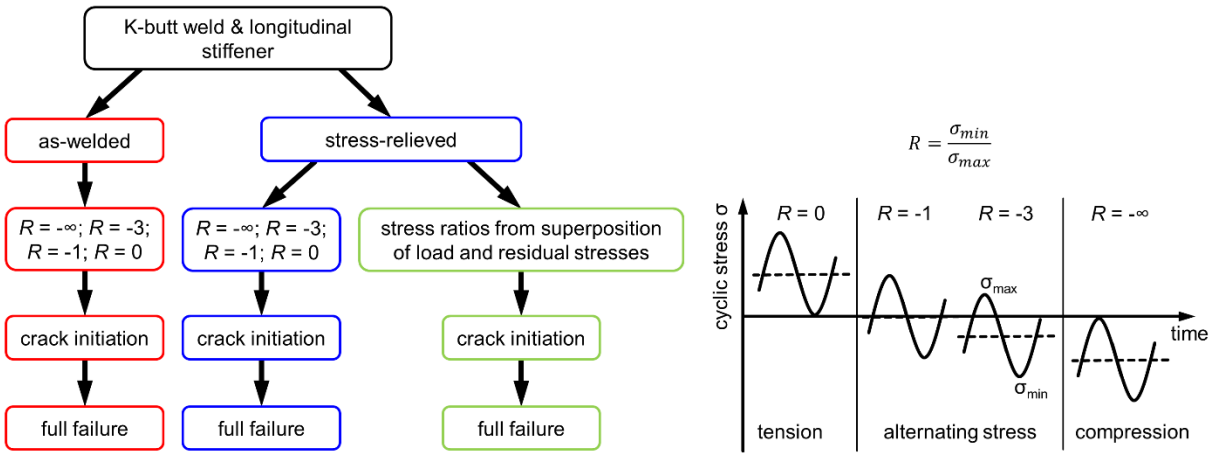

Figure 5-1: Fatigue tests and applied load ratios *R*.

To bring to light the influence of residual stresses other influencing factors have to be minimized. In particular the specimen distortion is critical. When the specimens are clamped the secondary bending moments will generate stresses in the specimen that act as mean stresses. This would cover up the effect of the residual stresses. During specimen production action was taken to minimize welding distortions. In the fatigue tests, levelling plates will be used when clamping the specimens to avoid the mean stress alteration due to clamping stresses.

The tests are accompanied by FE simulations. After calculating the welding residual stresses the models are loaded by applying the same loads as in the experimental tests. In this way the stresses at the weld under the applied loads are determined.

5.1 Test setup and procedure

5.1.1 Setup

The tests are performed on a 200 kN resonance testing machine (Figure 5-2). The specimen is clamped using hydraulic grips. The right side is fixed and equipped with a force sensor. On the other side the load is applied to the specimen. A static force, which will determine the applied mean stress, is applied through a spring loaded by an electric motor. A cyclic, constant amplitude load is applied by a second motor which acts on an unbalance and a second spring to excite the system formed by the test specimen and the two massive springs. The system will oscillate at the resonance frequency of the system which in this case is about 34 Hz. For the DIC measurements two cameras and four LED lights are installed over the specimen. The DIC system is used for two main purposes in the tests: first, to detect the initiation of macroscopic cracks and monitor crack propagation. Second, to measure strains caused by the clamping in order reduce them using levelling plates.

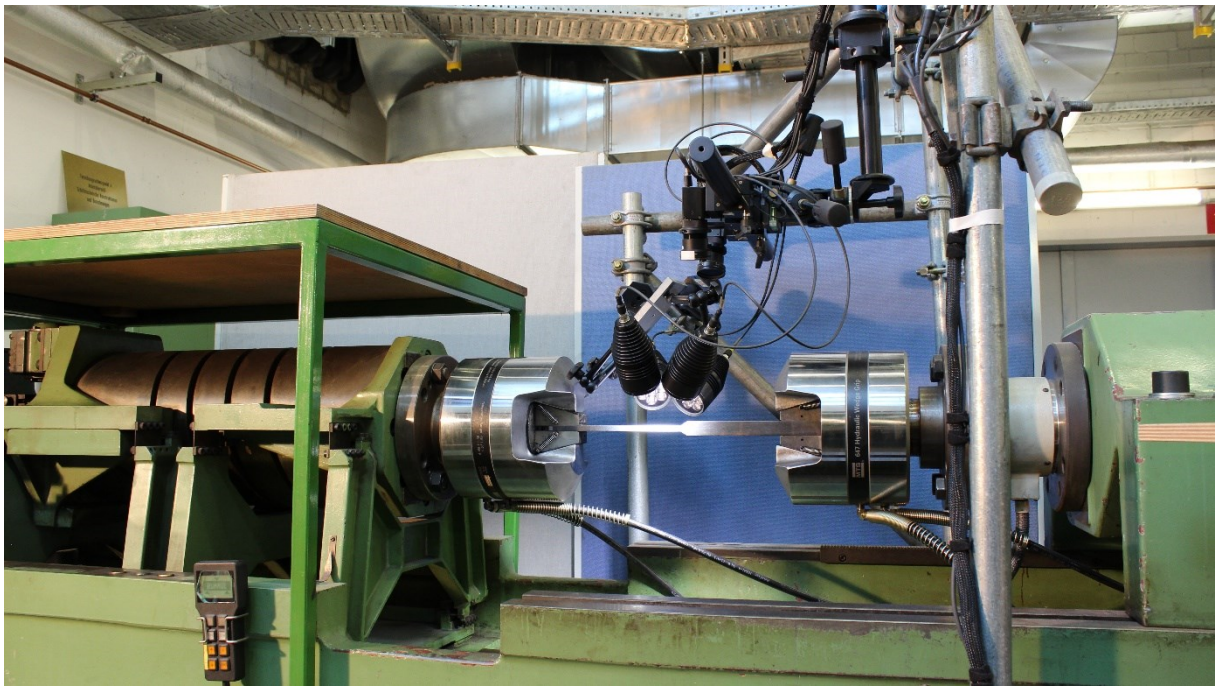

Figure 5-2: Resonance testing machine with DIC cameras and lights supported by a scaffold structure installed above the specimen (Friedrich and Ehlers 2019b).

5.1.2 Clamping with levelling plates

When clamping the specimens in the testing machine the angular distortion of the specimens causes a bending moment in the specimen. The resulting bending stresses act already before the actual load is applied and lead to a shift of effective mean stress. In order to reduce these clamping stresses levelling plates are used. The plates have thicknesses between 0.2 and 5.6 mm. The required thickness is determined iteratively by measuring the strain at the weld using DIC. The procedure is shown in Figure 5-3. First, the right end of the specimen is clamped. The strain at the weld is measured as reference. It should be zero since no force is applied, but depending on the quality of the DIC images some noise in the plotted strain is possible. The left grip is closed without any levelling plate and strains are measured again. On a distorted specimen the strain will be either positive or negative depending on the direction of the distortion. The left grip is reopened and an appropriate levelling plate is put under or on top of the specimen's end, depending on the direction of the distortion. The grip is closed again and strains are measured. This procedure is repeated until the measured strain is close zero.

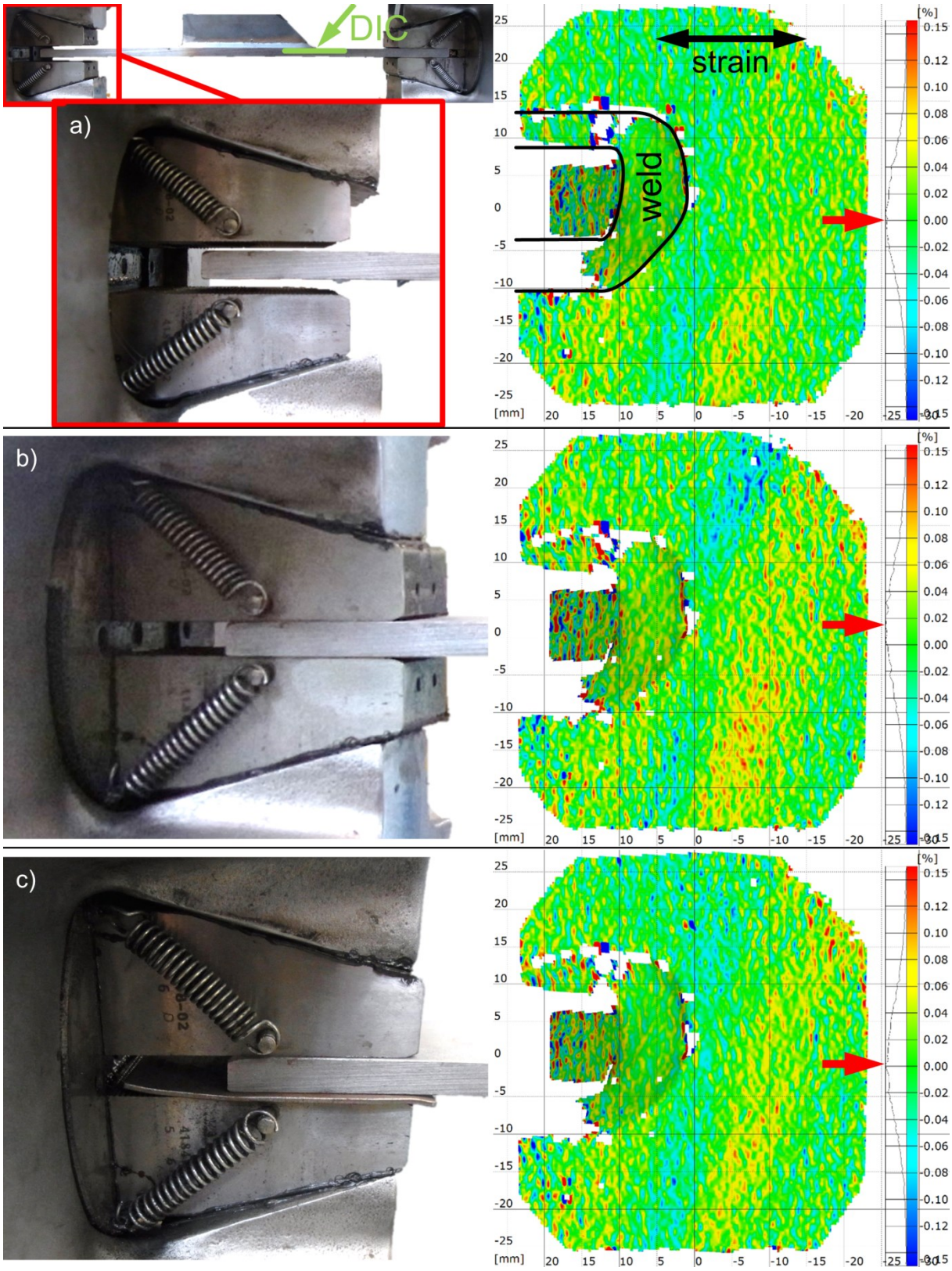

Figure 5-3: Grip at the left end of the specimen and strain measured by DIC at the end of the stiffener: a) grip open, b) grip closed and c) closed with levelling plate. Arrow indicates maximum in the strain histogram.

As shown in Figure 5-3 the strains measured by DIC are not perfectly uniform. The strains resulting from clamping are minimal and sometimes hard to quantify in the strain plot. With the help of the strain histogram (on the right in Figure 5-3) these difference can yet be distinguished. To verify the effectiveness of the procedure a K-butt weld specimen is

equipped with strain gauges on the top and bottom side. The strain gauges are placed on the centre line of the specimen about 20 mm from the weld toe on the 10 mm plate. The specimen is clamped and the DIC measurements are used to select the levelling plate (Figure 5-4). Clamping without levelling plate causes bending strains of about 0.011%, measured by both strain gauges and detectable in the histogram of the DIC measurement. After inserting a levelling plate of 1.2 mm the DIC results are close to zero. Strains measured by the strain gauges are 0.001%, corresponding to a bending stress of 2 MPa. This is acceptable small compared to the applied test loads and the accuracy of the involved equipment.

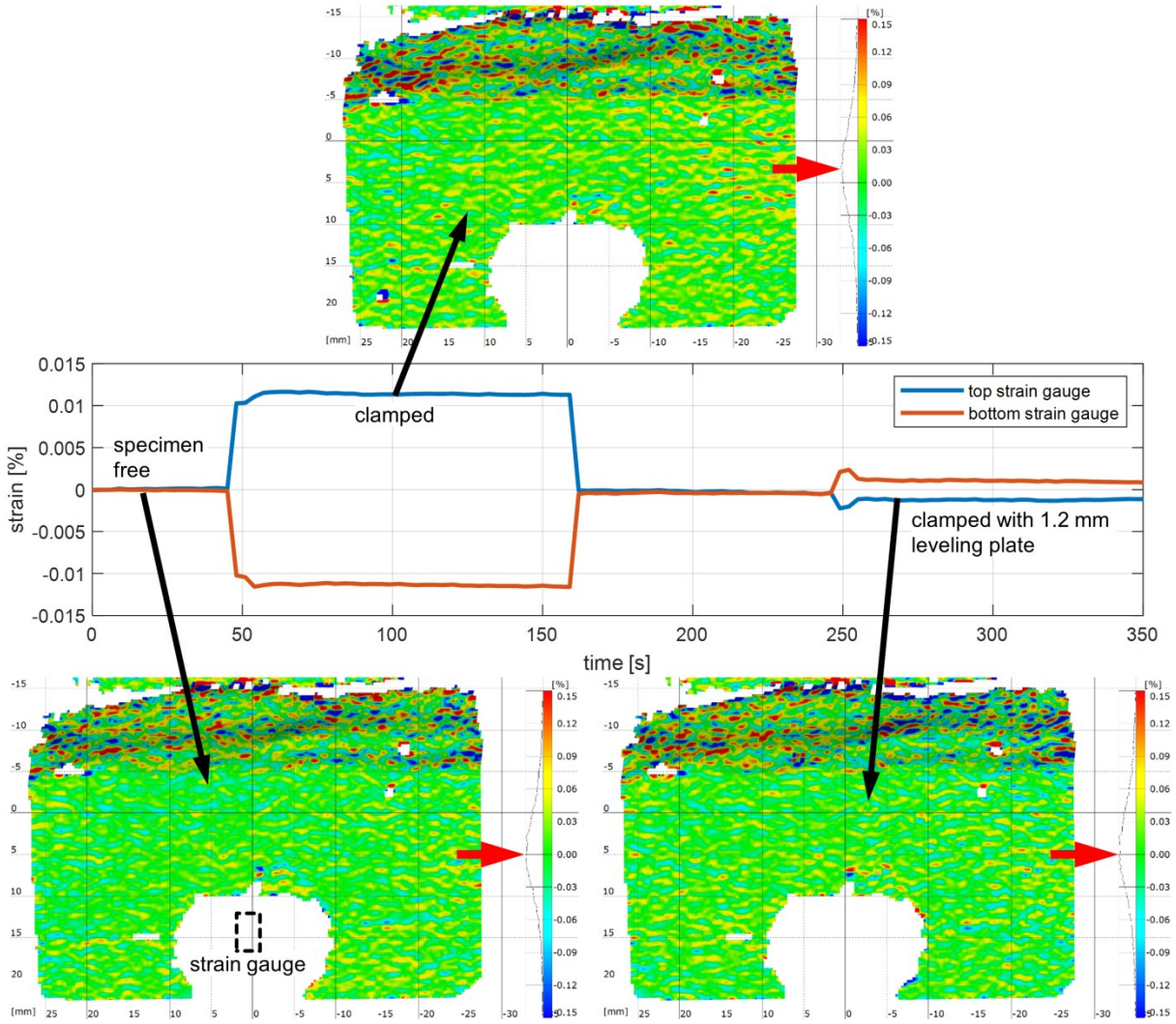

Figure 5-4: Percent strain in loading direction measured by DIC and strain gauges to verify the selection of the levelling plate based on the DIC measurements. Arrow indicates maximum in the strain histogram.

5.1.3 Stopping criterion for $R = -\infty$

The tests are run until complete rupture of the specimen. Under compressive loading ($R = -\infty$), although the crack has divided the specimen, it will not break because the applied load presses the parts together. In some cases the specimen is already completely divided but the test will continue running. Thus, a different failure criterion has to be adopted.

On resonance testing machines, as the crack expands it reduces the stiffness of the specimen and thus also the resonance frequency of the system. Usually, the moment when the specimen breaks is signed by a sudden decrease of the frequency (blue curves $R = 0$ in Figure 5-5). For $R = -\infty$ the loading frequency decreases slowly as the crack propagates and then stabilizes at a certain frequency (red curves in Figure 5-5). At this point the crack has almost reached the whole specimen cross-section and grows only very slowly. The value at which the frequency stabilises depends on the applied load and is therefore different for each test. These tests with $R = -\infty$ are stopped manually after the loading frequency has dropped and stabilised. The number of load cycles until failure is then determined at the point where the frequency has reached its final value (e.g. $N = 2.6 \cdot 10^6$ and $N = 1.3 \cdot 10^6$ in Figure 5-5).

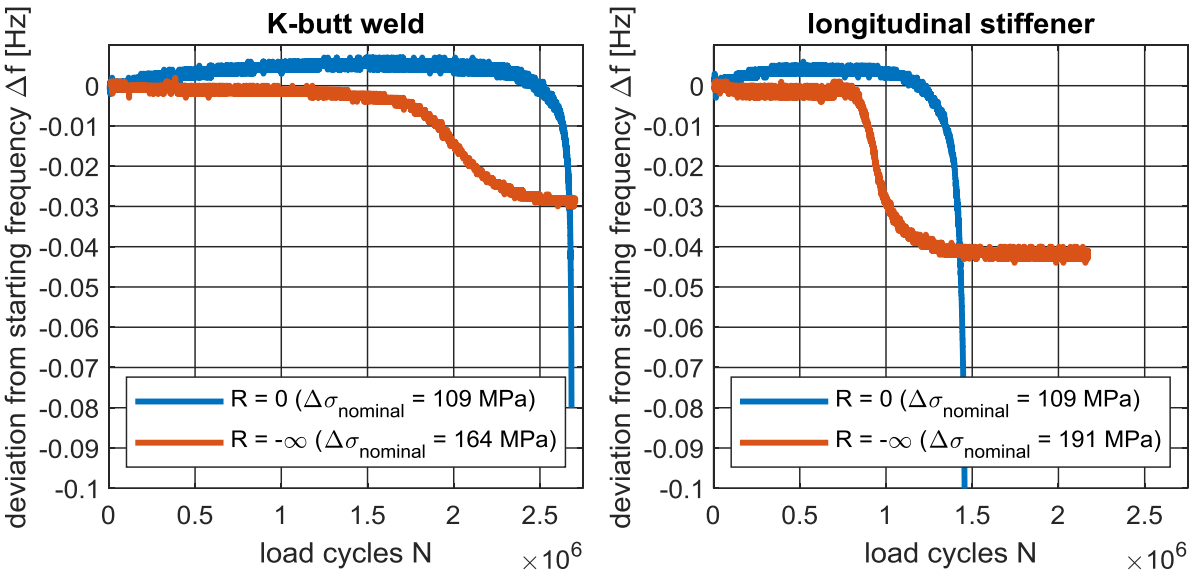

Figure 5-5: Development of the loading frequency during tests with tensile ($R = 0$) and compressive ($R = -\infty$) loading on K-butt weld and longitudinal stiffener specimens (Friedrich 2020).

The test setup and procedure presented in chapter 5 have been published by the author of this thesis in (Friedrich 2020).

5.2 Crack monitoring using DIC

One objective of the fatigue tests is to determine the residual stress influence on crack initiation, propagation and total fatigue life. For this purpose a procedure using DIC to detect macroscopic cracks and monitor crack propagation is adopted. For DIC, an irregular pattern is applied to the specimen surface and monitored by cameras. From the distortion of the pattern under loading, surface strains are computed. Cracks will appear as elevated strains exceeding a defined threshold value (> 1%) and therefore become visible. In the following, *crack initiation* is considered a macroscopic crack of 2 mm length. This crack length can reliably be detected with the applied DIC procedure. From an engineering point of view, this crack length would be detectable in service using available inspection techniques.

Compared to visual inspections or dye penetration testing, the proposed procedure is not based on subjective perception, which depends on an operator's experience and the local geometry at the weld toe. Even with high magnification it may be challenging to detect cracks at an early stage (i.e. crack initiation), especially if the exact location is not known in advance. Furthermore, using DIC the results are saved and therefore reproducible and comparable, whereas visual inspection is possible only momentarily. Using a full-field measurement the procedure allows monitoring the whole width of the specimen or length of the weld. This is important on the K-butt weld specimens where the exact location of crack initiation is not known. Another benefit of DIC is that it is visual and it gives a descriptive image of the crack. This facilitates the interpretation and validation of results compared to other methods where cracks are determined by changes in a measured signal, e.g. strain gauges or acoustic emission.

Various applications of DIC to monitor cracks in fatigue tests have been reported. In many cases DIC is used to assess the strain field at the crack tip (Carroll et al. 2013; Malitckii et al. 2019; Rabbolini et al. 2015; Carroll et al. 2008; Durif et al. 2010; Maletta et al. 2014) or detect fatigue damages on a microscopic scale (Rupil et al. 2011; Risbet et al. 2010) on specimens of machined base material. Larger measuring areas were recorded in (Tavares et al. 2015; Shrama et al. 2014; Hasheminejad et al. 2018), in (Poncelet et al. 2010) to detect crack initiation on specimens with a machined surface, in (Corigliano et al. 2018a; Corigliano et al. 2018b; Koster et al. 2014) to observe the development of cracks in the depth direction, on the edge of welded or brazed specimens. In general the experiments were conducted on servo-hydraulic testing machines with load frequencies of a few hertz (< 15 Hz), usually interrupting the tests to record the images for DIC. Images during the running test were taken in (Vanlanduit et al. 2009) and in (Lorenzino et al. 2014) tests on a resonance testing machine and with microscopic cameras were performed. Kovárík et al. (2016b; Kovárík et al. 2016a) performed tests on a resonance testing machine with a frequency of 100 Hz without interruptions, using a procedure very similar to the one presented here. The tests were conducted on flat, coated specimens under bending loads. A single camera and a triggered flash were used to capture images of an area of ~20 x 15 mm^2. Different crack assessments based on the strain field and on the displacement field were applied.

The procedure presented in the following is applied to welded specimens presenting a notch, and thus a stress concentration. A 3D DIC-system with two cameras is employed, which allows to account for out of plane displacements of the specimen. The cameras are triggered while lighting is constant. Crack detection is based on the strain field measured on an area of 55 x 40 mm^2.

5.2.1 Specimen preparation

To prepare the specimens for the DIC measurements all loose material is removed from the weld surface and weld toe using a brass wire brush. The specimen surface in the area around the weld is cleaned using a cleaning cloth and a cleaner to degrease.

The speckle pattern for DIC is applied using alternating applications of black and white spray paint. The spray is not pointed directly at the surface, so that only the spray mist settles on the specimen. The speckle size is in the magnitude of 0.1 mm (Figure 5-6). Matte paint is used in order to reduce reflections.

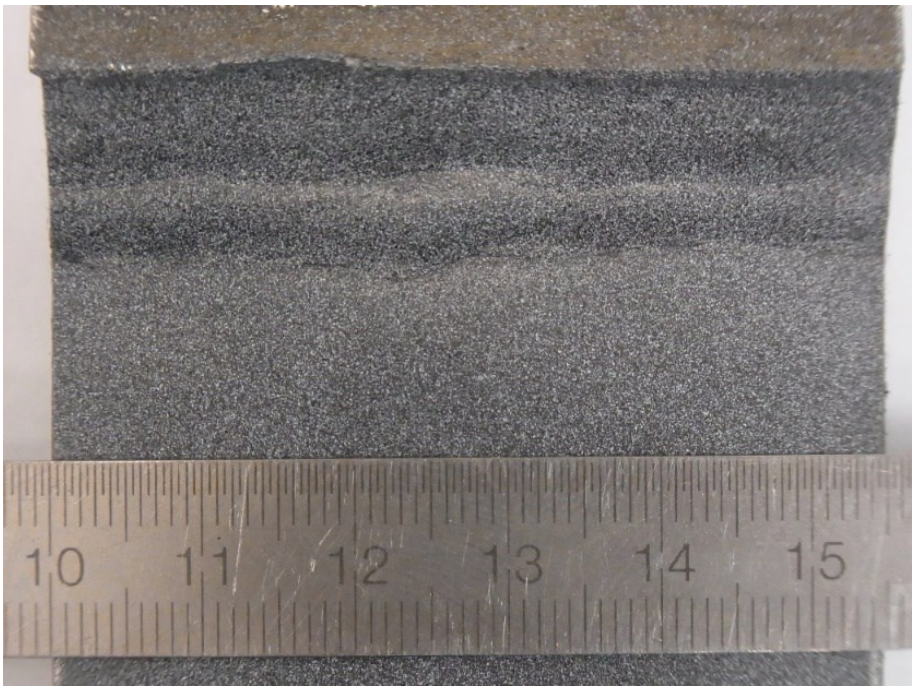

Figure 5-6: Speckle pattern for DIC at the weld (Friedrich and Ehlers 2019b).

5.2.2 Setup

The DIC measurements are performed with an ARAMIS 5M system. The cameras are mounted on a scaffold reaching over the specimen arranged horizontally in the testing machine (Figure 5-2) and positioned to capture the weld and the area in front of it. Four 16 Watt LED lights are used to achieve a uniform illumination of the measuring area. Polarization filters are installed on the lights and objectives to reduce reflections on the metallic surface.

The exposure time of the cameras is set to 0.8 ms. With a testing frequency of 34 Hz this corresponds to ~1/35 of the duration of one load cycle (Figure 5-7). The cameras are triggered before the peak of the load signal to compensate for the delay between the trigger signal and the camera exposure. It is not necessary for the images to be taken exactly at the load peak. Cracks will become visible nonetheless.

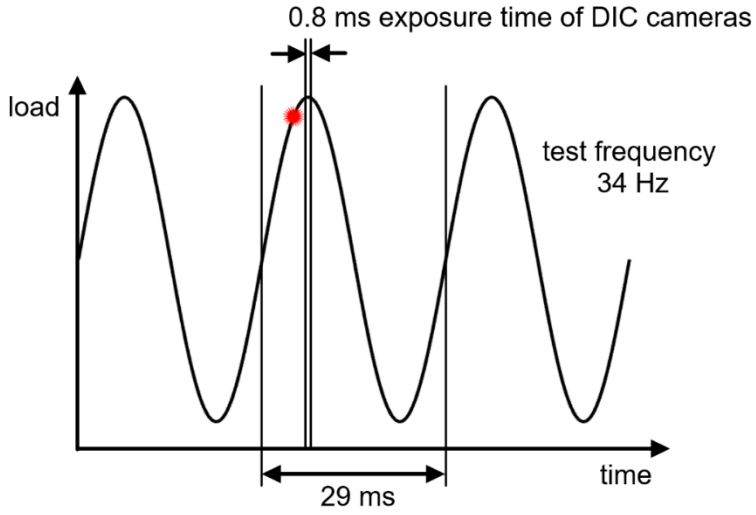

Figure 5-7: Exposure time and trigger signal compared to load cycle (Friedrich and Ehlers 2019b).

The force signal output from the testing machine is used to trigger the cameras (Figure 5-8). The first load cycle is applied statically. At maximum load some images for DIC are taken. One image should be sufficient, but because the quality of the DIC results may not always be optimal, it might be helpful to have a few more images to choose from for analysis. For these images, a longer exposure time is used as appropriate. This static load cycle can be omitted, but the images acquired statically are probably of better quality than those acquired during the dynamic test, thus improving DIC results. After applying the first load cycle statically the actual fatigue test is started and the DIC cameras are triggered off at specific intervals of load cycles. The trigger is set to an interval of load cycles so that the total number of images over the expected test duration is in the magnitude of 100−200 (e.g., every 10 000 cycles for a test with 10^6 load cycles).

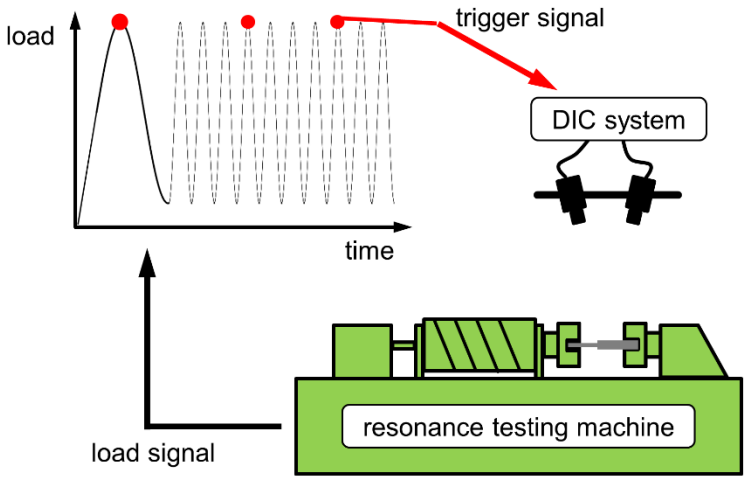

Figure 5-8: Test setup with DIC cameras triggered by the load signal from the testing machine.

5.2.3 Postprocessing

The acquired images are evaluated by DIC using ARAMIS v6.3.1-2 software. The distortion of the speckle pattern is used to calculate strains in the specimen's axial (loading) direction (Figure 5-9). The image from the first, static load cycle is used as reference image. A facet size of 19 x 19 pixels (~0.32 x 0.32 mm^2) and a facet distance of 15 x 15 pixels is applied for the DIC assessment.

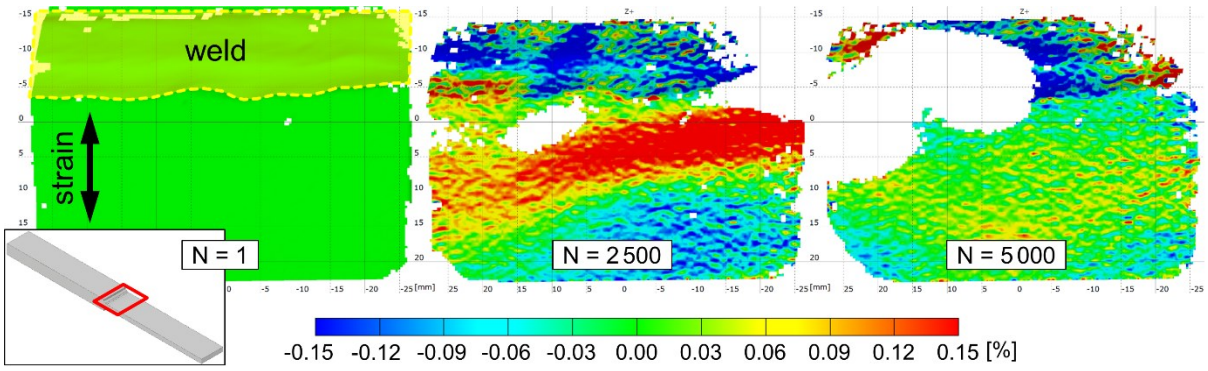

Figure 5-9: Percent strain in the loading direction at maximum load on the first, static load cycle (N = 1) and at the beginning of the fatigue test at different numbers of load cycles N.

The legend of the strain plot is set to relatively high values (0.5% to 1.0%) to suppress possible noise, as shown in Figure 5-10. Running through the image sequence acquired over the duration of the test a forming crack will become visible in terms of elevated strains. A crack is assumed when strains exceed 1%. Initiation of a macroscopic crack is counted when a crack length of ~2 mm is detected.

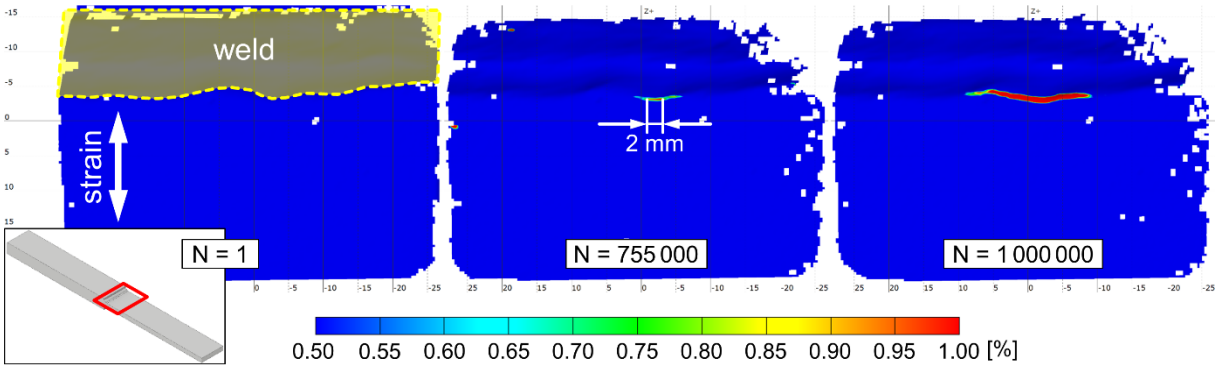

Figure 5-10: Percent strain in the loading direction on the first, static load cycle (N = 1) and at the initiation of a macroscopic crack (Friedrich 2020).

5.2.4 Representative results

Representative results of the DIC measurements on both specimen geometries are presented. To validate the detected crack length, it is compared to beach marks introduced in some of the tests. The beach marks are obtained by including intervals in which the upper load is maintained but the load range is reduced (Figure 5-11).

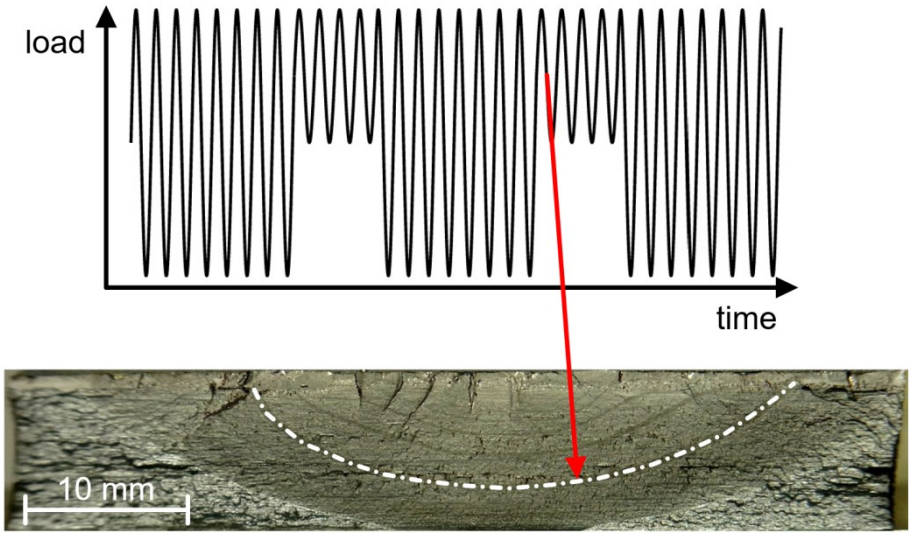

Figure 5-11: Beach marks on the crack surface introduced by intervals with a reduced load range (Friedrich and Ehlers 2019b).

The development of a crack in a K-butt weld specimen in as-welded conditions is shown in Figure 5-12. Transversal residual stresses at the weld are tensile in the middle of the specimen and compressive on the edges (compare Figure 4-12). Therefore, the crack initiates close the centre line. First, the strain begins to increase at the location of the forming crack. A macroscopic crack is assumed when strains exceeded 1% over a length of 2 mm (N = 755 000). The crack then propagates symmetrically to both sides. The detected crack lengths show good agreement with the beach marks generated during the test.

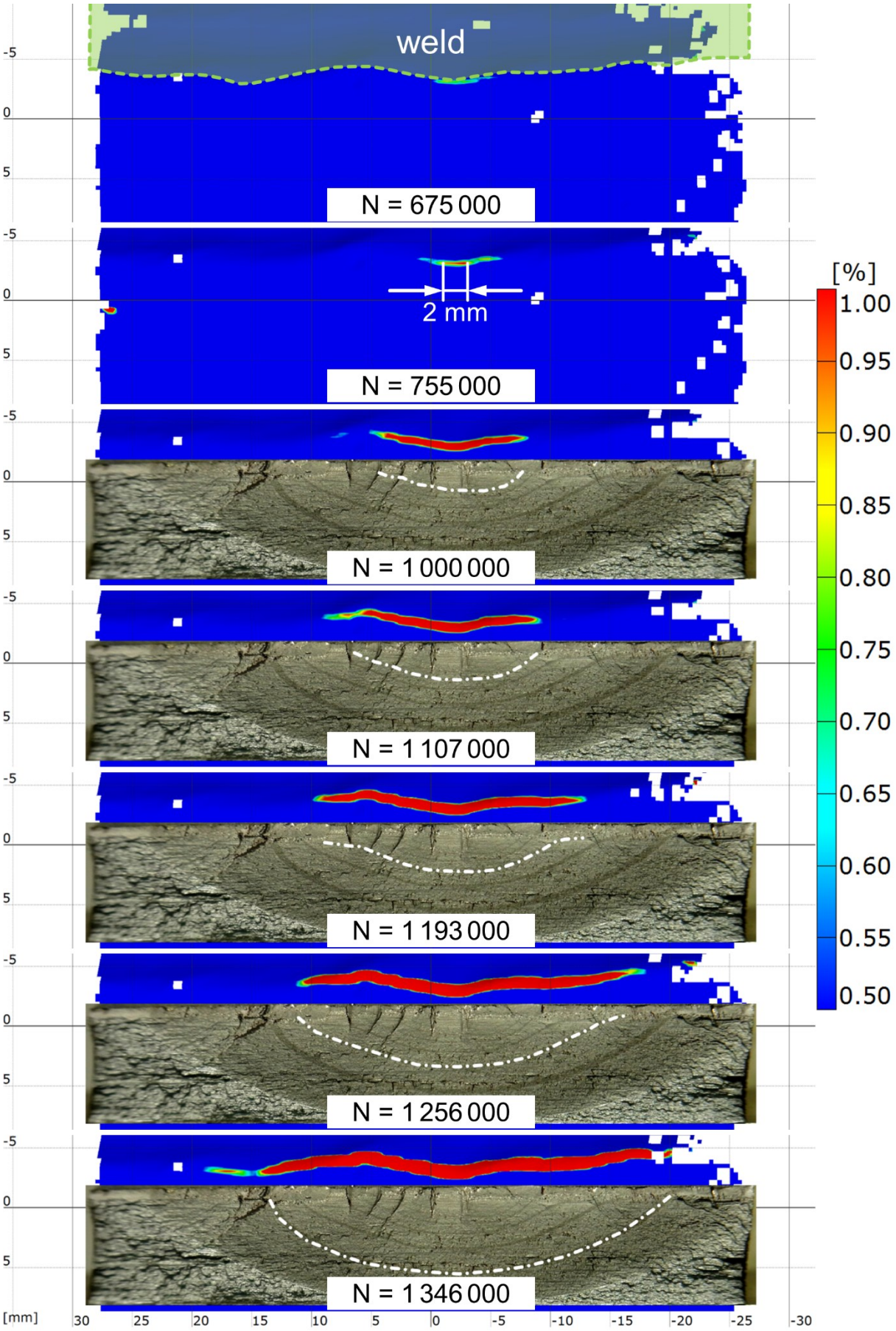

Figure 5-12: Percent strain in the loading direction showing the development of a crack and comparison with beach marks on a specimen in as-welded conditions (*N* = number of load cycles).

The development of a crack on a stress-relieved specimen is shown in Figure 5-13. Crack initiation is not influenced by residual stresses. Several cracks form at different locations along the weld. A crack of 2 mm is detected after 574 000 cycles. The single cracks then grow and eventually unify. The detected crack length is compared to the beach marks again.

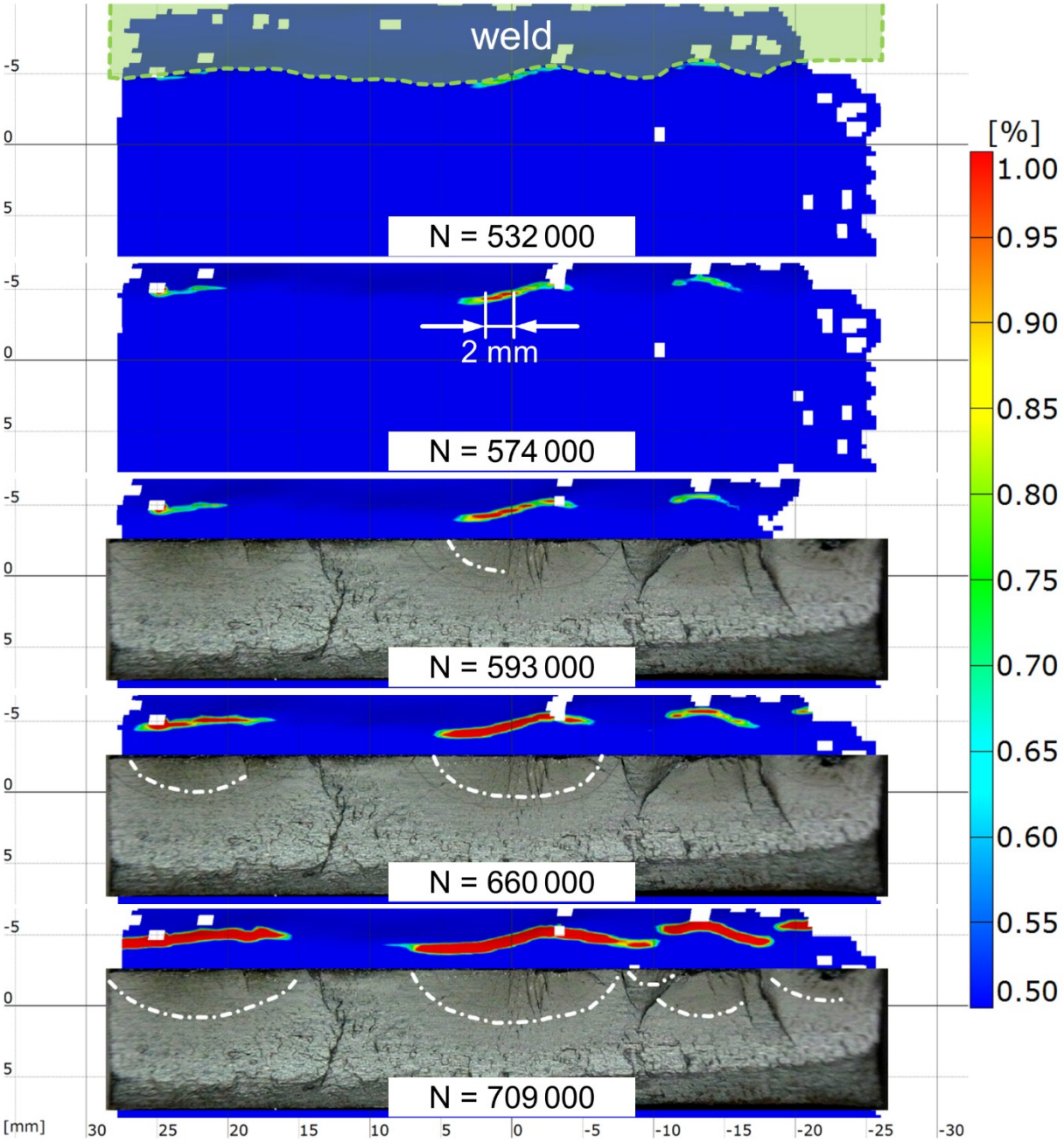

Figure 5-13: Percent strain in the loading direction showing the development of cracks and comparison with beach marks on a stress-relieved specimen (*N* = number of load cycles).

The previous test (Figure 5-12) and this (Figure 5-13) were performed at different loads and load ratios. The results are not intended for direct comparison between the two tests but represent typical outcomes of these tests and demonstrate the capabilities of the presented procedure.

Additionally, some K-butt weld specimens are equipped with strain gauges in front of the weld. In this way the crack detection by DIC can be compared to the use of strain gauges. The strain gauge signals and the strains measured by DIC are exemplarily plotted in Figure 5-14. Three strain gauges are positioned with the centre of the gauge about 2 mm from the weld toe (gauge length = 2 mm). After 281 500 load cycles a macroscopic crack has formed between strain gauge 2 and 3. Until 350 000 load cycles the strain gauge signals show a slight increase, possibly due to the forming crack. At 400 000 cycles the crack has a length of about 10 mm and reaches strain gauges 2 and 3, at this point the signals of these two strain gauges start to decrease. Strain gauge 1 starts to increase until it is reached by the crack after about 530 000 load cycles. From the comparison it can be seen that strain gauges are very sensitive to any changes in the specimen. From the strain gauge signal alone it is yet not possible to quantify the crack length. Furthermore, the influence on the measured strain gauge signal depends on the location of the crack relative to the strain gauge.

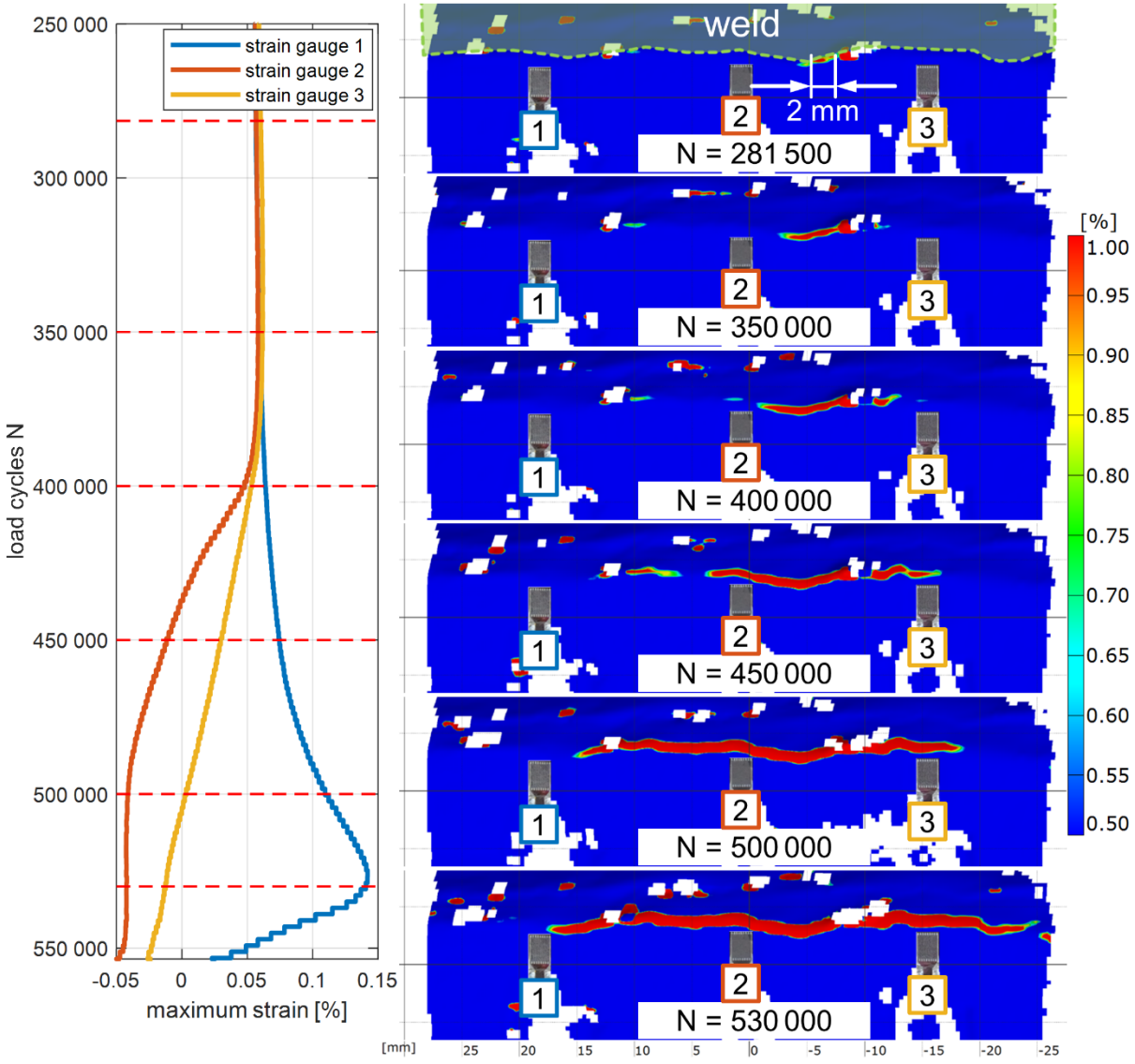

Figure 5-14: Percent strain in the loading direction showing the development of a crack and comparison with strain gauge measurements (*N* = number of load cycles).

The K-butt weld presented here has a relatively smooth weld toe compared to other weld geometries. Cracks are likely to initiate at imperfections along the weld toe with the sharpest notch and thus high stress concentration. Unfortunately, it may not be possible to evaluate strains by DIC at these exact locations because the facets used for the computation may not be recognised. For example, Figure 5-14 shows a crack initiating between strain gauge 2 and 3, where some of the facets are missing. But as shown in the example, even if some facets are not evaluated it is still possible to determine when the crack initiates and starts to grow. For welds with a steeper angle and sharper notches (e.g., longitudinal stiffener, fillet weld) it may help to tilt the cameras ~15° to increase the angle to the weld surface.

This change is applied for the measurements on the longitudinal stiffener specimens. The detected crack is compared to beach marks on an as-welded specimen in Figure 5-15. Despite the relatively sharp notch at the weld toe it is possible to detect the crack. Although in this particular case it is difficult to detect the crack at an early stage (N = 1 200 000). From the beach marks it is evident that a crack has already formed. On the DIC results it can be seen that some facets are missing at the origin of the crack. Elevated strains are visible too, although they have not reached the threshold value of 1% yet.

The results from a stress-relieved longitudinal stiffener specimen are shown in Figure 5-16. In this case the formation of the crack can be clearly detected. Increased strains are observed at the weld toe over a width of 7 mm. After 2 380 000 a localized maximum has formed that is counted as a macroscopic crack of 2 mm. The crack then expands steadily and propagates to the sides. The beach marks become visible only from a certain depth on.

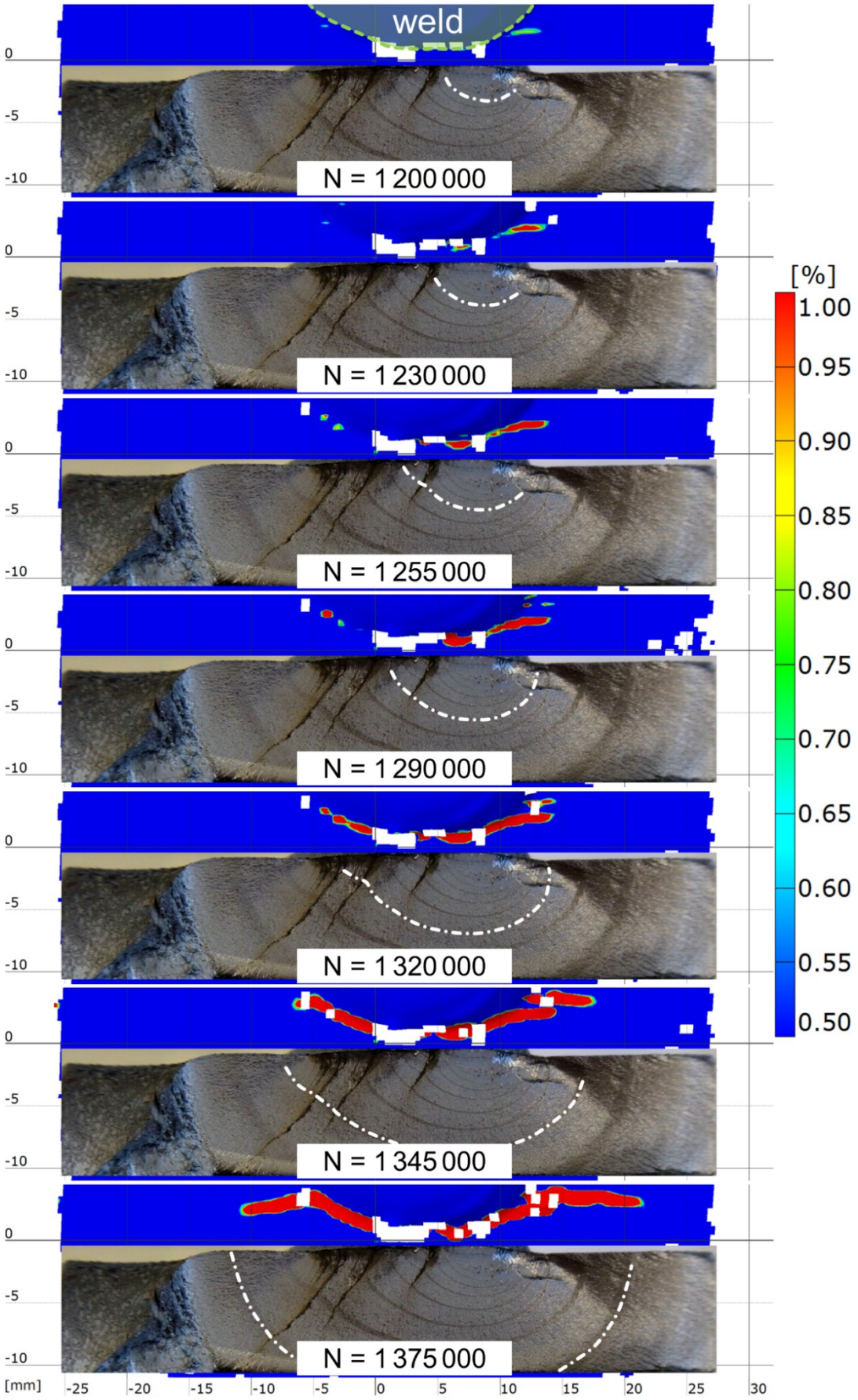

Figure 5-15: Percent strain in the loading direction showing the development of a crack and comparison with beach marks on an as-welded longitudinal stiffener specimen (*N* = number of load cycles).

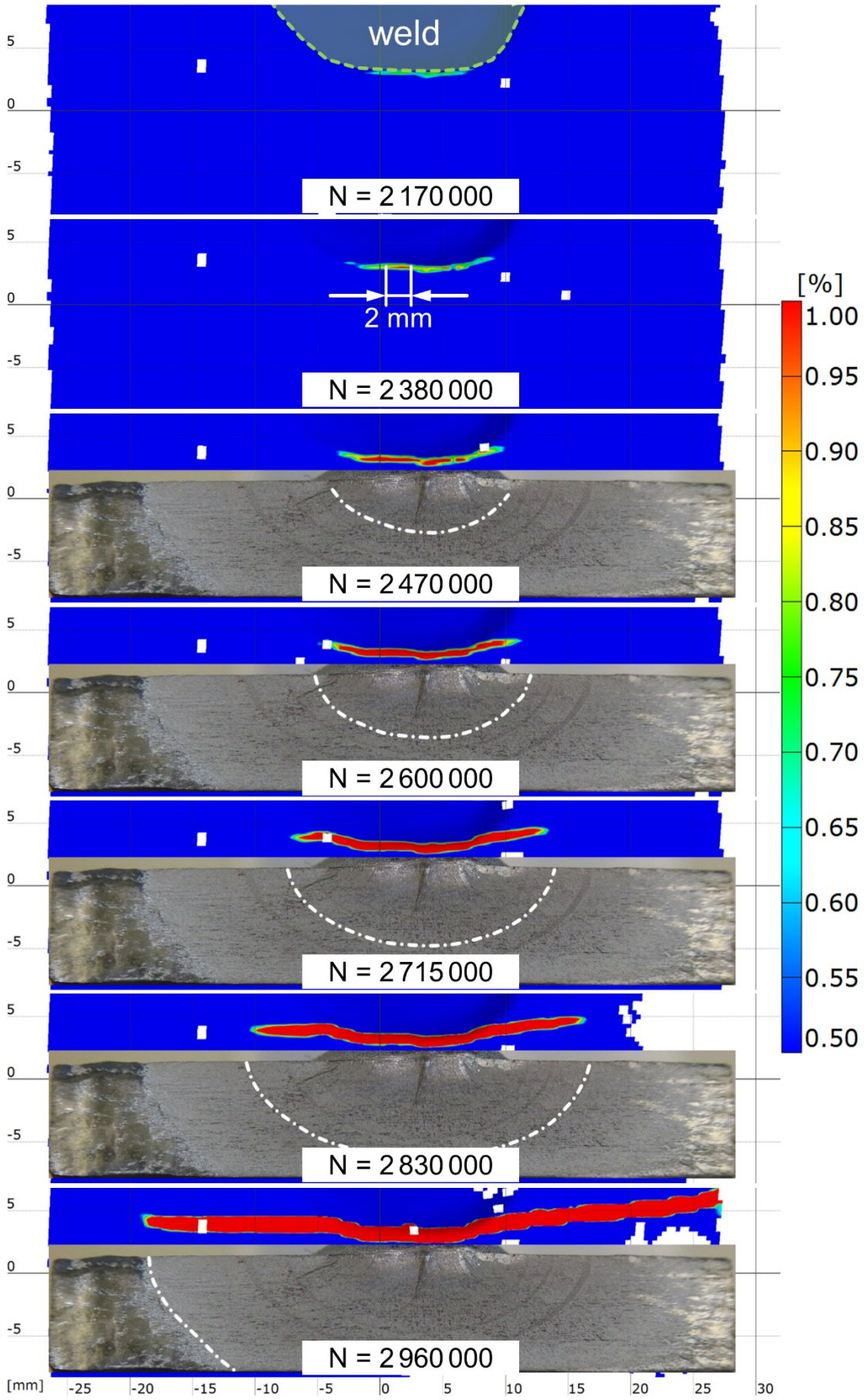

Figure 5-16: Percent strain in the loading direction showing the development of a crack and comparison with beach marks on a stress-relieved longitudinal stiffener (*N* = number of load cycles).

5.2.5 Discussion

The presented procedure consists in using DIC to detect and monitor fatigue cracks on welded specimens tested on a resonance testing machine without interrupting the test. The main challenge in the application is the high load frequency of the resonance testing machine. It requires relatively short exposure times and thus high illumination for the acquisition of the images for the DIC tests. Therefore, lighting has to be maximized. On the other hand, reflections on the metallic surface may require the use of polarization filters, which will reduce the amount of light entering the cameras. To make better use of the light available, the aperture of the objectives may be enlarged. This will reduce the depth of focus. It is therefore necessary to set the focus exactly at the distance of the specimen surface and the out of plane movement of the specimen should not exceed the focused range. The setup of the cameras and lighting requires particular care.

Nevertheless, the strains calculated by DIC might not be very accurate (Figure 5-9). The computed strains might show high noise. On some of the facets used for DIC, the speckle pattern might not be recognized and strains will not be calculated. But the proposed procedure has proven robust with respect to the quality of the DIC results. Even if the results are not good enough to determine the strains at the weld precisely, it should still be possible to detect cracks.

Macroscopic cracks are assumed when strains of 1% or more are reached. In a study by Kovárík et al. (2016b), DIC was applied to detect cracks on thermal spray-coated, unnotched specimens. It was stated that the threshold value for crack detection could be set in the range of 0.5% and 1% without significantly affecting the results. These values are confirmed by the comparison with the beach marks. A lower value will lead to an earlier crack detection but might be more prone to uncertainties and produce less comparable results. A higher value will lead to a later recognition of crack initiation, but the results will probably be more comparable and reproducible.

All in all, the procedure offers a robust and comparable way to detect cracks in fatigue tests. Furthermore, it provides a record of crack propagation. It is applicable on resonance testing machines with high loading frequencies. The tests do not have to be interrupted for measurements, and no operator needs to be present during the test. The procedure can therefore be efficiently applied to large numbers of tests to retrieve information on crack initiation and propagation.

The approach presented in section 5.2 has been published by the author of this thesis in (Friedrich and Ehlers 2019b).

5.3 FE simulations

FE simulations have already been used to calculate the residual stress distribution after welding (section 4.2). Together with the punctual measurements they delivered a complete impression of the distribution along the weld and through thickness. Now the simulations will be used to calculate the effective stresses under load. For this purpose the loads from the fatigue tests will be included in the simulations.

The FE models are the same as in section 4.2. As the experiments the simulations will be performed in the “as-welded” and the “stress-relieved” condition. For the “as-welded” models, after the welding simulation including cooling and cutting of the specimens, the simulation is restarted to simulate the loads of the fatigue tests. The restart is performed in the same FE software *ANSYS Mechanical 15.0* so that the residual stresses, distortions and material history from the welding simulation are included. For the “stress-relieved” models, an FE model that includes only the welding distortion is used. To create this model, after the welding simulation and cutting of the specimens, the displacement of each node is read out in all three dimensions. The nodes of the original, undeformed FE model are then moved by these values. The result is an FE model with the distortion of the model after welding but without any stresses or plastic strains. The simulation on this model is started as a new simulation. This is applied to the K-butt weld and the longitudinal stiffener models.

The boundary conditions are applied according to the experimental tests, as shown in Figure 5-17 and Figure 5-18. One end of the model is fixed. Here all three degrees of freedom are suppressed over a length of approximately 50 mm. For the K-butt weld model this fixed end is on the 25 mm thick side. On the longitudinal stiffener the right side, where the stresses at the weld are assessed, is fixed. At the opposite end the force is applied distributed uniformly on all nodes within 50 mm from the end.

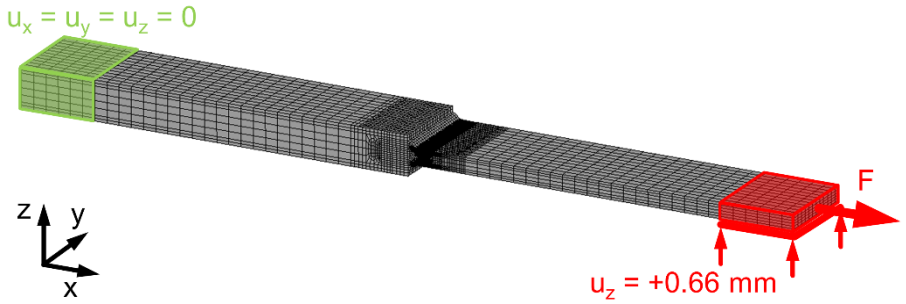

Figure 5-17: Boundary conditions and applied force for the K-butt weld model.

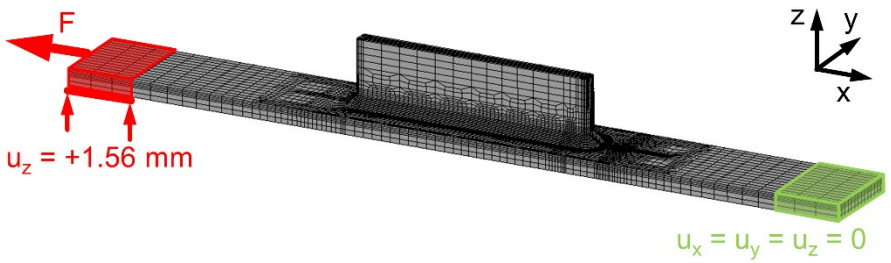

Figure 5-18: Boundary conditions and applied force for the longitudinal stiffener model.

In the experiments levelling plates are used to reduce clamping stresses due to specimen distortion. In the simulations this is modelled by applying a vertical (*z*-direction) displacement on the nodes where the force is applied. The height of this displacement is determined analogously to the experimental tests (compare section 5.1.2). The procedure is shown in

Figure 5-19 for the K-butt weld model. Stresses at the weld rise when the model is clamped at both ends, because both sides are forced to the same level. Keeping one end fixed, the vertical displacement at the other end is varied until the stresses at the weld are the same as on the unconstrained model. The result is a height difference of 0.66 mm for the K-butt weld model and 1.56 mm for the longitudinal stiffener. For the models including welding residual stresses these values are applied directly as vertical displacement boundary condition. In the distorted models without residual stresses the geometry includes already a difference of level between the two ends. This is subtracted from the applied values to result in the same height difference between the two ends of the model.

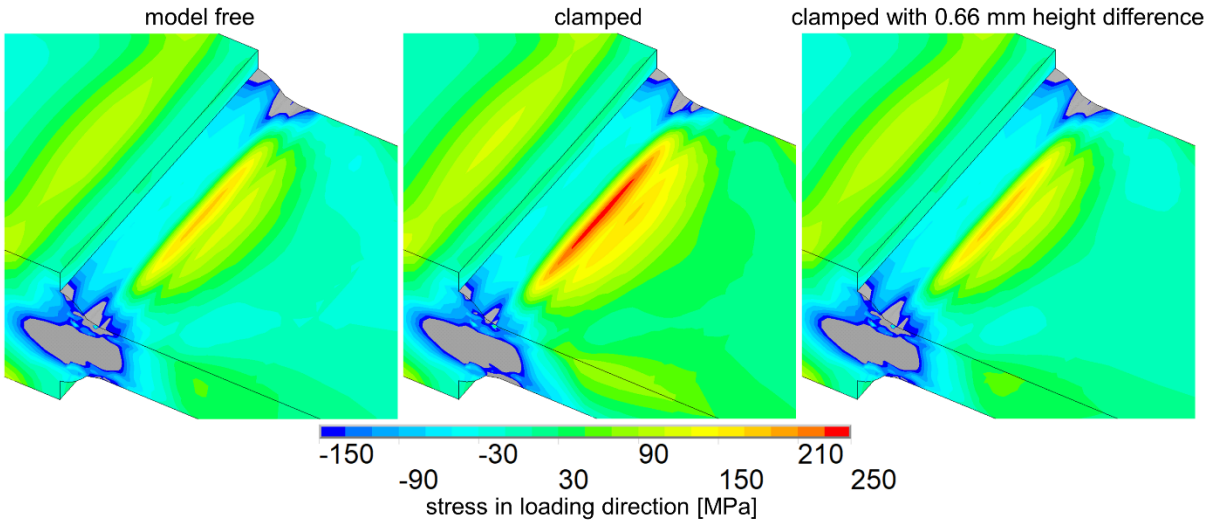

Figure 5-19: Transversal residual stresses and clamping stresses on the K-butt weld model when clamped without and with a height difference to simulate the levelling plates from the experiments.

Under compressive forces the simulations become unstable when the load exceeds a certain limit. This is overcome by applying additional boundary conditions. For the K-butt weld models, in the simulations with load ratio R = -∞ horizontal displacement in transversal direction (y-direction) is suppressed at the end where the load is applied. On the longitudinal stiffener models the transversal displacement is suppressed over the entire length of the model. It was verified that the calculated stresses at the weld are the same with and without these transversal boundary conditions up to the force where both gave results. Thus, these boundary conditions should have no influence on the resulting stresses.

The models are loaded with horizontal forces in the same load range up to 200 kN as the experimental specimens. The same load ratios as in the experiments are applied: compression (R = -∞), 3/4 compressive (R = -3), alternating (R = -1) and tension (R = 0). For each load ratio the force range is increased sequentially by 10 kN steps up to 200 kN. This is shown exemplarily for R = -1 in Figure 5-20. In this case, each 10 kN increment is performed in four load steps. First, the tensile force from the previous load range is applied. Then the tensile force is increased by 5 kN. Subsequently the compressive force from the previous load range is applied. Finally, this compressive force is increased by 5 kN. The next cycle starts with the tensile force from the current one. In this way, for each load range a closed cycle is simulated and the plastic strain increment between the load steps is reduced. For R = -∞ and R = 0 each cycle is performed in three load steps as the maximum, respectively minimum is always zero.

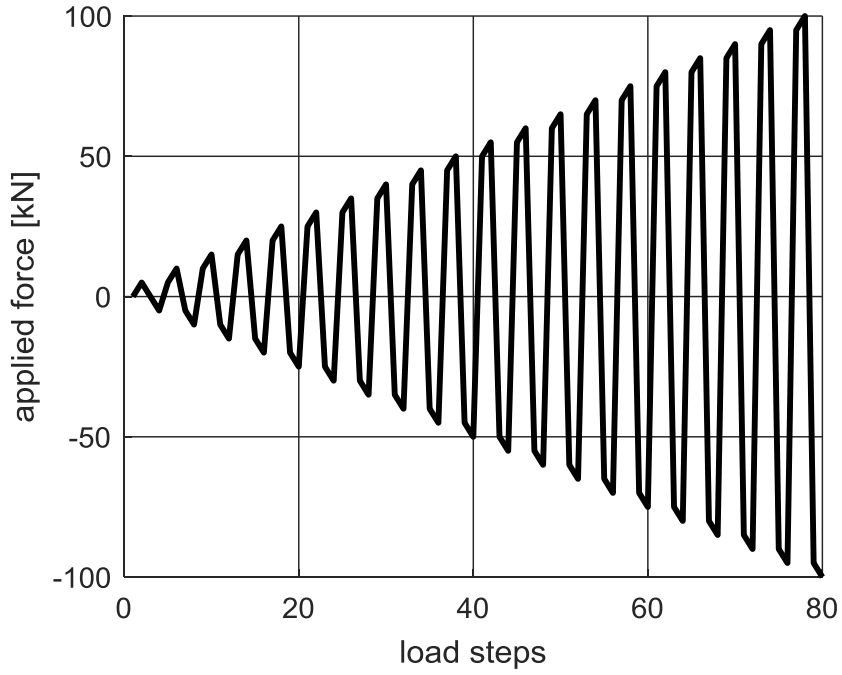

Figure 5-20: Forces applied on the FE model for a load ratio of R = -1.

5.3.1 K-butt weld

The four load ratios are simulated on the model including welding residual stresses and on the one without. The resulting stresses in loading direction at the weld toe depending on the applied nominal stress range are plotted in Figure 5-21. The curves with residual stresses (red) represent the as-welded tests, without (blue) stand for the stress-relieved tests. For pure tension (R = 0), without residual stresses the stress ratio corresponds to the nominal as long as the strains remain elastic. When the stress reaches 350 MPa plastic strains occur at the weld toe, the upper stress does not increase linearly anymore and the lower stress is shifted to compression. With residual stresses, the stress ratio at the weld toe is shifted towards tension (R_{toe} > 0). At a load range of 150 MPa the upper stress reaches the yield limit and does not increase further. For small stress ranges, the curves with residual stresses lie higher than without residual stresses. This would suggest, that in fatigue tests the as-welded specimen should fail earlier than the stress-relieved. At a nominal stress range of 280 MPa the curves cross each other. Thus, in a fatigue test the as-welded and the stress-relieved specimens should endure the same number of load cycles. Beyond this load, the curve without residual stresses runs higher than with. Here, the stress-relieved specimen should fail before the as-welded.

For alternating loads (R = -1) the curve without residual stresses respects the nominal stress ratio. Thus, half of the applied load range generates tensile and the other half compressive stresses at the weld. The plotted curves stay linear elastic over the whole simulated range. With residual stresses, the curves are shifted into tension by the amount of the initial residual stresses. Up to a load range of 200 MPa, the stress ratio at the weld toe is positive i.e. the whole load range results in tensile stresses at the weld. At a stress range of 280 MPa plasticity occurs and the difference to the curve without residual stresses is reduced.

The results for R = -3 are similar. With residual stresses, the curves are shifted towards tension by the amount of the initial residual stresses. On the model without residual stresses, plastic strains occur when the stress at the weld reaches -350 MPa.

For compressive loads (R = -∞) the upper stress remains almost constant at the level of the initial residual stresses. Without residual stresses, plastic strains occur at -350 MPa. For high load ranges the upper stress is shifted into tension due to compressive plastic strains.

Based on these results the following is expected for the experimental fatigue tests:

- The higher the calculated stresses, the shorter the expected fatigue life. If the calculated stresses at the weld toe are high, the effective stress ratio is high (tensile). Consequently, in the fatigue tests the endurable number of load cycles should be lower than for a load ratio resulting in lower stresses.
- If the curves for different load ratios or residual stress conditions cross each other, the endurable number of load cycles in the fatigue tests should be the same. Thus, also the S-N curves should cross each other.
- Assuming that tensile loads are more damaging and compressive loads add no or only little to the fatigue damage, the damaging effect of an applied load range depends on the tensile portion of the stress range at the weld (Gurney 1979). Thus, if the tensile portion of the stress increases rapidly with the applied load range, the increment of the damaging effect is high. The S-N curve should thus have a shallow slope. On the contrary, if the tensile load does not increase (the case if the upper stress is constant

and the lower compressive) the damaging effect does not increase for increasing load ranges. Consequently the S-N curve should be vertical.

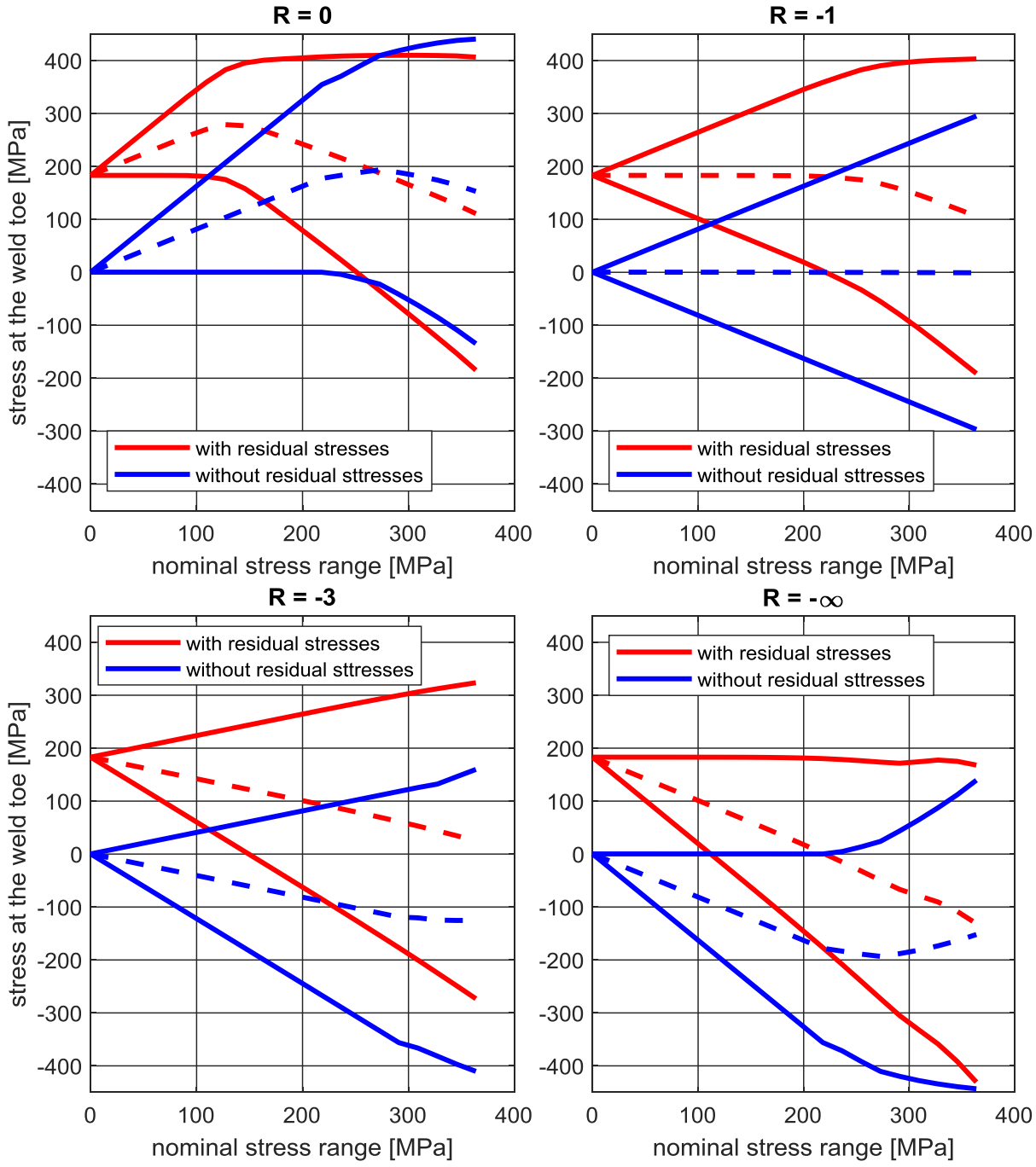

Figure 5-21: Calculated upper, lower and mean (dashed) stresses in loading direction, at the weld toe depending on the applied nominal stress range for different load ratios *R* (K-butt weld).

5.3.2 Longitudinal stiffener

The results for the longitudinal stiffener are plotted in Figure 5-22. For tensile loads (R = 0) with residual stresses plastic strains occur for load ranges over 40 MPa and the lower stress starts to decrease. The curve without residual stresses changes slope when the upper stress reaches 240 MPa due to plastic strains at the weld toe. For load ranges exceeding 180 MPa, upper and lower stresses are the same with and without residual stresses.

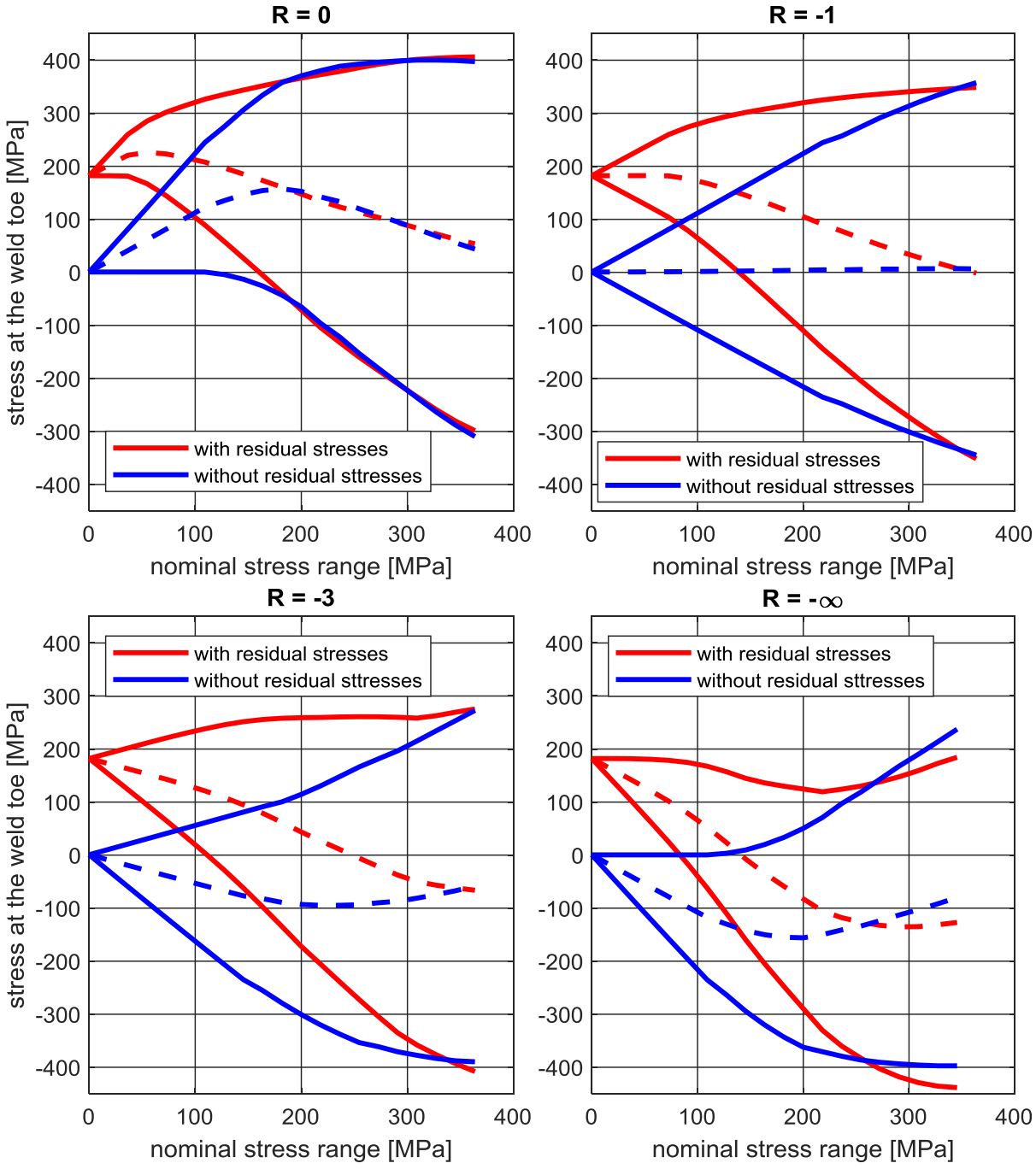

Figure 5-22: Calculated upper, lower and mean (dashed) stresses in loading direction, at the weld toe depending on the applied nominal stress range for different load ratios R (longitudinal stiffener).

For R = -1 the curve with residual stresses lies higher than without. The difference is steadily decreased as plastic strains occur and residual stresses are relieved. At a load range of 350 MPa both curves cross each other. The curve without residual stresses has a short almost horizontal portion at 250 MPa and continues with a reduced slope.

For R = -3 the curve without residual stresses shows plastic behaviour when the lower stress exceeds -250 MPa. The curve with residual stresses has a flat, almost horizontal upper stress for load ranges of more than 200 MPa. The curves with and without residual stresses cross each other at a load range of approximately 350 MPa.

For compressive loads (R = -∞) the curve with residual stresses is extraordinary. For load ranges over 100 MPa the upper stress decreases while the lower stress is negative. Assuming that the compressive portion has no or little influence on the fatigue damage, this would indicate that for higher load ranges the damaging effect decreases. Thus, the S-N curve should have an inverted slope and increase. Starting from a load range of 200 MPa the upper stress increases again and thus also the S-N curve should change slope again. The curve without residual stresses becomes plastic and shows tensile upper stresses for load ranges of more than 100 MPa. At a load range of 250 MPa the curves with and without residual stresses cross each other.

When the upper or lower stresses reach a certain value the curves do not proceed linearly anymore. This is caused by plastic strains occurring when the von Mises stress exceeds the yield limit. Plastic strains lead to a relaxation or in some cases the formation of new residual stresses. The residual stress relaxation under tensile loading can be seen directly looking at the load ratio of R = 0. The upper stress indicates the stress at the weld toe for the applied tensile load. The lower stress corresponds approximately to the residual stress acting without external forces applied, with exception of boundary conditions. If the value decreases and is lower than the initial residual stress, plastic strains have occurred and residual stresses have been relieved.

The same applies for compressive loads (R = -∞). The lower stress is the stress under load and the upper stress is the residual stress without external force, except for boundary conditions. Up to a load range of 200 MPa the upper stress decreases. This indicates that the tensile welding residual stresses are relieved under compressive loads. The results without residual stresses show increasing upper stresses for load ranges above 150 MPa. This indicates that compressive plastic strains have formed resulting in tensile residual stresses.

5.4 Residual stress relaxation

To verify the findings from the numerical simulations residual stress measurements after loading are performed to detect the possible residual stress relaxation. X-ray diffraction measurements are performed on a K-butt weld and a longitudinal stiffener specimen after applying a tensile load. Residual stresses have already been measured on these specimens so that the values before and after loading can be compared. Additional hole drilling measurements are performed on further specimens before and after loading.

5.4.1 K-butt weld

The results of the X-ray diffraction measurements on a K-butt weld specimen before and after applying a nominal stress of 291 MPa are shown in Figure 5-23. Longitudinal residual stresses close to the weld increase slightly after loading. Transversal values show no difference, although according to the simulations plastic strains should have occurred.

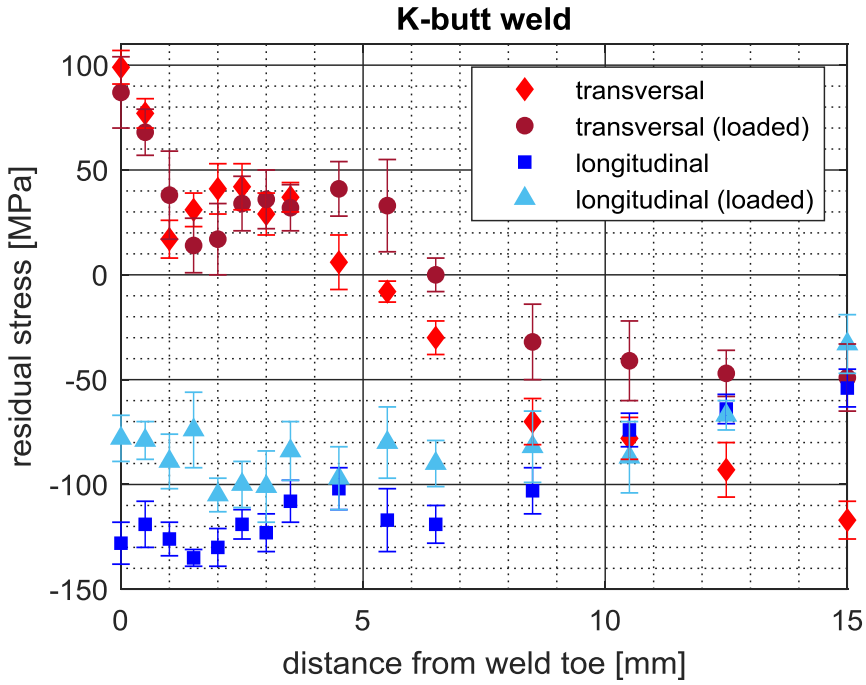

Figure 5-23: Residual stress measured by X-ray diffraction before and after applying a tensile load of 291 MPa nominal stress.

The results of hole drilling measurements on three K-butt weld specimens before and after loading to different loads are shown in Figure 5-24. On all specimens the transversal residual stresses after loading are lower than before loading. Though, the reduction is not as pronounced as predicted by the simulation.

The hole drilling method is not ideal to capture the residual stress changes. As it consists in drilling a hole, it is not possible to measure twice at the same point. Furthermore, the drilled hole has an effective diameter of approximately 1.8 mm. The measured residual stresses will represent a mean value over the drilled volume. Plastic strains will occur very locally at the notch of the weld toe. When comparing with the simulations, the residual stress relief will be different if assessed at the weld toe or 2 mm in front of it.

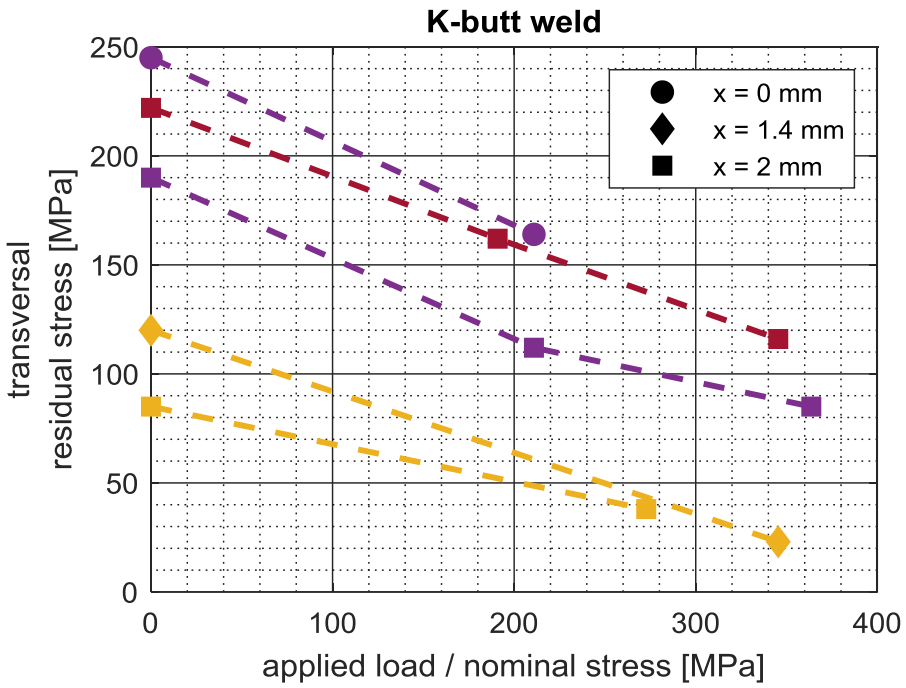

Figure 5-24: Transversal residual stress measured by hole drilling before and after applying tensile loads (x = distance from weld toe; same colour measured on same specimen).

5.4.2 Longitudinal stiffener

Residual stresses measured by X-ray diffraction on a longitudinal stiffener specimen before and after applying a nominal stress of 327 MPa are shown in Figure 5-25. The longitudinal residual stresses show a decrease of the compressive values. Also the tensile values at the weld are reduced. Transversal residual stresses 2 mm in front of the weld show a decrease from 210 MPa to approximately 60 MPa.

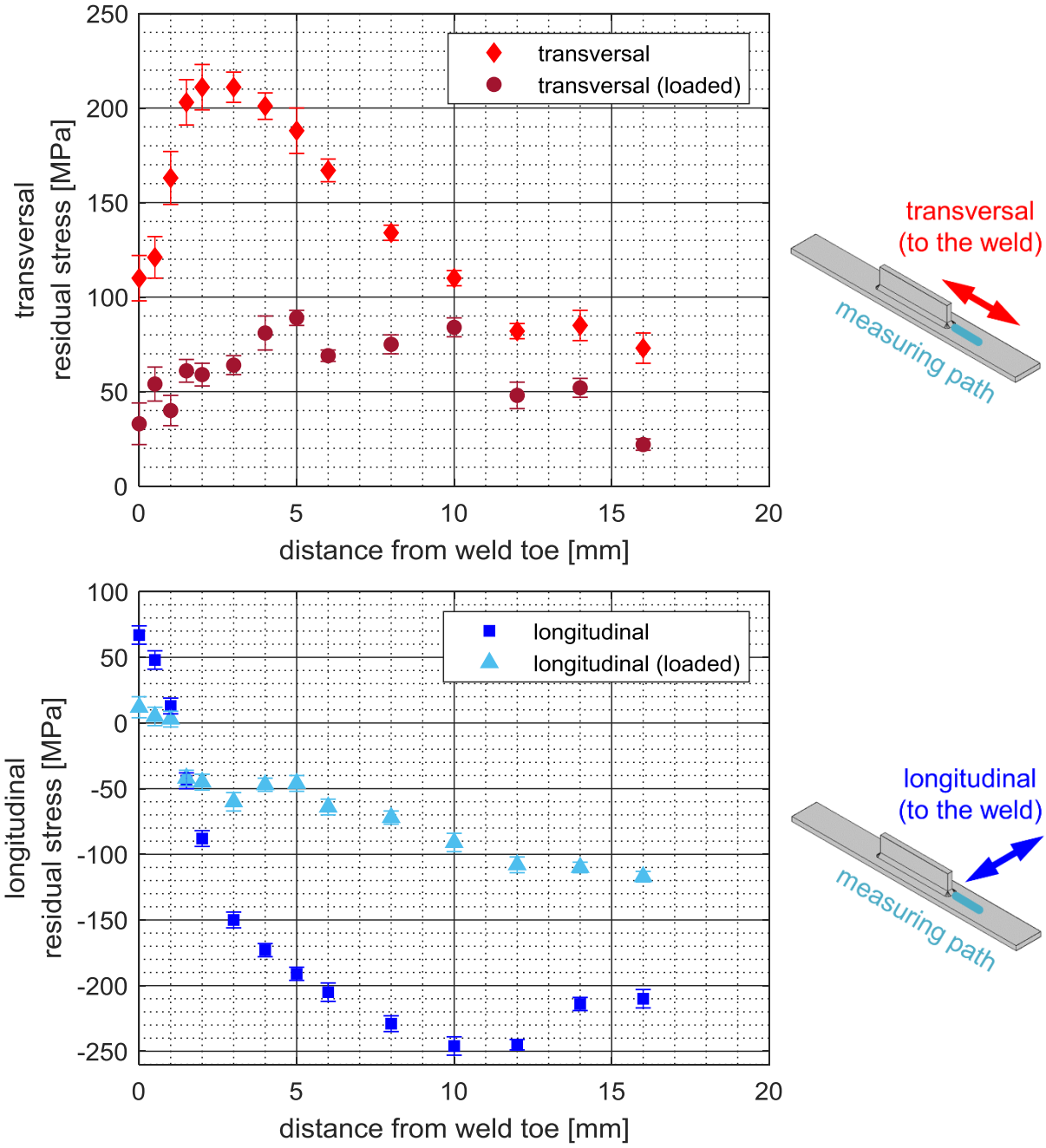

Figure 5-25: Residual stress measured by X-ray diffraction on a longitudinal stiffener specimen before and after applying a tensile load of 327 MPa nominal stress.

Additional hole drilling measurements are performed on four specimens, two loaded with tensile loads and two with compressive loads. The resulting transversal residual stresses before and after loading are shown in Figure 5-26. Under both tensile and compressive loads residual stresses are clearly reduced. This confirms the observations from the simulations at least qualitatively.

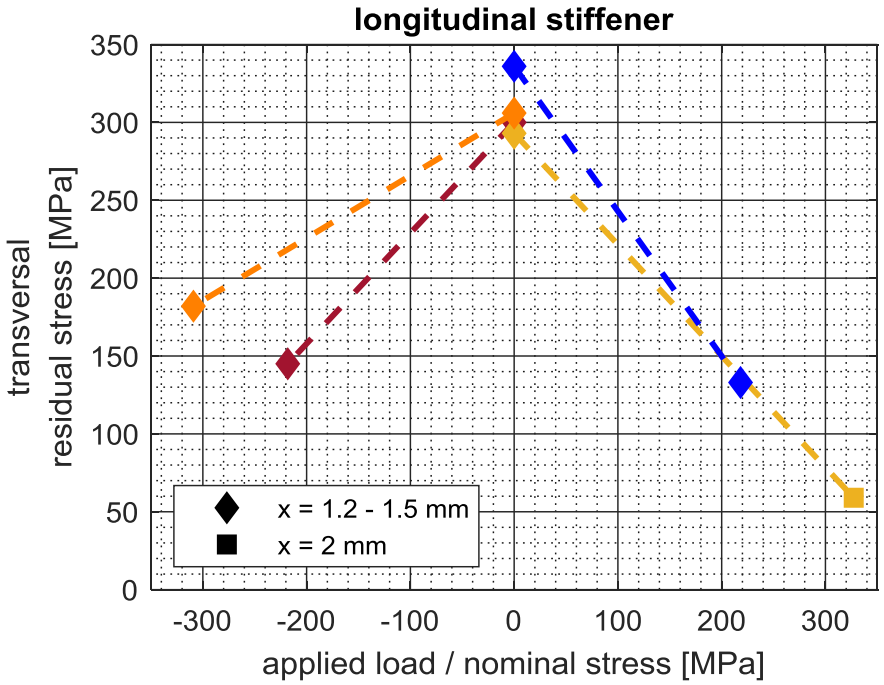

Figure 5-26: Transversal residual stress measured by hole drilling before and after applying compressive and tensile loads (x = distance from weld toe; same colour measured on same specimen).

5.5 Equivalent stress ratio

The simulation results in Figure 5-21 and Figure 5-22 show how the tensile residual stresses shift the stresses at the weld toe towards tension. Consequently, the stress ratio at the weld toe is higher than the applied nominal load ratio. To verify if this stress ratio at the weld toe determined by numerical simulations can be used for fatigue assessments, a third series of fatigue tests is performed in addition to the as-welded and stress-relieved specimens. For these tests, stress-relieved specimens are tested with loads that cause the same stresses at the weld toe as in the as-welded specimens. The necessary equivalent forces are determined using the simulation results as follows.

From the simulation without residual stresses the stress at the weld toe is determined depending on the applied external force. The values are plotted in the green curves in Figure 5-27. For small loads the factor between nominal stress and the calculated stress at the weld toe is 1.8 for the K-butt weld and 2.3 for the longitudinal stiffener. For loads over 100 kN the stress at the weld increases non-linearly.

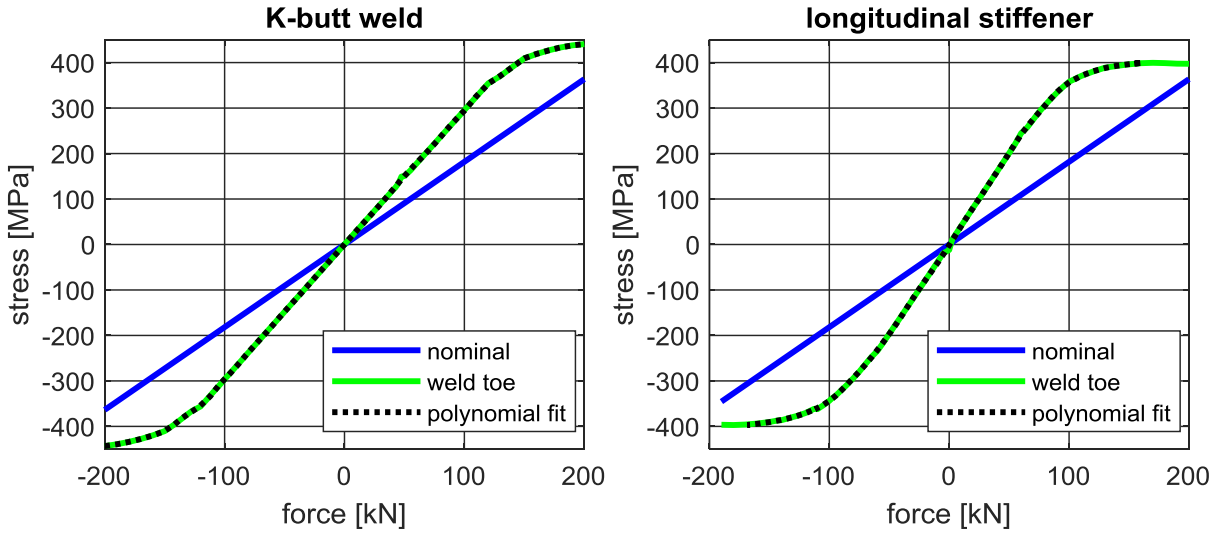

Figure 5-27: Stress at the weld toe depending on the applied force calculated on the models without residual stresses for the K-butt weld and the longitudinal stiffener.

The values at the weld toe are approximated by a polynomial curve.

From the simulations with residual stresses, red curves in Figure 5-21 and Figure 5-22, the upper and lower stress at the weld toe is read out depending on the applied load range and ratio.

Using the polynomial function, for each of these upper and lower stresses the force is determined, which has to be applied on the model without residual stresses to obtain the same stresses as with residual stresses.

The resulting equivalent forces are plotted in Figure 5-28 for the K-butt weld and in Figure 5-29 for the longitudinal stiffener. The black curves show the forces according to the nominal load ratios. These correspond to the loads applied on the as-welded and stress-relieved specimens. The curves for the equivalent forces (red) are the forces to apply on a model without residual stresses in order to obtain the same stress at the weld toe as with residual stresses.

These are also the forces applied in the third fatigue tests series on stress-relieved specimens to obtain the same stresses at the weld toe as on as-welded specimens.

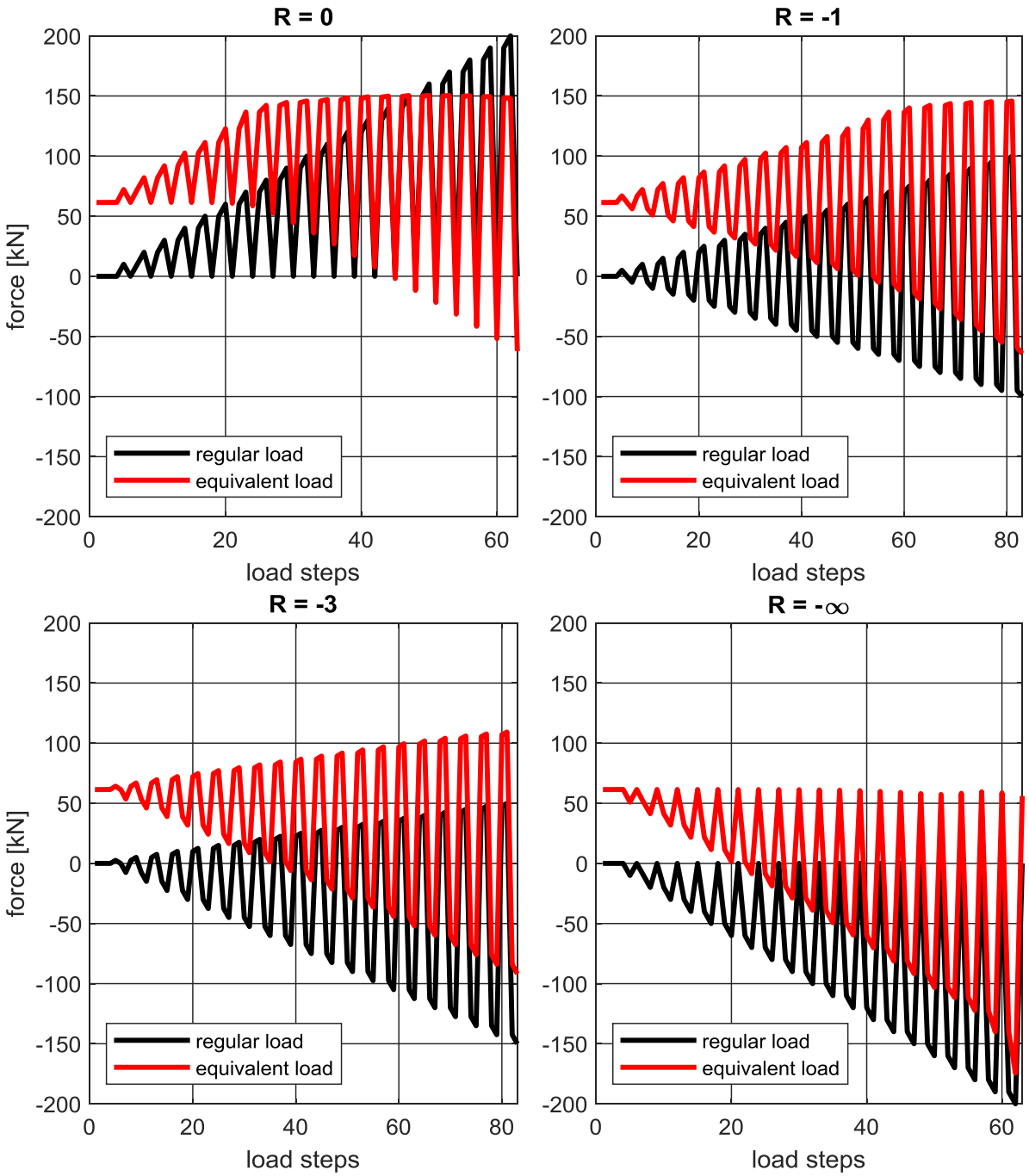

Figure 5-28: Regular loads for different load ratios and equivalent loads to apply on a model without residual stresses in order to obtain the same stresses at the weld toe as with residual stresses (K-butt weld).

For the longitudinal stiffener the green curve in Figure 5-27 runs almost horizontally at -400 MPa. The curve is based on the simulation results without residual stresses. With residual stresses and $R = -\infty$ the stresses at the weld toe exceed this value (compare Figure 5-22). The result are unrealistic compressive, equivalent loads in Figure 5-29 (bottom right). These loads are not considered in the fatigue tests.

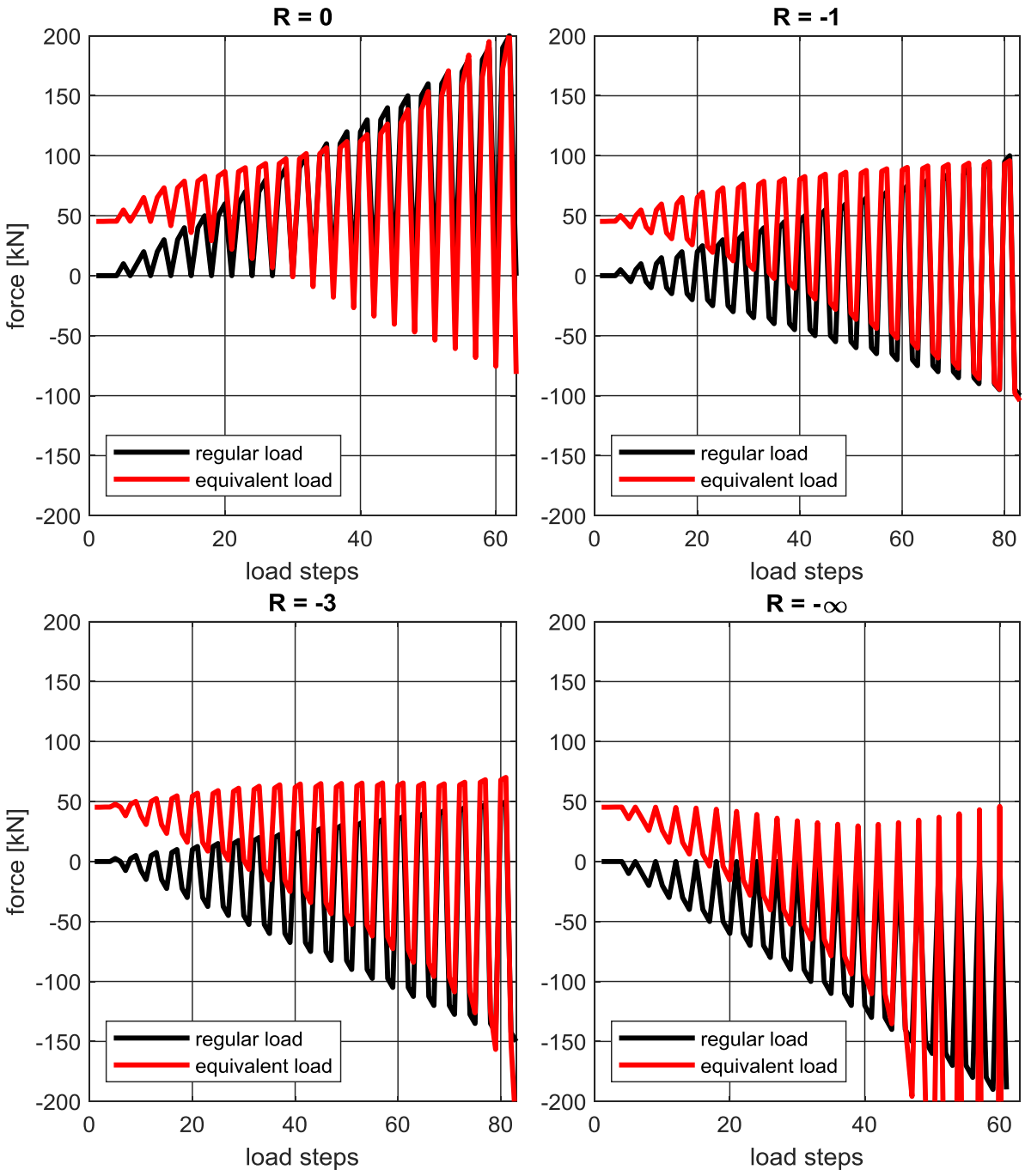

Figure 5-29: Regular loads for different load ratios and equivalent loads to apply on a model without residual stresses in order to obtain the same stresses at the weld toe as with residual stresses (longitudinal stiffener).

6 Fatigue test results

Fatigue tests have been conducted on the K-butt weld and longitudinal stiffener specimens, in as-welded and stress-relieved conditions. The initiation of macroscopic cracks was detected by DIC. Hence, for each load ratio *R* three S-N curves were established: for total fatigue life, for initiation of macroscopic cracks and for crack propagation. The S-N curves refer to the nominal stress range calculated by dividing the applied force range by the cross-section of the specimen.

6.1 K-butt weld

The resulting S-N curves for total fatigue life until complete rupture of the specimens are shown in Figure 6-1. The S-N curves are fit to the test results by linear regression and are described by the *Basquin* equation:

$$N = N_R \left(\frac{\Delta\sigma}{\Delta\sigma_R}\right)^{-k} \tag{6.1}$$

with the reference stress range $\Delta\sigma_R$ at the reference number of load cycles $N_R = 2 \cdot 10^6$ and the exponent k which defines the slope of the S-N curve in the double-logarithmic representation. The values for $\Delta\sigma_R$ and k are given in Table 6-1.

In the as-welded condition, the curves for *R* = 0 and *R* = -1 are close together. The results for *R* = -3 lie about 30 % higher. All three curves have a slope exponent of approximately 3 which is the usual value for welded details. The curve for *R* = -∞ is considerably steeper and differs from the others. In contrast, for the stress-relieved specimens the curves for the different load ratios lie far away from each other. The curve for *R* = 0 is similar to the as-welded condition with a slightly shallower slope. For *R* = -1 and *R* = -3 the curves run much higher and have a slope exponent *k* > 5. For *R* = -∞ only a run-out was produced, although the applied load was relatively high (309 MPa).

The S-N curve for FAT 71 which would apply for this type of weld according to the IIW recommendations (Hobbacher 2016) is plotted as reference.

Table 6-1: Reference stress range $\Delta\sigma_R\left(N_{total,R} = 2 \cdot 10^6\right)$ and slope exponent k for S-N curves for total fatigue life of the K-butt weld specimens.

	as-welded		stress-relieved	
load ratio *R*	$\Delta\sigma_R$	k	$\Delta\sigma_R$	k
R = 0	118	3,3	132	3,8
R = -1	113	2,6	215	5,1
R = -3	158	3,0	337	6,0
R = -∞	201	1,7	-	-

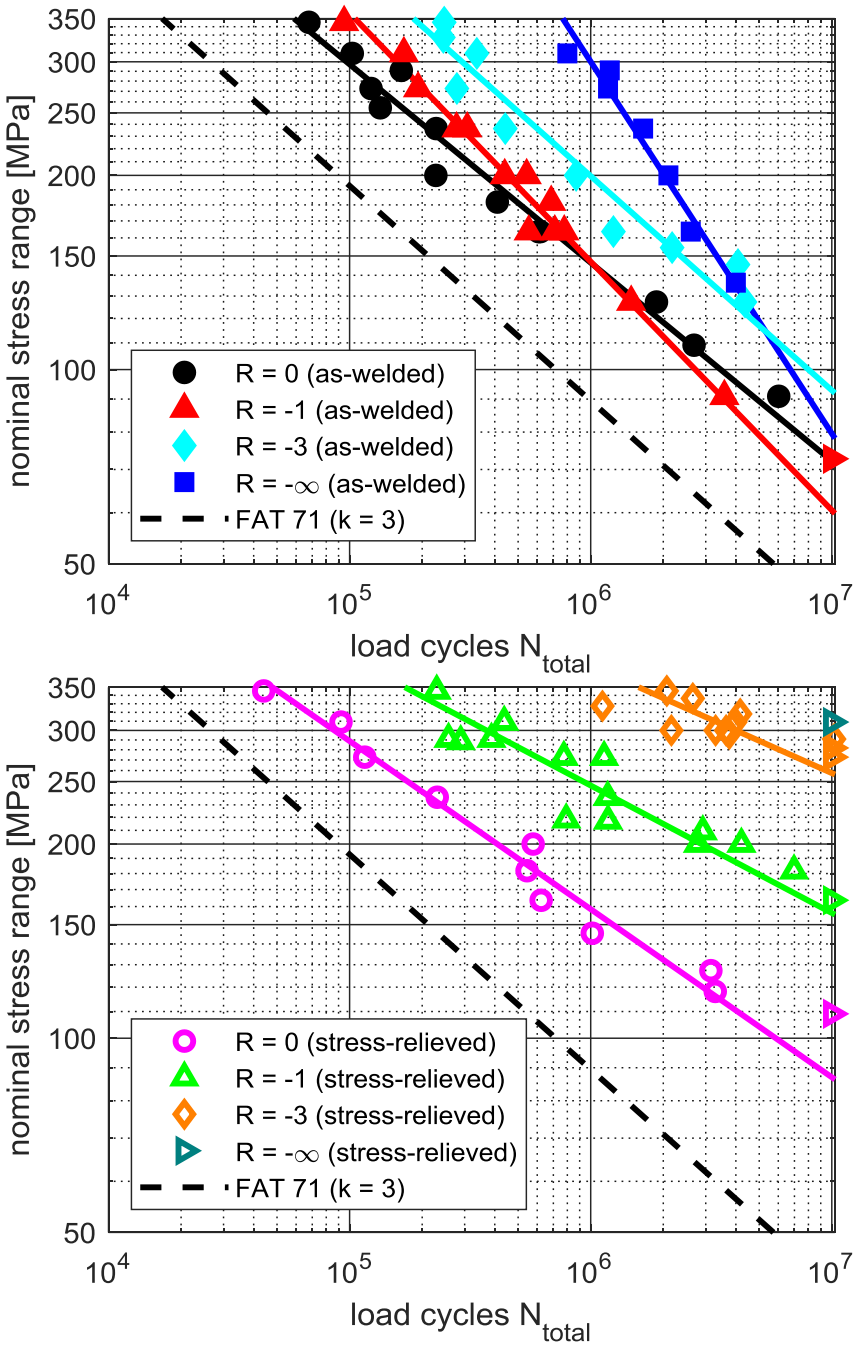

Figure 6-1: S-N curves for total fatigue life of as-welded (top) and stress-relieved (bottom) K-butt weld specimens (► symbol for run-out) (Friedrich 2020).

6.1.1 Crack initiation

The initiation of macroscopic cracks was assessed by DIC according to the procedure presented in section 5.2. Crack initiation was determined when a crack of 2 mm could be detected. The resulting S-N curves for crack initiation are shown in Figure 6-2. The parameters describing the S-N curves according to equation (6.1) are given in Table 6-2. The number of plotted results is smaller than in Figure 6-1 because it was not possible to determine crack initiation for all tested specimens. In some tests the DIC system failed. In others, mostly with low load ratios (R = -3 or R = -∞), cracks initiated on the bottom side of the specimen not covered by DIC. The distribution of the results is similar to the S-N diagrams for total fatigue life in Figure 6-1. In as-welded conditions, the curves for R = 0 and R = -1 are close together with a slope of approximately 3. The results for R = -3 lie slightly

higher with a similar slope. For R = -∞ the slope is again steeper. For the stress-relieved specimens, the distance between the S-N curves is larger and the slopes are shallower. For R = 0 at high load ranges the results are similar to the as-welded condition. For low load ranges the stress-relieved specimens show longer crack initiation periods and the S-N curve has a shallower slope than in the as-welded condition. For R = -3 the results lie too close together to determine a representative S-N curve by linear regression.

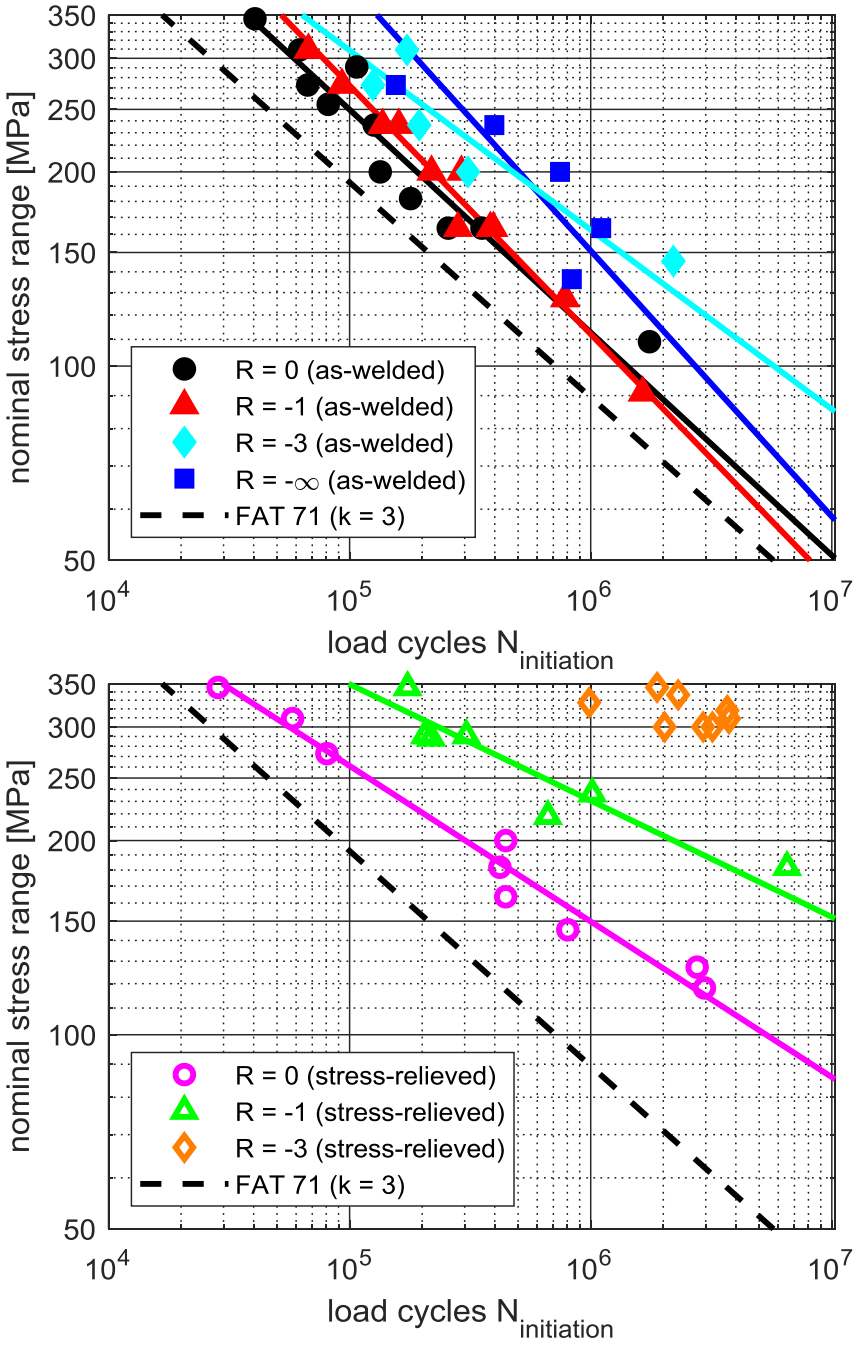

Figure 6-2: S-N curves for crack initiation for as-welded (top) and stress-relieved (bottom) K-butt weld specimens (Friedrich 2020).

Table 6-2: Reference stress range $\Delta\sigma_R\left(N_{initiation,R} = 2 \cdot 10^6\right)$ and slope exponent k for S-N curves for crack initiation of the K-butt weld specimens.

	as-welded		stress-relieved	
load ratio *R*	$\Delta\sigma_R$	k	$\Delta\sigma_R$	k
R = 0	89	2,9	127	4,1
R = -1	86	2,6	204	5,5
R = -3	134	3,6	-	-
R = -∞	113	2,4	-	-

6.1.2 Crack propagation

The crack propagation phase is determined by subtracting the crack initiation from the total number of load cycles until rupture:

$$N_{propagation} = N_{total} - N_{initiation} \tag{6.2}$$

The resulting S-N curves are plotted in Figure 6-3 and the parameters defining the S-N curves are listed in Table 6-3. In the as-welded condition the curves are in the same range of the crack initiation curves, indicating a similar proportion of crack initiation and propagation in the total fatigue life. For the stress-relieved specimens the crack propagation periods are shorter than the crack initiation and the difference between the load ratios is less pronounced. In fact, the stress-relieved results lie close to the as-welded curves for the corresponding load ratio. For *R* = -3 in stress-relieved conditions cracks did occur only for relatively high loads. The results lie too close together to determine a representative S-N curve by linear regression. The smaller numbers of load cycles ($N_{propagation} \approx 2 \cdot 10^5$) are close to the as-welded results.

Table 6-3: Reference stress range $\Delta\sigma_R\left(N_{propagation,R} = 2 \cdot 10^6\right)$ and slope exponent k for S-N curves for crack propagation of the K-butt weld specimens.

	as-welded		stress-relieved	
load ratio *R*	$\Delta\sigma_R$	k	$\Delta\sigma_R$	k
R = 0	86	3,1	68	2,8
R = -1	83	2,5	105	3,2
R = -3	139	3,5	-	-
R = -∞	161	1,4	-	-

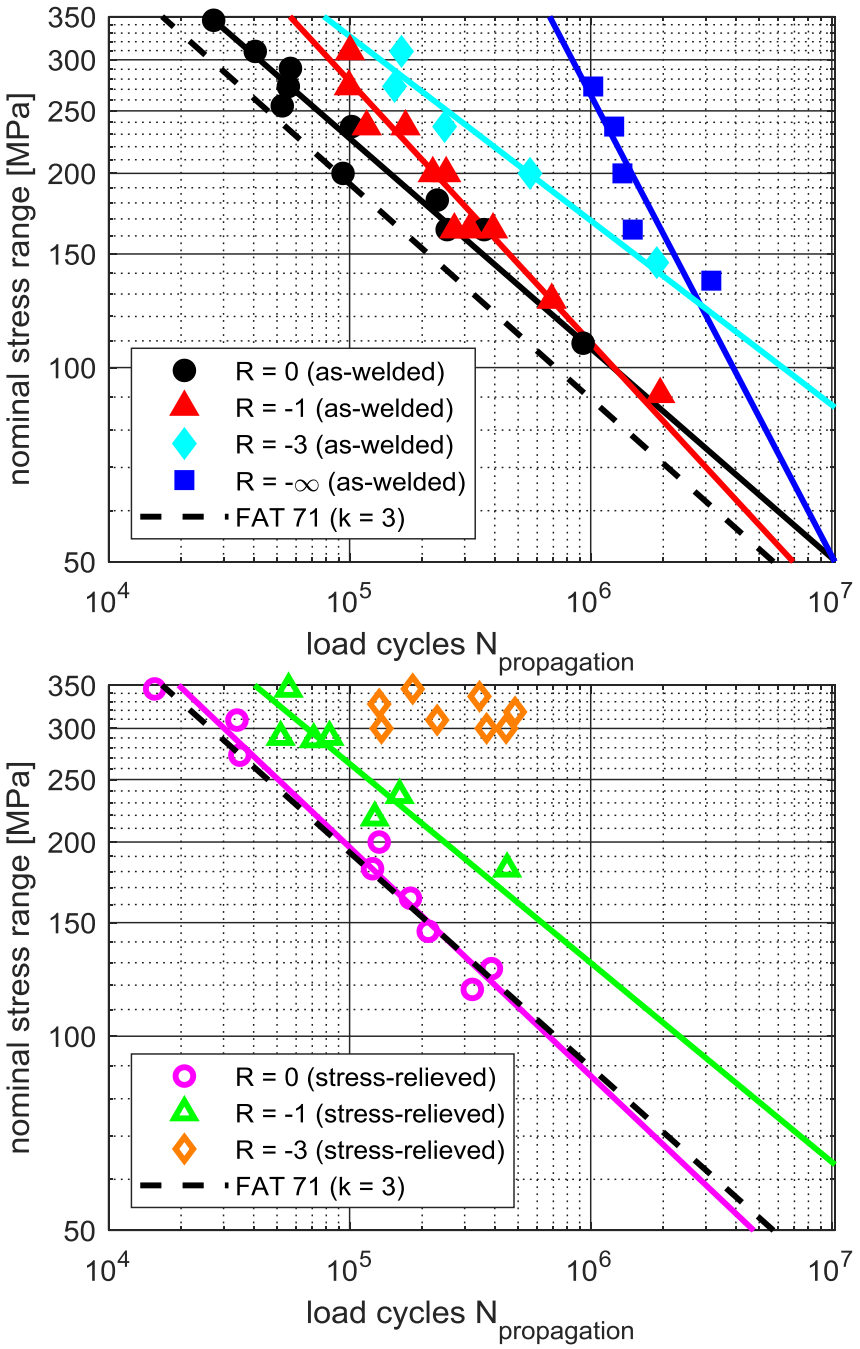

Figure 6-3: S-N curves for crack propagation for as-welded (top) and stress-relieved (bottom) K-butt weld specimens (Friedrich 2020).

6.1.3 Discussion

The presented fatigue test results show a clear influence of the welding residuals stresses. The as-welded results distinguish themselves from the stress-relieved. In the as-welded condition the S-N curves lie relatively close together because the tensile residual stresses reduce the influence of the load ratio. In the stress-relieved condition the influence of the load ratio is more pronounced. By plotting all results in one S-N diagram, it becomes visible that the residual stress influence is more evident for lower load ratios (Figure 6-4). For tensile loading (R = 0) the results in as-welded and stress-relieved conditions are similar. With increasing compressive loads (R = -1 and R = -3) also the difference between as-welded and stress-relieved increases.

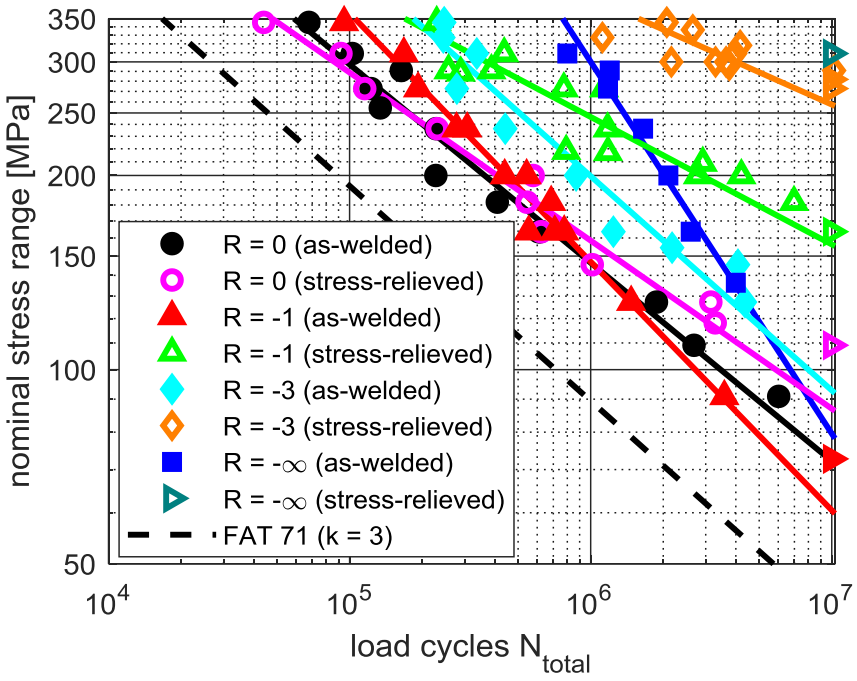

Figure 6-4: S-N curves for total fatigue life for as-welded and stress-relieved K-butt weld specimens (► symbol for run-out) (Friedrich 2020).

By plotting all results together it becomes also visible that the S-N curves have different slopes and consequently cross each other. The slope can be interpreted as the increase of the damaging effect with an increase of the stress range. If by increasing the stress range the damaging effect increases rapidly, the endurable number of load cycles decreases faster and the slope of the S-N curve is shallower. If with increasing stress range the damage increases slowly, the reduction of endurable load cycles is slow and the S-N curve steep.

These differences in the slopes and the crossing points of the curves can be explained by looking at the simulation results for the stresses at the weld toe. In the following plot three exemplary sets of S-N curves, crossing each other, are plotted together with the simulation results (Figure 6-5). From the results it can be seen that the S-N curves cross when the upper and lower stresses at the weld toe are the same. Thus, when the stress range and ratio at the weld toe are the same.

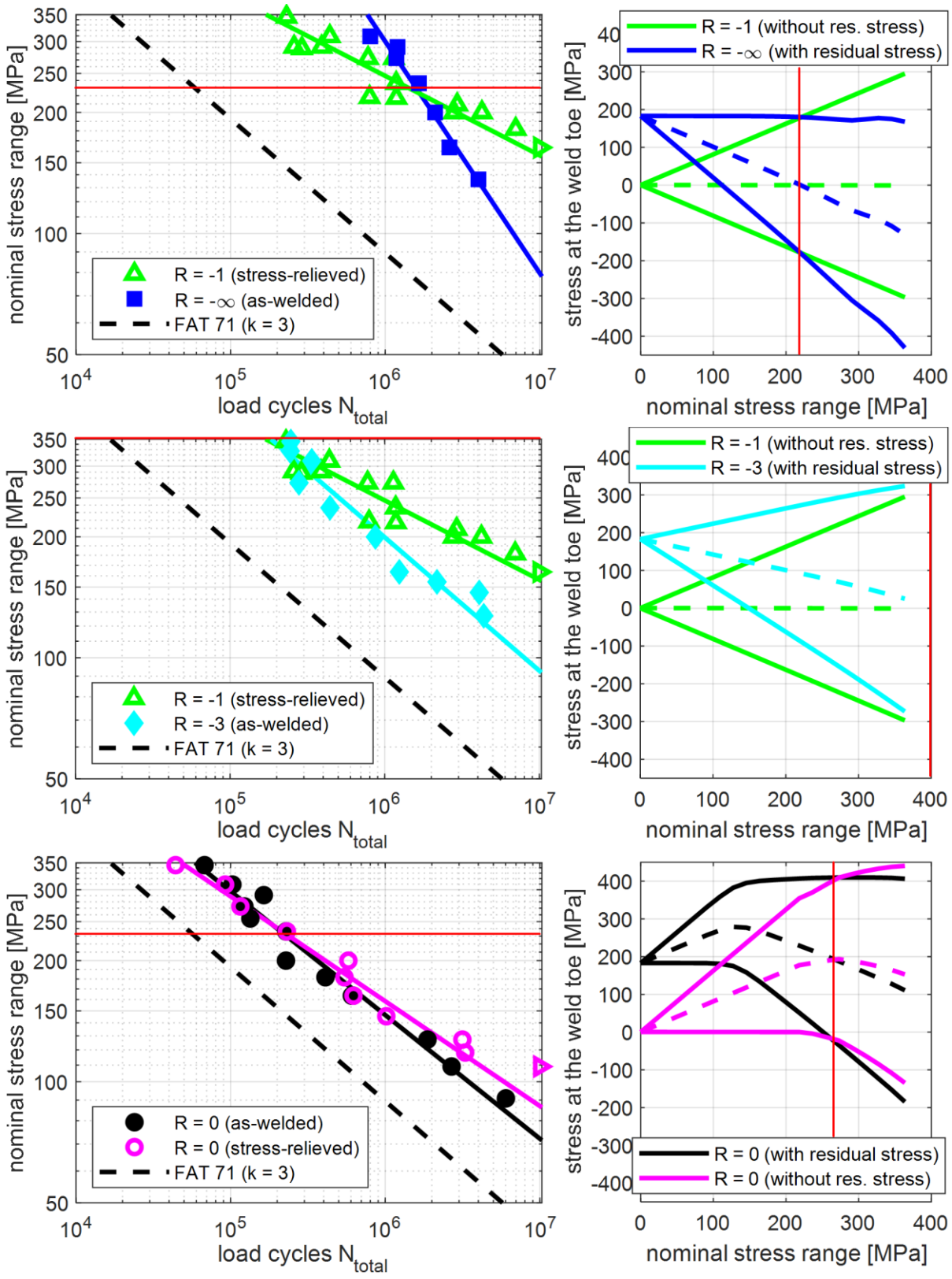

Figure 6-5: Crossing S-N curves and respective simulation results of the stresses at the weld toe (same colours indicate same load ratio and residual stress condition).

The simulation results do also explain the different slopes. In the first example (Figure 6-5, top), with residual stresses and compressive load (R = -∞) the upper stress at the weld toe is constant at 200 MPa independently of the applied load range. The lower stress is negative for loads greater than 120 MPa. Assuming that the damage is caused mainly by the tensile

portion of the load, the damage induced by loads greater than 120 MPa will stay the same, or at least similar. Thus, also the endurable number of load cycles will be the same and the S-N curve will be relatively steep. Without residual stresses and alternating load (R = -1), half of the applied load range is tensile. With increasing load range, the tensile portion of the load increases constantly. So with increasing loads also the damaging effect will increase. Thus, the number of endurable load cycles will decrease with increasing loads causing a shallower slope of the S-N curve compared to R = -∞. Due to the double logarithmic scale and the large differences in the numbers of load cycles, a direct comparison between the S-N curves is possible only when they fall closely together. From the third example, as-welded and stress-relieved tensile load (R = 0), it appears that even slight changes of the slope, that could otherwise be interpreted as scatter, are explainable by the stresses at the weld toe. For small stress ranges, with residual stresses the upper and lower stresses are higher due to the superimposed tensile residual stresses. With increasing loads the difference between the curves with and without residual stresses decreases and for high loads stresses on the model without residual stresses result higher than on the model with residual stresses. In accordance with this, the S-N curves have slightly different slopes. For small stress ranges, the as-welded specimens fail earlier than the stress-relieved. While for high loads, the stress-relieved specimens tend to fail earlier.

The stresses in the considerations above are determined at the weld toe and should therefore affect mainly crack initiation. In fact, the fatigue test results for crack initiation show a clear difference between as-welded and stress-relieved specimens (Figure 6-2). Crack propagation seems to be less affected by residual stresses. All test results for crack propagation on as-welded and stress-relieved specimens are plotted in one S-N diagram in Figure 6-6. For each load ratio the results from both residual stress conditions lay relatively close together. This indicates that residual stresses have little effect on the duration of crack propagation.

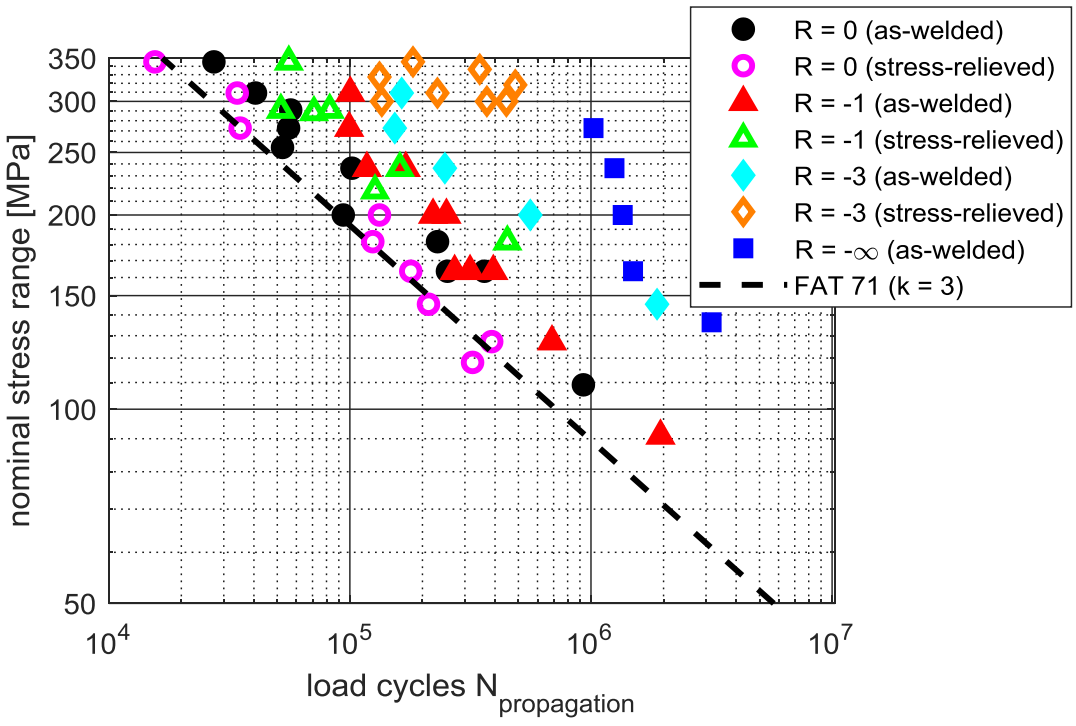

Figure 6-6: S-N diagram for crack propagation in as-welded and stress-relieved K-butt weld specimens.

Crack propagation detected by DIC for the same load range on as-welded and stress-relieved specimens is compared in Figure 6-7. On the as-welded specimen a single crack forms close to the centre of the specimen and expands to both sides. On the stress-relieved specimen several cracks form over the length of the weld. The cracks unify and in the end the resulting duration of crack propagation is similar to the as-welded specimen.

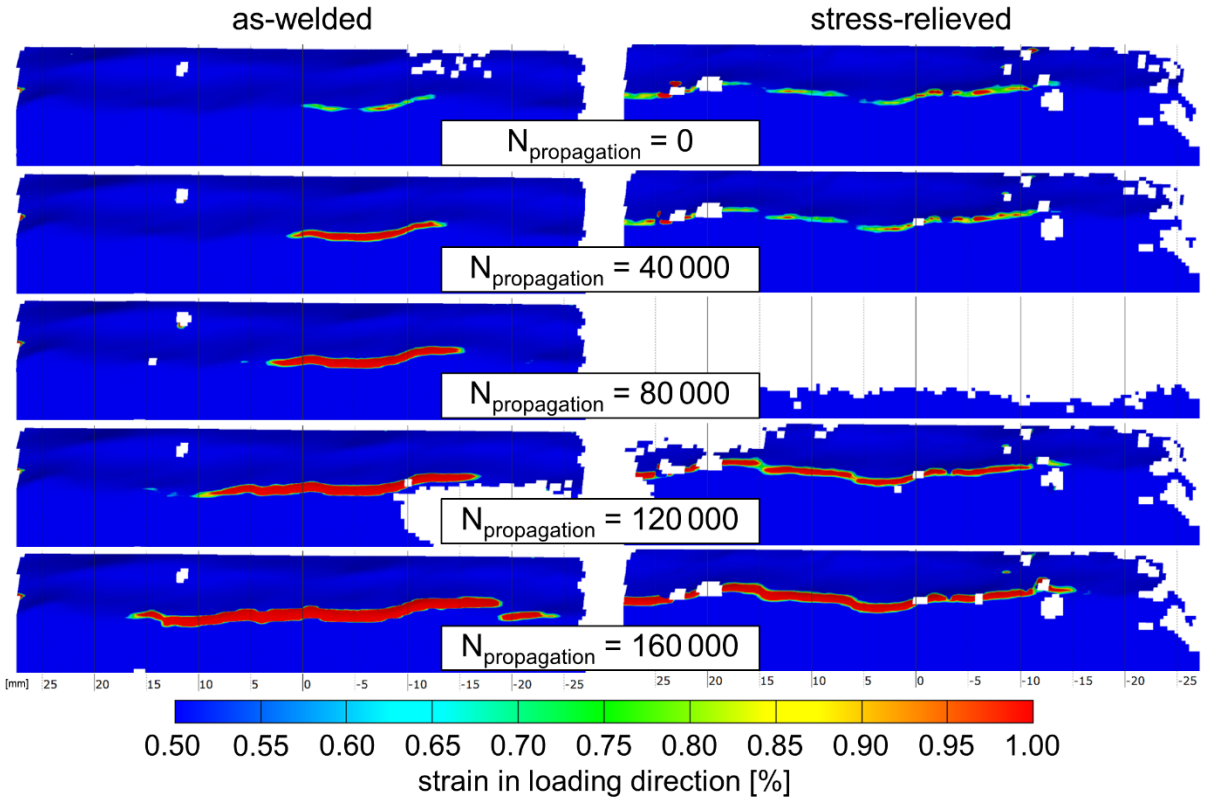

Figure 6-7: Crack propagation determined by DIC on an as-welded and a stress-relieved K-butt weld specimen (R = -3, nominal stress range = 309 MPa) (Friedrich 2020).

6.2 Longitudinal stiffener

The S-N curves for total fatigue life until complete rupture of the longitudinal stiffener specimens are plotted in Figure 6-8 and the parameters describing the curves according to equation (6.1) are given in Table 6-4. The design curve for this weld geometry is again FAT 71 according to the IIW recommendations (Hobbacher 2016) and it is plotted as reference. In the as-welded condition the curves for R = 0 and R = -1 lie close together and have the same slope. For R = -3 the curve is close to the first two curves up to 200 MPa. For higher load ranges the number of endurable load cycles stays constant and the S-N curve rises vertically. For compressive loads (R = -∞) failures are observed only between 160 MPa and 195 MPa. For lower and higher load ranges only run-outs were obtained. The stress-relieved curves clearly show the influence of the different load ratios. Except for tensile loads (R = 0) the curves run higher than the as-welded curves and have a shallower slope. For compressive loads (R = -∞) only a run-out was produced.

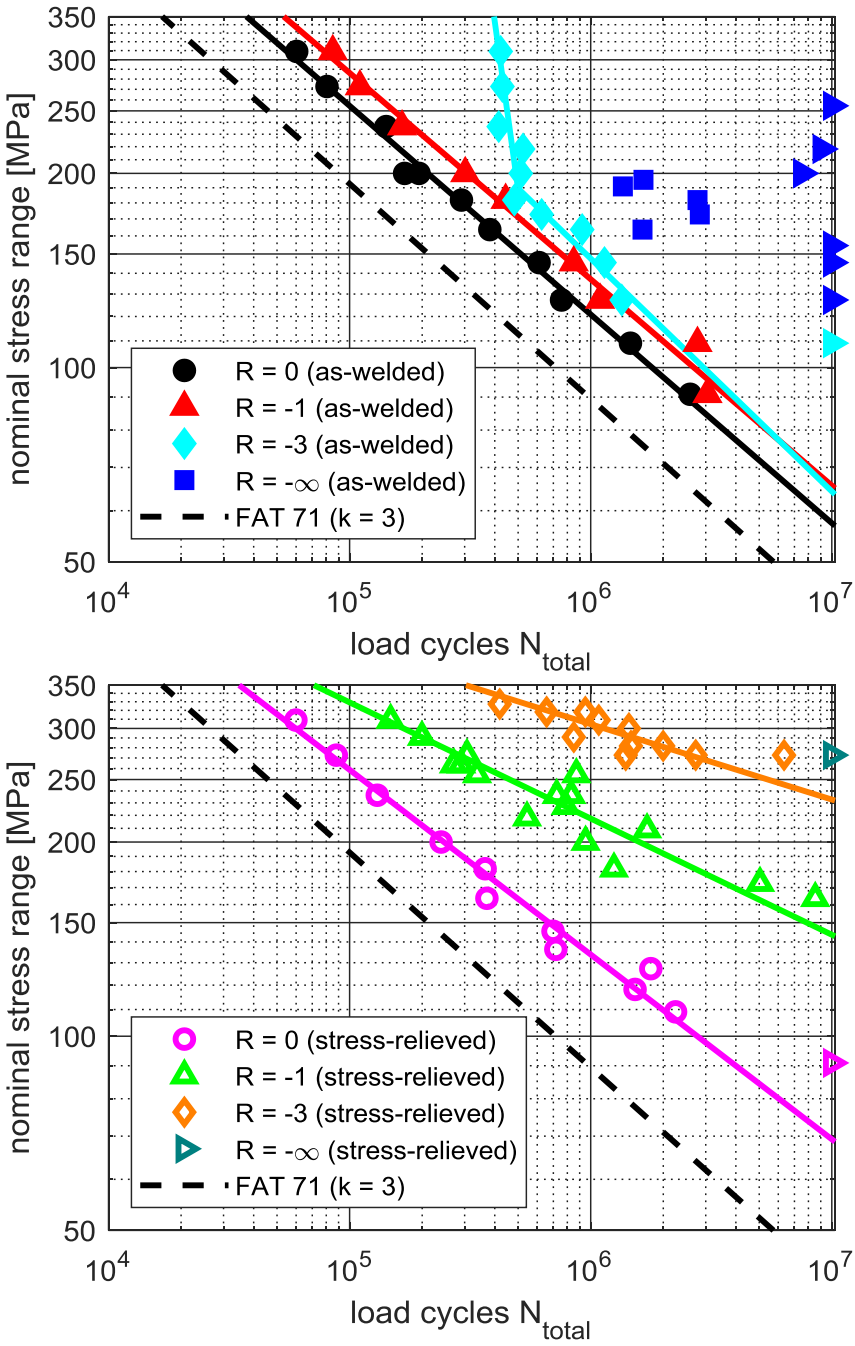

Figure 6-8: S-N curves for total fatigue life of as-welded (top) and stress-relieved (bottom) longitudinal stiffener specimens (► symbol for run-out) (Friedrich 2020).

Table 6-4: Reference stress range $\Delta\sigma_R\left(N_{total,R} = 2 \cdot 10^6\right)$ and slope exponent k for S-N curves for total fatigue life of the longitudinal stiffener specimens.

	as-welded		stress-relieved	
load ratio *R*	$\Delta\sigma_R$	k	$\Delta\sigma_R$	k
R = 0	97	3,1	110	3,5
R = -1	110	3,1	192	5,6
R = -3	115	2,8	281	8,6
R = -∞	-	-	-	-

6.2.1 Crack initiation

The S-N curves for the initiation of macroscopic cracks are shown in Figure 6-9 and the values describing the S-N curves are listed in Table 6-5. The results for the as-welded specimens are qualitatively similar to the previous curves for total fatigue life. The curves for R = 0 and R = -1 lie close together. For R = -3 the curve runs vertical above 200 MPa. For R = -∞ cracks were detected only between 160 MPa and 195 MPa. For the stress-relieved specimens the influence of the different load ratios is clearly visible. The curves run higher and with a shallower slope than in the as-welded condition.

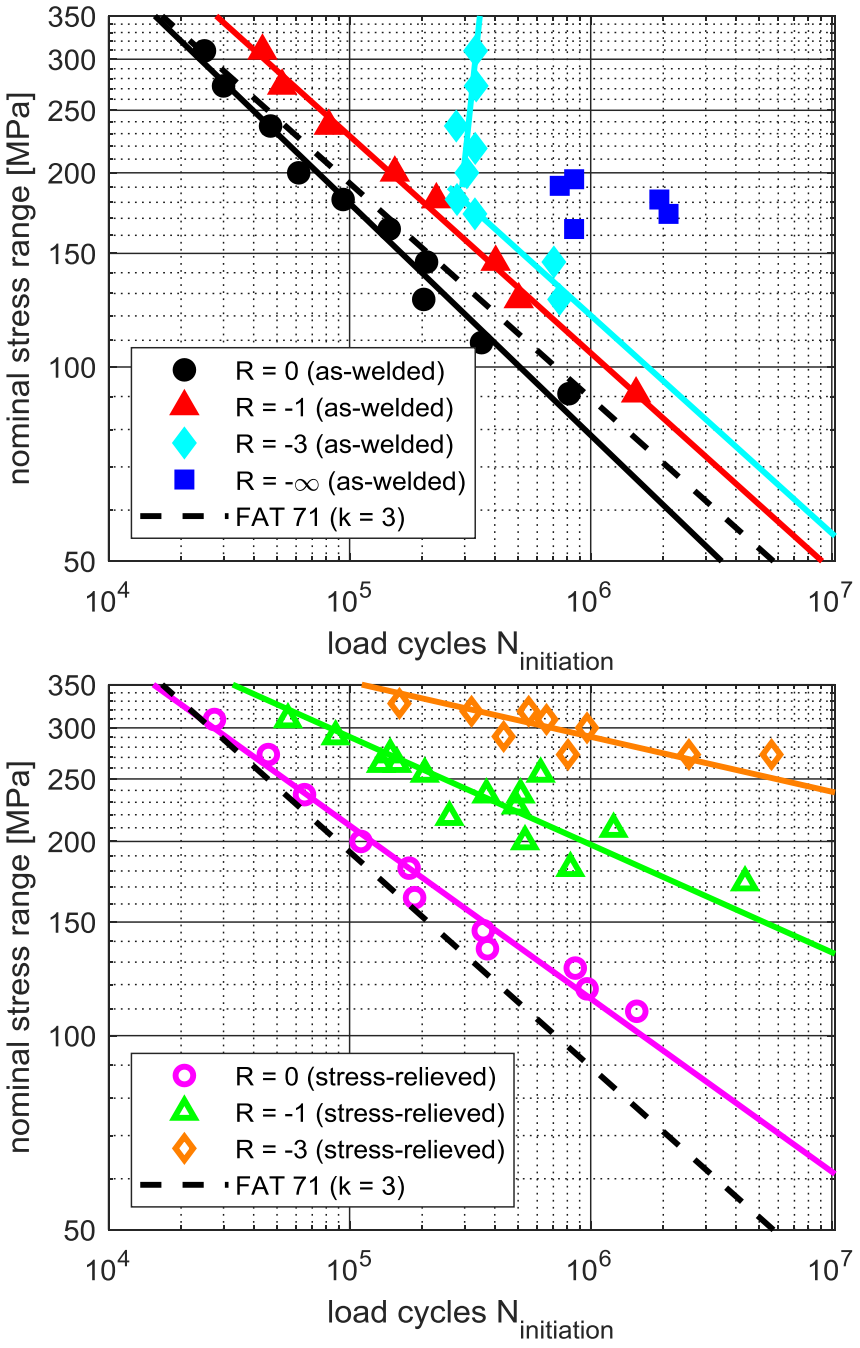

Figure 6-9: S-N curves for crack initiation for as-welded (top) and stress-relieved (bottom) longitudinal stiffener specimens (Friedrich 2020).

Table 6-5: Reference stress range $\Delta\sigma_R\left(N_{initiation,R} = 2 \cdot 10^6\right)$ and slope exponent k for S-N curves for crack initiation of the longitudinal stiffener specimens.

	as-welded		stress-relieved	
load ratio *R*	$\Delta\sigma_R$	k	$\Delta\sigma_R$	k
R = 0	61	2,8	95	3,7
R = -1	83	3,0	176	6,0
R = -3	95	3,0	274	11,7
R = -∞	-	-	-	-

6.2.2 Crack propagation

The number of load cycles for crack propagation is calculated by subtracting the number of load cycles until initiation of a macroscopic crack from the total number of load cycles. The resulting S-N curves are shown in Figure 6-10 and the values describing the S-N curves are given in Table 6-6. For the as-welded specimens, the curves for load ratios from *R* = 0 to *R* = -3 overlap. Thus, no influence of the load ratio is apparent. For compressive loads (*R* = -∞) the results lie close together and higher than for the other three load ratios. The stress-relieved specimens show clear differences for the different load ratios. For tensile loads (*R* = 0) the crack propagation phase is slightly shorter than in the as-welded condition. For *R* = -1 and *R* = -3 the curves lie considerably higher than for the as-welded specimens.

Table 6-6: Reference stress range $\Delta\sigma_R\left(N_{propagation,R} = 2 \cdot 10^6\right)$ and slope exponent k for S-N curves until crack initiation of the longitudinal stiffener specimens.

	as-welded		stress-relieved	
load ratio *R*	$\Delta\sigma_R$	k	$\Delta\sigma_R$	k
R = 0	88	3,2	83	3,2
R = -1	85	3,0	126	3,4
R = -3	84	2,8	207	4,1
R = -∞	-	-	-	-

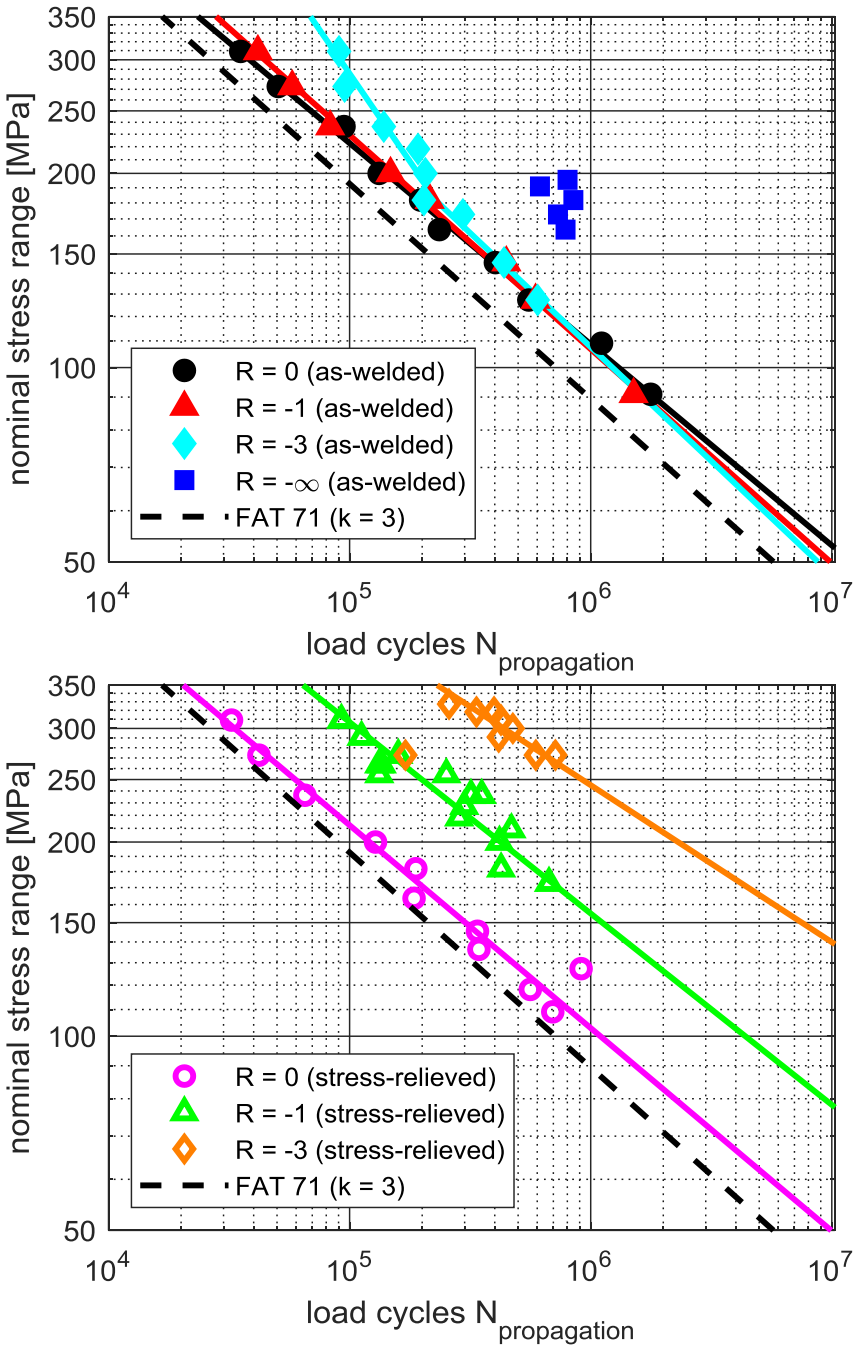

Figure 6-10: S-N curves for crack propagation for as-welded (top) and stress-relieved (bottom) longitudinal stiffener specimens (result for R = -3 (stress-relieved) at $N_{propagation} = 1.7 \cdot 10^5$ not included in linear regression) (Friedrich 2020).

6.2.3 Discussion

The S-N curves for the longitudinal stiffeners present some peculiarities which can be explained with the help of the simulation results. The correlation between the fatigue test results and the simulation results for three exemplary cases are shown in (Figure 6-11). As for the K-butt weld, the crossing of the S-N curves coincides with the crossing of the calculated stresses at the weld toe. For as-welded R = -3 the S-N curve has a distinctive shape with a vertical branch above 200 MPa stress range. From the simulation results it appears that for these loads the upper stress is constant at approximately 260 MPa while the lower stress is negative. Assuming that only tensile loads contribute to the fatigue damage, the endurable number of load cycles will not change, although the applied stress range is increased. The third example (Figure 6-11, bottom) compares tensile loads (R = 0) on the as-welded and stress-relieved specimens. With residual stresses the stresses at the weld toe are shifted towards tension. For increasing loads the stresses for both residual stress conditions converge and above 180 MPa they are the same with and without residual stresses. This is in agreement with the S-N curves. For higher loads, as-welded and stress-relieved results coincide while for small loads the stress-relieved specimens tend to fail later.

Overall, the results for the longitudinal stiffener show little scatter and where the results are distributed linearly, they are well approximated by the linear regression curves. An exception are the results of the stress-relieved R = -1 load ratio between 200 and 250 MPa. Here the results do not seem to follow the straight line of the remaining results. This could be due to the normal scatter in this kind of tests. But remarkably, it coincides with the load where, according to the simulation, the weld toe begins to be affected by plastic strains. This is indicated by a slightly changing slope in the upper and lower stresses, green curves in Figure 6-11 (centre, right).

Another remarkable S-N curve is the one for compressive loads R = -∞ in as-welded conditions (Figure 6-12). Here the specimens fail only between 160 and 195 MPa. From the simulation results it appears that the upper stress decreases for loads greater than 100 MPa and raises again above 220 MPa. Assuming that only the tensile part causes the fatigue damage, the highest damage and thus shortest fatigue life should result when the lower stress becomes compressive. At this point the tensile portion of the stress range would reach a local maximum. In this case the simulation results at the weld toe agree only qualitatively with the fatigue tests. Therefore, the simulation results are plotted also for the first two nodes below the weld toe. Here the welding residual stresses result higher than on the surface and the results correlate better with the fatigue tests.

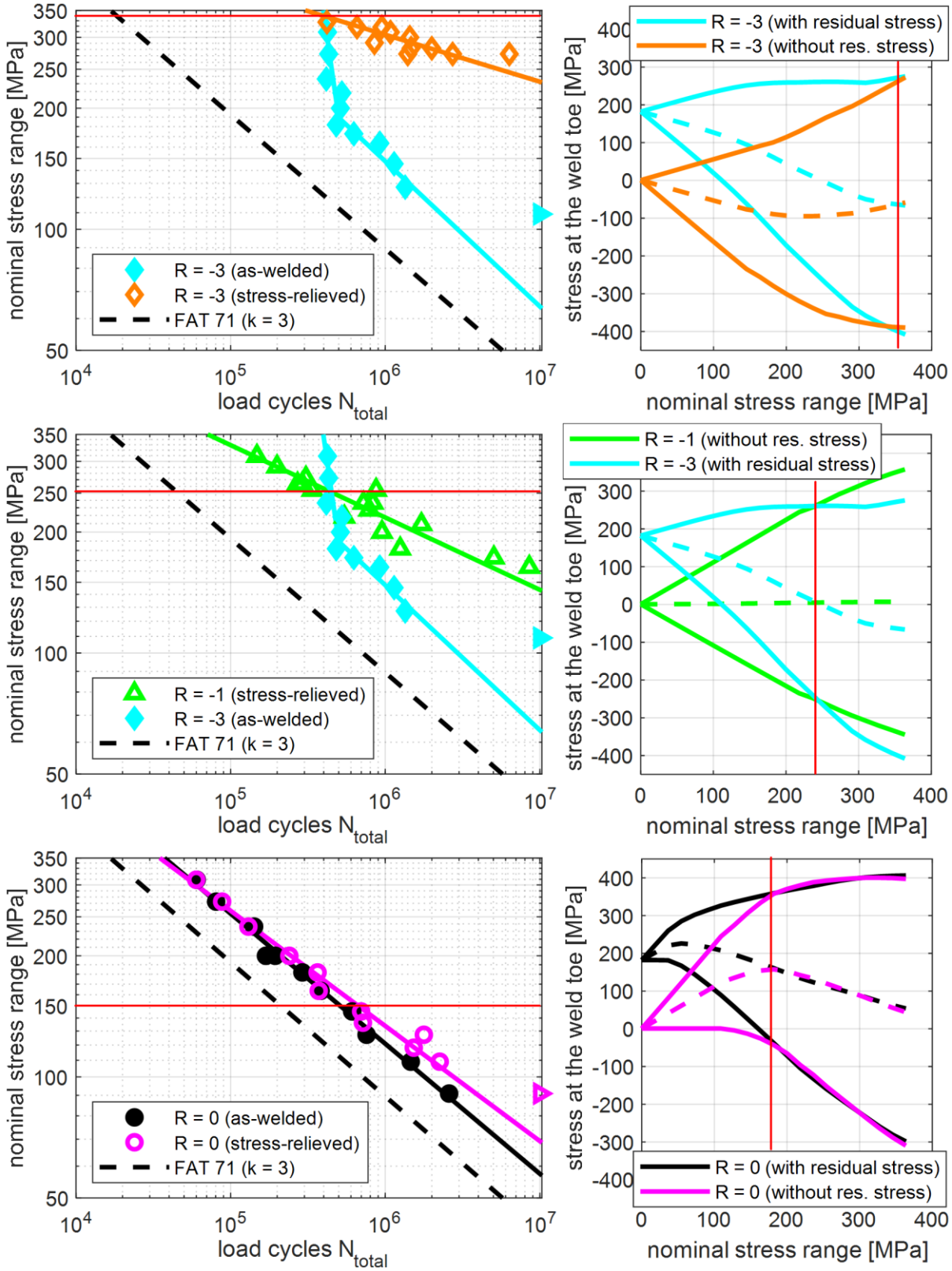

Figure 6-11: Crossing S-N curves and respective simulation results of the stresses at the weld toe (same colours indicate same load ratio and residual stress condition).

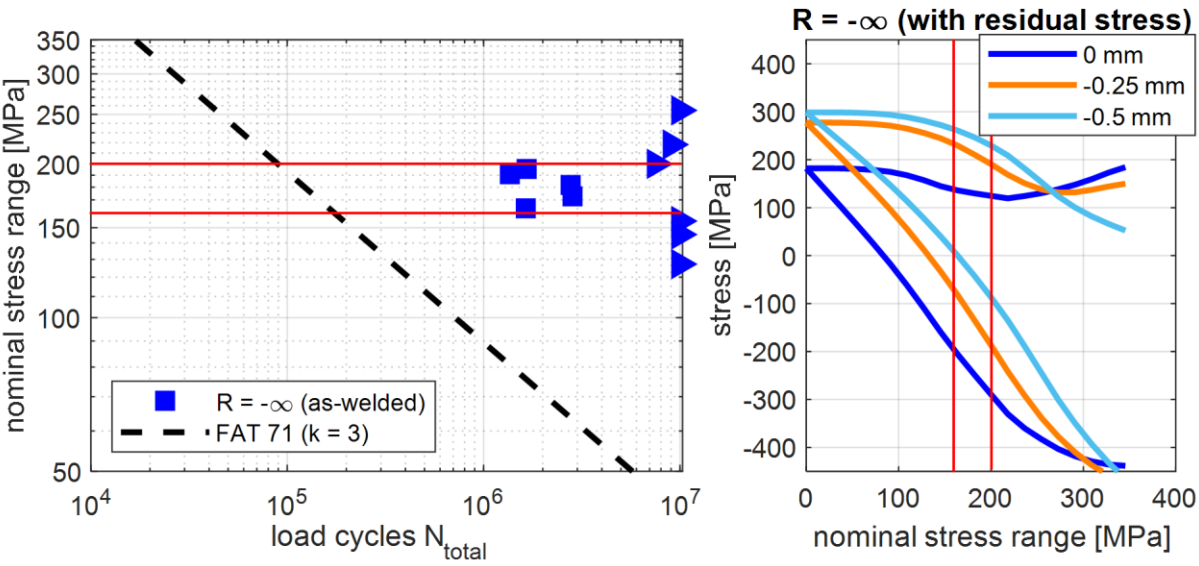

Figure 6-12: S-N diagram and respective simulation results at different depth below the weld toe for compressive loads R = -∞ (as-welded).

For compressive loads (R = -∞) the upper stress corresponds approximately to the residual stresses, as no load is applied to the specimen except for boundary conditions. The decreasing upper stress in Figure 6-12 (right) implies that residual stresses are reduced under compressive loading, which was already shown by residual stress measurements in section 5.4.2. This is also the reason for the constant upper stress and the vertical part of the S-N curve for the as-welded R = -3 specimens (Figure 6-11). A reduction of the residual stresses occurs when the von Mises stress exceeds the yield limit and plastic strains form. Strains measured by DIC before, during and after applying a compressive load are plotted in Figure 6-13. Under load the highest compressive strains occur at the weld toe and to the sides of the stiffener. After unloading, compressive strains persist on the sides of the stiffener. Also at the weld toe strains remain compressive. From the DIC measurements it cannot be determined whether these are plastic strains or elastic strains caused by the surrounding compressive field. Elastic compressive strains would reduce the tensile residual stresses at the weld toe. Plastic compressive strains could cause tensile residual stresses themselves.

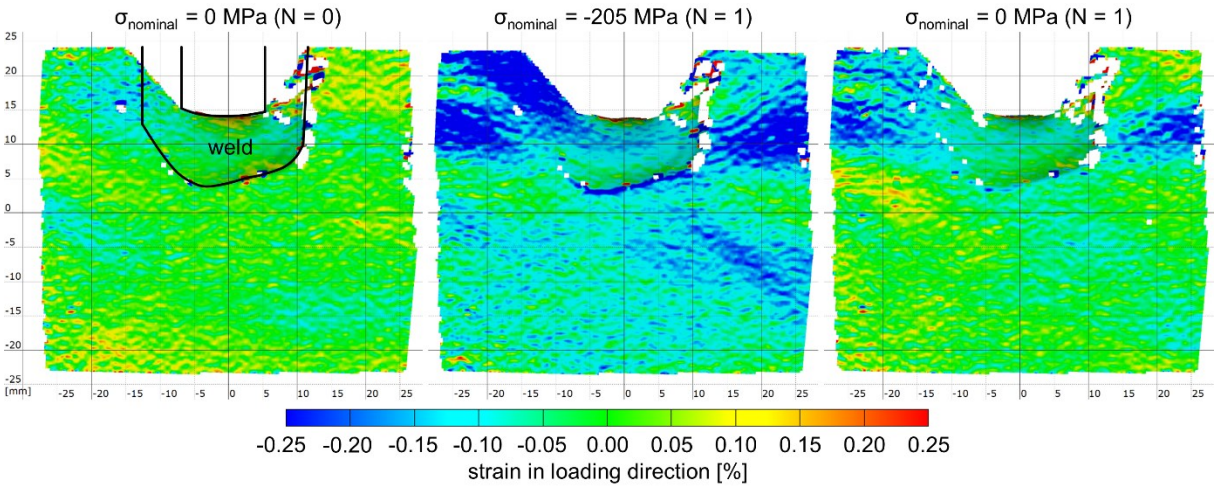

Figure 6-13: Strain measured by DIC at the end of the longitudinal stiffener before, during and after applying a compressive load (Friedrich 2020).

Information on the residual stress reduction is obtained from the simulations (Figure 6-14). Before loading, residual stresses are tensile at the weld and compressive on the sides of the specimen. Under load the highest compressive stresses occur on the edges of the specimen. After loading the compressive residual stresses on the sides of the specimen and the tensile residual stresses at the weld are reduced.

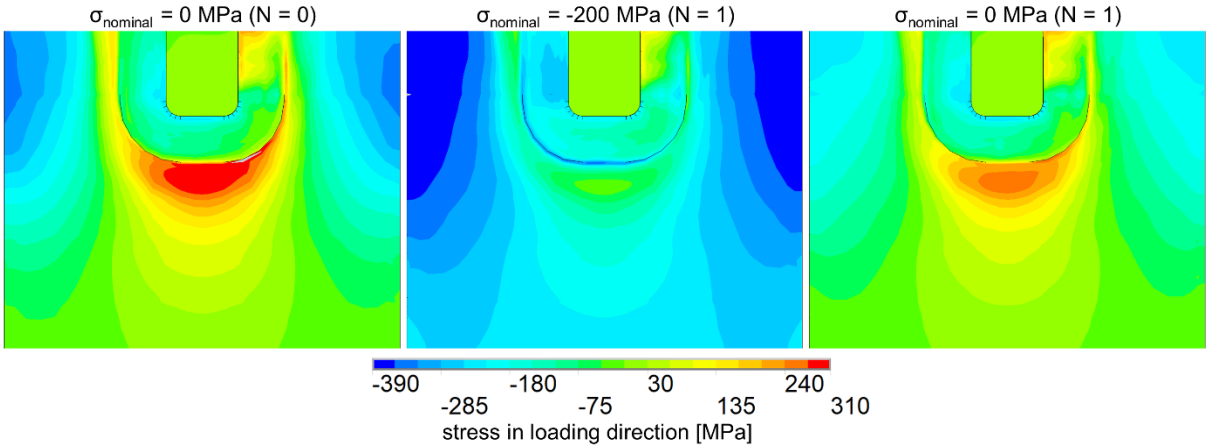

Figure 6-14: Calculated stress (including residual stresses) at the end of the stiffener before, during and after applying a compressive load

The calculated von Mises stress for three different compressive loads is plotted in Figure 6-15. The yield limit is exceeded first on the sides of the stiffener. Only for higher loads it is reached at the weld toe. Looking at the stresses at the weld toe, blue curve in Figure 6-12 (right), the upper stress decreases for nominal stresses of more than 100 MPa. Here, plastic strains start to occur on the sides of the specimen. The curve increases again for loads exceeding 220 MPa, when plastic strains start at the weld toe (Figure 6-15, right).

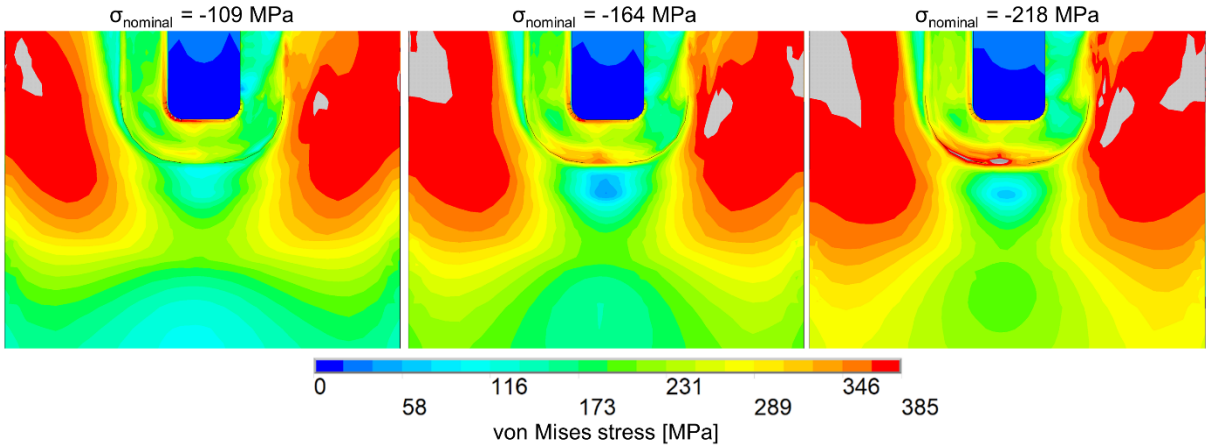

Figure 6-15: Calculated von Mises stress at the end of the stiffener under different compressive loads (grey areas exceed the yield limit of 385 MPa).

These stresses at the weld toe will influence crack initiation. But the residual stress influence is also visible in the S-N diagram for crack propagation (Figure 6-16). For the stress-relieved specimens the influence of the load ratio is clearly visible. In the as-welded condition crack propagation seems to be independent of the applied load ratio, with exception of compressive loads (R = -∞). Crack lengths measured on as-welded specimens tested with load ratios of R = 0, R = -3 and R = -∞ at the same nominal stress range are compared in Figure 6-17. For R = 0 and R = -3 the development of the crack is similar. For compressive loads (R = -∞) the crack length visible on the surface is initially comparable, as long as the crack grows in front of the weld ($N_{propagation}$ < 150 000). As it extends into the girder, crack propagation is slower than for the other two load ratios.

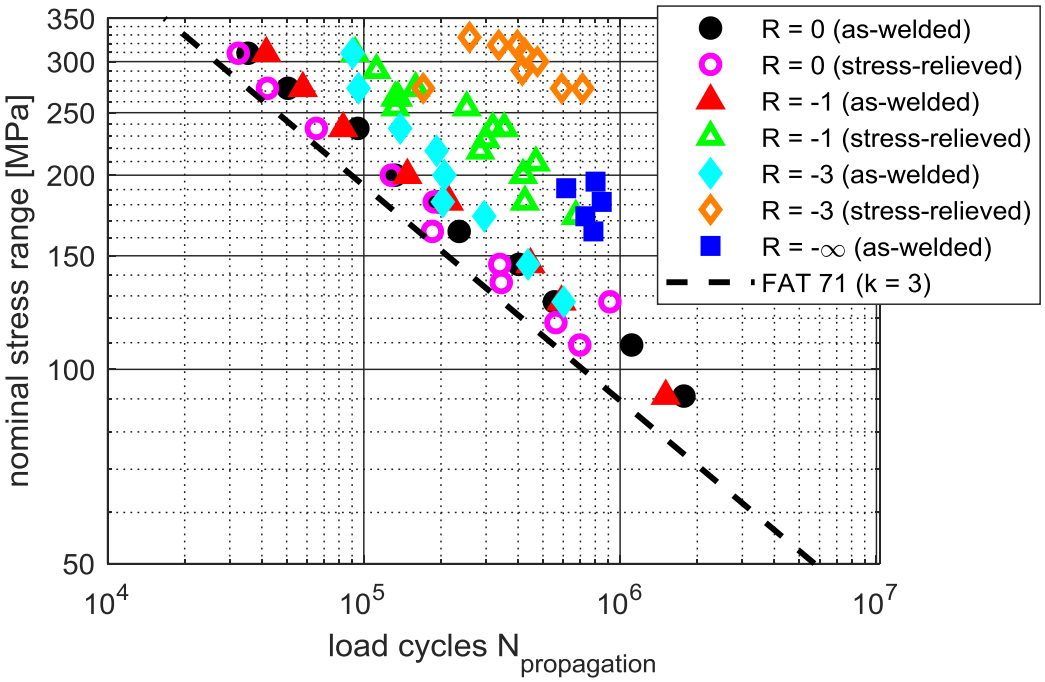

Figure 6-16: S-N diagram for crack propagation for as-welded and stress-relieved longitudinal stiffener specimens.

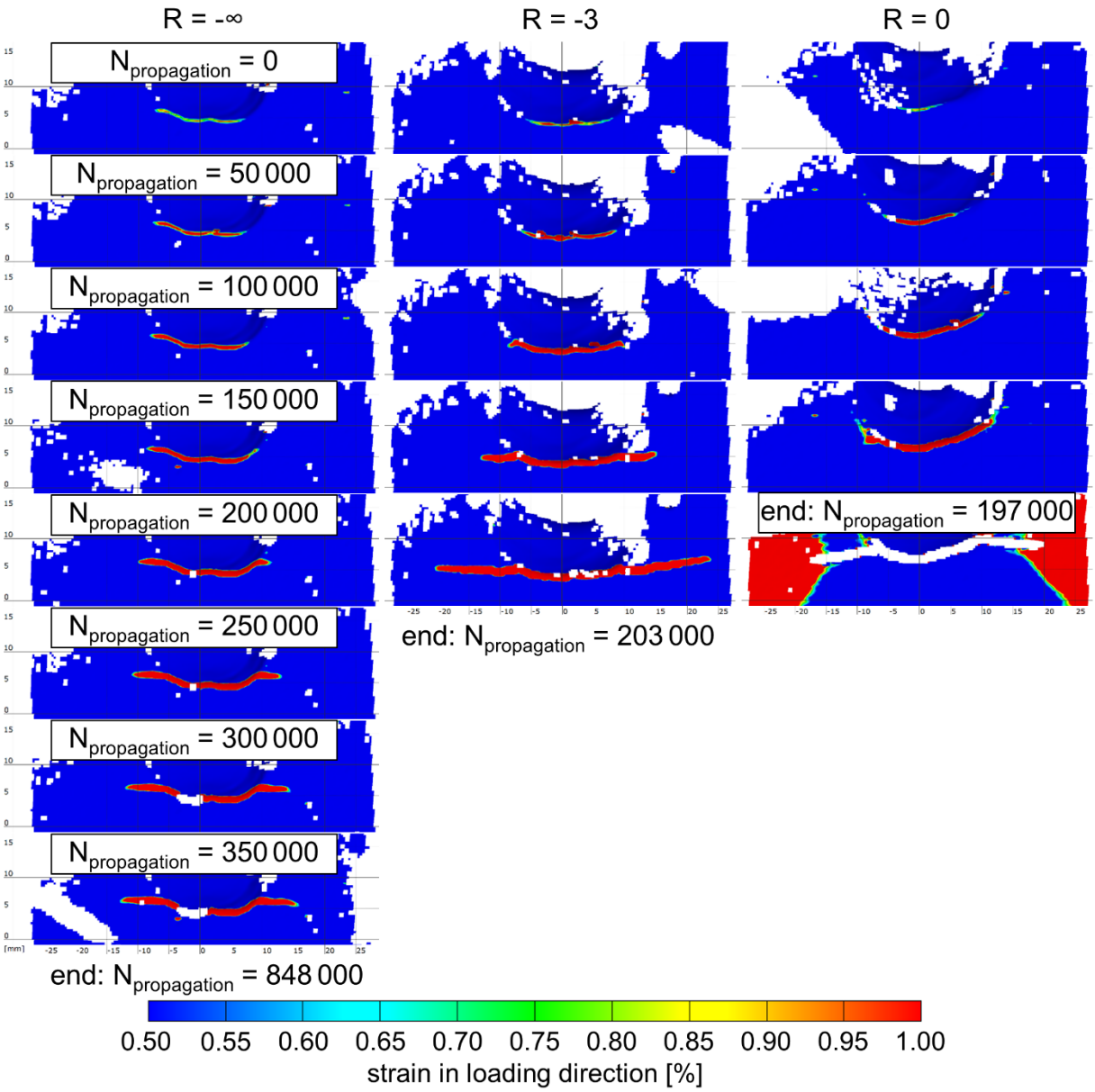

Figure 6-17: Crack propagation determined by DIC on as-welded specimens tested with different load ratios *R* (nominal stress range = 182 MPa) (Friedrich 2020).

This is in line with the simulation results in Figure 6-18. The plots show the stress including welding residual stresses at different depths up to 3 mm below the weld toe. According to the simulations the highest stresses do not occur at the surface but about 1 mm below the weld toe. Up to a load range of 200 MPa, stresses between 1 and 3 mm are tensile independently of the applied load ratio *R*. Thus, a crack should see similar stresses and grow similarly as long as it is in front of the weld. When the crack leaves the weld and grows to the sides into the girder, the crack tip is not located within this field of tensile residual stresses anymore (compare Figure 6-14). Here the crack growth is slowed down in particular for $R = -\infty$ as no tensile load is applied. These considerations do not include residual stress redistribution due to the propagating crack or actual crack tip opening.

Despite the fact that crack growth is accelerated by tensile residual stresses, from the S-N diagram (Figure 6-16) it appears that the fastest crack growth is achieved on stress-relieved specimens with tensile loading ($R = 0$). This S-N curve runs even lower than in the as-welded condition. A reason could be the slightly higher distortions of the stress-relieved specimens.

But, the distortion should affect also crack initiation. From the DIC measurements it appears that the crack development is different for the as-welded and the stress-relieved specimens. Exemplarily the crack development for a nominal stress range of 145 MPa at R = 0 is shown in Figure 6-19. On the as-welded specimen the crack grows quickly to a length of about 18 mm at which it covers the entire front of the weld. Then the crack length increases only slowly and the crack tip stays at the weld toe, before leaving the weld and advancing into the girder ($N_{propagation}$ > 300 000). On the stress-relieved specimen, initially the crack grows slower, but it proceeds steadily from the weld into the girder. In the end the crack propagation phase is shorter than on the as-welded specimen. A similar development of the crack length was observed also on other specimens tested at different stress ranges and a load ratio of R = 0.

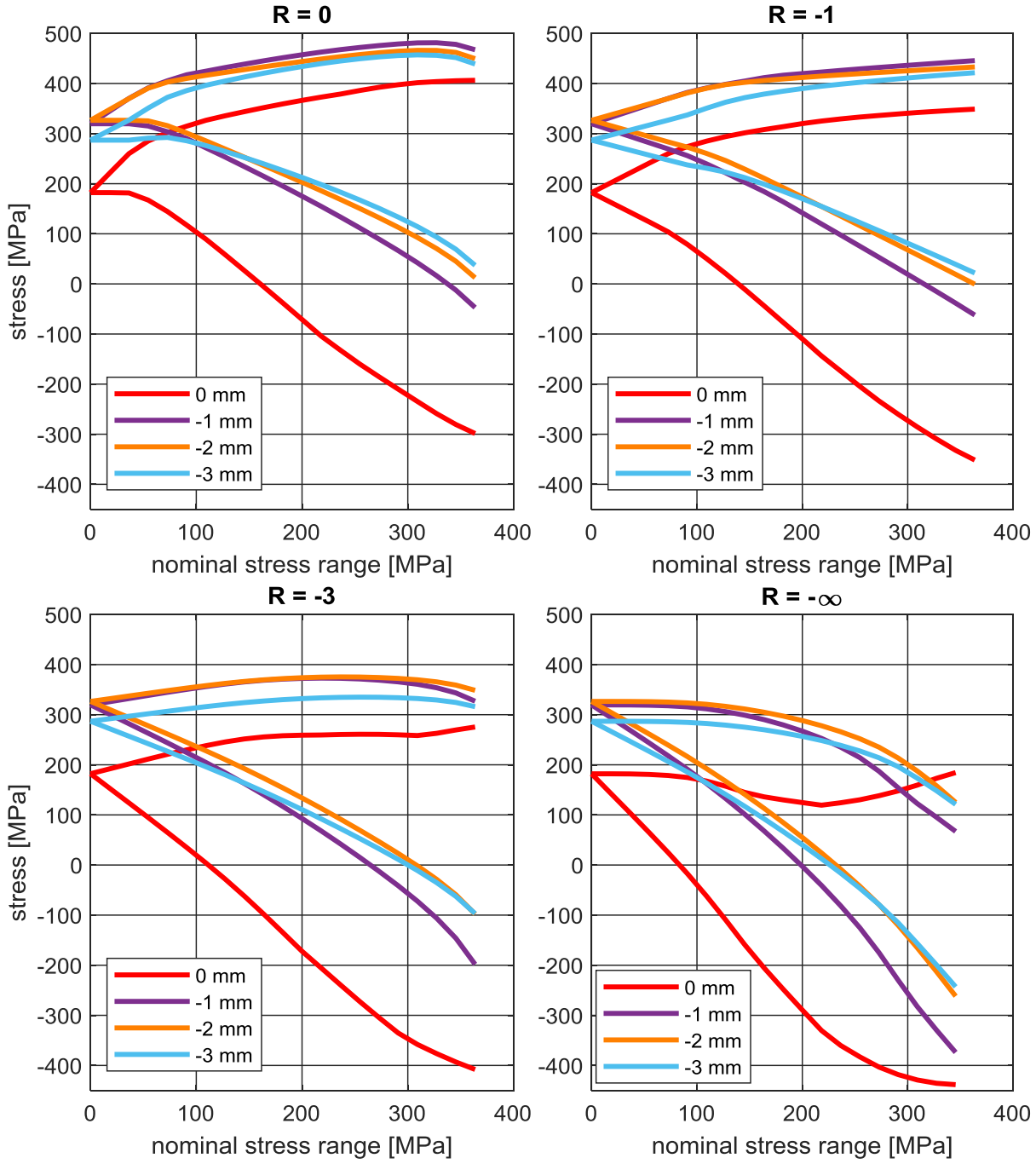

Figure 6-18: Upper and lower stresses at different depths below the weld toe calculated for the longitudinal stiffener model with residual stresses.

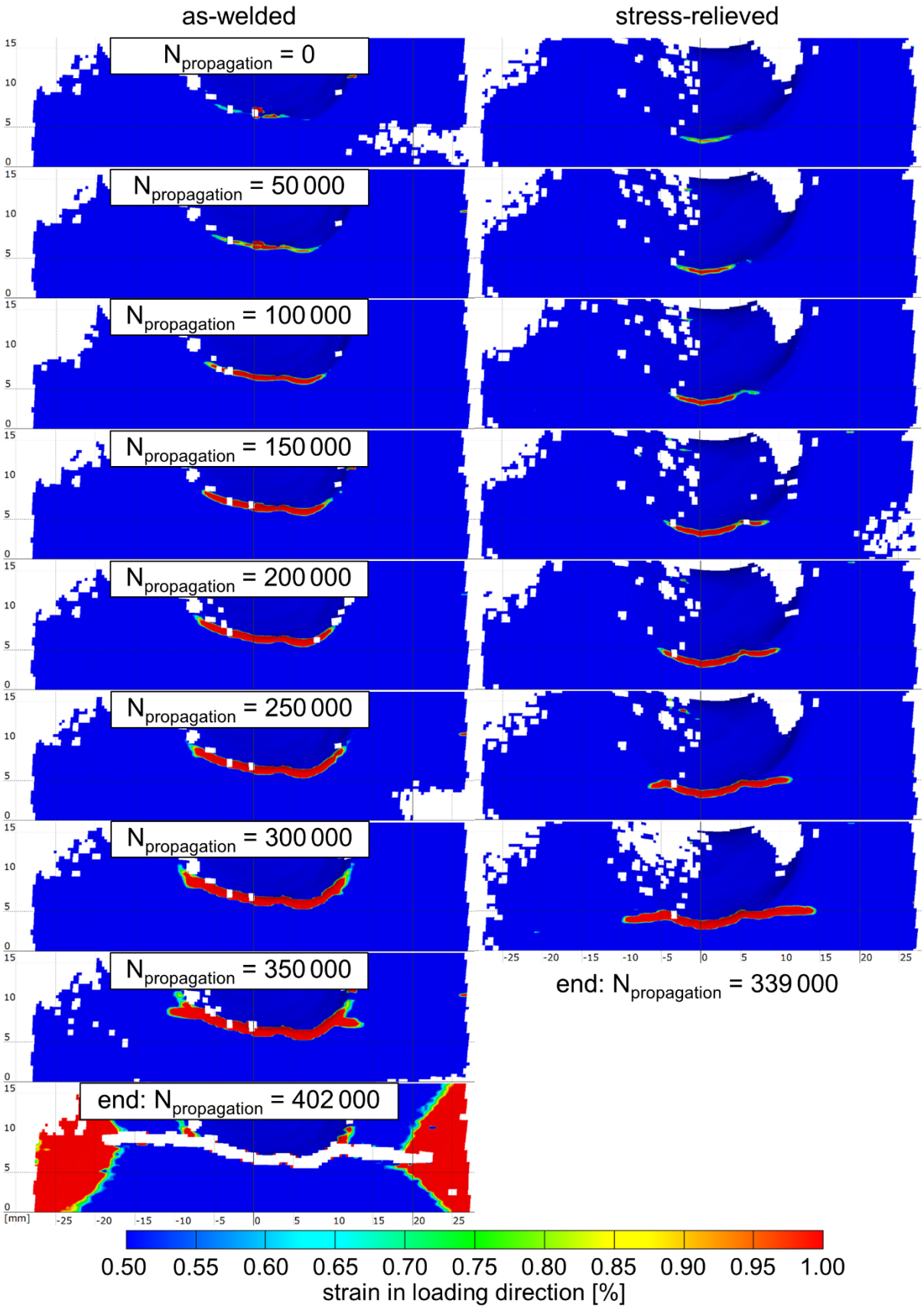

Figure 6-19: Crack propagation determined by DIC on an as-welded and a stress-relieved specimen under tensile loading R = 0 (nominal stress range = 145 MPa) (Friedrich 2020).

The test results presented in chapter 65.2 has been published by the author of this thesis in (Friedrich 2020).

6.3 Equivalent stress ratio

In these tests stress-relieved specimens are loaded with equivalent forces to obtain the same stresses and stress ratios at the weld toe as on the as-welded specimens. The necessary loads have been determined using the numerical simulations as described in section 5.5. The results will allow to compare the influence of welding residual stresses determined on the specimen surface to that of elevated stress ratios. Furthermore, the tests serve to verify if the residual stresses determined by the applied simulation approach are suitable to assess the residual stress influence on fatigue.

6.3.1 K-butt weld

The results of the fatigue tests with equivalent stress ratios are compared to the results from the as-welded specimens in Figure 6-20. The S-N diagram shows the number of load cycles for total fatigue life of the specimens. Overall, the results of the tests with equivalent loads are in good agreement with the as-welded specimens. For alternating loads (R = -1) at high stress ranges the number of load cycles is underestimated using the equivalent loads.

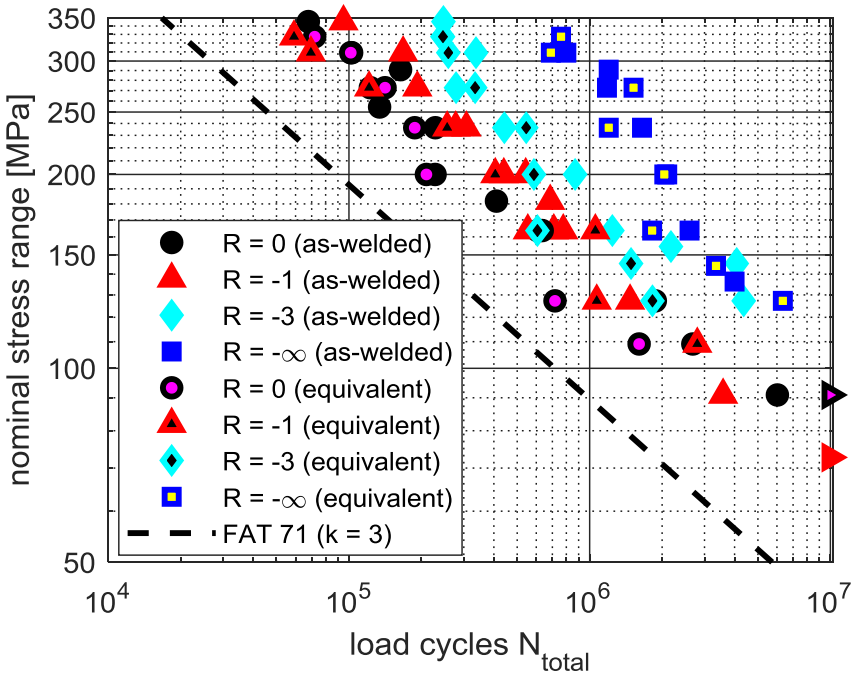

Figure 6-20: S-N diagram for total fatigue life for as-welded specimens and stress-relieved specimens with equivalent loads resulting in the same stresses at the weld toe (► symbol for run-out).

The S-N diagram for the initiation of macroscopic cracks is plotted in Figure 6-21. The results obtained with the equivalent loads are again in agreement with the as-welded specimens. Both test series show the same distribution of the different load ratios. Single tests show larger discrepancies from the as-welded results. This may be caused by the determination of crack initiation which adds more sources of imprecision compared to the results for total fatigue life.

The resulting S-N diagram for crack propagation is plotted in Figure 6-22. The crack propagation phase for the equivalent loads are shorter than on the as-welded specimens, especially for low load ratios (R = -3 and R = -∞) but also for R = -1 at high stress ranges.

Overall, it was possible to reproduce the results of the as-welded specimens using the equivalent loads determined from the numerical simulations. While for crack initiation the

numbers of load cycles agree with the as-welded specimens, crack propagation phase is underestimated using the equivalent loads. This indicates that the tensile residual stresses determined on the surface affect crack initiation, but are higher than those acting during crack propagation. Thus, the stress ratio is not constant over the duration of the fatigue tests. The difference in the crack propagation increases for lower load ratios. Here the shift towards tension from the regular loads to the equivalent loads is particularly high, compare Figure 5-28. In the final result for total fatigue life the error from the underestimated crack propagation phase is however relatively small.

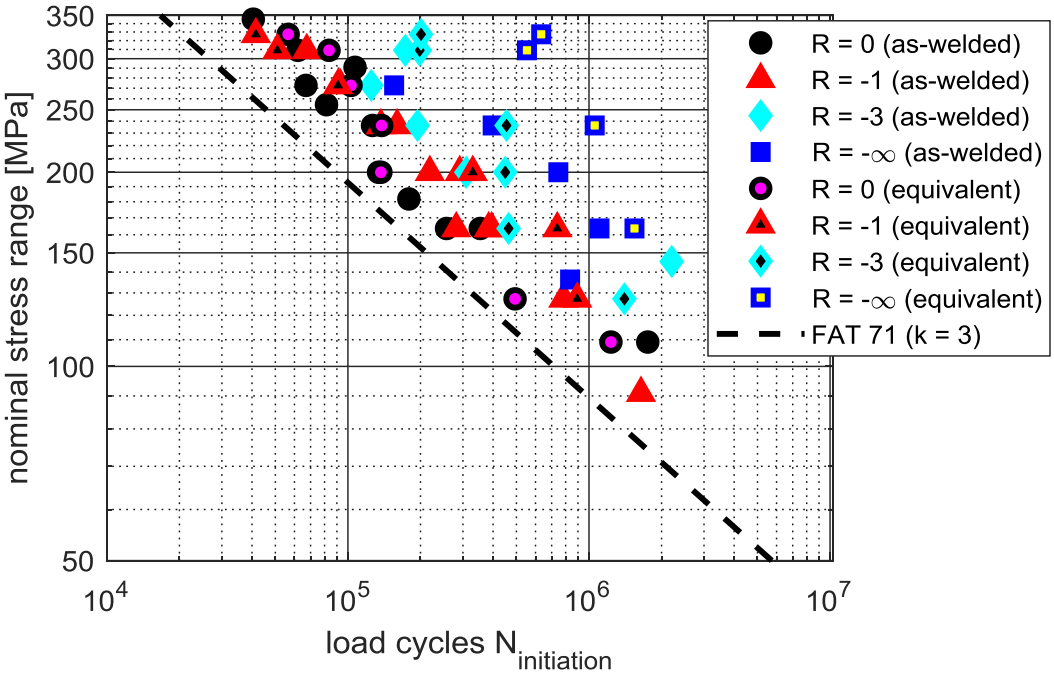

Figure 6-21: S-N diagram for crack initiation for as-welded specimens and stress-relieved specimens with equivalent loads resulting in the same stresses at the weld toe (K-butt weld).

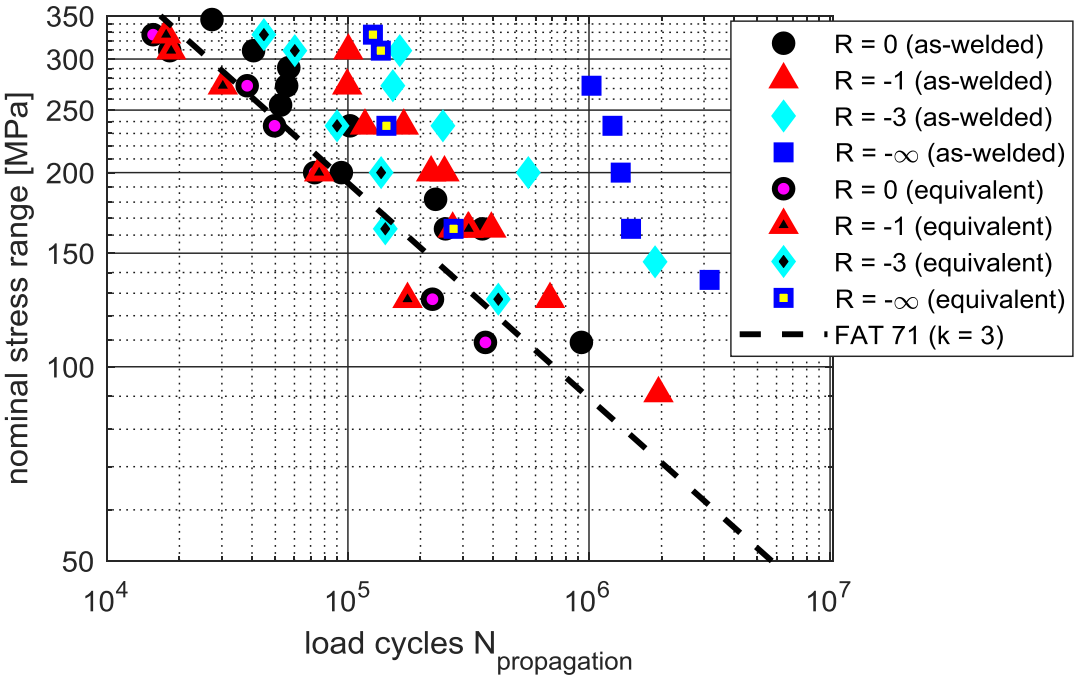

Figure 6-22: S-N diagram for crack propagation for as-welded specimens and stress-relieved specimens with equivalent loads resulting in the same stresses at the weld toe (K-butt weld).

6.3.2 Longitudinal stiffener

The results of the fatigue tests with equivalent loads on stress-relieved longitudinal stiffeners are compared to the as-welded results in Figure 6-23. The resulting numbers of load cycles are in good agreement with the as-welded specimens. For R = -3 the characteristic kink at 200 MPa is reproduced. For compressive loads (R = -∞) the numbers of load cycles do not coincide exactly. However, the results show qualitative agreement as the specimens failed only between 164 and 200 MPa with run-outs below and above these values.

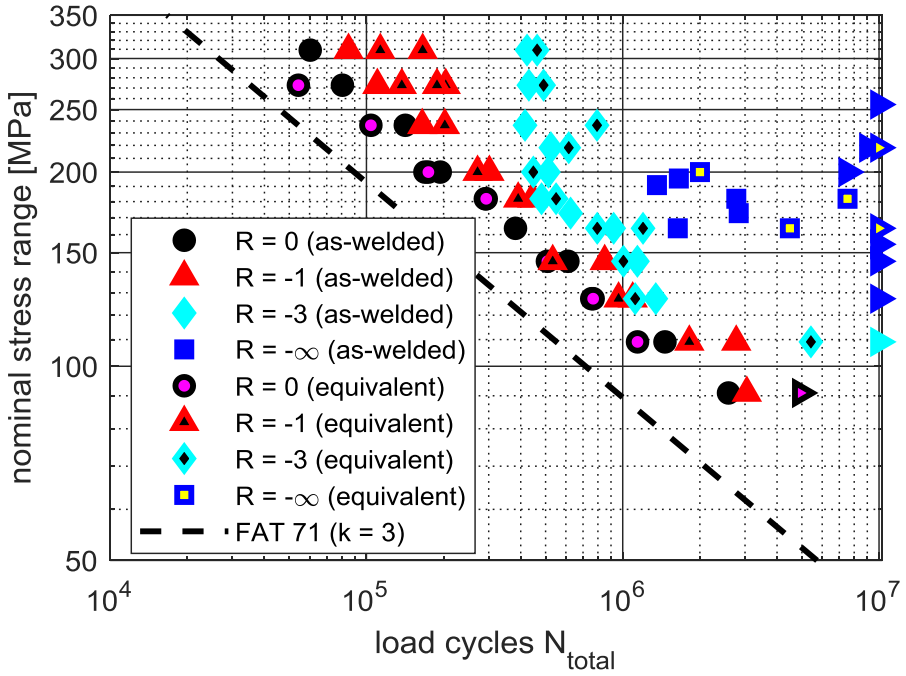

Figure 6-23: S-N diagram for total fatigue life for as-welded specimens and stress-relieved specimens with equivalent loads resulting in the same stresses at the weld toe (► symbol for run-out).

Seven of the stress-relieved specimens used in the equivalent load tests were made of base material from a different charge than the rest of the longitudinal stiffener specimens. For these specimens the material of the K-butt weld specimens was used. The steels were of type S355J2C+N and S355J2+N. Yield strength was 394 MPa for the K-butt weld and 370 MPa for the longitudinal stiffeners. Compared to the other longitudinal stiffeners the distortion of these specimens was smaller, also after stress-relieving. The specimens also showed a more abrupt rupture of the specimen at the end of the tests. These differences might be caused by the less pronounced Lüders plateau, compare Figure 3-11 and Figure 3-14. The specimens were distributed on three different load ratios. No systematic difference in the fatigue test results was observed compared to the other specimens.

The S-N diagram for crack initiation is shown in Figure 6-24. Overall, the results for the equivalent loads agree with the as-welded. For tensile loads (R = 0) the number of load cycles is overestimated slightly. Also for compressive loads (R = -∞) the crack initiation phase is longer than on the as-welded specimens.

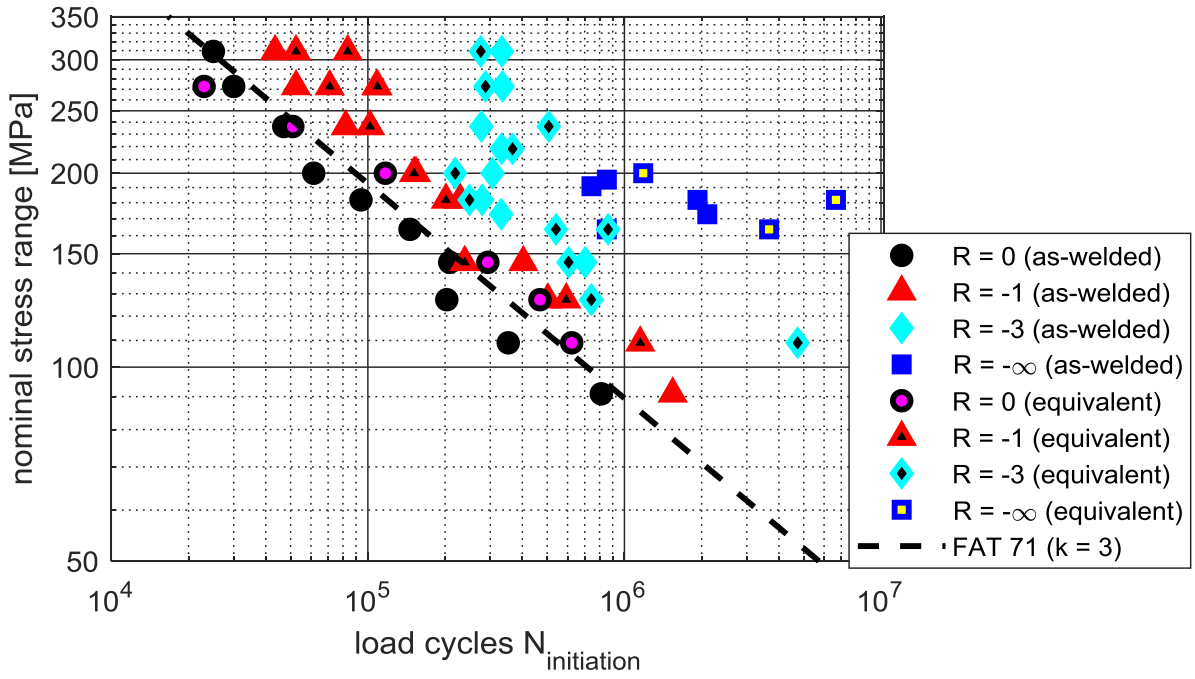

Figure 6-24: S-N diagram for crack initiation for as-welded specimens and stress-relieved specimens with equivalent loads resulting in the same stresses at the weld toe (longitudinal stiffener).

The S-N diagram for crack propagation is plotted in Figure 6-25. The results of the as-welded specimens are reproduced by the equivalent loads. For R = 0 crack propagation periods are slightly underestimated. For R = -∞ the results show a narrow distribution, close to the as-welded results. For R = -3 the equivalent loads produce a vertical branch above 200 MPa as for crack initiation. This is not the case for crack propagation of the as-welded specimens. The equivalent forces are calculated to reproduce the stresses on the surface, at the weld toe. Since for R = -3 the upper stress is constant for load ranges above 200 MPa, also the upper equivalent forces are constant (Figure 5-29). Consequently, with the equivalent loads, crack initiation and propagation result in a constant number of load cycles for load ranges exceeding 200 MPa. On the as-welded specimens the constant upper stress at the surface leads to the vertical distribution of the test results for crack initiation. According to the simulations, some millimetres below the weld toe the tensile portion of the stress range still increases when the applied load range is above 200 MPa (Figure 6-18). Therefore the S-N curve for crack propagation for R = -3 in as-welded conditions results linear.

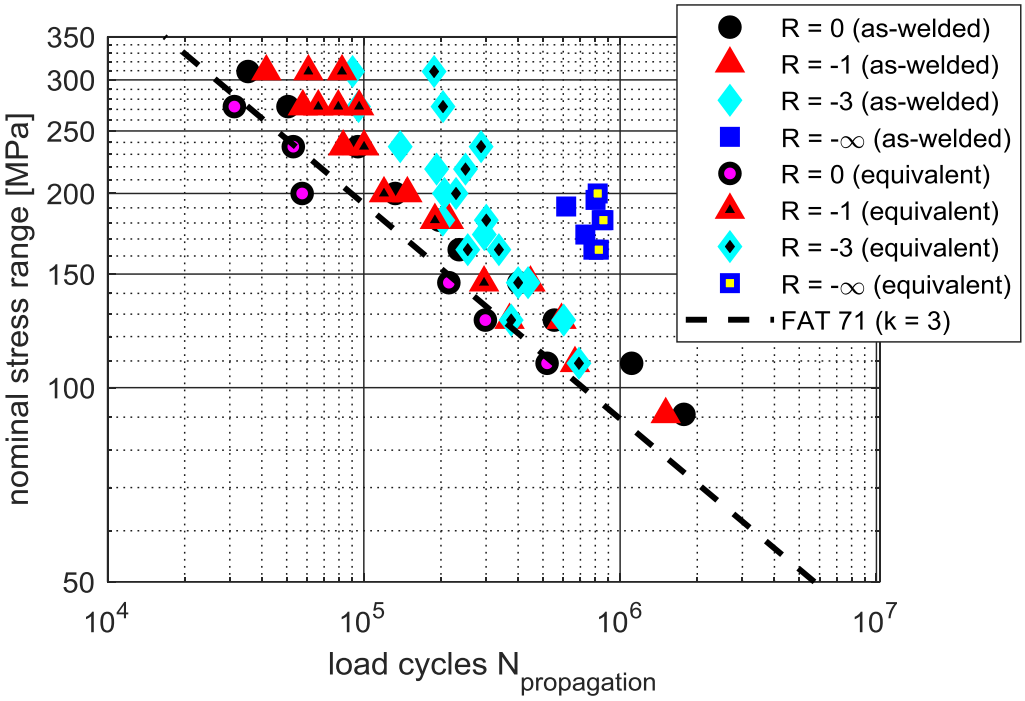

Figure 6-25: S-N diagram for crack propagation for as-welded specimens and stress-relieved specimens with equivalent loads resulting in the same stresses at the weld toe (longitudinal stiffener).

Overall, the results for the equivalent loads and the as-welded specimens are in agreement for crack initiation and crack propagation. This indicates that on the longitudinal stiffeners crack propagation is influenced by residual stresses of a similar magnitude as the residual stresses at the weld toe.

7 Approach to consider welding residual stresses

In chapter 6 a correlation between the stresses at the weld toe obtained from the numerical simulations and the fatigue test results was found. The crossing of the calculated stresses depending on the applied load coincides with the crossing of the S-N curves. The different slopes of the S-N curves could be explained considering the tensile portion of the calculated stress ranges. Furthermore, the calculated stresses were used to determine equivalent loads applied on stress-relieved specimens to reproduce the as-welded fatigue test results.

It was found that the residual stress influence on crack initiation and propagation is different for the K-butt weld and longitudinal stiffener specimens. On the longitudinal stiffeners tensile residual stresses affect crack initiation and propagation. On the K-butt weld the tensile residual stresses determined at the weld toe affect crack initiation but are higher than those influencing crack propagation. Nevertheless, the number of load cycles for total fatigue life could be reproduced for both specimen geometries using the equivalent forces based on the stresses calculated at the weld toe.

The simulation results help to understand and interpret the experimental results. The agreement between simulation and experimental results also confirms the validity of the applied simulation approach. Furthermore, it indicates that the simulation results should be suitable to predict the influence of welding residual stresses and load ratios on fatigue.

On this basis, an approach is developed that uses the results of the welding simulations to predict S-N curves considering the influence of welding residual stresses and the applied load ratio. The approach consists in calculating the welding residual stresses at the weld using numerical welding simulations as described in chapter 2. Then, the stresses at the weld toe, with and without residual stresses, are calculated for different load ranges and ratios, compare section 5.3. The S-N curve for a defined load ratio and residual stress condition (e.g. R = 0, as-welded) is determined in fatigue tests. Using the simulation results the S-N curve is transferred from nominal stress range to the stress range at the weld toe. The stress ratio at the weld toe is considered through a correction factor. For the target load ratio and residual stress condition, for which the S-N curve will be predicted, the stresses at the weld toe are calculated. Based on these stresses and the previously determined S-N curve for stresses at the weld toe the endurable number of load cycles is determined. From these numbers of load cycles the predicted S-N curve for nominal stress is formed.

In the following the single steps of the approach are described exemplarily for the K-butt weld specimens. In the example, the fatigue test results for a load ratio of R = 0 in as-welded conditions are used to predict the S-N curve for R = -3 in stress-relieved conditions.

1. Welding residual stresses are calculated with the simulation approach presented in chapter 2. Alternatively, other validated and suitable simulation approaches could be adopted. A necessary requirement is that after the welding simulation also the loading can be simulated.
2. Loading is simulated to calculate the stresses at the weld toe as described in section 5.3. The loads should reflect the actual loading conditions. In the example of the K-butt weld specimen, axial forces and the boundary conditions as in the testing machine are applied. The different load ratios are simulated with and without residual stresses to determine the upper and lower stresses at the weld toe depending on the applied nominal stress range (Figure 7-1).

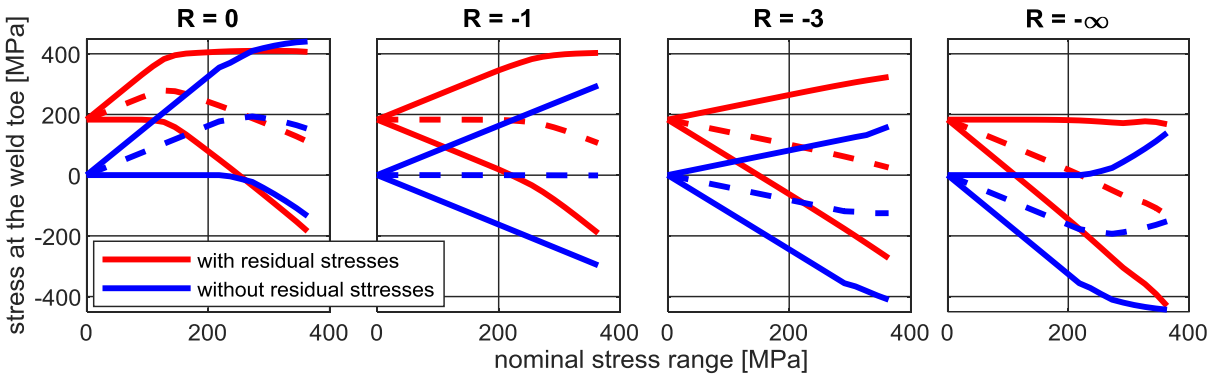

Figure 7-1: Calculated upper, lower and mean (dashed) stresses at the weld toe for different load ratios *R* (K-butt weld).

3. The S-N curve for a defined load ratio and residual stress condition, here *R* = 0 and as-welded, is determined (Figure 7-2).

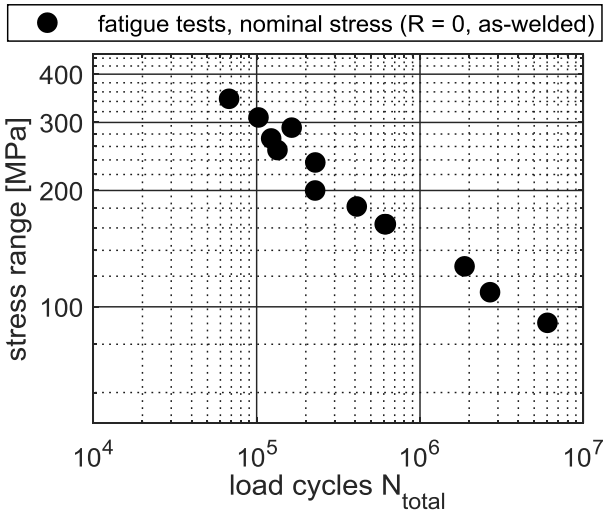

Figure 7-2: Fatigue test results for K-butt weld specimens.

4. Using the simulation results, the nominal stress range is transformed to the stress range at the weld toe including a factor to consider the stress ratio at the weld toe R_{toe} (Figure 7-3). For each nominal stress range applied in the fatigue tests the upper and lower stress at the weld toe is read out from the simulation results. The stress ratio R_{toe} is determined and used to determine the following correction factor:

$$\begin{aligned} f(R_{toe}) &= -0.8 \cdot R_{toe} + 0.8 && \text{for } R_{toe} < -1 \\ f(R_{toe}) &= -0.4 \cdot R_{toe} + 1.2 && \text{for } -1 \le R_{toe} \le 0.5 \\ f(R_{toe}) &= 1 && \text{for } R_{toe} > 0.5 \end{aligned} \tag{7.1}$$

For R_{toe} > -1 the factor corresponds to the enhancement factor for stress ratio in the case of “low residual stresses” according to the IIW recommendations (Hobbacher 2016), where it is used to adapt the design S-N curves valid for *R* = 0,5 to other stress ratios. Here, the correction factor according to equation (7.1) is used to weight the stress range at the weld toe so that for decreasing stress ratios the stress range is considered only partially effective. Therefore, the stress range is divided by the correction factor:

$$\Delta\sigma_{effective} = \frac{\Delta\sigma_{toe}}{f(R_{toe})} \tag{7.2}$$

For R_{toe} < -1 the slope of the function defining the factor is doubled. In this way it is taken into account that the compressive portion of the stress range contributes less to the fatigue damage. The effective stress ranges, including the correction factor, are plotted in the S-N diagram at the number of load cycles of the corresponding nominal stress range (Figure 7-3, left). The values are approximated by linear regression in the double logarithmic S-N diagram.

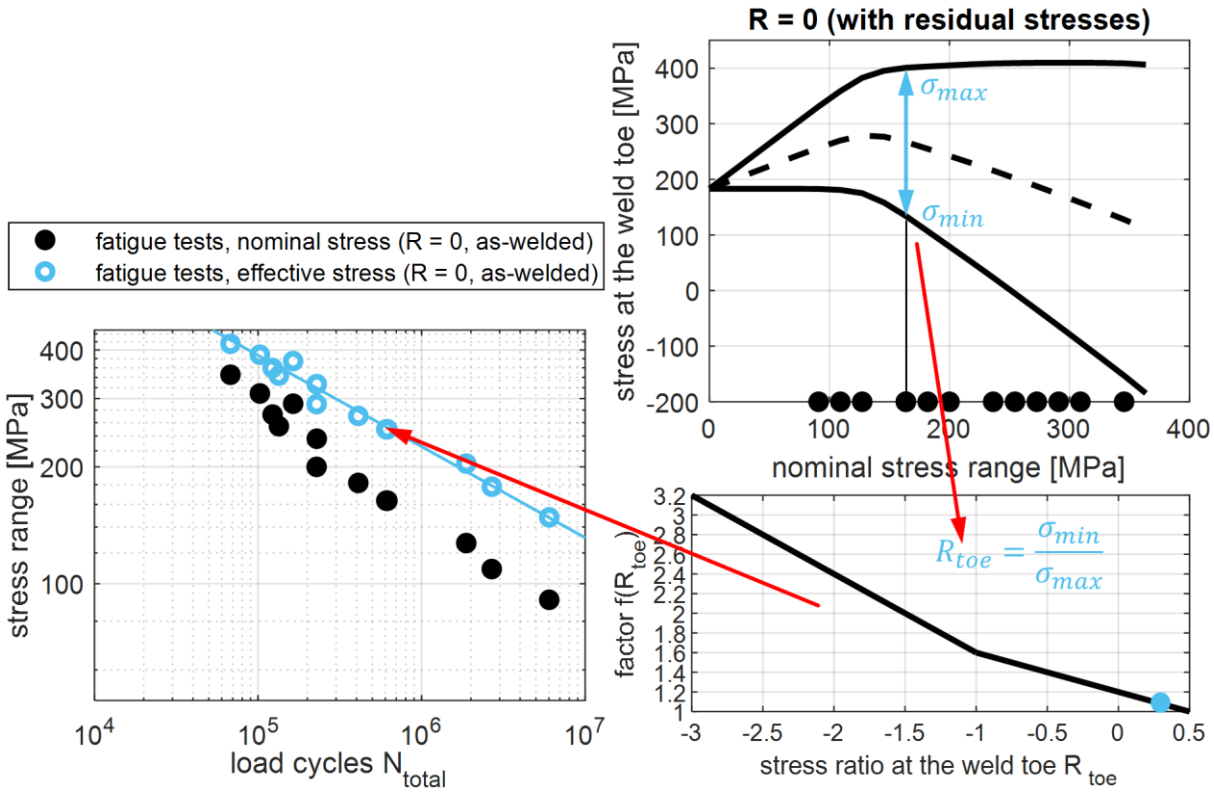

Figure 7-3: Fatigue test results transferred from nominal stress to effective stress considering the stress ratio at the weld toe through the correction factor defined in equation (7.1).

5. From the simulation results for the target S-N curve, here R = -3 and stress-relieved, the stresses at the weld toe are determined for a number of supporting points (Figure 7-4). The stress ranges are corrected by the factor according to equation (7.1) and allocated on the linear regression curve in the S-N diagram. The supporting points are chosen at the same loads that were used for the simulations, with an increment of the nominal stress range of 18 MPa corresponding to an increment of the applied force range of 10 kN.

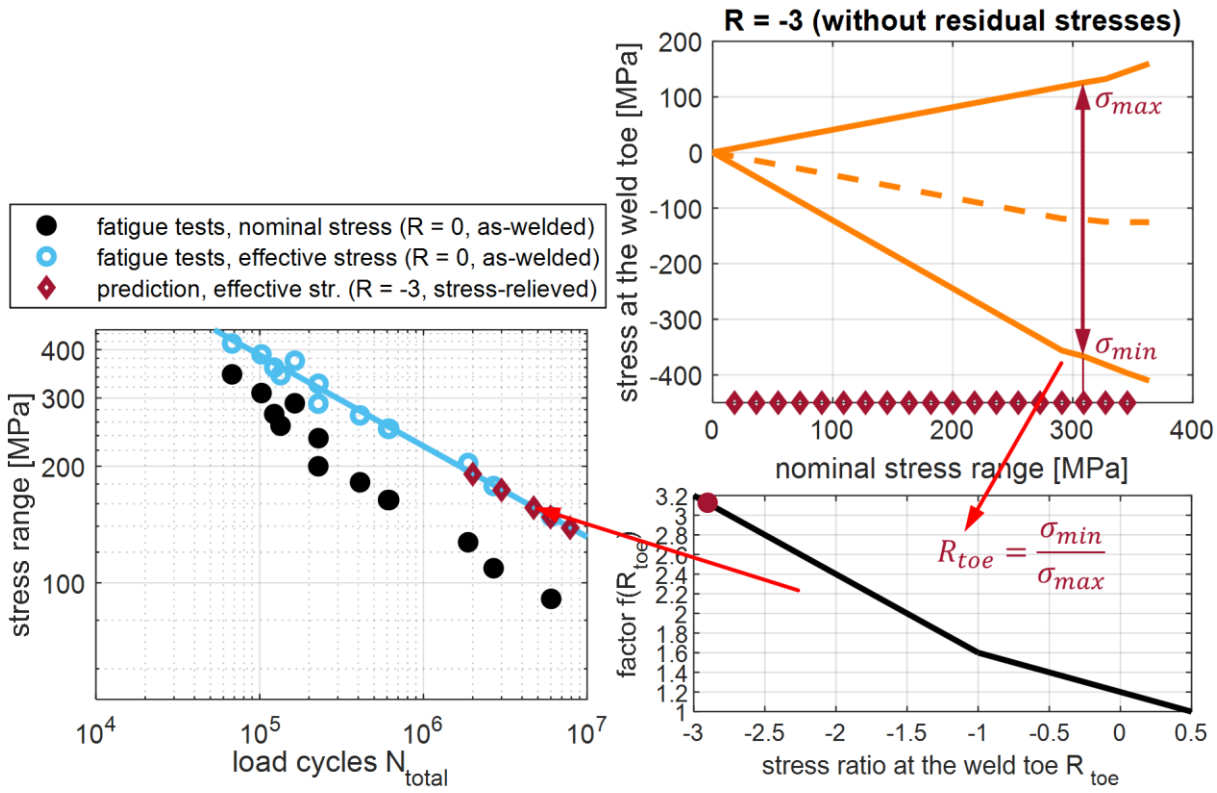

Figure 7-4: For a set of supporting points the effective stress range is determined considering the stress ratio at the weld toe through the correction factor defined in equation (7.1) and it is allocated on the previously defined linear regression curve in the S-N diagram.

6. The points in the S-N diagram are transformed from effective stress range to nominal stress range (Figure 7-5). The nominal stress range is that of the supporting points in Figure 7-4 and thus known. The resulting points form the target S-N curve and can again be approximated by a linear regression.

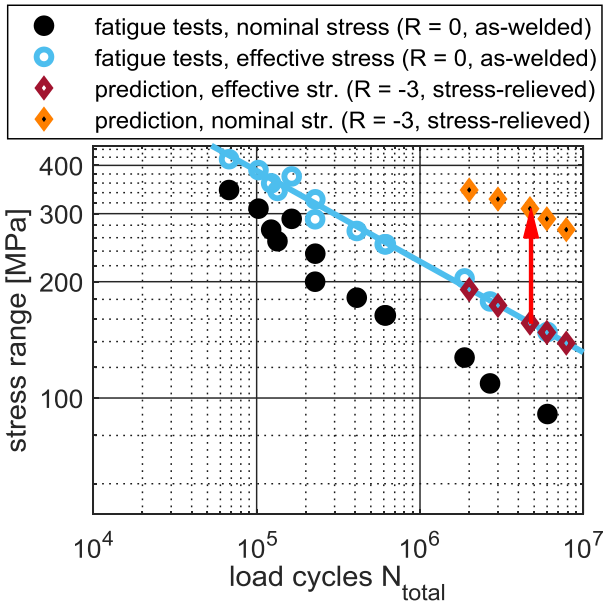

Figure 7-5: The target S-N curve (*R* = -3, stress-relieved) is transformed from effective to nominal stress range, which is known for the supporting points in Figure 7-4.

7. Steps 5 and 6 are repeated for other load ratios and residual stress conditions to predict the S-N curves.

The approach is summarized in Figure 7-6.

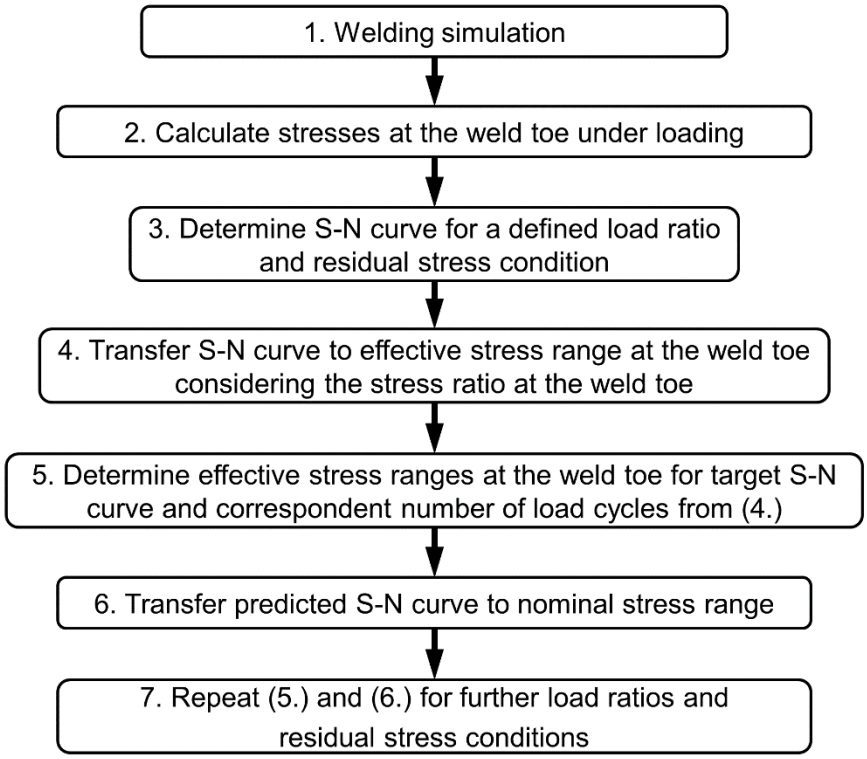

Figure 7-6: Approach to predict S-N curves for different load ratios and residual stress conditions.

7.1 K-butt weld

The resulting S-N curves for the K-butt weld are plotted in Figure 7-7. All predicted results are based on the S-N curve for tensile loads (R = 0) in as-welded conditions. On the as-welded specimens the load ratio has only little influence on the resulting S-N curves. Nevertheless, the differences in the test results are recognizable also in the predicted curves. For R = 0 the prediction is in good agreement with the test results. This was expectable since these tests are the base for all predicted curves. For R = -1 the prediction lies between the results for R = 0 and R = -3, as in the test results, but the prediction does not present the relatively steep slope of the R = -1 tests. For R = -3 the prediction matches the test results, except for high stress ranges. For R = -∞ the prediction reflects the relatively steep slope and lies close to the test results. At 220 MPa the predicted curve bends upwards. Here the calculated stress ratio at the weld toe becomes lower than R_{toe} = -1 and the slope used to calculate the correction factor according to equation (7.1) increases.

In the stress-relieved condition the influence of the load ratio is more distinct and this is represented also in the predicted curves. For R = 0 the prediction agrees with the tests. For low stress ranges the results lie slightly above the as-welded condition, which is in agreement with the test results. For R = -1 and R = -3 the prediction matches the test results, although the slope is too steep.

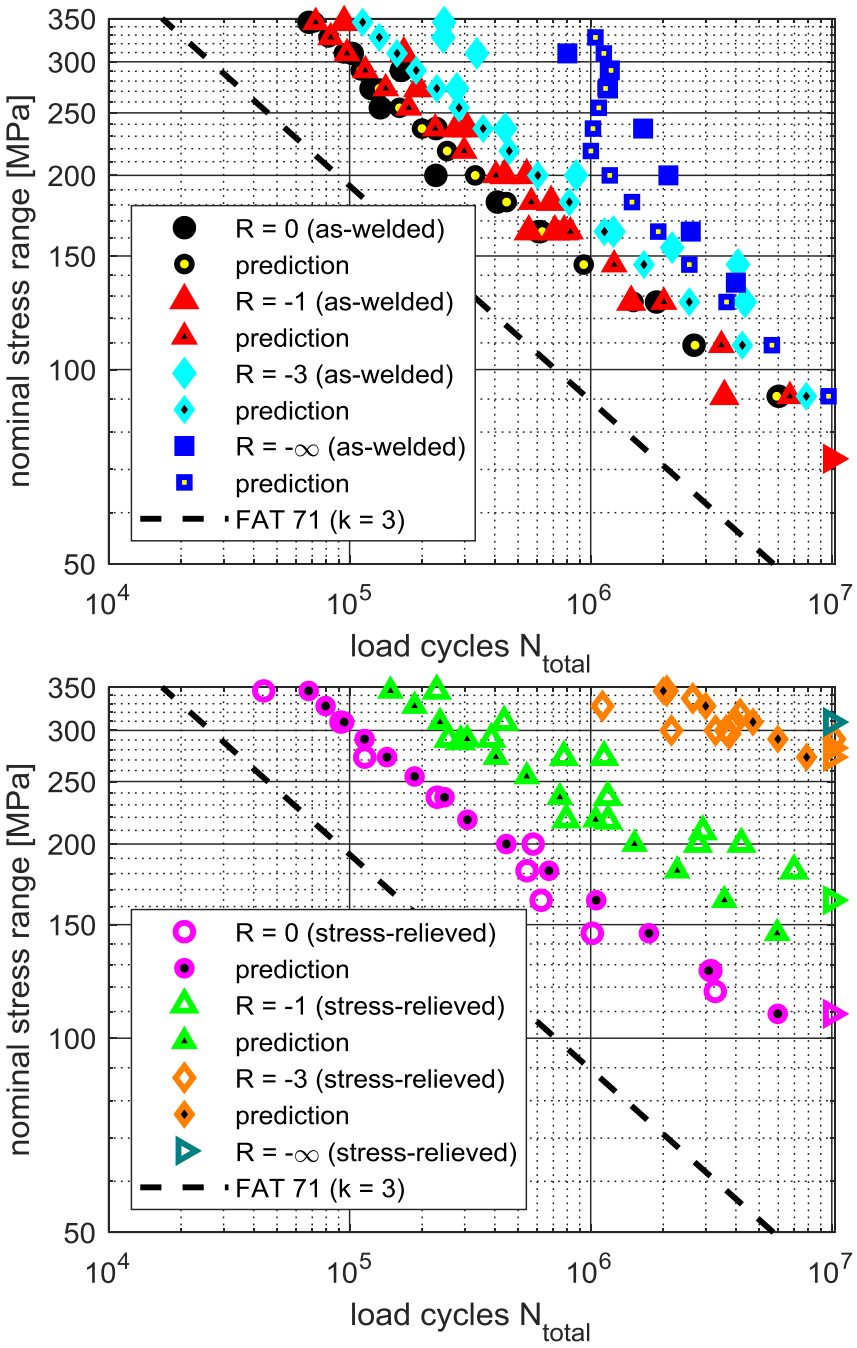

Figure 7-7: Fatigue test results and prediction based on R = 0 (as-welded) for as-welded (top) and stress-relieved (bottom) K-butt weld specimens (► symbol for run-out).

7.2 Longitudinal stiffener

The S-N curves for the longitudinal stiffener are predicted in the same way. Starting from the (longitudinal stiffener) fatigue test results for R = 0 in as-welded conditions and using the simulation results for the different load ratios (Figure 5-22). The resulting S-N curves are compared to the fatigue test results in Figure 7-8. For the as-welded condition with load ratios of R = 0 and R = -1 the predictions are in good agreement with the test results, with the values for R = -1 slightly above R = 0. For R = -3 the transition into the vertical part of the S-N curve is predicted at a higher stress range than in the fatigue tests. For R = -∞ the agreement is qualitative. The predicted curve shows a distinctive Z-shape. A local minimum in the number of load cycles is predicted for a stress range of 140 MPa. Although the prediction does not coincide exactly with the test results, the shape of the curve matches the

observation that the specimens failed only between 160 and 195 MPa and ran out below and above these values.

For the stress-relieved specimens, predictions and test results show a higher influence of the applied load ratio. For R = 0 the prediction matches the test results: for high stress ranges the values correspond to the as-welded condition, while for low stress ranges the stress-relieved results lie slightly more to the right. For R = -1 and R = -3 the predictions are close to the test results at high stress ranges. The slope is slightly steeper and for lower stress ranges the endurable number of load cycles is underestimated. For R = -∞ the prediction shows failures for loads above 250 MPa. These would be caused by tensile residual stresses resulting from compressive loads exceeding the yield limit (compare Figure 5-22). Only one specimen was tested, at 309 MPa, resulting in a run-out.

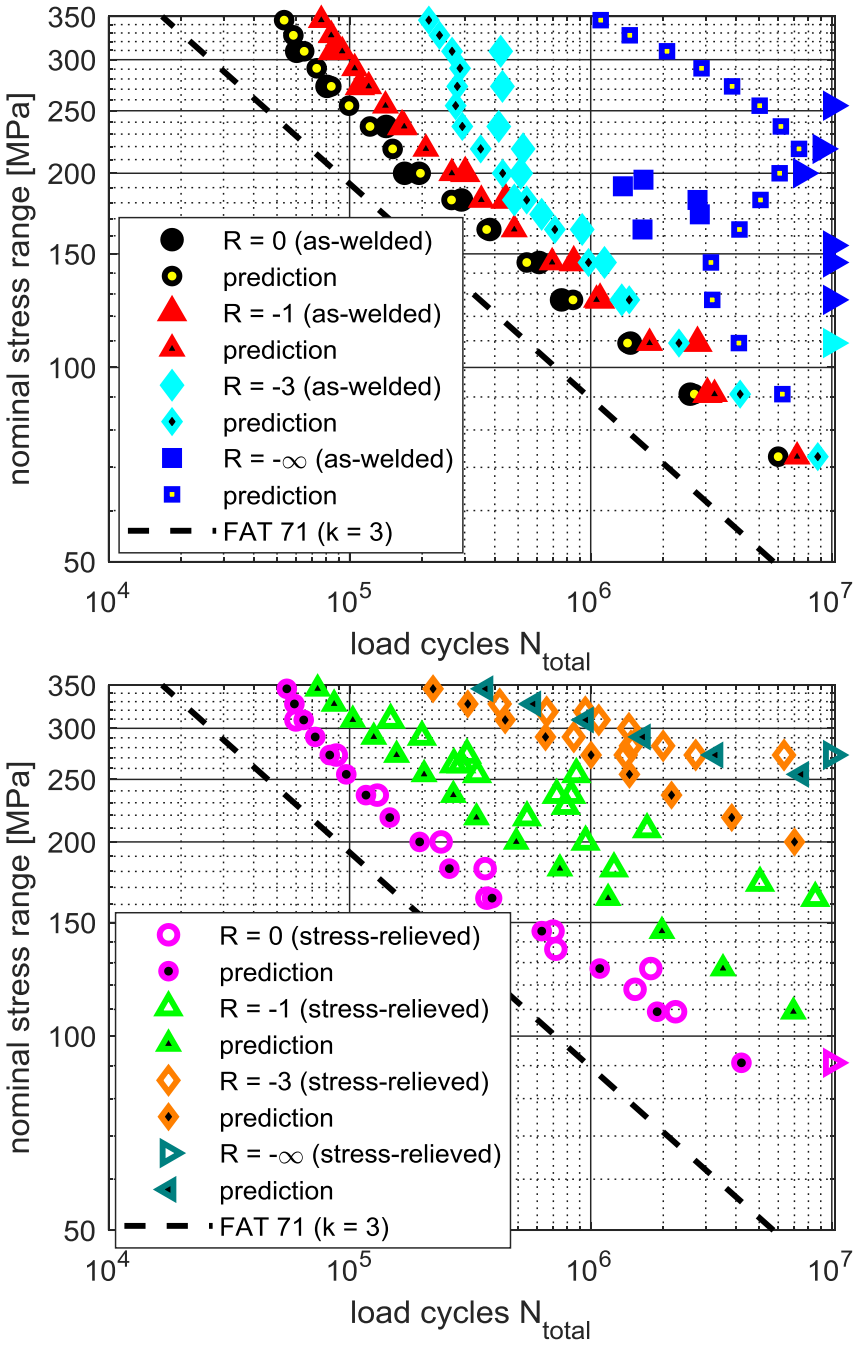

Figure 7-8: Fatigue test results and prediction based on R = 0 (as-welded) for as-welded (top) and stress-relieved longitudinal stiffener specimens (► symbol for run-out).

8 Discussion

The influence of welding residual stresses on fatigue was investigated using numerical simulations and experimental tests to develop an approach to predict the influence of welding residual stresses on fatigue.

A numerical welding simulation approach using a prescribed temperature heat source was described and the influence of various simulation parameters on the resulting residual stresses was assessed. The simulations were used to design small-scale specimens containing a multilayer K-butt weld with tensile transversal residual stresses at the weld toe. Residual stresses were measured using X-ray diffraction and hole drilling on this specimen geometry and on longitudinal stiffener specimens. Fatigue tests were conducted in which, besides the total fatigue life, the initiation of macroscopic cracks and the following crack propagation were detected using DIC. Including the loads from the tests in the numerical simulations a correlation between the fatigue test results and the calculated stresses was found. Based on these findings an approach to consider the influence of welding residual stresses in fatigue analysis was developed.

The numerical welding simulations were used to calculate residual stresses after welding. They form the base of the proposed approach to include welding residual stresses in fatigue assessments. For this reason the simulations should work without experimental calibration and a simple prescribed temperature heat source was chosen. The simulated temperature distributions in the weld will therefore not be realistic. The parameter study showed that the resulting residual stresses are influenced only little by the selected simulation parameters. Simulations with a double ellipsoid Goldak heat source, calibrated with temperature measurements and macrographs, did not yield much different or more accurate results for the investigated geometries (results included in appendix 12.2). The experimental investigations showed that the results obtained with the simplified simulation are suitable for fatigue assessments. However, residual stresses within the plate or weld have not been verified. Furthermore this thesis focused on arc welding (MAG) of mild steel (S355) and the simulation procedure should not be applied for other welding processes or materials with significantly different properties without further validation.

On the longitudinal stiffener model an unrealistic peak on the first element in front of the weld occurred in the calculated residual stresses. A variation of the element size in front and inside the weld, different heat sources or radii at the weld toe did not eliminate this error. Results close to the weld are influenced by the temperature distribution around the heat source, phase transformation and element activation after being reached by the heat source. Furthermore, the sharp notch at the weld toe represents a singularity in the FE model which will lead to unrealistic results. Stresses directly at the weld toe should therefore be assessed with caution. X-ray diffraction measurements at the longitudinal stiffener indicated that transversal residual stresses decrease towards the weld toe. Despite the peak at the first node, this can also be observed in the simulation results. However, the values calculated at the weld toe are in the same magnitude as the maximum in front of the weld and could thus be interpreted as a conservative approximation. Alternatively, stresses could be determined at a node in front or below the weld toe. But considering the steep gradients the result would be arbitrary and not necessarily more correct. The error due to the singularity at the weld toe is relativized since all simulations, with and without residual stresses, are performed on the same geometry and mesh. In the final approach the stresses at the weld toe are not used as absolute values but as comparative values for the different load cases. Although this

pragmatic procedure was suitable for the investigated specimens and FE models, further verifications are necessary to ensure the general validity of the approach and transferability to other geometries.

It was shown that the general assumption that small-scale specimens do not contain substantial residual stresses is too simplified. They may contain relatively high tensile residual stresses also without any external constraint. However, for transversal welds (e.g. cruciform joint, butt weld) the maximum may be located in front of the weld and not have a noticeable effect on fatigue. By modifying the weld pass sequence, transversal residual stresses at the weld toe can significantly be increased. In the presented investigations this was used to produce test specimens which presented a clear residual stress influence on fatigue. On the other hand, it shows that in practice the weld pass sequence can have a significant and possibly undesired influence on residual stresses and strength properties.

In the fatigue tests DIC was used to detect macroscopic crack initiation and monitor crack propagation. Over visual inspection this procedure offers the advantage that the measurements are automated and the data is saved for post processing. Compared to other methods that measure a certain physical quantity from which crack initiation is derived, e.g. strain gauges, it offers the advantage that the crack is visualised. In this way the location and number of cracks can be determined and their development over time can be tracked. Crack initiation was defined relatively coarse at a length of 2 mm. This length could reliably be determined. The detected length depends on the threshold value of strain above which a crack is assumed. A value of 1% was used which was in agreement with the beach marks. On some specimens elevated strains were observed before exceeding the threshold value. A lower value, e.g. 0.5%, would lead to an earlier crack detection. Though, the overall result would not change significantly.

The correlation between the calculated stresses and the fatigue test results, i.e. the crossing points of the stresses at the weld toe and of the S-N curves, indicates the validity of the numerical results. The agreement was not exact for every case, but considering the scatter in the measured residual stresses and in the fatigue tests, the agreement was remarkable. This allowed to use the simulations to analyse and understand the test results in a way that would not have been possible only by measurements.

In the fatigue tests the residual stress influence resulted different for both investigated geometries. On the K-butt weld specimens residual stresses affected mainly crack initiation. However, also crack propagation showed differences. The as-welded specimens usually showed a single crack while on the stress-relieved specimens multiple cracks formed. The duration of the crack propagation phase resulted similar in the end. On the longitudinal stiffener specimens residual stresses influenced the duration of both crack initiation and propagation. Haigh diagrams for crack initiation, propagation and total fatigue life, showing the mean stress sensitivity and thus the residual stress influence for both weld geometries, are included in appendix 12.3.

In the tests with equivalent stress ratios the as-welded results were reproduced based on the stresses from the numerical simulations. This confirmed the validity of the applied simulation approach. Furthermore, the tests confirmed the findings on the different residual stress influence on crack initiation and propagation for both specimen geometries. The tests also showed the different influence of welding residual stresses compared to elevated mean stresses. On the K-butt weld specimens, where residual stresses affected mainly the crack

initiation, applying the high tensile stresses from the weld toe resulted in a shorter crack propagation phase compared to the as-welded tests. On the longitudinal stiffeners, crack initiation and propagation were in agreement with the as-welded results since tensile residual stresses affected both phases. However, the results for total fatigue life were in good agreement with the as-welded tests for both specimen geometries.

In the developed approach to include welding residual stresses in fatigue analysis, the stress ratio at the weld toe is taken into account by a correction factor. For $R_{toe} > -1$ the factor is based on the IIW recommendations. For lower stress ratios the curve describing the factor is continued with a different slope (Figure 7-4). Thus, the curve has a kink at $R_{toe} = -1$ which implicates that stress ratios below this value are less damaging. Theoretically, such nonlinear behaviour could be expected at $R_{toe} = 0$, where the stress range changes from fully tensile to partly compressive. The slope and the stress ratio, where the correction factor changes, were determined iteratively to achieve the best agreement between the predicted and the experimental S-N curves. The change of slope causes a nonlinear shape of the predicted S-N curves. This is necessary to predict the vertical branch of the $R = -3$ (as-welded) longitudinal stiffener results. For these specimens the stress ratio at the weld toe reaches a value of $R_{toe} = -1$ at a nominal stress range of approximately 250 MPa (Figure 5-22). For higher load ranges, the von Mises stress reaches the yield limit and plastification occurs at the weld toe. As mentioned above, the stresses calculated at the notch of the weld toe do not represent correct absolute values. Nevertheless, the observed plastifications could explain the nonlinear behaviour when the loads reach these values. However, for most of the investigated combinations of residual stresses and load ratios, the stress ratio at the weld toe does not cross the value of $R_{toe} = -1$. In the majority of cases stress ratios lie above or below this value for all applied nominal stress ranges (compare Figure 5-21 and Figure 5-22). A similar factor was proposed by Hensel et al. (2017) in an approach based on effective mean stresses determined by the nominal mean stress and estimated stabilised residual stresses.

The developed approach allows to predict S-N curves for different load ratios and residual stress conditions based on numerical simulations and the S-N curve for a defined load ratio. If no experimental data for the specific geometry is available also a design S-N curve, e.g. FAT class according to IIW, could be used instead. Since these curves are established for high probabilities of survival also the predicted curves should be conservative.

9 Conclusions

Numerical welding simulations were successfully applied to investigate welding residual stresses and their influence on fatigue. Although a simple prescribed temperature heat source was used in the simulations, the calculated residual stresses lay within the scatter of the measurements. The correlation between the fatigue tests and the numerical simulations confirmed the validity of the results. Crossing points and different slopes of the S-N curves could be explained by the calculated stresses at the weld toe. Furthermore, the calculated stresses were applied to perform fatigue tests on stress-relieved specimens with the equivalent stress ratios of the as-welded specimens. Overall, numerical welding simulations offer a practical and profitable addition to experimental techniques for research involving welding residual stresses.

Small-scale specimens without structural constraints may present considerable tensile welding residual stresses. These are preserved also after cutting orthogonal to the weld to produce test specimens of reduced width. Depending on the weld pass sequence, tensile transversal residual stresses can form at the weld toe of cruciform joints or K-butt welds and thus have a relevant influence on fatigue. This might be used for experimental investigations, but have undesired effects for other applications.

The presented procedure using DIC allows to detect the initiation of macroscopic cracks and monitor crack propagation in fatigue tests. It is applicable on resonance testing machines and welded specimens.

The influence of welding residual stresses on fatigue depends on the weld geometry. Residual stresses affected crack initiation and propagation differently for both investigated geometries. On the K-butt weld specimens residual stresses affected mainly crack initiation. On the longitudinal stiffener specimens residual stresses influenced both crack initiation and propagation. Overall, this differentiated effect on crack initiation and propagation distinguishes the influence of residual stresses on fatigue from that of mean stresses.

Despite this different influence on crack initiation and propagation, it is possible to assess the residual stress influence based on the stresses at the weld toe. For the investigated K-butt weld the tensile residual stresses from the weld toe resulted in an underestimation of the crack propagation phase. On the longitudinal stiffener, according to the simulations residual stress some millimetres below the weld toe are in the same magnitude as on the surface and thus affect also crack propagation. For both geometries, assuming the stresses from the weld toe as effective through crack initiation and propagation, resulted in only a small error in total fatigue life.

The presented approach allows to predict S-N curves for different welding residual stress conditions and load ratios R based on numerical simulations without residual stress measurements. In this way it allows to consider the influence of welding residual stresses in fatigue analysis. In research involving fatigue tests the approach could be used to assess if results are affected by welding residual stresses and stress-relieve treatments or costly residual stress measurements might be required. In fatigue design it could help to possibly take advantage of low stress ratios in welded structures.

10 Outlook

The presented numerical and experimental investigations contribute to the knowledge about residual stresses and fatigue. The proposed approach offers a new and practical utilisation for numerical welding simulations. From this, possible future works might be derived.

The proposed simulation approach with a prescribed temperature heat source does not take into account the actual welding energy input. The approach was applied here for hand, metal active gas welding. It has to be verified if this procedure is applicable for variations of heat input or different welding processes. Furthermore, the application to high strength steels may be investigated as residual stresses might result more relevant.

On the cruciform joint models a decrease of the transversal residual stresses towards the weld toe was observed. This is often attributed to phase transformation. But the simulations showed this occurs also without phase transformation. This indicates that the decrease might in part be caused by geometrical or heat distribution effects which might be studied. On the longitudinal stiffener the stress evaluation at the weld toe resulted problematic. Stresses were read out directly at the weld toe, in the notch, which is not completely correct because of the singularity and the unrealistic residual stress distribution at this location. It should be verified how this might be improved, what restrictions apply to the mesh size and exact modelling of the weld toe.

To make practical use of the developed approach to consider welding residual stresses in fatigue analysis the general reliability of the numerical welding simulations should be verified. The requirements and quality criteria for the simulations have to be defined in detail, possibly by adopting existing standards on the execution and validation of numerical welding simulations or by defining a specific guideline and requirements. Furthermore, it would have to be verified how the approach may be adopted within the framework of current standards and regulations on fatigue design.

The presented fatigue tests were performed with constant amplitude loading. As shown, residual stresses may be altered under loading. Variable amplitude loading, as it occurs in many real applications, will probably have an impact on the residual stress influence on fatigue. This may also include static preloads. Exemplarily a longitudinal stiffener specimen was tested after preloading with a tensile force (appendix 12.4). The specimen showed a prolonged fatigue life compared to the as-welded specimens. Further investigations might verify if this behaviour is reproducible in the simulations and if the presented approach is adoptable for variable amplitude loading.

The fatigue tests focused on small-scale specimens without external constraints. In large structures constraints will affect residual stresses and possibly their influence on fatigue. This might be investigated by large-scale experimental tests or numerical simulations to verify how the presented approach is applicable to larger structures.

The adopted procedure using DIC to monitor cracks allowed to determine the initiation of macroscopic cracks. To improve the comparability of the results and the applicability of the procedure it should be further developed. This might include a systematic study of the strain-threshold value defining cracks, the detectable crack length assumed as crack initiation or the comparison with alternative methods such as strain gauges.

11 References

ASTM E837-13a, *Test Method for Determining Residual Stresses by the Hole-Drilling Strain-Gage Method* (West Conshohocken, PA: ASTM International).

Barsoum, Z., and Barsoum, I. (2009), 'Residual stress effects on fatigue life of welded structures using LEFM', *Engineering failure analysis 16 (1)*, 2009: 449–467.

Bate, S. K., Green, D., and Buttle, D. (1997), *A review of residual stress distributions in welded joints for the defect assessment of offshore structures*.

Baumgartner, J. (2013), *Schwingfestigkeit von Schweißverbindungen unter Berücksichtigung von Schweißeigenspannungen und Größeneinflüssen, Dissertation* [Fatigue strength of welded joints under consideration of welding residual stresses and size effect, in german].

Baumgartner, J., and Bruder, T. (2013), 'Influence of weld geometry and residual stresses on the fatigue strength of longitudinal stiffeners', *Welding in the World 57*, 2013: 841–855.

Bhatti, A., and Barsoum, Z. (2012), 'Development of efficient three-dimensional welding simulation approach for residual stress estimation in different welded joints', *The Journal of Strain Analysis for Engineering Design 47 (8)*, 2012: 539–552.

Bhatti, A., Barsoum, Z., van der Mee, V. et al. (2013), 'Fatigue strength improvement of welded structures using new low transformation temperature filler materials, 5th Fatigue Design Conference', *Procedia Engineering 66*, 2013: 192–201.

Buxbaum, O. (1986), *Betriebsfestigkeit*: *Sichere und wirtschaftliche Bemessung schwingbruchgefährdeter Bauteile* [Fatigue strength: safe and economic design of fatigue-prone components, in german] (Düsseldorf: Verlag Stahleisen).

Caprace, J.-D., Fu, G., Carrara, J. F. et al. (2017), 'A benchmark study of uncertainness in welding simulation', *Marine Structures*, 56: 69–84.

Carroll, J. D., Abuzaid, W., Lambros, J. et al. (2013), 'High resolution digital image correlation measurements of strain accumulation in fatigue crack growth', *International Journal of Fatigue*, 57: 140–150.

Carroll, J. D., Efstathiou, C., Lambros, J. et al. (2008), 'Multiscale Analysis of Fatigue Crack Growth Using Digital Image Correlation', in , *Proceedings of the XIth International Congress and Exposition on Experimental and Applied Mechanics* (Orlando, FL), 163–8.

Chattopadhyay, A., Glinka, G., El-Zein, M. et al. (2011), 'Stress Analysis and Fatigue of welded structures', *Welding in the World 55*, 2011.

Cho, D. W., Na, S.-J., Cho, M.-H. et al. (2013), 'Simulation of weld pool dynamics in V-groove GTA and GMA welding', *Welding in the World*, 57: 223–233.

Christian, H., and Elfinger, F.-X. (1978), 'Eigenspannungen in Schweißnähten' [Residual stresses in welds, in german], *Der Maschinenschaden 51 Heft 3,* 1978: 124–130.

Corigliano, P., Crupi, V., and Guglielmino, E. (2018a), 'Fatigue assessment of Ti-6Al-4V titanium alloy laser welded joints in absence of filler material by means of full-field techniques', *Frattura ed Integrità Strutturale*, 43: 171–181.

Corigliano, P., Crupi, V., Guglielmino, E. et al. (2018b), 'Full-field analysis of AL/FE explosive welded joints for shipbuilding applications', *Marine Structures*, 57: 207–218.

Curtois, M., Carin, M., Le Masson, P. et al. (2019), 'Complete 3D heat and fluid flow modeling of keyhole laser welding and methods to reduce calculation times', in C. Sommitsch, N. Enzinger, and P. Mayr (eds.), *Mathematical Modelling of Weld Phenomena 12* (Mathematical Modelling of Weld Phenomena, 12, Graz: Verlag d. Technischen Universität Graz), 5–15.

Deng, D. (2010), 'Theoretical prediction of welding distortion in large and complex structures', *Frontiers of Materials Science in China 4(2)*, 2010: 202–209.

Dilger, K. (2006) (ed.), *Schlussbericht zum BMBF-Verbundprojekt SST-Schweißsimulationstool*: *Werkzeug zur vollständigen numerischen Simulation des Schmelzschweißens* [Report to the BMBF-project SST – welding simulation tool, in german] (Forschungsberichte des Instituts für Füge- und Schweißtechnik, 16, Aachen: Shaker).

Do, V., Lee, C.-H., and Chang, K.-H. (2015), 'High cycle fatigue analysis in presence of residual stresses by using a continuum damage mechanics model', *International Journal of Fatigue*, 70: 51–62.

Dong, P., Zhang, J., and Bouchard, P. (2002), 'Effects of Repair Weld Length on Residual Stress Distribution', *Journal of Pressure Vessel Technology 124*, 2002: 74–80.

Durif, E., Fregonese, M., Rethore, J. et al. (2010), 'Development of a Digital Image Correlation controlled fatigue crack propagation experiment', *EPJ Web of Conferences*, 6/31012.

Eigenmann, B., and Macherauch, E. (1995), 'Röntgenographische Untersuchung von Spannungszuständen in Werkstoffen. Teil I', *Mat.-wiss. u. Werkstofftech.*, 26: 148–160.

Elcoate, C. D., Dennis, R. J., Bouchard, P. J. et al. (2005), 'Three dimensional multi-pass repair weld simulations', *International Journal of Pressure Vessels and Piping*, 82/4: 244–257.

Eurocode 3 (2010), *Bemessung und Konstruktion von Stahlbauten - Teil 1-9: Ermüdung; Deutsche Fassung EN 1993-1-9:2005 + AC:2009* (Berlin).

Farajian, M. (2011), *Stability and relaxation of welding residual stresses* (Forschungsberichte des Instituts für Füge- und Schweißtechnik, 27, Aachen: Shaker).

Farajian, M. (2013), 'Welding residual stress behaviour under mechanical loading', *Welding in the World 57*, 2013: 157–169.

Farajian, M., Nitschke-Pagel, T., and Dilger, K. (2010), 'Residual stress relaxation of quasi-statically and cyclically-loaded steel welds', *Welding in the World*, 54/1/2: R49-R60.

FKM (2012), *Rechnerischer Festigkeitsnachweis für Maschinenbauteile aus Stahl, Eisenguss- und Aluminiumwerkstoffen, 6. Überarbeitete Ausgabe* [Strength assessment for mechanical parts of steel, cast iron and aluminium materials, in german].

Foehrenbach, J., Hardenacke, V., and Farajian, M. (2016), *Fatigue life calculation of high frequency mechanical impact (HFMI) treated welded joints by means of numerical process simulation and critical plane approaches. IIW-Doc. XIII-2637-16*.

Francis, J. A., Bhadeshia, H. K. D. H., and Withers, P. J. (2007), 'Welding residual stresses in ferritic power plant steels', *Materials Science and Technology*, 23/9: 1009–1020.

Fricke, W. (2005), 'Effects of residual stresses on the fatigue behaviour of welded steel structures', *Materialwissenschaft und Werkstofftechnik*, 36/11: 642–649.

Fricke, W., Friedrich, N., Musumeci, L. et al. (2014), 'Low-cycle fatigue analysis of a web frame corner in ship structures', *Weld World*, 58/3: 319–327.

Fricke, W., Lilienfeld-Toal, A., and Paetzold, H. (2009), *Versteifte Plattenstrukturen aus dem Stahlschiffbau im Cluster Anwendbarkeit von Festigkeitskonzepten für schwingbelastete geschweißte Bauteile*, CMT 14/2009, AiF-Vorhaben 14517N [Stiffened plate structures in steel shipbuilding in the cluster of applicability of strength concepts for welded components under fatigue loads, in german] (Hamburg).

Fricke, W., and Tchuindjang, D. (2016), *Abschlussbericht zum AiF-Vorhaben 17519 N Rissfortschrittsuntersuchung an Längssteifen zur Validierung der IBESS-Prozedur* [Report to the AiF-project 17519 N crack propagation investigations on longitudinal stiffeners for validation of the IBESS-procedure, in german].

Fricke, W., and Zacke, S. (2014), 'Application of welding simulation to block joints in shipbuilding and assessment of welding-induced residual stresses and distortions', *International Journal of Naval Architecture and Ocean Engineering*, 2014: 459–470.

Friedrich, N. (2020), 'Experimental investigation on the influence of welding residual stresses on fatigue for two different weld geometries', *Fatigue Fract Eng Mater Struct*, 2020: 1–16.

Friedrich, N., and Ehlers, S. (2019a), 'A simplified welding simulation approach used to design a fatigue test specimen containing residual stresses', *Ship Technology Research*, 66/1: 22–37.

Friedrich, N., and Ehlers, S. (2019b), 'Crack Monitoring in Resonance Fatigue Testing of Welded Specimens Using Digital Image Correlation', *Journal of visualized experiments : JoVE*, 2019.

Friedrich, N., and Ehlers, S. (2019c), 'Experimental validation of a simplified welding simulation approach for fatigue assessments', in C. Sommitsch, N. Enzinger, and P. Mayr (eds.), *Mathematical Modelling of Weld Phenomena 12* (Mathematical Modelling of Weld Phenomena, 12, Graz: Verlag d. Technischen Universität Graz), 875–91.

Goldak, J., Chakravarti, A., and Bibby, M. (1984), 'A new finite element model for welding heat sources', *Metallurgical Transactions B*, 1984: 299–305.

Goldak, J. A., and Akhlaghi, M. (2005), *Computational welding mechanics* (New York: Springer).

Grünitz, L., and Fricke, W. (2004), *Buckling Strength of Welded HY-80 Spherical Shells - A Direct Approach* (TU Hamburg-Harburg).

Günther, H.-P., and Kuhlmann, U. (2009), 'Nachweiskonzepte zur Bemessung ermüdungsbeanspruchter Bauteile unter Berücksichtigung von Schweißnahtnachbehandlungsverfahren durch höherfrequentes Hämmern' [Approval concept for fatigue design under consideration of high frequency peening post-weld treatment, in german], *Stahlbau*, 78/9: 613–621.

Gurney, T. R. (1979), *Fatigue of welded structures, 2nd edition* (Cambridge: Cambridge University Press).

Hänsch, H. (1984), *Schweißeigenspannungen und Formänderungen an stabartigen Bauteilen*: *Berechnung u. Bewertung* [Welding residual stresses and distortions on beam shaped components. Calculation and assessment] ((Fachbuchreihe Schweißtechnik, 81), Düsseldorf: Dt. Verl. für Schweißtechnik).

Hasheminejad, N., Margaritis, A., Ribbens, B. et al. (2018), 'Digital Image Correlation to Investigate Crack Propagation and Healing of Asphalt Concrete', in , *Proceedings of the 18th International Conference on Experimental Mechanics* (Brussels, Belgium).

Hensel, J., Nitschke-Pagel, T., and Dilger, K. (2016), 'Effects of residual stresses and compressive mean stresses on the fatigue strength of longitudinal fillet-welded gussets', *Welding in the World*, 60: 267–281.

Hensel, J., Nitschke-Pagel, T., and Dilger, K. (2017), 'Engineering model for the quantitative consideration of residual stresses in fatigue design of welded components', *Weld World*, 61/5: 997–1002.

Hildebrand, J. (2008), *Numerische Schweißsimulation - Bestimmung von Temperatur, Gefüge und Eigenspannung an Schweißverbindungen aus Stahl- und Glaswerkstoffen* [Numerical welding simulation - determination of temperature, microstructure and residual stresses in welded joints of steel and glass materials, in german].

Hill, M., and Nelson, D. V. (1995), 'The inherent strain method for residual stress determination and its application to a long welded joint', *ASME PVP*, 1995: 343–352.

Hobbacher, A. F. (2016), *Recommendations for fatigue design of welded joints and components* (IIW collection; Second edition, Cham: Springer).

Hong, J., Tsai, C., and Dong, P. (1998), 'Assessment of Numerical Procedures for Residual Stress Analysis of Multipass Welds', *Welding Journal, Welding Research Supplement*, 1998: 372–382.

Hutchings, M. T. (2005), *Introduction to the characterization of residual stress by neutron diffraction* (Boca Raton: Taylor & Francis).

Jang, C., Ha, Y., and Ko, D. (2003), 'An Improved Inherent Strain Analysis for the Prediction of Plate Deformations Induced by Line Heating Considering Phase Transformation of Steel', *Proceeding of The Thirteenth International Offshore and Polar Engineering Conference*, 2003: 147–152.

Josefson, B., and Karlsson, C. (1988), *FE-calculated Sresses in a Multi-pass Butt-welded Pipe - A Simplified Approach* (Göteborg).

Kandil, F. A. (2001), *A review of residual stress measurement methods*: *A guide to technique selection* (NPL report, MATC (A), Teddington: National Physical Laboratory).

Karlsson, L., Pahkamaa, A., Karlberg, M. et al. (2011), 'Mechanics of materials and structures: a simulation-driven design approach', *Journal of mechanics of materials and structures 6 (1-4)*, 2011: 277–301.

Kim, J., Jang, B., and Kang, S. (2014), 'A study on an efficient prediction of welding deformation for T-joint laser welding of sandwich panel, Part II: Proposal of a method to use shell element model', *International Journal of Naval Architecture and Ocean Engineering 6*, 2014: 245–256.

Klassen, J. (2018), *Beitrag zur vereinfachten Eigenspannungsberechnung von Mehrlagenschweißverbindungen* [Contribution to simplified residual stress calculations for multilayer welds, in german] (Forschungsberichte des Instituts für Füge- und Schweißtechnik, 46; 1. Auflage, Herzogenrath: Shaker).

Klassen, J., Friedrich, N., Fricke, W. et al. (2016), *Entwicklung von Methodiken zur Bewertung von Eigenspannungen an Montagestößen bei Stahl-Großstrukturen*, Schlussbericht [Development of

assessment methods for residual stresses of large-scale welded assembly joints, in german] (IGF-Vorhabennummer 17652N).

Klassen, J., Friedrich, N., Fricke, W. et al. (2017), 'Influence of residual stresses on fatigue strength of large-scale welded assembly joints', *Weld World*, 61/2: 361–374.

Kong, X., Asserin, O., Gounand, S. et al. (2012), '3D finite element simulation of TIG weld pool', *IOP Conference Series: Materials Science and Engineering*, 33.

Koster, M., Kenel, C., Lee, W. J. et al. (2014), 'Digital image correlation for the characterization of fatigue damage evolution in brazed steel joints', *Procedia Materials Science*, 3: 1117–1122.

Kovárík, O., Hausild, P., Capek, J. et al. (2016a), 'Resonance bending fatigue testing with simultaneous damping measurement and its application on layered coatings', *International Journal of Fatigue*, 82: 300–309.

Kovárík, O., Hausild, P., Medrický, J. et al. (2016b), 'Fatigue crack growth in bodies with thermally sprayed coating', *Journal of Thermal Spray Technology*, 25/1-2: 311–320.

Krebs, J., Hübner, and Kaßner, M. (2012), *Eigenspannungseinfluss auf Schwingfestigkeit und Bewertung in geschweißten Bauteilen, DVS-Berichte Band 234, 2. überarbeitete Auflage* [Residual stress influence on fatigue strength and assessment in welded components, in german] (Düsseldorf).

Krebs, J., and Kassner, M. (2007), 'Influence of Welding Residual Stresses on Fatigue Design of Welded Joints and Components', *Weld World*, 51/7-8: 54–68.

Lee, C.-H., Chang, K.-H., and Do, V. (2016), 'Modeling the high cycle fatigue behavior of T-joint fillet welds considering weld-induced residual stresses based on continuum damage mechanics', *Engineering Structures*, 125: 205–216.

Leitner, M., Simunek, D., Shah, S. F. et al. (2016), *Numerical fatigue assessment of welded and HFMI-treated joints by notch stress/strain and fracture mechanical approaches*.

Leitner, M., Stoschka, M., and Eichlseder, W. (2014), 'Fatigue enhancement of thin-walled, high-strength steel joints by high-frequency mechanical impact treatment', *Welding in the World, 58*, 2014: 29–39.

Lindgren, L.-E. (2007), *Computational welding mechanics - Thermomechanical and microstructural simulations* (Cambridge: Woodhead Publishing in Materials).

Lorenzino, P., Beretta, G., and Navarro, A. (2014), 'Application of Digital Image Correlation (DIC) in resonance machines for measuring fatigue crack growth', *Frattura ed Integrità Strutturale*, 30: 369–374.

Maddox, S. J. (1991), *Fatigue strength of welded structures* (Cambridge, UK: Abington Publishing).

Maletta, C., L.Bruno, P.Corigliano et al. (2014), 'Crack-tip thermal and mechanical hysteresis in Shape Memory Alloys under fatigue loading', *Materials Science & Engineering A*, 616: 281–287.

Malisius, R. (1977), *Schrumpfungen, Spannungen und Risse beim Schweißen (4., überarb. u. erw. Aufl.)* [Shrinkage, stresses and cracks in welding, in german] (Düsseldorf: Deutscher Verlag für Schweisstechnik GmbH).

Malitckii, E., Remes, H., Lehto, P. et al. (2019), 'Full-field Strain Measurements for Microstructurally Small Fatigue Crack Propagation Using Digital Image Correlation Method', *Journal of Visualized Experiments*, 143.

Murakawa, H., Deng, D., and Ma, N. (2010), 'Concept of inherent strain, inherent stress, inherent deformation and inherent force for prediction of welding distortion and residual stress', *Transactions of JWRI Vol. 39, No. 2*, 2010: 103–105.

Neumann, A. (1996), *Schweißtechnisches Handbuch für Konstrukteure. Teil 1: Grundlagen, Tragfähigkeit, Gestaltung (7., überarb. Aufl.)* [Manual of welding techniques for constructing engineers. part 1: fundamentals, load capacity, design, in german] (Düsseldorf: Deutscher Verlag für Schweißtechnik GmbH).

Neumann, A., and Röbenack, K.-D. (1978), *Verformungen und Spannungen beim Schweißen. Untersuchungsergebnisse aus Forschung und Literatur* [Distortions and stresses in welding, in german] (Düsseldorf: Deutscher Verlag für Schweißtechnik GmbH).

Niemi, E., Fricke, W., and Maddox, S. J. (2006), *Fatigue Analysis of Welded Components, Designer's Guide to the Structural Hot-Spot Stress Approach* (Cambridge: Woodhead Publishing).

Nitschke-Pagel, T. (1995), *Eigenspannungen und Schwingfestigkeitsverhalten geschweißter Feinkornbaustähle* [Residual stresses and fatigue strenght of welded fine grained steel, in german].

Nitschke-Pagel, T., and Dilger, K. (2006), 'Eigenspannungen in Schweißverbindungen - Teil 1: Ursachen der Eigenspannungsentstehung beim Schweißen' [Residual stresses in welded joints - part 1: causes for residual stresses in welding, in german], *Schweißen und Schneiden*, 9: 466–479.

Ohta, A., Maeda, Y., Nihei, M. et al. (1984), 'Variable effects of stress relief on fatigue strength of butt welded joints with different plate thickness', *Int. Journ. of Fracture*, 24: R81-R87.

Olsen, T., Runnemalm, H., and D., B. (2001), *Simulation of welding using MSC.Marc* (Schweden).

Pahkamaa, A., Karlsson, L., Pavasson, J. et al. (2010), *A method to improve efficiency in welding simulations for simulation driven design*.

Pohle, C. (1990), *Zerstörende Werkstoffprüfung in der Schweißtechnik* [Destructive material analysis in welding, in german] (Düsseldorf: Deutscher Verlag für Schweißtechnik).

Poncelet, M., Barbier, G., Raka, B. et al. (2010), 'Biaxial High Cycle Fatigue of a Type 304L Stainless Steel: Cyclic Strains and Crack Initiation Detection by Digital Image Correlation', *European Journal of Mechanics / A Solids*, 29/5.

Rabbolini, S., Beretta, S., Foletti, S. et al. (2015), 'Crack closure effects during low cycle fatigue propagation in line pipe steel: An analysis with digital image correlation', *Engineering Fracture Mechanics*, 148: 441–456.

Radaj, D. (1988), *Wärmewirkungen des Schweißens. Temperaturfeld, Eigenspannungen, Verzug* (Berlin: Springer-Verlag).

Radaj, D. (1992), *Heat effects of welding*: *Temperature field, residual stress and distortion* (Berlin: Springer).

Radaj, D. (2003), *Welding residual stresses and distortion* (Düsseldorf: DVS-Verlag).

Risbet, M., Feissel, P., Roland, T. et al. (2010), 'Digital Image Correlation technique: application to early fatigue damage detection in stainless steel', *Procedia Engineering*, 2: 2219–2227.

Rörup, J. (2003), *Einfluss von Druckmittelspannungen auf die Betriebsfestigkeit von geschweißten Schiffskonstruktionen, Dissertation, Schriftenreihe Schiffbau Bericht 619*.

Rupil, J., Roux, S., Hild, F. et al. (2011), 'Fatigue microcrack detection with digital image correlation', *The Journal of Strain Analysis for Engineering Design*, 46/6: 492–509.

Schajer, G. (1988), 'Measurement of non-uniform residual stresses using the hole drilling method', *J. of Engineering Materials and Technology*, 110/4: Part I:338-343, Part II:344-349.

Schajer, G. S. (2013) (ed.), *Practical residual stress measurement methods* (Chichester West Sussex United Kingdom: John Wiley & Sons Inc).

Shiga, C., Murakawa, H., Hiraoka, K. et al. (2015), *Development of elongated bead weld method for improvement of fatigue properties in welded joints of ship hull structure using low transformation temperature welding materials. IIW-Doc. IX-2519-15*.

Shim, Y., Feng, Z., Lee, S. et al. (1992), 'Determination of Residual Stresses in Thick-Section Weldments', *Supplement to the Welding Journal*, 1992: 305–312.

Shrama, K., Clarke, A., Pullin, R. et al. (2014), 'Detection of Cracking in Mild Steel Fatigue Specimens Using Acoustic Emission and Digital Image Correlation', in , *31st Conference of the European Working Group on Acoustic Emission* (Dresden, Germany).

Siegele, D., Baumgartner, J., Varfolomeev, I. et al. (2013), 'Lebensdauerbewertung von Schweißverbindungen unter besonderer Berücksichtigung von Eigenspannungen' [Fatigue life assessment of welds under consideration of residual stresses, in german], *Schweißen und Schneiden 65 Heft 3*, 2013: 128–135.

Smith, M. C., Akrivos, V., and Vasileiou, A. (2019), 'How reliable are prediction and measurement of weld residual stresses? Lessons from the NeT Network.', in C. Sommitsch, N. Enzinger, and P. Mayr (eds.), *Mathematical Modelling of Weld Phenomena 12* (Mathematical Modelling of Weld Phenomena, 12, Graz: Verlag d. Technischen Universität Graz), 305–36.

Spieß, L., Behnken, H., Genzel, C. et al. (2009), *Moderne Röntgenbeugung* (Vieweg+Teubner).

Stadtaus, M., and Dilger, K. (2004), *Fügeprozesssimulation - Innovative Anwendungen der Informatik. DVS-Studie* [Simulation of joining processes - innovative applications of informatics, in german] (TU-Braunschweig).

Stoschka, M., Ottersböck, M. J., and Leitner, M. (2014), *Integration of phase-dependent work-hardening into transien weld simulation*.

Sudnik, W., Radaj, D., Breitschwerdt, S. et al. (2000), 'Numerical simulation of weld pool geometry in laser beam welding', *Journal of Physics, D: Applied Physics 33*, 2000: 662–671.

Tateishi, K., Takeshi, H., Tsuruta, Y. et al. (2013), *Fatigue life extension of cracked welded joints by ICR treatment under tensile loading*.

Tavares, P. J., Ramos, T., Braga, D. et al. (2015), 'SIF determination with digital image correlation', *International Journal of Structural Integrity*, 6/6: 668–676.

Tsutsumi, S., Ueda, K., and Fincato, R. (2016), *Relaxation behavior of peening induced residual stresses predicted ba an elastoplasticity model with cyclic hardening and softening effects. IIW-Doc. XIII-2663-16*.

Ummenhofer, T., and Weidner, P. (2014), 'Verbesserungsfaktoren zur Berücksichtigung höherfrequenter Hämmerverfahren beim Ermüdungsnachweis' [Enhancement factors to consider high frequency peening in fatigue assessments, in german], *Stahlbau*, 83/S2: 16–25.

Vanlanduit, S., Vanherzeele, J., Longo, R. et al. (2009), 'A digital image correlation method for fatigue test experiments', *Optics and Lasers in Engineering*, 47: 371–378.

Varfolomeev, I., Moroz, S., Brand, M., Siegele, D. et al. (2011), *Lebensdauerbewertung von Schweißverbindungen unter besonderer Berücksichtigung von Eigenspannungen, Schlussbericht* [Fatigue assessment of welds under consideration of residual stresses, in german] (Freiburg).

VDI (2010), *VDI heat atlas* (Springer reference; 2. ed., Heidelberg: Springer).

Weich, I. (2008), *Ermüdungsverhalten mechanisch nachbehandelter Schweißverbindungen in Abhängigkeit des Randschichtzustands, Dissertation* [Fatigue properties of mechanically post-weld treated welds depending on the surface layer conditions, in german] (TU-Braunschweig).

Wichers, M. (2006), 'Schweißen unter einachsiger, zyklischer Beanspruchung. Experimentelle und numerische Untersuchungen' [Welding under uniaxial cyclic loads – Experimental and numerical research, in german], dissertation (TU-Braunschweig).

Wohlfahrt, H., Nitschke-Pagel, T., Dilger, K. et al. (2012), 'Residual stress calculations and measurements - review and assessment of the IIW round robin results', *Welding in the World*, 56/9: 120–140.

Xu, J., Chen, L., Wang, J. et al. (2008), 'Prediction of welding distortion in multipass girth-butt welded pipes of different wall thickness', *International Journal of Advanced Manufacturing 35*, 2008: 987–993.

Yuan, K., and Sumi, Y. (2013), *Welding residual stress and its effect on fatigue crack propagation after overloading* (London).

Yuan, K., and Sumi, Y. (2015), 'Modelling of ultrasonic impact treatment (UIT) of welded joints and its effect on fatigue strength', *Frattura ed Integrità Strutturale, 34*, 2015: 551–561.

Yuan, K., and Sumi, Y. (2016), 'Simulation of residual stress and fatigue strength of welded joints under the effects of ultrasonic impact treatment (UIT)', *International Journal of Fatigue*, 92: 321–332.

Zacke, S. (2012), *Eigenspannungs- und Fertigungseinflüsse an Sektionsstößen von Schiffen* [Residual stress and fabrication influences at section joints of ships, in german] (TU Hamburg-Harburg).

12 Appendix

12.1 Variation of the number of weld passes

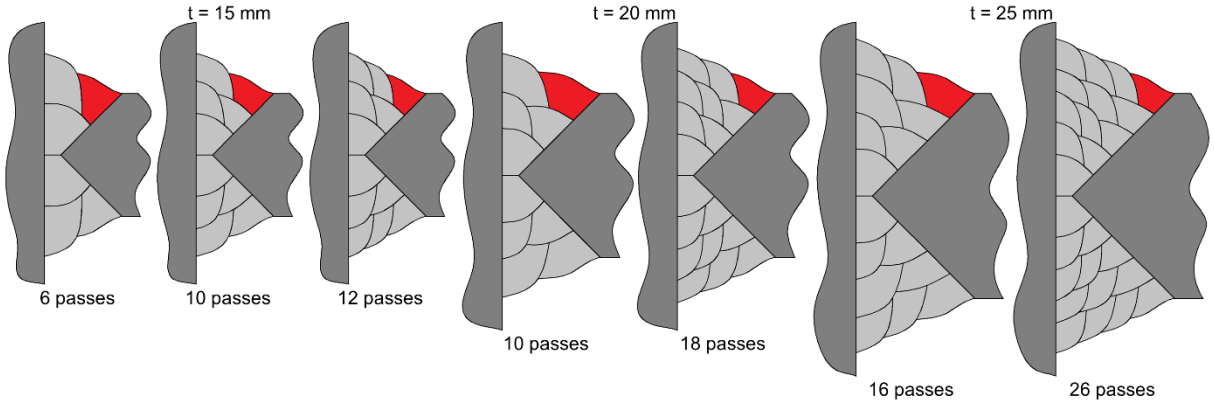

Figure 12-1: Variation of the number of weld passes for three plate thicknesses (last weld pass marked red).

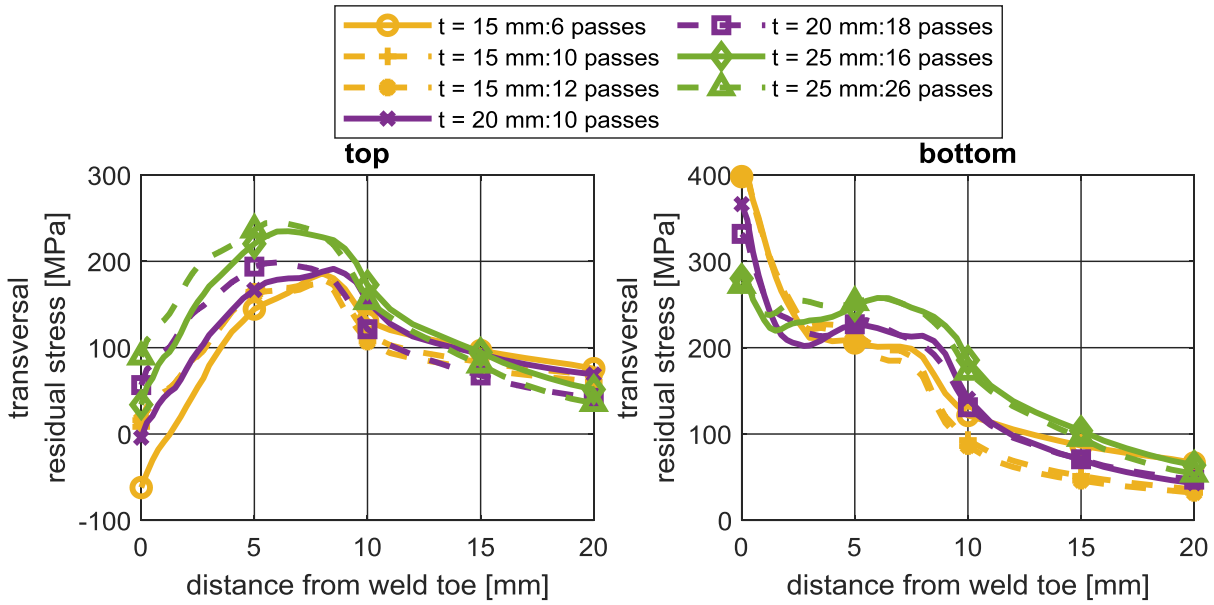

Figure 12-2: Calculated transversal residual stress depending on the number of weld passes for different plate thicknesses *t* (compare Figure 12-1).

12.2 Simulations with calibrated double ellipsoid heat source

12.2.1 K-butt weld

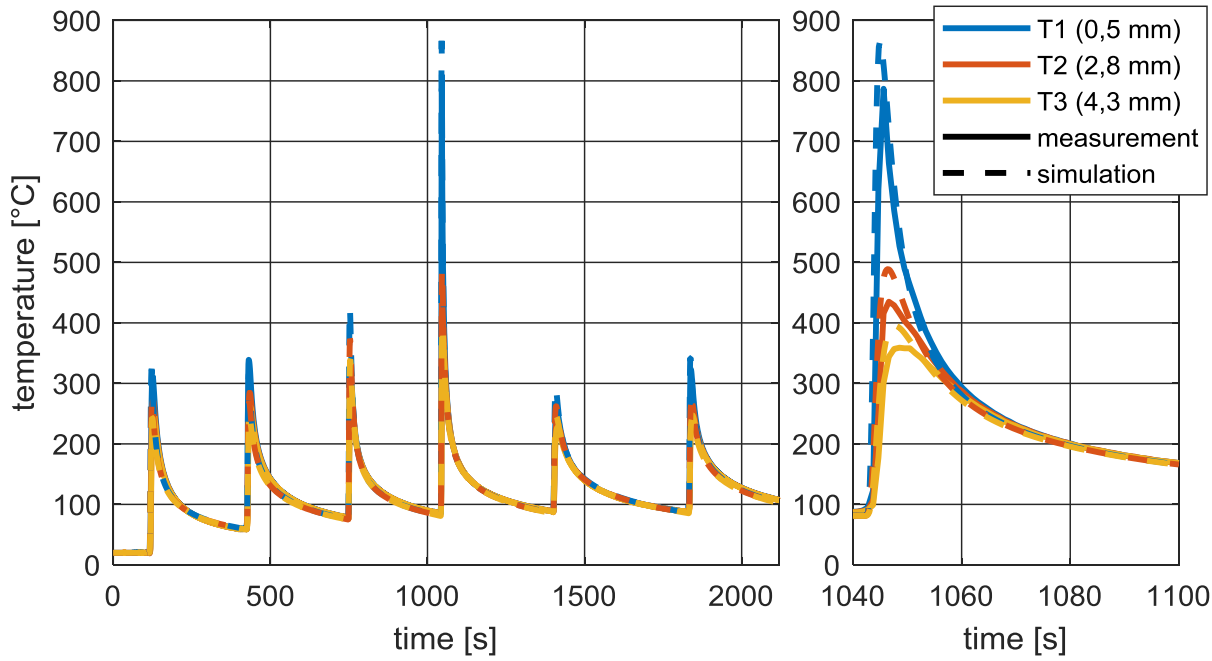

Figure 12-3: Comparison of temperatures from measurements (thermocouples T1-T3 at different distances from the weld toe) and simulation with calibrated double ellipsoid heat source (right: detail of the temperature peak at the fourth weld pass) (Friedrich and Ehlers 2019a).

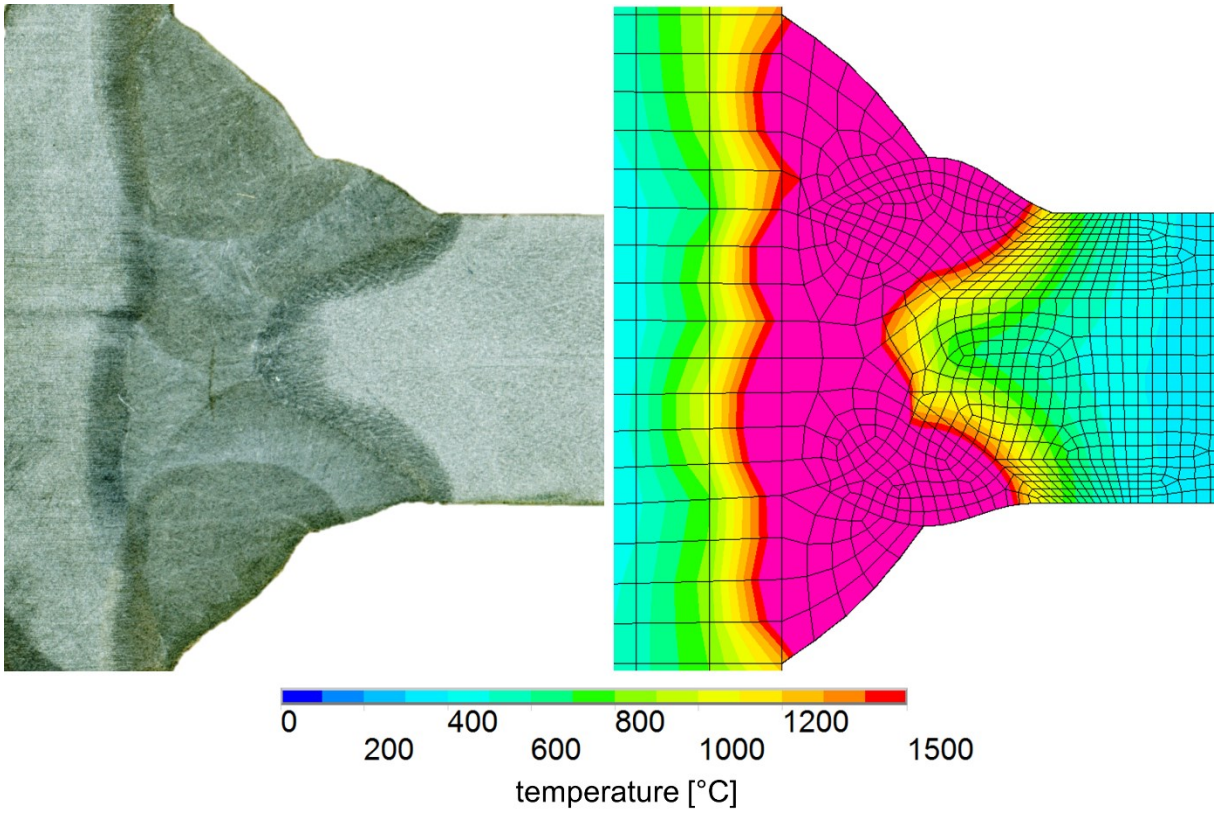

Figure 12-4: Comparison of a macrograph of the weld (left) and maximum temperatures calculated with the calibrated heat source (right) (Friedrich and Ehlers 2019a).

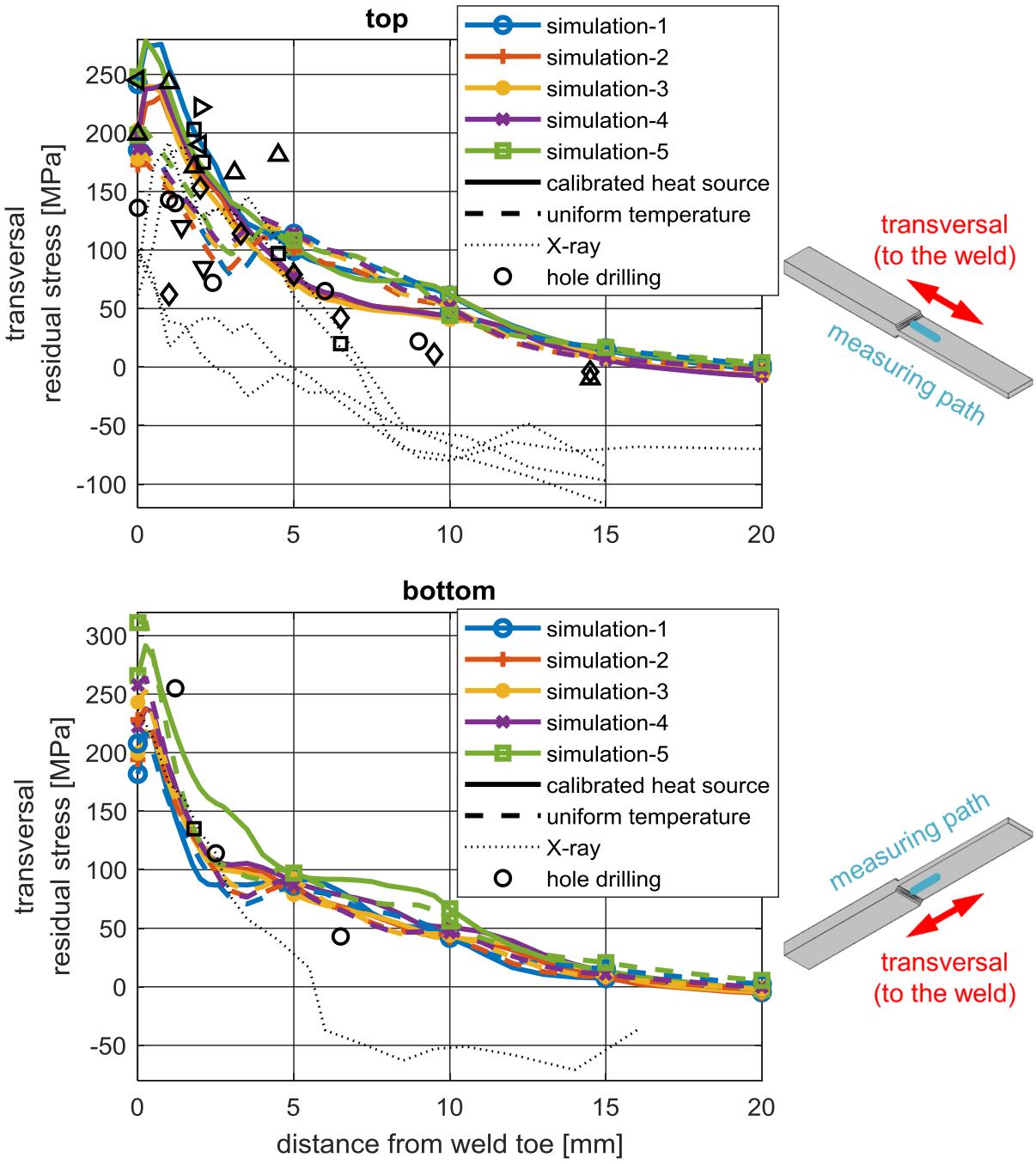

Figure 12-5: Transversal residual stress calculated with a calibrated heat source and applying a uniform prescribed temperature to the weld cross-section (simulation 1-5 refers to specimen numbers according to Figure 3-10) (Friedrich and Ehlers 2019a).

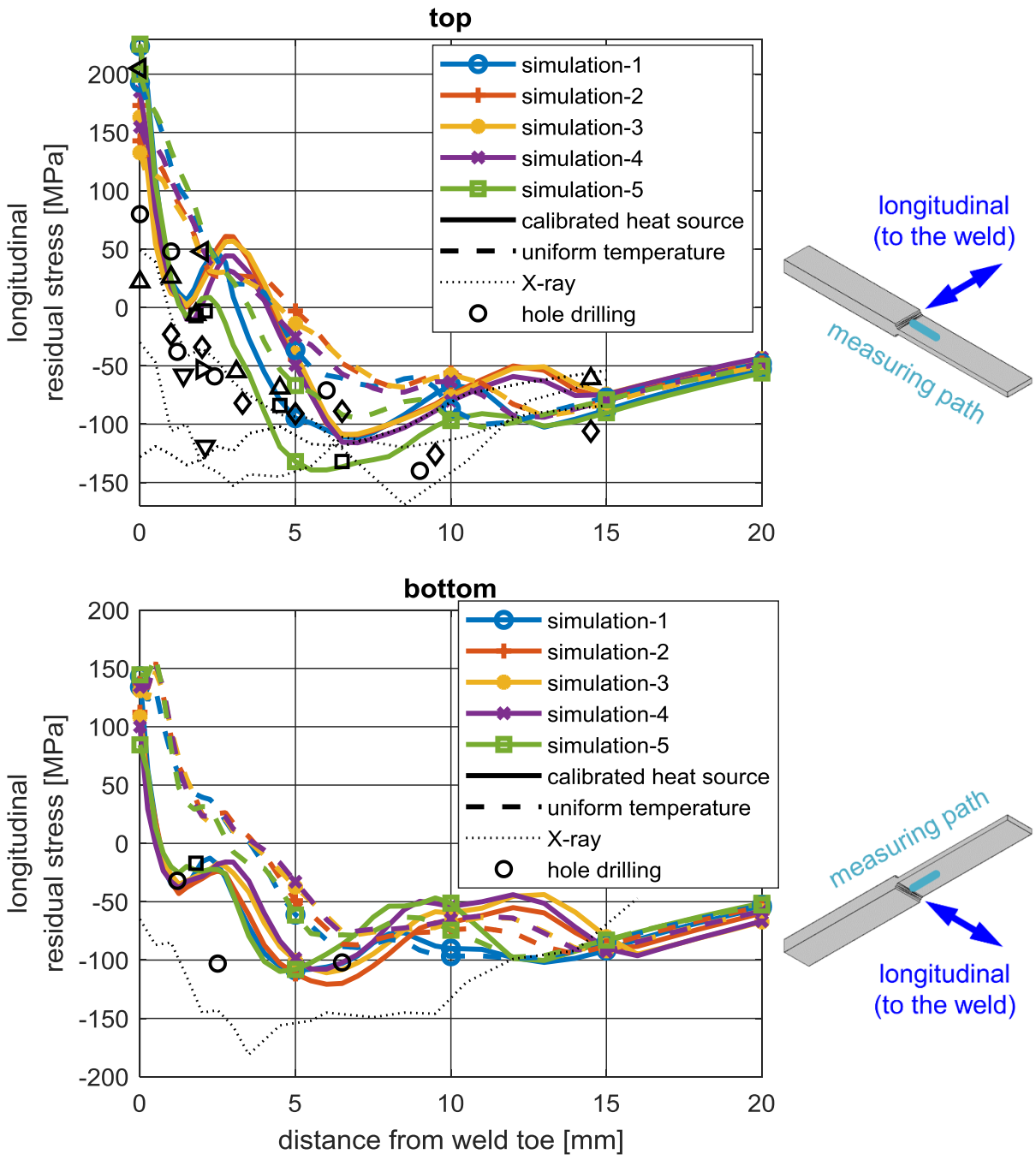

Figure 12-6: Longitudinal residual stress calculated with a calibrated heat source and applying a uniform prescribed temperature to the weld cross-section (simulation 1-5 refers to specimen numbers according to Figure 3-10) (Friedrich and Ehlers 2019a).

12.2.2 Longitudinal stiffener

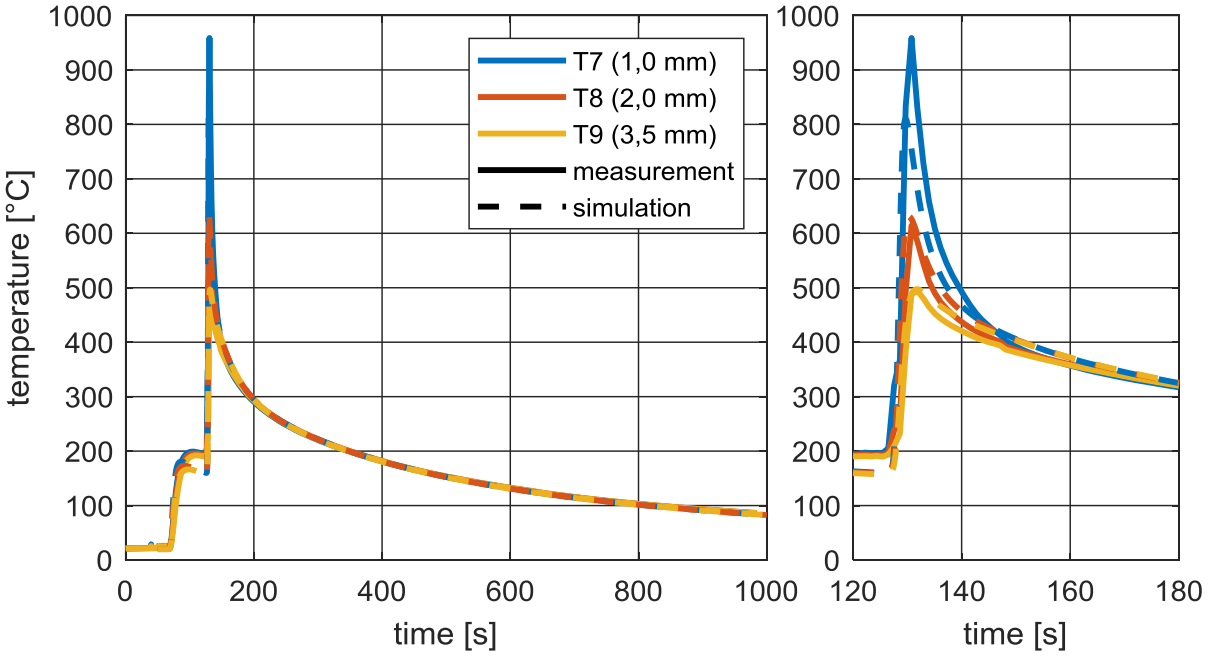

Figure 12-7: Comparison of temperatures from measurements (thermocouples T7-T9 at different distances from the weld toe) and simulation with calibrated double ellipsoid heat source (right: detail of the temperature peak).

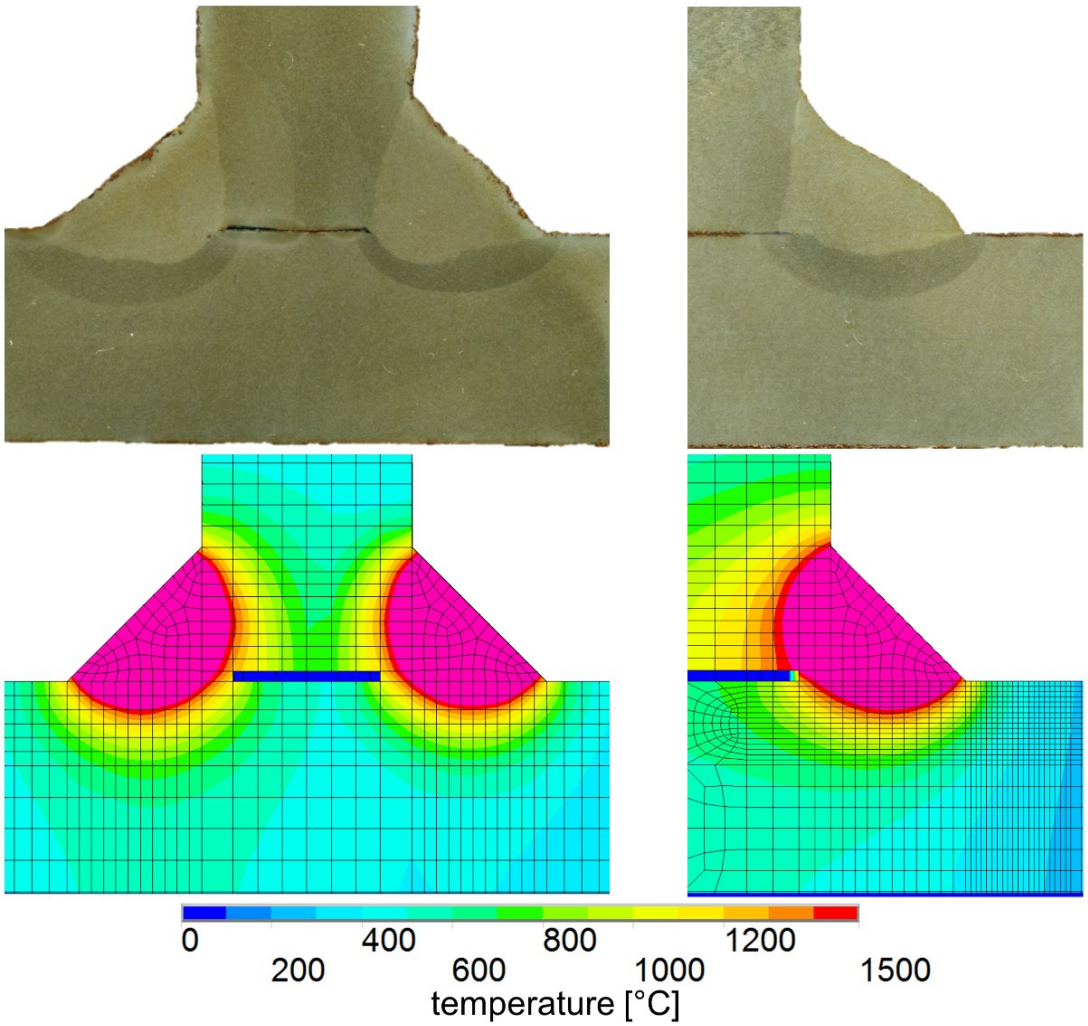

Figure 12-8: Comparison of macrographs of the weld (top) and maximum temperatures calculated with the calibrated heat source (bottom) on the cross-section (left) and at the end of the stiffener (right).

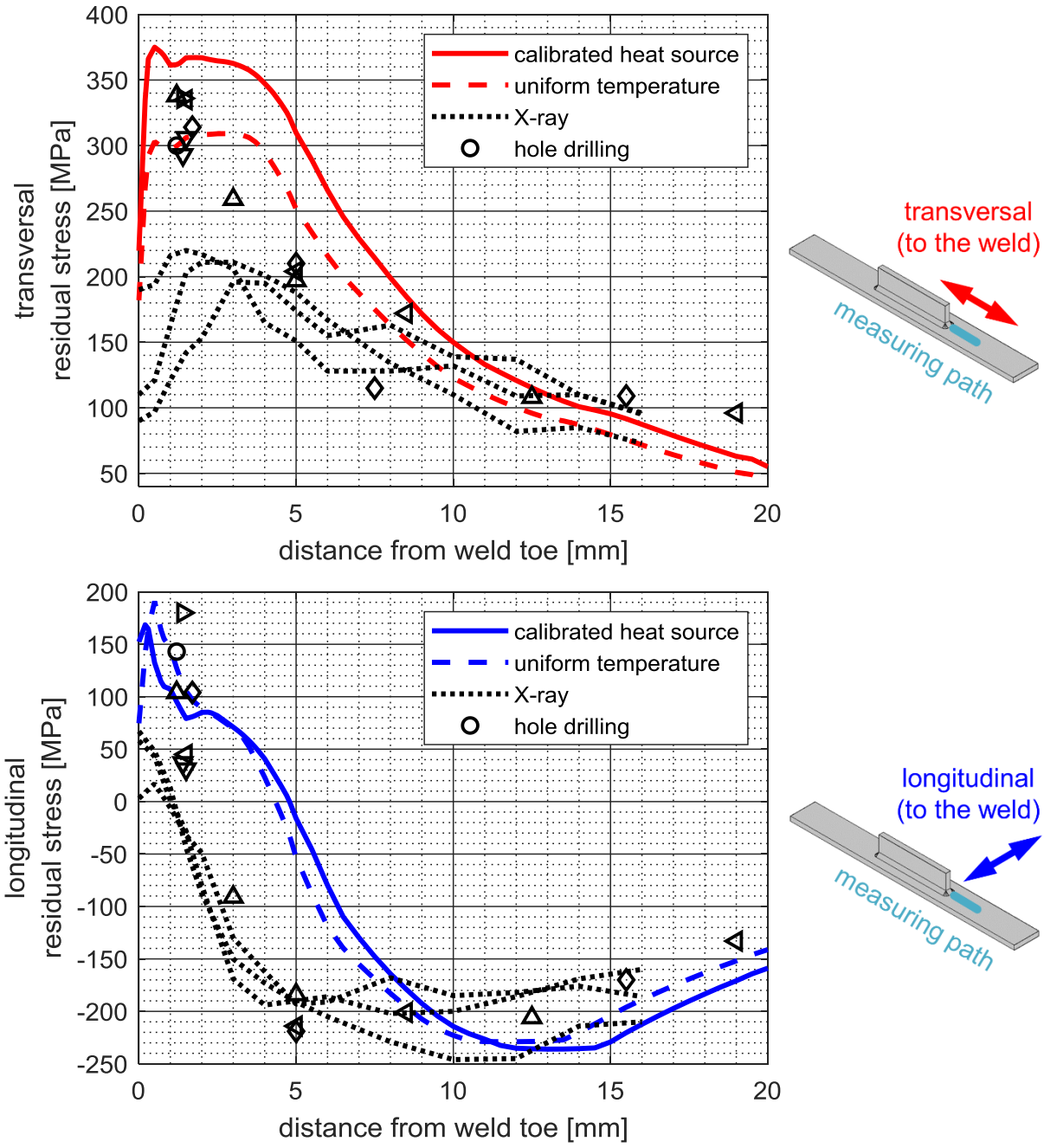

Figure 12-9: Residual stress calculated with a calibrated heat source and applying a uniform prescribed temperature to the weld cross-section.

12.3 Haigh diagrams

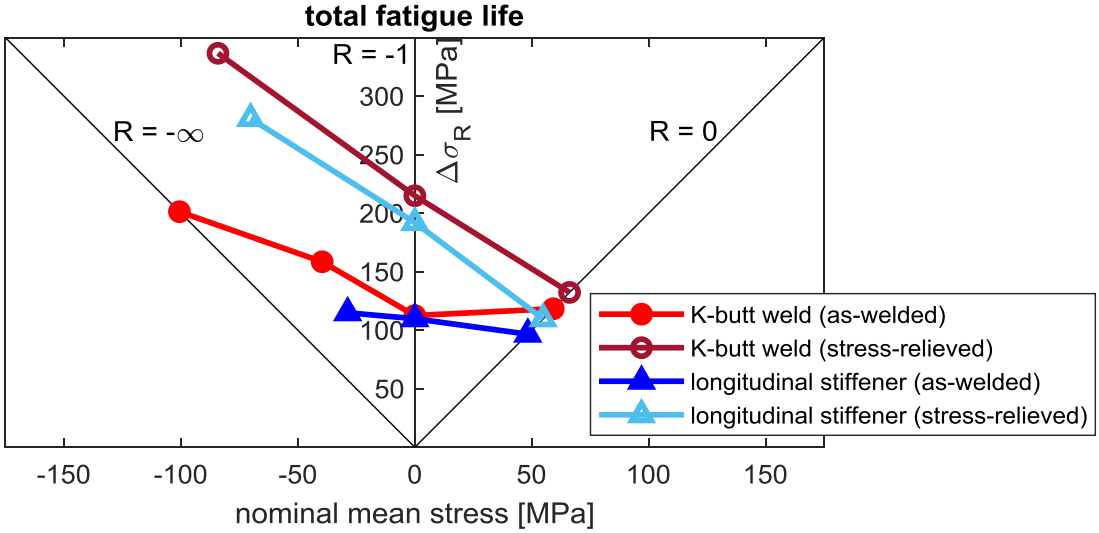

Figure 12-10: Haigh diagram for reference stress range $\Delta\sigma_R$ at $N_{total} = 2 \cdot 10^6$ load cycles (Table 6-1 and Table 6-4).

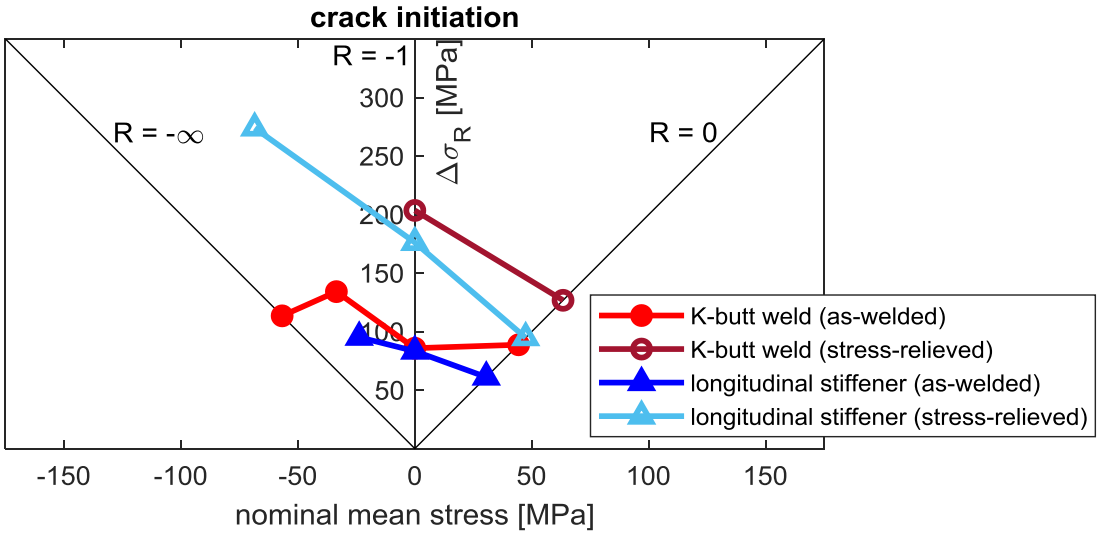

Figure 12-11: Haigh diagram for reference stress range $\Delta\sigma_R$ at $N_{initiation} = 2 \cdot 10^6$ load cycles (Table 6-2 and Table 6-5).

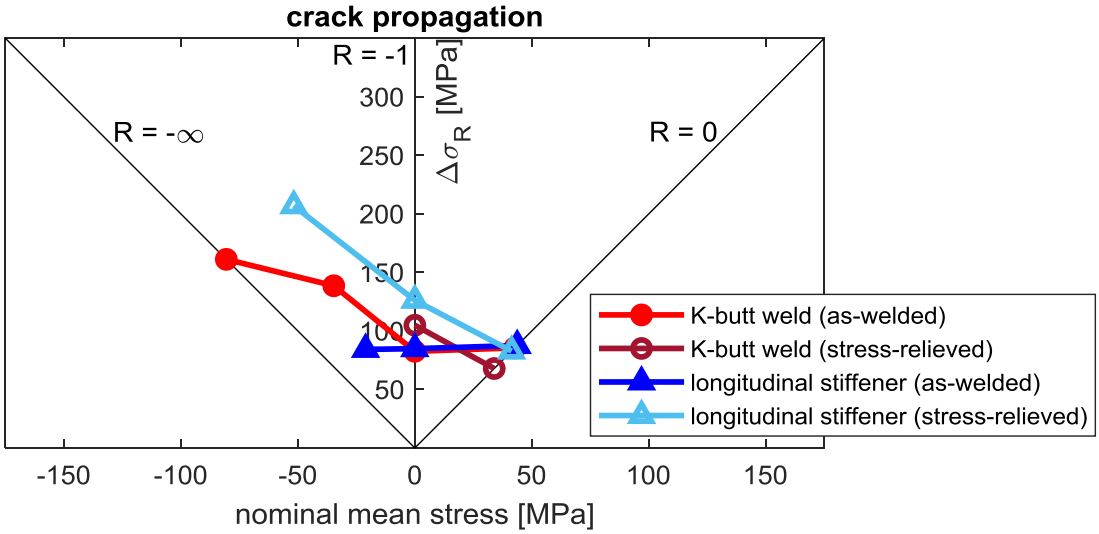

Figure 12-12: Haigh diagram for reference stress range $\Delta\sigma_R$ at $N_{propagation} = 2 \cdot 10^6$ load cycles (Table 6-3 and Table 6-6).

12.4 Preloaded longitudinal stiffener

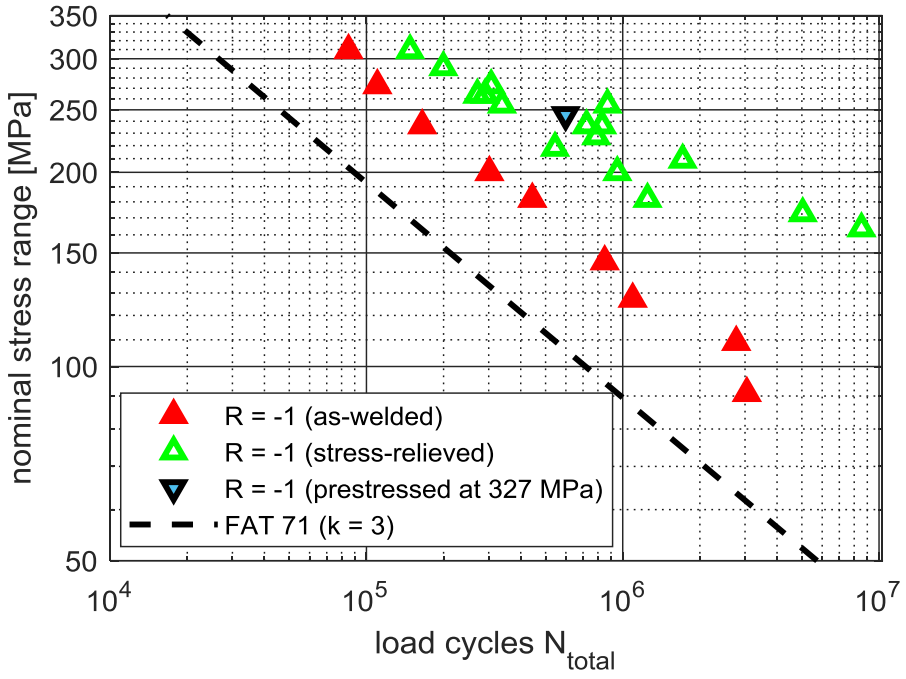

Figure 12-13: Fatigue test result for a preloaded longitudinal stiffener specimen.